HYDRODYNAMICS OF THE FREE SURFACE FLOW IN PELTON TURBINE BUCKETS

THÈSE N^{O} 3715 (2007)

PRÉSENTÉE LE 9 FÉVRIER 2007
À LA FACULTÉ DES SCIENCES ET TECHNIQUES DE L'INGÉNIEUR
Laboratoire de machines hydrauliques
SECTION DE GÉNIE MÉCANIQUE

ÉCOLE POLYTECHNIQUE FÉDÉRALE DE LAUSANNE

POUR L'OBTENTION DU GRADE DE DOCTEUR ÈS SCIENCES

PAR

Alexandre PERRIG

ingénieur mécanicien diplômé EPF
de nationalité suisse et originaire de Brigue (VS)

acceptée sur proposition du jury:

Prof. P. Xirouchakis, président du jury
Prof. F. Avelan, Dr M. Farhat, directeurs de thèse
Dr E. Parkinson, rapporteur
Prof. A. Schleiss, rapporteur
Prof. F. Sotiropoulos, rapporteur

ÉCOLE POLYTECHNIQUE
FÉDÉRALE DE LAUSANNE

Lausanne, EPFL
2007

"Non quia difficilia sunt non audemus,
sed quia non audemus difficilia sunt[1]*."*

Sénèque

---

[1] "Ce n'est pas parce que les choses sont difficiles que nous n'osons pas, c'est parce que nous n'osons pas qu'elles sont difficiles". *Lettre* 104 à *Lucilius*

À la femme de ma vie,

Remerciements

Il m'importe de témoigner ma reconnaissance, ici, en préambule de ce document, à toutes celles et ceux qui ont contribué d'une façon ou d'une autre au succès de cette thèse.

Ce travail de recherche n'aurait pas été possible sans l'appui scientifique et financier de la CTI, de VATech Hydro SA et du CSCS. Merci pour leur engagement tourné vers la réussite du projet.

Que les membres du jury soient salués pour leur sagacité, leurs questions pertinentes et les remarques intéressantes formulées lors de l'examen oral du 12.12.2006 !

Je me dois d'exprimer ma sincère gratitude à l'encontre de mes deux directeurs de thèse, le Prof. François Avellan et le Dr. Mohamed Farhat pour la confiance qu'ils m'ont témoignée en me proposant de venir faire ma thèse au LMH. Merci au premier pour la grande liberté d'action qu'il m'a accordée, et d'avoir toujours exigé le meilleur de moi-même. Accessoirement merci également pour les séances d'analyse, peut-être que je gère un peu mieux mon "nœud" aujourd'hui. Quant à Mohamed, merci pour l'encadrement, et de m'avoir fait confiance malgré des divergences de vue, parfois, ou quand les résultats tardaient. Merci de m'avoir confié la caméra rapide alors flambant neuve pour mes essais peu conventionnels.
Il me tient à cœur de témoigner ma reconnaissance au Prof. Jean-Louis Kueny pour ses précieux conseils, et les mots-clés lâchés au détour d'une discussion qui m'ont plus d'une fois ouvert les yeux. Merci également d'avoir souvent été le seul à croire à mes idées souvent jugées trop farfelues et irréalisables par mes collègues.

J'exprime ma gratitude à l'encontre du Dr. Etienne Parkinson pour l'intérêt qu'il a gardé tout au long du projet. Je garderai un excellent souvenir des séances de brainstorming dans la mansarde de VATech à Vevey, au milieu des archives. Merci à Hélène Garcin pour avoir dépensé sans compter son temps précieux pour m'aider à réaliser et traiter les calculs numériques.

Une mention spéciale à l'équipe de visualisations du CSCS. La grande maîtrise et le professionnalisme du Dr. Jean Favre et de Mario Valle m'ont impressionné, et parfois intimidé. Un coup de chapeau à Théophane Foggia pour son enthousiasme et sa passion communicative. C'est en discutant avec lui que je me suis plus d'une fois rendu compte que ce que je faisais était réellement intéressant...

Un énorme merci aux équipes du Bureau d'étude, Pierre Barmaverain en tête, et des

mécaniciens du LMH, sans lesquels rien n'aurait été possible. Une palme à notre inénarrable chef d'atelier, Louis Bezençon, qui a toujours su transformer mes élucubrations et mes concepts compliqués en mécanismes simples, robustes, fiables, bref made in Switzerland. Je n'oublierai jamais ses expressions quand je venais lui soumettre mes dernières idées. ”Hou! Colonel, mais c'est une charognerie du diable, cette histoire-là, ça veut jamais tenir!”, lançait-il en levant les bras au ciel. Je me souviendrai en tout cas toute ma vie de ce jour funeste de novembre 2004 quand la roue instrumentée est tombée sur le sol de l'atelier. Violacé, chancelant, Louis s'était écrié: ”Tout est foutu!” avant de se remette au travail et de tout réparer... en 2 jours. Merci à Maxime pour les longues discussions à échanger nos souvenirs de voyage, à Christian pour son humour sympathique, à Raymond pour son caractère bien trempé, et à Jean-Daniel avec qui nous avons échangé nos souvenirs militaires.

Mes pensées vont également à l'équipe du laboratoire de VATech Hydro à Vevey, surtout à MM. Charles-André Pérusset et Edouard Pauly pour leur disponibilité, leur patience lors des interminables séances de mise au point, et des retouches permanentes apportées au stand d'essai.

Naturellement, je tire un coup de chapeau à mes collègues doctorants, compagnons d'infortune dans le grand voyage vers l'Inconnu que représente une thèse. Une mention toute particulière pour Bob : un grand merci à ce cher Silverback, pour sa disponibilité, ses conseils toujours avisés et son inaltérable passion. J'admire ses compétences et sa rigueur, et je dois avouer m'être senti souvent un peu ridicule et terriblement superficiel en comparaison. Il restera un peu comme mon troisième directeur de thèse. Je remercie Ali, Youcef, Faiçal, Lluis, avec qui je partage le même pessimisme, Philippe pour son humour, Olivier, Stefan pour les discussions auf Deutsch, Nicolas ”Konichiwa”, Monica, Lavinia, ainsi que ceux que j'oublie au moment de rédiger ces quelques lignes. Une mention particulière à Sonia qui a posé avec son travail des fondations solides sur lesquelles j'ai pu construire mes recherches. Merci aux nouveaux venus, notamment à Cécile pour son aide précieuse sur Latex, bien utile lors de la rédaction.
Merci à tous les autres collaborateurs du LMH, Henri-Pascal Mombelli, Georges Crittin pour les discussions aéronautiques, Tino pour son éternelle bonne humeur, et à Maria pour sa présence sympathique.

Je remercie naturellement ma famille, mes parents et mon frère David, de m'avoir poussé à me lancer dans ce travail, et de m'avoir encouragé et soutenu tout au long de ces années.

Et je terminerai par la personne sans laquelle ma vie ne serait pas ce qu'elle est aujourd'hui, ma femme Glaucia. Je la remercie de m'avoir soutenu lors des moments les plus difficiles, d'avoir sauvé ma thèse en me convainquant de ne jamais abandonner quand tout paraissait perdu, et de m'avoir probablement sauvé la vie une certaine avant-veille de Noël quelque part au fin fonds du Brésil.

Alexandre Perrig

Résumé

Le design des turbines Pelton est plus difficile que celui des turbines à réaction, et leurs performances inférieures. En effet, les turbines Pelton comportent 4 types d'écoulements: (i) confinés en régime permanent, (ii) jets libres, (iii) $3D$ à surface libre dans les augets, (iv) dispersés biphasiques dans le bâti. L'écoulement dans les turbines Pelton n'a donc pas été analysé avec autant de détail que dans les turbines à réaction, et donc la compréhension de la physique de phénomènes clés, comme l'interaction jet/auget ou la coupure du jet, est faible.

Dans le cadre de la présente étude, l'écoulement dans les augets est étudié au moyen de 4 approches expérimentales et numériques: (i) Mesures embarquées des pressions pariétales instationnaires sur la surface intérieure, le dos, ainsi que les côtés des augets. (ii) Visualisations rapides de l'écoulements (embarquées et externes). Des endoscopes de petite dimension sont installés soit dans un auget, pour observer l'écoulement relatif, soit dans le bâti pour observer l'interaction jet/auget. (iii) Mesures embarquées des épaisseurs des nappes d'eau dans l'auget. (iv) Simulations numériques. Le modèle biphasique homogène et le modèle diphasique complet sont confrontés aux résultats des mesures. Le modèle biphasique complet offre la meilleure précision, tandis que le modèle biphasique homogène est trop diffusif.

L'interaction jet/auget initiale met en évidence de possibles effets de compressibilité, conduisant à l'éclatement du jet ainsi qu'à de l'érosion. Lors de l'impact du jet sur la surface interne de l'auget, un pic de pression d'origine compressible apparaît, dont l'amplitude est supérieure à celle d'un point d'arrêt machine bloquée.

Le jet reste attaché au dos de l'auget tard dans le cycle de travail, le détachement étant dépendant de la chute d'essai. Le dos de l'auget se comporte comme l'extrados d'un profil hydrodynamique soumis à l'effet Coanda, créant une dépression, donc une force de portance ayant une contribution positive sur le couple des augets et de la machine. Cependant, la dépression induit l'apparition de cavitation, et donc d'érosion.

L'écoulement principal est indépendant de la chute d'essai. Des pertes par mélange sont mises en évidence, dues soit au croisement de lignes de courant, soit à des interférences entre écoulements.

L'analyse de la distribution de puissance de l'auget met en évidence la contribution importante de la région centrale. Le signal de puissance de la roue entière présente d'importantes fluctuations modulées par les conditions d'écoulement.

L'influence respective des différentes forces agissant sur l'écoulement est mise en évidence à partir de l'équation de conservation de la quantité de mouvement. Si les forces d'inertie dominent, c'est-à-dire l'effet de la déviation, ainsi que les forces de Coriolis et centrifuge, les forces de tension superficielle et les forces visqueuses les surpassent à la fin du processus d'évacuation de l'eau et dans le processus de coupure du jet.

L'amélioration des performances des turbines Pelton nécessite de tenir compte des forces secondaires, c'est-à-dire des forces de tension superficielle et de viscosité pour l'écoulement dans l'auget, et d'améliorer le dos de l'auget pour maximiser la contribution au couple tout en permettant une découpe nette du jet.

Mots-clés:
Cavitation, compressibilité, érosion, impact, instationnarité, jet libre, similitude, surface libre, tension superficielle, transfert d'énergie, turbine Pelton.

Abstract

The design of Pelton turbines has always been more difficult than that of reaction turbines, and their performances lower. Indeed, the Pelton turbines combine 4 types of flows: (i) confined, steady-state flow in the piping systems and injector, (ii) free water jets, (iii) $3D$ unsteady free surface flows in the buckets, and (iv) dispersed 2-phase flows in the casing.

The flow in Pelton turbines has not been analyzed so far with such detail as the flow in the reaction turbines, thus the understanding of the physics of key phenomena, *i.e.* the initial jet/bucket interaction or the jet cut process, is weak. Moreover, some machines present erosion damages that have not been satisfactorily explained so far.

In the framework of this study, the flow in the buckets is investigated with 4 experimental and numerical approaches: (i) Unsteady onboard wall pressure measurements. 43 piezo-resistive pressure sensors are distributed on the bucket inner surface, backside and sides. (ii) High-speed flow visualizations (onboard and external). Small rigid endoscopes are fitted either in a bucket, to observe the relative flow, or in the casing to observe the jet/bucket interaction. (iii) Onboard water film thickness measurements. (iv) CFD simulations. The 2-Phase Homogeneous Model and the 2-Fluid Models are compared with the experimental data. The 2-Fluid Model appears to be more accurate, while the 2-Phase Homogeneous Model is too diffusive.

The initial jet/bucket interaction evidences the probable occurrence of compressible effects, generating an outburst of the jet and leading to erosion damages. When the jet impacts the bucket inner surface, a high-pressure pulse, which amplitude is larger than the equivalent stagnation pressure, is generated, caused by compressible effects.

The jet appears to remain attached to the backside of the buckets far in the duty cycle, and the separation to be dependent on the test head. The bucket backside acts as the suction side of a hydrofoil undergoing the Coanda effect, generating a depression, and in turn a lift force contributing positively to the bucket and runner torques. The depression nevertheless onsets cavitation, causing erosion damages.

The main bucket flow is independent on the test heads. Mixing losses are put into evidence, either due to the crossing of streamlines or due to flow interferences.

An analysis of the bucket power budget highlights the important contribution of the central area in terms of power transferred from the fluid to the bucket. The power signal of the whole runner shows important fluctuations that are modulated by the operating conditions.

From the Momentum conservation equation, the respective influence of the different forces acting on the flow are evidenced. Even if the inertia forces, *i.e* the deviation, Coriolis and centrifugal forces, globally dominate, the viscous and surface-tension forces outweigh the formers at the end of the evacuation process and in the jet separation process.

Obtaining significant improvements of the performances of Pelton turbines requires to adequately take into account the secondary forces, *i.e.* surface tension and viscosity, for the bucket flow and to improve the design of the backside in order to maximize the torque while promoting a neat separation.

Keywords:
Cavitation, compressibility, energy transfer, erosion, free jet, free surface, impact, similitude, surface tension, Pelton turbine, unsteadiness.

Contents

INTRODUCTION 3

1 Pelton turbine and Free-surface flows 3
  1.1 Foreword 3
  1.2 Pelton turbines: historical introduction 3

2 Framework of the study 7
  2.1 Problem to solve 7
  2.2 Literature review 9
    2.2.1 Research and development 9
    2.2.2 Analytical studies 9
    2.2.3 Experimental studies 9
    2.2.4 Numerical models 10
  2.3 Methodology and objectives 11
  2.4 Case study 12
    2.4.1 Hillchart and operating points investigated 12
  2.5 Thesis document organization 13
    2.5.1 Part I 14
    2.5.2 Part II 14
    2.5.3 Part III 14

I FREE-SURFACE FLOWS IN ROTATING FRAMES 17

3 Euler's equation for turbomachines 19
  3.1 Kinetic Momentum theorem 19
    3.1.1 Power transferred to the runner 20
    3.1.2 Euler's equation 21

4 The Pelton turbine 23
  4.1 Operating principle 23
    4.1.1 Hydraulic efficiency 25
  4.2 Pelton turbine design 26
    4.2.1 Number of buckets 26
    4.2.2 Bucket angle of setting 26
    4.2.3 Bucket surface shape 26
  4.3 Influence of head and speed variations 28

5 Rotating free surface flows **29**
5.1 Fundamental equations of fluid mechanics 29
5.1.1 Surface tension 30
5.2 Rotating flows 31
5.2.1 Governing equations 31
5.2.2 Dimensionless form 32
5.2.3 Step-up procedure 33

6 Physical models **35**
6.1 Foreword 35
6.2 Multi-Fluid Models 35
6.3 Homogeneous Models 37
6.3.1 Brackbill's surface tension model 39
6.4 Turbulent homogeneous flow formulation 39
6.4.1 Zero-equation models 40
6.4.2 k-ε models 40
6.4.3 k-ω models 41
6.4.4 SST models 42
6.5 Turbulent multifluid flow formulation 42
6.5.1 Reynolds Stress Turbulence Models 43

7 Main definitions **45**
7.1 Duty cycle and angular datum definitions 45
7.2 Non-dimensionalization of pressure 46
7.3 Non-dimensionalization of water thickness 46

II INVESTIGATION TOOLS **47**

8 Experimental facilities **49**
8.1 Test rig 49

9 Onboard pressure measurements **51**
9.1 Measurement tools 51
9.1.1 Piezo-resistive pressure transducers 51
9.1.2 Instrumented shaft 52
9.2 Instrumented runner 52
9.2.1 Sensors location and distribution 53
9.2.2 Machining 54
9.2.3 Transducers installation 54
9.2.4 Final assembly 54
9.3 Calibration procedures 54
9.3.1 Static calibration 54
9.3.2 Dynamic calibration 56
9.3.3 Data reduction 56

10 Flow visualizations **59**
10.1 Requirements 59
10.1.1 Optical requirements 59
10.1.2 Exposure time requirements 59
10.1.3 Lighting requirements 60
10.2 Observation tools 60
10.2.1 Borescopes 60
10.2.2 High speed camera 60
10.2.3 Lighting systems 61
10.3 Onboard flow visualizations 61
10.3.1 Endoscope location 61
10.3.2 Setup 62
10.3.3 Trigger chain 63
10.3.4 Images processing 64
10.4 External flow visualizations 64
10.4.1 Positions of observation 64
10.4.2 Trigger chain, frame rate and exposure time 65

11 Water film thickness measurements **69**
11.1 Water thickness by refraction 69
11.2 Processing technique 71
11.3 Validation test 71
11.4 Error estimation and propagation 72

12 Numerical approaches **75**
12.1 setup 75
12.1.1 Discretization 75
12.1.2 Boundary conditions 76
12.1.3 Initial conditions 76
12.2 Quality check 76
12.2.1 Mesh dependency 76
12.3 Discussion of the results 77
12.3.1 Pressure distribution 77
12.3.2 Water film thickness 79
12.3.3 Flow Patterns 80
12.3.4 Most suited numerical Model 84

III RESULTS AND ANALYSIS **87**

13 Bucket duty cycle **89**
13.1 Description 89

14 Inlet flow **97**
14.1 Impact of the bucket tip on the jet surface 97
14.1.1 Approach 98
14.1.2 $2D$ simplification: kinematic study 98

14.1.3 Impact problem formulation 101
14.1.4 Impact problem solution 104
14.1.5 Spillway effect 105
14.2 Jet impact and waterhammer 105
14.2.1 Zone delimitation 105
14.2.2 Peak of pressure versus operating conditions and head 107
14.2.3 Impact pressure theory 107
14.2.4 Pressure signal and onboard visualization synchronization 108
14.2.5 Time constants 111
14.2.6 Peak real amplitude estimation 111

15 Backside flow 113
15.1 Observations 113
15.2 Kinematic problem 113
15.3 Bucket hydrodynamic chord, BHC 118
15.4 Influence of the test head 118
15.5 Effect of ventilation 123
15.6 Coanda effect 123
15.7 Cavitation 125
15.7.1 Erosion damages 126
15.8 Consequences on performances 126
15.8.1 Backside torque 126
15.8.2 Jet deviation 127

16 Bucket Flow 131
16.1 Pressure and water film thickness signals 131
16.1.1 Zone 1 139
16.1.2 Zone 2 139
16.1.3 Zone 3 139
16.1.4 Zone 4 139
16.1.5 Zone 5 140
16.1.6 Analysis of the results 140
16.2 Mixing losses 140
16.2.1 Mixing losses 140
16.2.2 Crossing of streamlines 141
16.2.3 Flow interferences 141
16.3 Flow stratification 142
16.4 Draining-off 143

17 Outflow heeling 147
17.1 Lateral pressure distribution 147
17.1.1 Frontal area 147
17.1.2 Central area 147
17.1.3 Aft area 147
17.1.4 Consequences 147

18 Power Budget **155**
18.1 Local Power definition 155
18.2 Power distribution 155
18.3 Bucket and runner power fluctuations 158
    18.3.1 Amplitude spectra 159

19 Momentum transfer **161**
19.1 Energy balance 161
19.2 Energy transfer mechanism 161
    19.2.1 Assessment test 163

SUMMARY AND CONCLUSION 169

20 Summary and conclusion **169**
20.1 Summary 169
    20.1.1 Investigation tools 169
    20.1.2 Flow analysis 170
20.2 Contribution of the present work 171
20.3 Perspectives 172
    20.3.1 Experiments 172
    20.3.2 Numerical simulation 173
    20.3.3 Optimum design 173

APPENDICES 177

A Signal processing **177**
A.1 Average and standard-deviation 177
A.2 Phase average 178
A.3 Fourier transform 178
A.4 Spectral analysis of random signals 179
    A.4.1 Hanning's Window 179

B Measurement error assessment **181**

C Free water jet **183**
C.1 Jet boundary stratification 183
C.2 Fundamental equations 184
C.3 Turbulent diffusivity 184
C.4 Spread angle 185
C.5 Application to the case studied 186
C.6 Speed of sound and void fraction 186

D Coanda effect **189**
D.1 Definition 189
D.2 Potential flow problem 190
D.3 Viscous flow problem: boundary layer along a curved wall 190

D.4 Inviscid wall-jet 190
D.5 Influence of the Reynolds number 191
D.6 Free-surface flows 191

Bibliography 195

List of figures 205

List of tables 208

Index 209

List of publications 215

Vitae 217

Notations

LATIN CHARACTERS

Pelton turbines

B_2	Bucket width	[m]
D_0	Injector nozzle diameter	[m]
D_1	Runner tangent diameter	[m]
D_2	Jet contracted diameter	[m]
D_b	Runner tip diameter	[m]
H	Test head	[m]
k_{c_o}	Injector speed coefficient	[-]
k_{c_u}	Peripheral speed coefficient	[-]
P	Power	[W]
Q	Discharge	[m^3/s]
s	Needle stroke	[m]
z_o	Number of injectors	[-]
z_1	Number of buckets	[-]

Vectorial

$\overrightarrow{C}$	Absolute velocity	[m/s]
$\overrightarrow{F}$	Force	[N]

$\overrightarrow{f}$	Body force	[N]
$\overrightarrow{g}$	Universal gravity acceleration	[m/s^2]
$\overline{\overline{I}}$	Identity matrix	[-]
$\overrightarrow{n}$	Unit outward normal vector	[m]
$\overrightarrow{r}$	Position vector	[m]
$\overrightarrow{T}$	Torque	[Nm]
$\overrightarrow{U}$	Peripheral velocity	[m/s]
$\overrightarrow{W}$	Relative velocity	[m/s]

Optical

D	Lamp-to-subject distance	[m]
d_{blur}	Motion blur distance	[m]
$f/$	Lens aperture	[-]
n	Refraction indice	[-]
s	Film sensitivity speed	[-]
t_{exp}	Required exposure time	[s]
$t_{shutter}$	Shutter speed	[s]

Miscellaneous

a	Speed of sound	[m/s]
C	Reference velocity	[m/s]
Cp	Pressure coefficient	[-]
e	Internal energy	[J/kg]
Fr	Froude number	[-]
f_N	Runner rotation frequency	[Hz]
H	Test head	[m]
H'	Relative head	[m]
h_n	Enthalpy of phase n	[J/kg]
k	Turbulent kinetic energy	[J/kg]
L	Reference length	[m]
M	Mach number	[-]
m	Mass	[Kg]
P	Pressure	[bar]
Q	Heat transfer	[J/kg]
R	Free-surface radius of curvature	[m]
Re	Reynolds number	[-]
Ro	Rossby number	[-]

t	Time	[s]
t	Water film thickness	[m]
t'	Water film thickness	[-]
U	Potential energy	[J/kg]
W	Work delivered	[J/kg]
We	Weber number	[J/kg]

GREEK SYMBOLS

Pelton turbines

α	Bucket angle of attack	[°]
β	Bucket splitter angle	[°]
$\beta_{\overline{I}}$	Bucket outflow angle	[°]
γ	Bucket tip angle of impact	[°]
δ_{ribs}	Bucket ribs angle	[°]
Δ	Loss factor	[-]
η	Hydraulic efficiency	[-]
θ_j	Bucket j angular position	[°]
κ	Bucket tip slope angle	[°]
ρ	Bucket angle of setting	[°]
φ_{B_2}	Discharge coefficient	[-]
ψ_1	Energy coefficient	[-]

Vectorial

$\overline{\overline{\tau}}$	Stress tensor	[N/m^2]
$\overrightarrow{\omega}$	Angular velocity	[rad/s]

Optical

ϵ	Relative error	[-]
θ	Refraction angle	[-]
τ_{flash}	Flashlight duration	[s]

Miscellaneous

α_n	Volume fraction of phase n	[-]

Γ_n	Production rate of phase n	[kg/s]
ϵ	Relative error	[-]
ε	Turbulent rate of viscous dissipation	[-]
μ	Dynamic viscosity	[Ns/m^2]
μ_t	Eddy viscosity	[Ns/m^2]
ν	Kinematic viscosity	[m^2/s]
Ω	Reference angular velocity	[rad/s]
ω	Specific turbulent dissipation rate	[1/s]
ρ	Fluid density	[Kg/m^3]
σ	Surface tension coefficient	[N/ms^2]
ξ, η, ζ	Local curvilinear coordinates	[m]

SUBSCRIPTS

b	Referred to bucket backside
cal	Referred to calibration
1	High-pressure section
$\overline{1}$	Low-pressure section
i	Referred to bucket inner surface
j	Referred to reference bucket
k	Referred to operating point k
l	Referred to sensor l
M	Referred to reduced-scale model
m	Referred to mixture
n	Referred to phase n
p	Referred to full-scale prototype
r	Referred to runner r
ST	Referred to surface tension
t	Referred to turbulence
$\wedge$	Best efficiency

ACRONYMS

BHC	Bucket hydrodynamic chord
BCP	Bucket center of pressure
BCPS	Beam-Candela-seconds
CFD	Computational fluid dynamics

DA	Guide factor
EPFL	École polytechnique fédérale de Lausanne
FFT	Fast Fourier transform
LMH	Laboratory for hydraulic machines
MPS	Moving semi-implicit method
PVDF	PolyVinylidine DiFluoride
RMS	Root mean square
SPH	Smoothed particle hydrodynamics
SST	Shear stress tensor
STI	Sciences et techniques de l'ingénieur
VOF	Volume of fluid

BUCKET GEOMETRIC DEFINITIONS

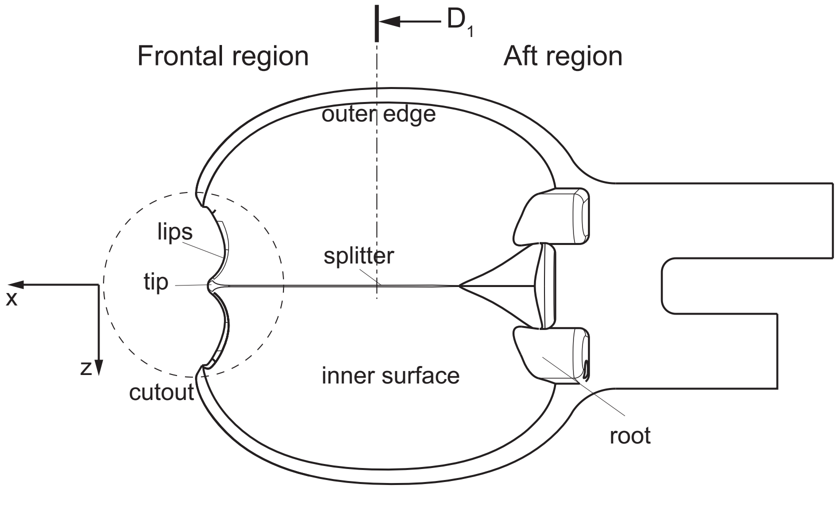
D$_1$
Frontal region
Aft region
outer edge
lips
tip
splitter
x
z
inner surface
cutout
root

(a) Top view

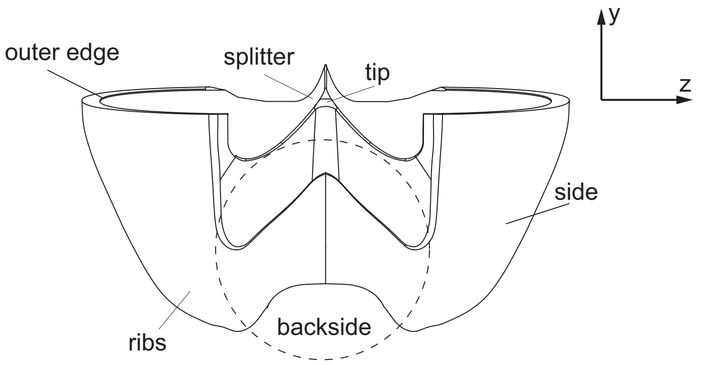
y
z
outer edge
splitter
tip
side
ribs
backside

(b) Front view

INTRODUCTION

Chapter 1

Pelton turbine and Free-surface flows

1.1 Foreword

Free-surface flows are flows constituted by 2 distinct phases separated by a thin interface. Mass or energy transfer may occur through the latter. Free-surface flows are either liquid-liquid flows, *i.e.* a drop of oil in water, or liquid-gas flows, *i.e.* air-water flows. They arise in Chemistry, Thermodynamics, and Turbomachinery and Civil engineering.

Pelton turbines differ from the other modern hydraulic machines by the presence of the free-surface flow.

1.2 Pelton turbines: historical introduction

All common water machines until the late 19^{th} century, including water wheels, are reaction machines: the potential energy of water acts on the machine and produces work. At that time a great demand for new power sources appear to run the machinery and mills necessary for the expanding gold mines. Many mines depend on steam engines, however those require exhaustible supplies of wood or coal. On the other hand water power from the fast running mountain creeks and waterfalls is abundant. Waterwheels used to power flour mills, work best on larger rivers but not in the faster moving and less voluminous mountain creeks and waterfalls. In 1866, California millwright Samuel Knight invents the first machine to work off a completely different concept, the impulse turbine. Inspired by the high pressure jet systems used in hydraulic mining in the gold fields, Knight develops a bucketed wheel which captures the energy of a free jet, which has converted a high head (hundreds of vertical feet in a pipe or "penstock") of water to kinetic energy. The water velocity, roughly twice the velocity of the bucket periphery, does a u-turn in the bucket and drops out of the runner at 0 velocity.

Lester Pelton is born in 1829 in Vermillion, Ohio. In 1850, he immigrates to California during the time of the gold rush. Pelton makes his living as a carpenter and a millwright. In 1879, experimenting with a Knight Wheel, he develops a double bucket design, exhausting the water to the side, eliminating some energy loss of the Knight wheel which exhausted some water back against the center of the wheel [22], Fig.1.1. In about 1895, William Doble improves on Pelton's half-cylindrical bucket form with an elliptical bucket introducing the cutout providing the jet a cleaner bucket entry, giving to the Pelton turbine the appearance it still has today.

The modern Pelton turbines, Fig.1.2 and Fig.1.3, develop up to $450 MW$ with heads ranging from 250 to $1900 m$. The facilities feature either a horizontal shaft for the single- or twin-injector low output units or a vertical shaft for the larger multi-jets units. The number of injectors can be up to 7.

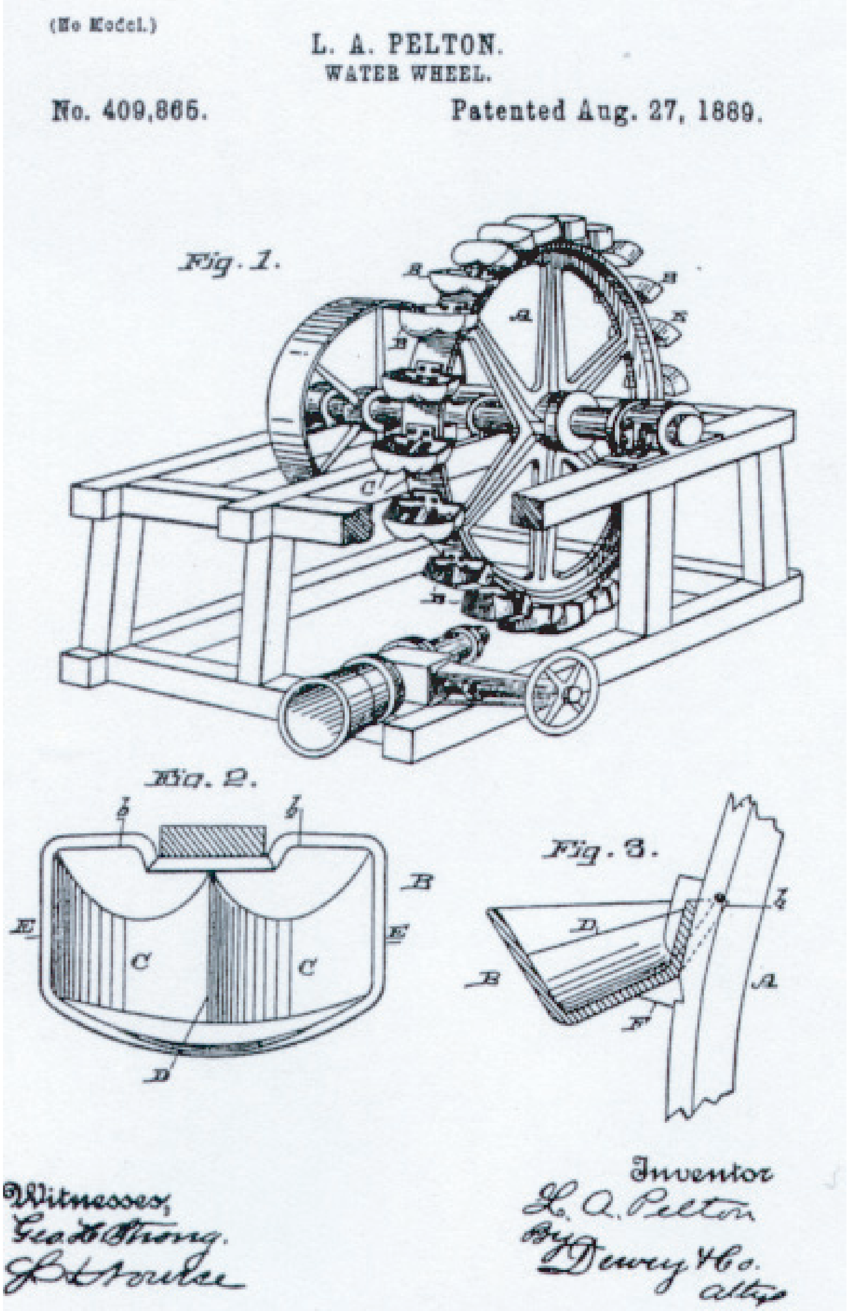
(No Model.)
L. A. PELTON.
WATER WHEEL.
No. 409,865.
Patented Aug. 27, 1889.
Fig. 1.
A
B
C
Fig. 2.
b
b
B
E
E
C
C
D
Fig. 3.
D
B
F
A
b
Witnesses,
Geo. H. Strong.
Inventor
L. A. Pelton
By Dewey & Co.
attys

Figure 1.1: Pelton turbine original patent document.

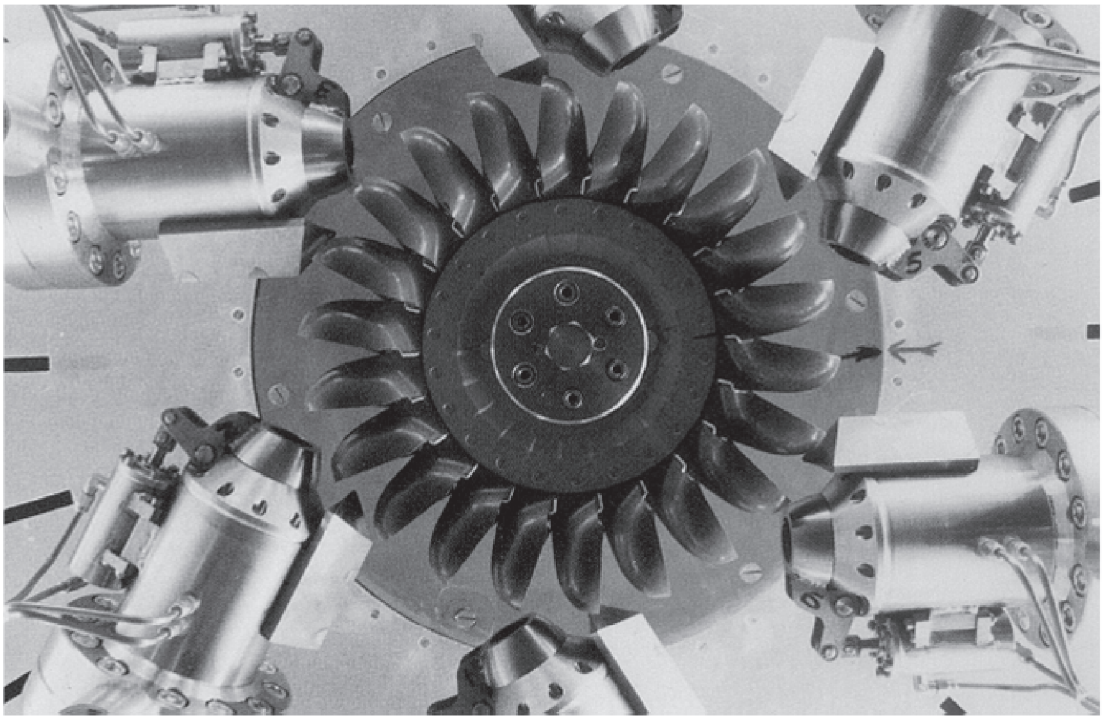

Figure 1.2: 6-injector vertical-axis Pelton runner [40].

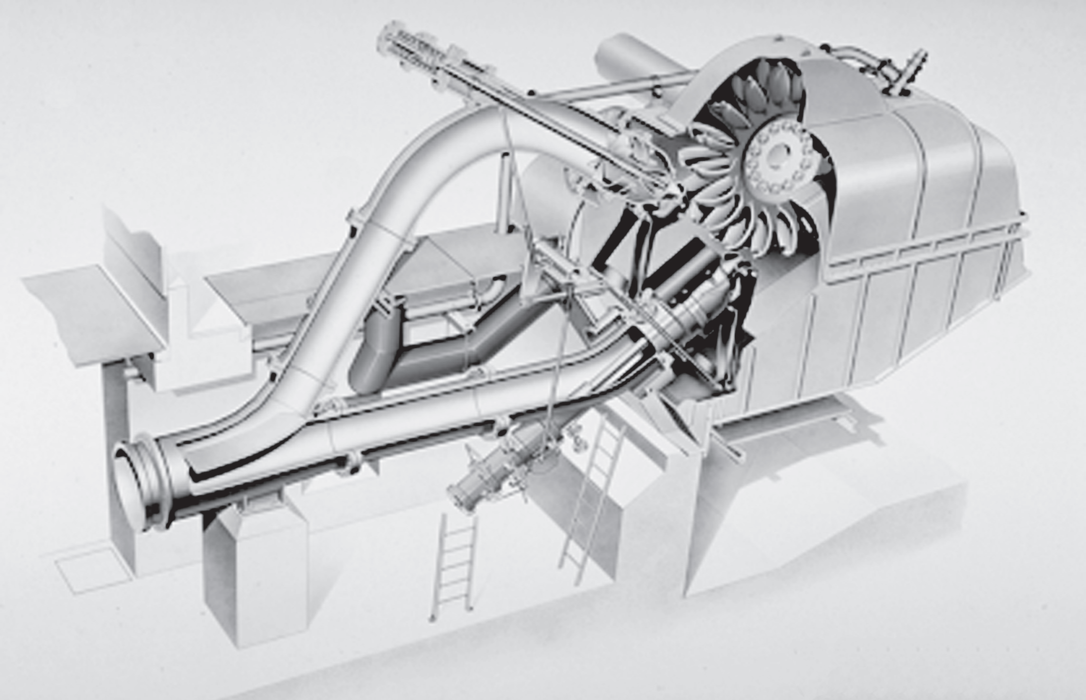

Figure 1.3: 2-injector horizontal-axis Pelton turbine [40].

Chapter 2

Framework of the study

2.1 Problem to solve

Performance prediction of hydraulic machines, such as efficiency and dynamic behavior under different operating conditions, is of high interest to manufacturers. In today's highly competitive market of turbine upgrading and refurbishment, the performance guarantees are often difficult to determine in the short term. An accurate prediction of the machines by numerical simulation permits to reduce the time required for the design phase. This is the reason why the design of reaction turbines, *i.e.* Francis, Kaplan, or Bulb turbines, has been significantly improved over the last 15 years by the introduction of efficient CFD tools.

The design of Pelton turbines, however, has always been more difficult than that of reaction turbines. It is mainly conducted from know-how and extensive experimental testing on reduced-scale models. Nevertheless, the transposition from scaled-down models to prototype-size machines is often unreliable. Indeed, the flow in a Pelton turbine facility combines 4 different regimes of flows: (i) confined steady-state flows in the upstream pipes and distributor, (ii) free jets past the injectors, (iii) transient free-surface flows in the buckets, and (iv) 2-phase dispersed flows in the casing. Each regime features a different characteristic length, a different velocity scale, and is therefore dominated by different forces, as summarized in Table 2.1. As a consequence, the scale-up rules differ for each of these regimes. It is for instance impossible to fulfill the similitude criteria for the piping and bucket flows at the same time. Various empirical approach have been developed over

Table 2.1: Characteristic scales of the flow in a Pelton turbine model.

	Length scale	Velocity scale	Reynolds number	Froude number	Weber number
Flow regime	D $[mm]$	C $[m/s]$	$Re = \frac{C \cdot D}{\nu}$ $[-]$	$Fr = \frac{C}{\sqrt{gD}}$ $[-]$	$We = \frac{\rho C^2 D}{\sigma}$ $[-]$
Confined flow	200	4.5	$5 \cdot 10^5$	3	–
Water jet	30	40	$6 \cdot 10^5$	80	15
Bucket flow	300	20	$3.2 \cdot 10^6$	12	40
Isolated water droplet	1	5	$3 \cdot 10^3$	100	0.03

the years to go round the scale-up problem, yielding to the so-called 'step-up' formulation [30], [115].
Model tests, apart from efficiency measurements, are based on rudimentary flow observations made with stroboscopic lighting systems. The flow observations carried out so far, performed with conventional lenses protected by tubes, provide limited information about the structures of the flow for 3 reasons: (i) the observation distance is too far, providing only low resolution images. (ii) The stroboscopic lighting systems used provides averaged images of the flow. (iii) The typical duration of one stroboscope pulse is about 30-40μs, not enough to avoid motion blur, even at reduced heads. As a matter of fact, accurate flow visualizations are difficult to perform. The space between the Pelton runner and the casing is commonly considered as very hostile, making visualizations of the buckets flow a challenging task. Indeed, the visibility is poor, as the atmosphere surrounding the turbine is made of (i) water sheets ejected by the buckets, (ii) a large population of droplets of different sizes stemming from the water sheets break-up, the jet spray, and the water sheets collision with the casing walls, and (iii) fog, see Fig.2.1. The air in the casing becomes thus rapidly saturated. Moreover, features of interest hide between the buckets, far from the casing walls, and are spread on a significant depth. The flow in Pelton turbines has therefore not been analyzed so far with such detail as the flow in the reaction turbines, and the understanding of the physics of key phenomena is weak.

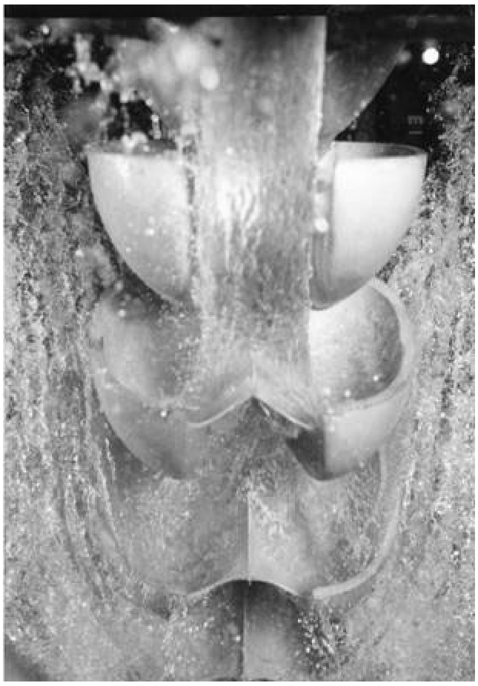

Figure 2.1: External stroboscopic flow visualization (Courtesy of VATech Hydro SA).

The initial jet/bucket interaction has never been observed, while some machines suffer erosion damages on the tip and on the cutout lips [29]. These damages are usually attributed to cavitation, but no study has been carried on to assess the assumption.
The jet cut process by the bucket backside remains vague: if the jet appears to stick to some extend to the backside, the reasons and consequences of this phenomenon are not well understood [7], [87].
Peaks of pressure and erosion damages have been observed on the bucket inner surfaces

of a large number of Pelton turbines, but no convincing explanation has been provided so far [29], [66], [15].

On the other hand, the recent development of numerical models with multiphase flow capability let foresee that in the near future similar performance improvements could be reached with Pelton turbines as obtained for reaction turbines [84]. Indeed, the first results obtained from CFD simulations are partially validated [87]: the predicted pressures match the experimental results well in the zones where the flow is dominated by inertia effects and where the flow is not affected by the jet/bucket interaction, but still lack the required accuracy otherwise.

It is therefore needed to improve the physical models available, and to do so, the fully understanding of the physical phenomena involved in the Pelton turbine bucket flow must be obtained by experimental means.

2.2 Literature review

2.2.1 Research and development

Research and development in the field of Pelton turbines are mainly performed by experimental or analytical studies [56]. The turbine design is carried on from long and fastidious laboratory tests, not only to determine and predict the performances of the machine, but also to estimate the service life, the rupture threshold due to fatigue or corrosion [32], [31], [2], [3], [4].

2.2.2 Analytical studies

Brekke [11], [12], reconstructed the path of a water particle in a bucket from the relative acceleration equations. Hana [36] improved this method. Kubota [61], [60], developed a method to define the position and shape of the water film in the bucket by successive infinitesimal displacements of the buckets with respect to the jet.

2.2.3 Experimental studies

Few experimental investigations of the flow in Pelton turbines are presented in the literature. They can be divided in 3 classes, *i.e.* (i) flow observations, (ii) pressure measurements, and (iii) water film thickness measurements.

Flow observations

Lowy [69] investigated the flow in a non-moving bucket and, more particularly, the cutting process of the jet by the bucket cutout, pointing out the main sources of losses. Bachman *et al.* [7] performed external flow visualizations around a Pelton runner using stroboscopic light, describing the main steps of the bucket flow.

Pressure measurements

Grozev *et al.* [33] performed the fist pressure measurements in a non-moving Pelton bucket. 42 pressure taps were machined in a half bucket connected to a static pressure

measurement device. This work provided the first insight of the static pressure distribution on the bucket inner surface. Kvicinsky *et al.* [67], [66] also performed pressure measurements in non-rotating Pelton buckets in steady state to validate numerical simulations.
The first measurement of the unsteady pressure in a rotating bucket was carried out by Avellan *et al.* [6]. 3 piezo-electric pressure sensors were installed in a bucket. These results permitted to enhance the design of the Pelton turbines [5], [1].
Kvicinsky *et al.* [65], [66], fitted a reduced scale Pelton runner with 32 flush-mounted unsteady pressure sensors, providing the first set of unsteady pressure measurement in a runner under normal operating conditions. According to the shape of the measured signals, 5 distinct zones could be defined on the bucket inner surface.
All the unsteady pressure measurement campaigns evidenced the presence of high-pressure pulses in the central region of the bucket inner surface as shown by Fig.2.2. No satisfactory explanation has been provided so far. The phenomenon was attributed to a stagnation point with the formation of a re-entrant micro jet [66], or to rain erosion [15], induced by the repetitive impact of water droplets escaped from the jet. The pulse amplitude was found not to be related to the pressure in the turbine casing [16].

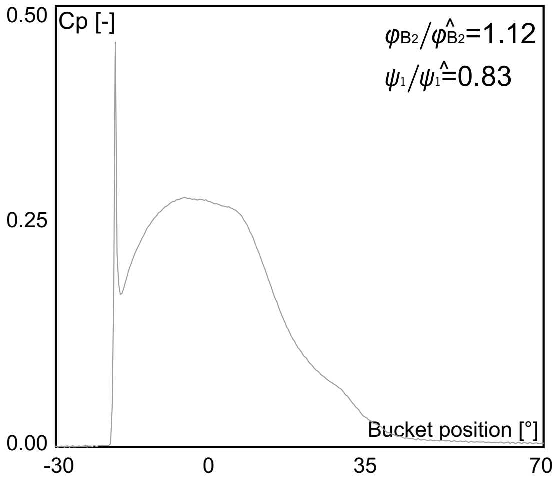

Figure 2.2: Pressure pulse signal [66].

Water film thickness measurements

Water-layer thickness measurements were first performed by Guilbauld *et al.* [35] on a simplified $2D$ bucket using an electrical probe. The first non-intrusive measurements in a $3D$ bucket were made by Kvicinsky *et al.* [65]. This approach was performed using a plane Laser beam to put into evidence the air-water interface. The water film thickness itself was obtained with a still camera and image processing techniques. These measurements were essentially carried on to validate CFD simulations.

2.2.4 Numerical models

Physical models allowing complex free-surface flow modeling have been developed and refined over the last 3 decades [51]. The first model was the Volume of Fluid (VOF), developed by Hirt and Nichols [44], [43], referred as VOF method. Stewart [102] and Brackbill [10] refined this model. The 2-Phase Homogeneous Model and more recently the Mixture Model, also known as Multifluid Model, have been introduced. However, as the Navier-Stokes equations are solved on a fixed grid, numerical diffusion arises due to the existence of the advection term. The numerical diffusion becomes severe especially when the deformation of the free surface is large and complicated.

Mesh-free approaches have become increasingly popular to overcome this problem. Among them, the methods based on fully Lagrangian particle approaches appear promising, such as the Smoothed Particle Hydrodynamics (SPH) and Moving Particle Semi-Implicit (MPS). In both methods, the modelled media, such as the water, is modelled as an assembly of particles. All the terms in the governing equations are described as the interaction between the reference particle and its neighbors, thus no computational grid is required. Initially developed by Koshizuka *et al.* [58], the MPS method has been widely applied in both the hydrodynamics and nuclear mechanics, to deal with a variety of practical problems such as dam-breaking, vapor explosion, or 2 phase flows such as Pelton turbines [78], [77]. On the other hand, the conception of SPH method was performed by Lucy [70] for astrophysics applications and extended to fluid flow by Monaghan [76]. The SPH method was also applied to Pelton turbine problems by Marongiu *et al.* [73].

Non-rotating buckets

The numerical simulations in the Pelton turbines start with the study made by Guibauld *et al.* [35]. Jet simulations were performed by Nonoshita [80]. Hana [37] presents the first free-surface simulation of a $2D$ bucket with the VOF and 2-Phase Homogeneous models. Janetzky *et al.* [53] and Avellan [6] inaugurated the simulation of the free-surface flow in a $3D$ non-rotating bucket with the VOF model.

Kvicinsky *et al.* [67] investigated both the VOF and the 2-Phase Homogeneous models and experimentally validated them in the cases of a jet impinging a flat plate and a non-moving Pelton turbine bucket [66]. The 2-Phase Homogeneous Model appeared to provide the best compromise in terms of accuracy and computational cost. Similar results were obtained by Traversaz *et al.* [106].

Rotating buckets

The first attempts to numerically simulate the flow in a moving Pelton turbine bucket were conducted by Hana [38], Sick *et al.* [100], Janetzky *et al.* [52], Mack and Moser [71] and Zoppé [121]. The first simulation of a complete multi-jet Pelton turbine including the repartitor, jets runner and casing was performed by Parkinson *et al.* [97]. Perrig *et al.* [88], [87] performed a deep study of the flow in a Pelton turbine bucket, putting into evidence the importance of further investigating the bucket flow with powerful experimental tools.

2.3 Methodology and objectives

Performing a complete set of non intrusive experimental investigations of the rotating $3D$ free-surface flow in a real, unmodified Pelton turbine bucket under normal operating conditions is paramount to fill the gap of knowledge towards complete and accurate physical models and more efficient designs.

In order to do so, the following experimental and numerical approaches are developed and carried through in the present study:

- Unsteady pressure distribution (full coverage of bucket inner surface, bucket backside, and bucket sides).
- High-speed flow visualizations (onboard and external).
- Instantaneous water film thickness measurements.
- State-of-the-art CFD computations.

Based on the aforementioned methodology, the objectives of the present work consist in:

- Decomposing the successive steps of the bucket duty cycle.
- Describing of the jet/bucket interaction process.
- Identifying the origin and estimate the amplitude of the pressure pulses.
- Analyzing the physics of the backside flow and its consequences.
- Surveying the energy distribution in the buckets.

2.4 Case study

The single-injector horizontal shaft Pelton turbine model investigated is illustrated by Fig.2.3, and its main characteristics summarized by Table 2.2. The bucket design is derived from an existing unit, with the outflow angle $\beta_{\overline{1}}$ reduced to promote the occurrence of a slight outflow heeling. The buckets, made of resin injected on a fiberglass matrix, are fixed on a metallic (steel or bronze) flange by means of brass pins. The rigidity in flexion is obtained by casting epoxy-resin in the intersticial space between the buckets, see Fig.2.4.

Table 2.2: Test runner data.

z_0	z	D_1/B_2	scale
1	21	4.09	10.375

2.4.1 Hillchart and operating points investigated

Figure 2.5 shows the hillchart of the test runner and the set of operating conditions investigated, referred as OP1...OP15. Unsteady wall pressure measurements are performed for all the operating conditions marked on the hillchart for 4 different test heads, *i.e.* 20, 35, 60, and 80m, while the onboard and external flow visualizations are carried on for the operating points colored in dark grey for a test head of 20m. The hydraulic specifications of the respective operating points are provided by Table 2.3. The discussion to follow in the successive chapters will be focused on OP1 and OP3 (same jet diameters with different energy coefficients) and on OP5 and OP14 (same energy coefficients with different jet diameters).

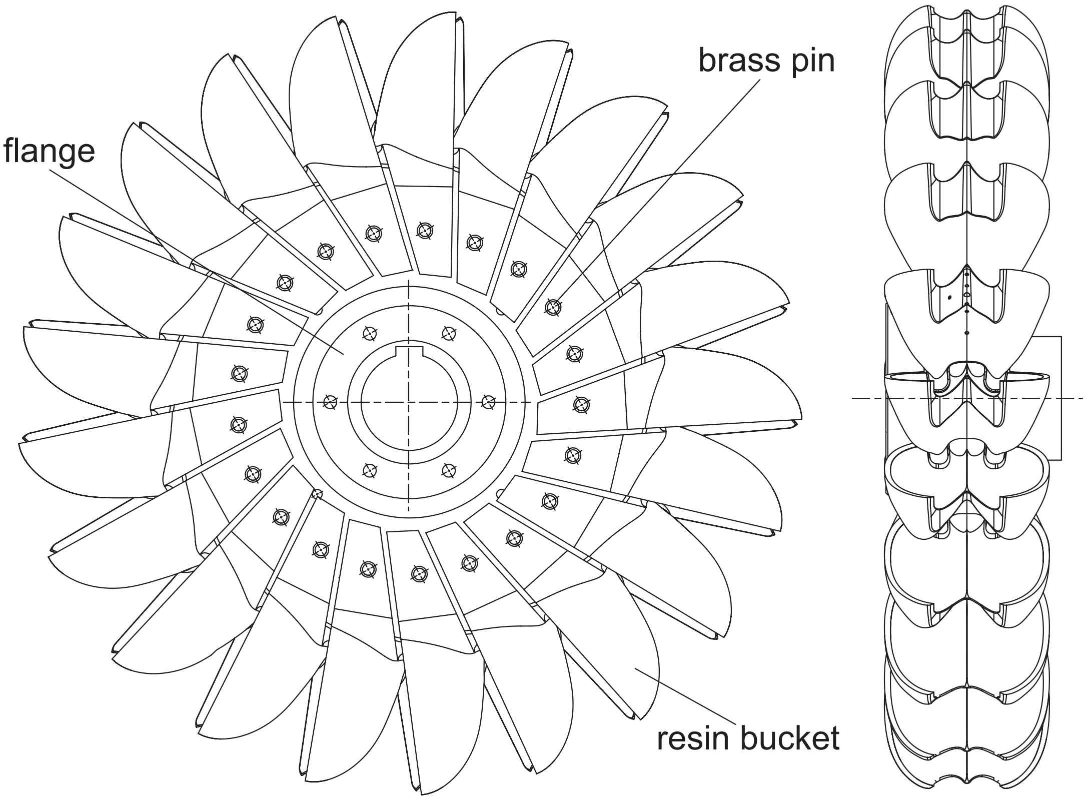

Figure 2.3: Test runner.

2.5 Thesis document organization

The present document is divided in 3 parts, dealing (i) with the fundamental equations describing $3D$ rotating free-surface flows, the flow in Pelton turbines, and the available numerical models (**Part I**), (ii) experimental and numerical tools chosen and developed for the purpose of this study (**Part II**), (iii) and the physical analysis of the results obtained from both approaches (**Part III**).

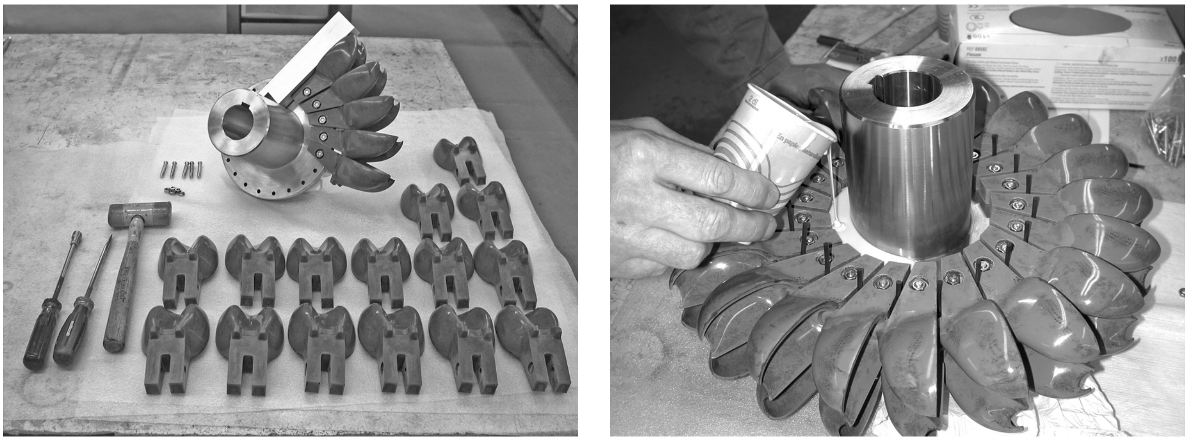

(a) Resin buckets and steel flange. (b) Epoxy casting.

Figure 2.4: Test runner during assembly.

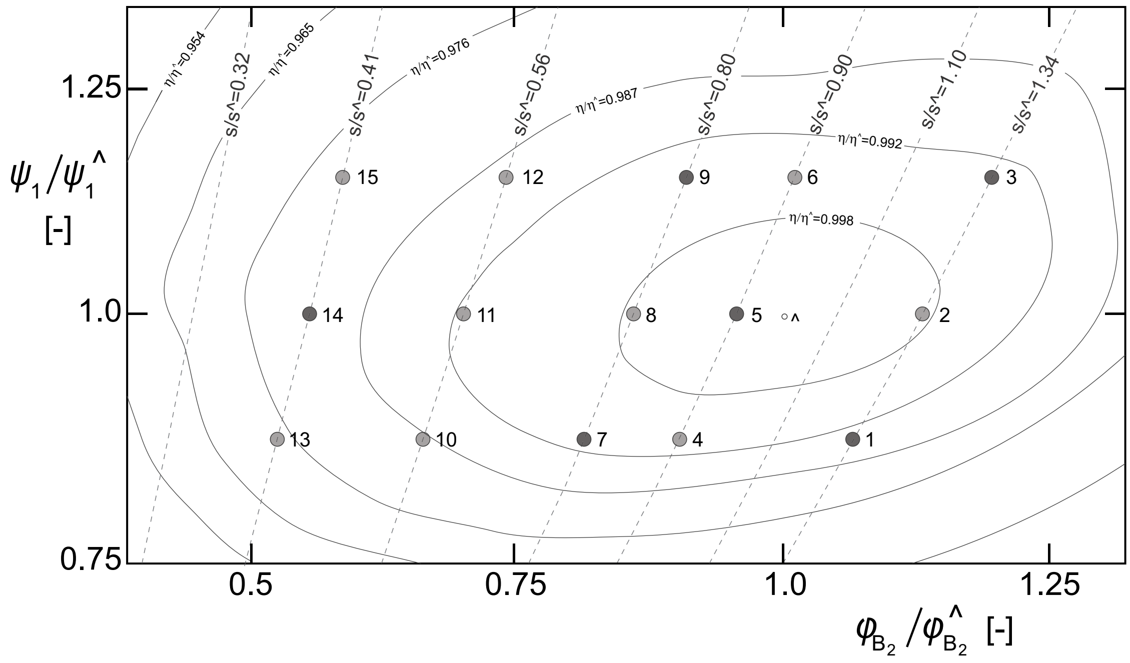

Figure 2.5: Hillchart and operating points investigated.

2.5.1 Part I

Chapter 3 is a review of the fundamental theory of hydraulic turbomachines. The classic Pelton turbine theory and the traditional design approaches are looked over in **Chapter** 4. **Chapter** 5 deals with the fundamental equations of $3D$ free-surface flows, surface tension, and introduces the dimensionless numbers. The physical models available to numerically model such flows are explained in **Chapter** 6, together with a recall of the models developed for turbulent flows. **Chapter** 7 evidences the main the definitions to be used in the present document.

2.5.2 Part II

Chapter 8 describes the development, the construction, and the calibration procedures of the reduced scale model intended for the unsteady wall pressure measurements. In **Chapter** 9, the techniques developed for the high-speed flow visualizations of the bucket flow are detailed. The optical requirements and the technical devices (camera, flashlights, experimental apparatus) are presented in **Chapter** 10. The water film instantaneous thickness measurement technique developed is presented in **Chapter** 11. A description of the numerical set-ups made for the CFD simulations, together with validations and comparison of different numerical models, is provided in **Chapter** 12.

2.5.3 Part III

The bucket duty cycle is described into details by the light of the onboard flow visualizations in **Chapter** 13. The whole initial bucket feeding process is dissected in **Chapter** 14, while the jet cutting process and bucket backside flow is dealt with in **Chapter** 15. The bucket flow itself is treated in **Chapter** 16 and the outflow heeling in **Chapter** 17.

Table 2.3: Operating points investigated.

OP	$s/s^\wedge$	$\psi_1/\psi_1^\wedge$	$\varphi_{B_2}/\varphi_{B_2}^\wedge$	$\eta/\eta^\wedge$
1	1.34	0.89	1.07	0.991
2	1.34	1.00	1.14	0.998
3	1.34	1.12	1.20	0.994
4	0.90	0.89	0.90	0.995
5	0.90	1.00	0.95	0.999
6	0.90	1.12	1.01	0.996
7	0.80	0.89	0.81	0.994
8	0.80	1.00	0.86	0.998
9	0.80	1.12	0.91	0.995
10	0.56	0.89	0.65	0.986
11	0.56	1.00	0.69	0.993
12	0.56	1.12	0.74	0.988
13	0.41	0.89	0.51	0.975
14	0.41	1.00	0.54	0.983
15	0.41	1.12	0.58	0.979

The bucket energy transfer mechanisms and power distribution are discussed respectively in **Chapter** 18 and **Chapter** 19.

Part I

FREE-SURFACE FLOWS IN ROTATING FRAMES

Chapter 3

Euler's equation for turbomachines

3.1 Kinetic Momentum theorem

When a water particle passes through the turbine surfaces, a reciprocal action takes place. The particle deviates from its initial direction, the Momentum change induces a pressure on the blade surfaces and causes the rotation of the latter, thereby generating a torque upon the turbine shaft. The runner reaction on the particle of water at steady operational conditions may be determined. Indeed, the well-known Kinetic Momentum theorem applied to a fluid particle is expressed as [59]:

$$\overrightarrow{T} = \frac{d}{dt}(\overrightarrow{r} \times m\overrightarrow{c}) \tag{3.1}$$

The law expresses that the rate of total variation of the Momentum of angular Momentum

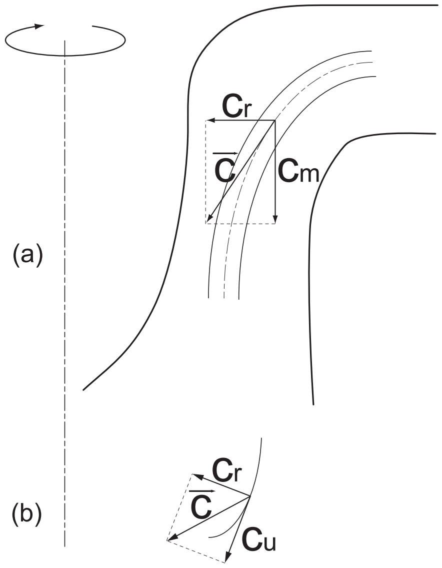

Figure 3.1: Velocity of a water particle in a runner channel (a) in meridian and (b) horizontal planes.

of the fluid particle is equal to the Momentum of the external forces exerting an influence or an action on it. Considering a rotating channel, see Fig.19.2, Eq.3.1 can be rewritten, developing the terms:

$$\overrightarrow{T} = \frac{d}{dt}\overrightarrow{r} \times m\overrightarrow{c} + \overrightarrow{r} \times \frac{d}{dt}(m\overrightarrow{c}) \tag{3.2}$$

At the entrance of the channel the particle of mass m, animated by the velocity $\overrightarrow{c}$, carries the momentum mc_I and at the outlet of the channel the momentum $mc_{\overline{I}}$. Let the velocity have radial, c_r, axial, c_z, and tangential components, c_u. Equation 3.2 can be rewritten as:

$$\overrightarrow{T}dt = d(m\overrightarrow{c}) \tag{3.3}$$

Integrating Eq.3.3 between the inlet and outlet of the channel yields to:

$$\overrightarrow{T}\Delta t = m((\overrightarrow{r} \times m\overrightarrow{c})_{\overline{1}} - (\overrightarrow{r} \times m\overrightarrow{c})_1). \tag{3.4}$$

As can be seen from Fig.19.2, the Momentum of the components c_r and c_z with respect to the turbine axis is zero. Hence, the moment of the velocity $\overrightarrow{c}$ is determined only by the component c_u. The variation in the Momentum of Momentum of the mass m during time Δt equals the product of the Momentum of the driving forces, T, and their action during the time interval Δt:

$$T\Delta t = m(r_{\overline{1}}c_{u_{\overline{1}}} - r_I c_{u_1}), \tag{3.5}$$

where r_I is the radius of the center of gravity of the water mass at the inlet of the channel and $r_{\overline{I}}$ is the radius of the center of gravity of the water mass at the outlet of the channel [113]. Introducing the massflow of particles, Q,

$$Q = \frac{m}{\Delta t} \tag{3.6}$$

Equation 3.5 becomes:

$$T = Q(r_{\overline{1}}c_{u_{\overline{1}}} - r_1 c_{u_1}). \tag{3.7}$$

3.1.1 Power transferred to the runner

The power transferred by the fluid particle to the runner is obtained by performing the scalar product of the resulting Momentum $\overrightarrow{T}$ with the machine angular velocity $\overrightarrow{\omega}$:

$$P = \overrightarrow{T} \cdot \overrightarrow{\omega}. \tag{3.8}$$

Introducing the definition of the peripheral velocity $\overrightarrow{U}$:

$$\overrightarrow{U} = \overrightarrow{\omega} \times \overrightarrow{r} = -\overrightarrow{r} \times \overrightarrow{\omega} \tag{3.9}$$

the expression of the power, Eq.3.8 becomes:

$$P = Q(U_1 c_{u_1} - U\overline{1}c_{u_{\overline{1}}}). \tag{3.10}$$

3.1.2 Euler's equation

The energy transferred from the particles to the machine is then:

$$E_t = (U_1 c_{u_1} - U_{\overline{1}} c_{u_{\overline{1}}}). \tag{3.11}$$

Equation 3.11, referred as Euler's equation, was found by Leonard Euler in 1764, who was also the first to prove the necessity of a distributor, *i.e.* guide vanes, in the hydraulic machines [91]. Euler's equation show that the Momentum transmitted to the runner equals the difference between the moments of Momentum, at the inlet and the outlet of the runner, of a massflow Q of water flowing through the turbine per unit time.

Chapter 4

The Pelton turbine

4.1 Operating principle

The Pelton turbine is an impulse turbine that only converts kinetic energy of the flow into mechanical energy. The transfer of the total energy from the nozzle exit to the downstream reservoir occurs at atmospheric pressure. The jet stemming from the injector impinges on buckets, located at the periphery of a wheel. Figure 4.1 shows a Pelton turbine and its main dimensions, while Fig.4.2 schematizes an idealized Pelton turbine bucket in $2D$. The bucket is assumed to be permanently fed by the full jet impinging on the splitter with an angle of attack equal to 90°. According to Euler's equation, Eq.3.11, the kinetic energy is entirely converted by the bucket when the peripheral component of the absolute velocity of the flow at outlet, $c_{u_{\overline{1}}}$ is zero. At the inlet of the bucket, the absolute velocity $\overrightarrow{c_1}$ of the water particles and the driving speed of the runner $\overrightarrow{U_1}$ have the same direction and orientation. The tangential component of the absolute velocity at inlet, c_{u_1} is therefore:

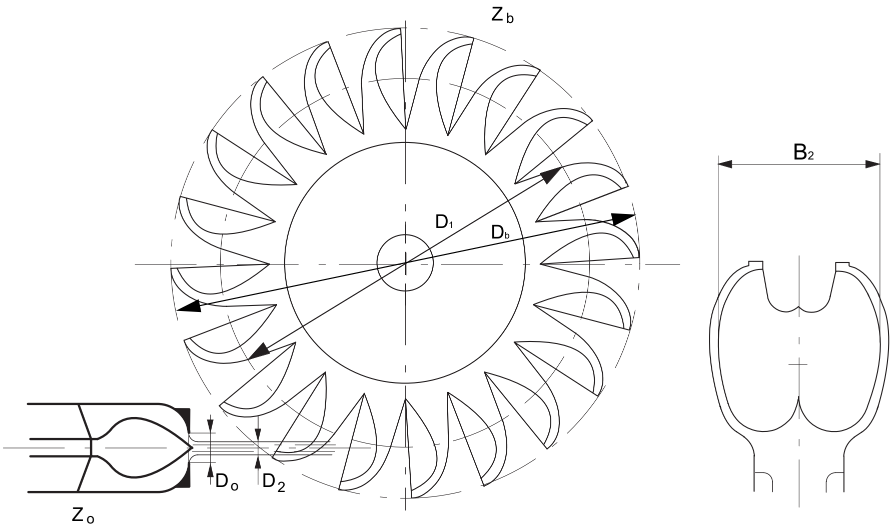

Figure 4.1: Schematized view of a Pelton turbine.

$$c_{u_1} = c_1. \tag{4.1}$$

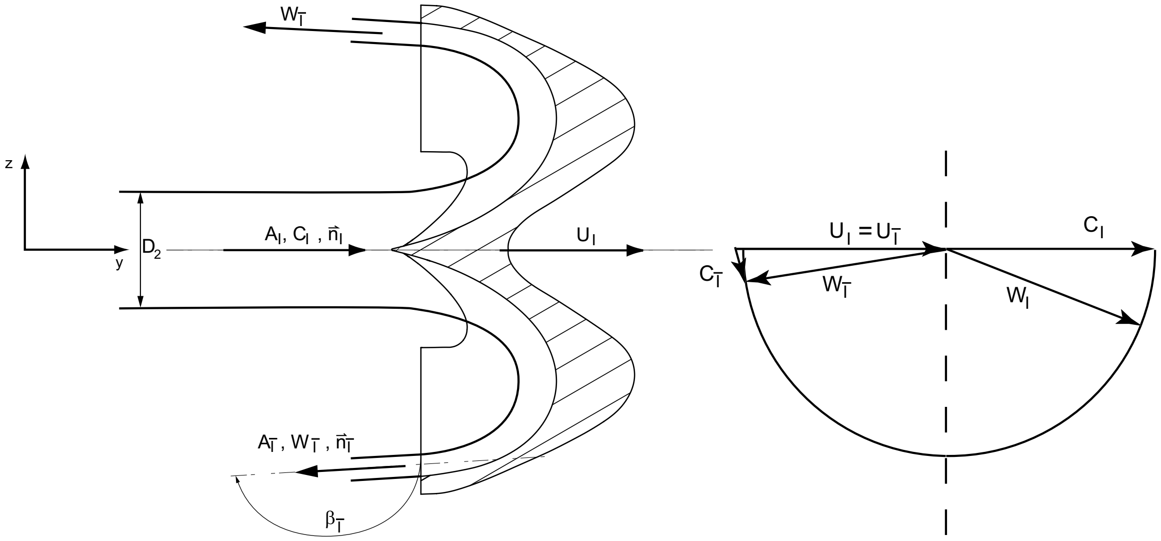

Figure 4.2: Idealized velocity triangle in a $2D$ bucket.

The peripheral component of the outflow velocity, $c_{u_{\bar{1}}}$, is a function of the outflow angle $\beta_{\bar{1}}$:

$$c_{u_{\bar{1}}} = U_{\bar{1}} - W_{\bar{1}} \cos \beta_{\bar{1}}. \tag{4.2}$$

Assuming that the mean flow enters and leaves the bucket at the same radial location, the peripheral velocity can be considered constant:

$$\|\overrightarrow{U_1}\| = \|\overrightarrow{U_{\bar{1}}}\| = \|\overrightarrow{U}\|. \tag{4.3}$$

From Euler's equation, Eq.3.11, the energy transferred becomes:

$$E_t = U(W_1 + W_{\bar{1}} \cos \beta_{\bar{1}}). \tag{4.4}$$

Introducing the loss factor $\Delta = 1 - \frac{W_{\bar{1}}}{W_1}$ taking into account the flow deceleration in the bucket induced by the surface friction and because the outflow angle $\beta_{\bar{1}}$ is larger for water than that of the bucket [111], the hydraulic power transmitted to the runner becomes:

$$P_t = \rho Q U W_1 (1 + (1 - \Delta) \cos \beta_{\bar{1}}). \tag{4.5}$$

By definition, c_0 is the flow velocity at the injector nozzle is:

$$c_0 = k_{c_0} \sqrt{2gH} \qquad k_{c_0} \simeq 0.96...0.98 \tag{4.6}$$

Let introduce the runner speed coefficient k_u defined such that

$$u = k_u \sqrt{2gH}. \tag{4.7}$$

The expression for the power transferred becomes:

$$P_t = 2\rho Q H k_u (k_{c_0} - k_u)(1 + (1 - \Delta) \cos \beta_{\bar{1}}). \tag{4.8}$$

The maximum power that can be extracted by the runner is obtained from the mathematical condition:

$$\frac{\partial P_t}{\partial k_u} = 0 \tag{4.9}$$

$$\frac{\partial P_t}{\partial k_u} = (2\rho Q H)(1 + (1 - \Delta)\cos\beta_{\bar{1}})(k_{c_0} - 2k_u) = 0 \tag{4.10}$$

The condition for the buckets to extract the maximum power is therefore $k_u = \frac{k_{c0}}{2} \approx 0.45...0.5$ [18]. The expression of the torque is

$$T_t = \rho Q \sqrt{\frac{H}{2g}} D_1 (k_{c_0} - k_u)(1 + (1 - \Delta)\cos\beta_{\bar{1}}). \tag{4.11}$$

Figure 4.3 shows the torque and power evolution as a function of the peripheral speed coefficient k_u . The runaway condition is fulfilled when the peripheral speed U is equivalent to the jet velocity c_0. The resulting power is zero.

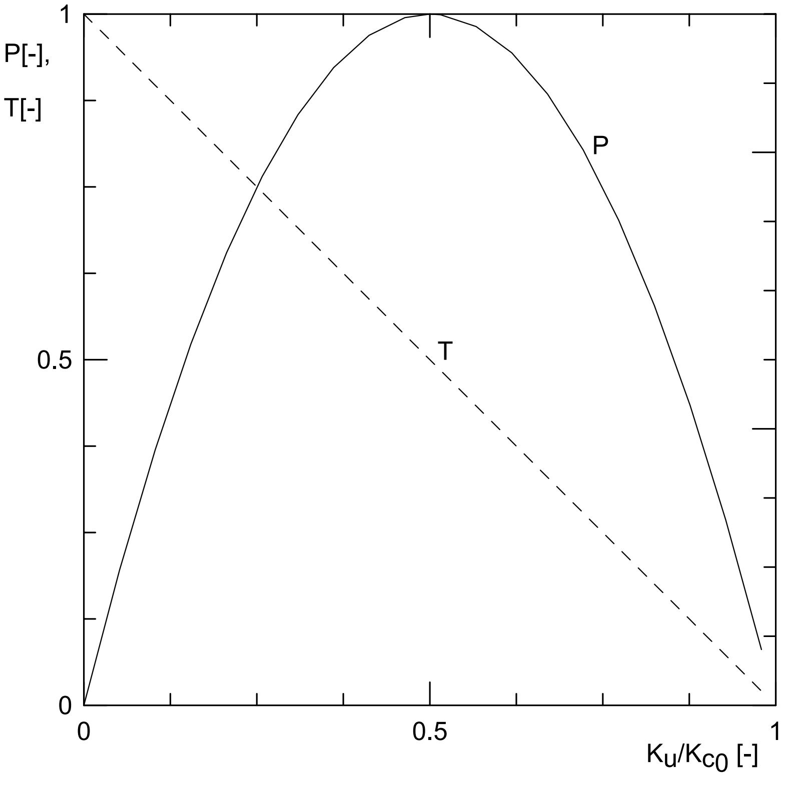

Figure 4.3: Power and torque output as a function of peripheral velocity coefficient.

4.1.1 Hydraulic efficiency

The hydraulic efficiency of a Pelton turbine is defined from the φ_{B_2}-ψ_1 characteristics of the machine. Let φ_{B_2} the discharge coefficient be defined as:

$$\varphi_{B_2} = \frac{Q}{Q_{ref}} = \frac{2\sqrt{2E} c_0 D_0^2}{\omega D_1 B_2^2 z_0}. \tag{4.12}$$

Let the energy coefficient ψ_1 be defined as:

$$\psi_1 = \frac{2E}{U^2}. \tag{4.13}$$

The hydraulic efficiency η is by definition expressed by:

$$\eta = \frac{P_t}{P_h} = \frac{P_t}{\rho Q E}. \tag{4.14}$$

With substitutions, Eq.4.14 finally reduces to:

$$\eta = 2(\frac{c_0}{\sqrt{\psi_1}} - \frac{1}{\sqrt{\psi_1}})(1 + (1 - \Delta)\cos\beta_{\bar{1}}). \tag{4.15}$$

Equation 4.15 shows that the smaller the flow deviation, *i.e.* $\beta_{\bar{1}}$, the grater efficiency.

4.2 Pelton turbine design

Whenever it comes to hydraulic turbine design, the input data are usually the available discharge, the head and the rotational speed. The first step of the design process involves calculating the specific speed coefficient, and defining the number of jets z_0 to reach it [9]. The target values are depending upon the experiences of the various manufacturers. The design is traditionally carried out from a kinematic study of the flow, and from experiences made on reduced scale models.

4.2.1 Number of buckets

The number of buckets for a given runner must be determined so that no water particle is lost while minimizing the risks of detrimental interactions between the outflowing water particles and the adjacent buckets [103], [9]. The runner pitch is determined by the paths of the bucket tip (diameter D_p), the Pelton diameter (D_1), and the relative paths of the water particles stemming from the upper and lower generators of the jet, respectively AA' and BB' on Fig.4.4. The bucket pitch must be selected so that no particle stemming from the lower generator of the jet can escape the runner without encountering any bucket, *i.e* it must be smaller than the arc BB' [82].

4.2.2 Bucket angle of setting

The splitter is not radially oriented, but inclined towards the jet. The bucket angle of setting, ρ, is set so that the splitter lies perpendicular to the jet axis when the center of gravity of the jet reaches the bucket [9].

4.2.3 Bucket surface shape

The dimensions of the bucket are in proportion to the jet diameter. Usually, $B_2 \simeq 3.0 - 3.4 D_2$ [115]. To avoid a rapid destruction of the splitter the splitter angle α is usually never smaller than 20°, while the outflow angle $\beta_{\bar{1}}$ is around 10° on D_1 to avoid outflow heeling [9]. Moreover, the water leaving in a rearward direction should not impinge on the

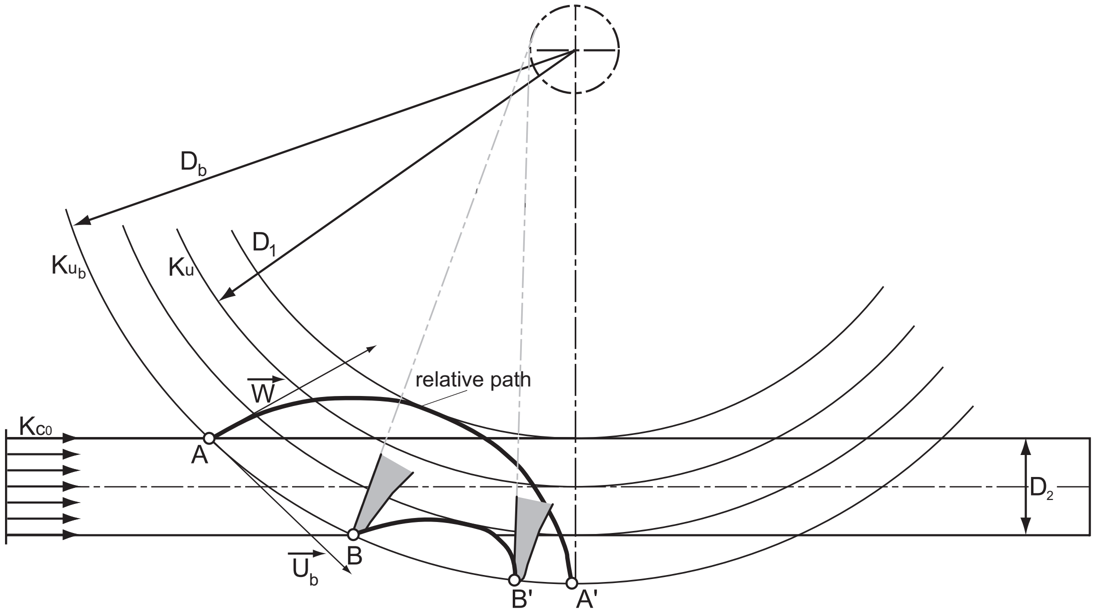

Figure 4.4: Relative paths of the water particles.

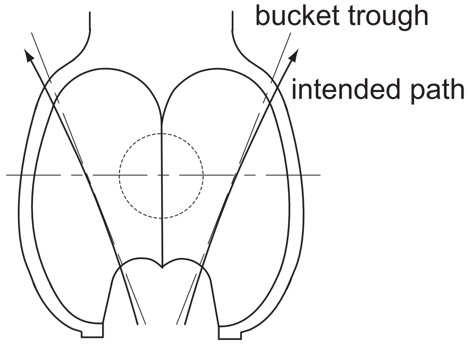

Figure 4.5: Bucket rearward flow deviation.

runner flange. It must be deviated to the exterior, as evidenced by the orientation of the trough of the iso-elevation lines of the inner surface on Fig.4.5. The bucket design process consists in defining the elevation curves of the inner surface. From the main sections, and the aforementioned criteria, a network of iso-elevation curves is drawn. According to this first design, and from the manufacturer in-house know-how, the final bucket shape is defined. Model tests are carried on to assess the validity of the results, and modifications are performed if necessary until the final shape is obtained. The cutout area and the bucket backside shapes are to be designed so that the jet does not impinge on the rear side of the cutout too early (inlet heeling). The direction of the relative velocity shall be towards the exterior of the buckets [104], [9].

4.3 Influence of head and speed variations

The runner speed coefficient K_u are modified and the relative paths of the water particles distorted as a result of speed or head variation away from the design best efficiency operating point.

- Overspeed or head decrease. The relative paths become shorter, and a portion of the water slips off the runner;
- Underspeed or head increase. The relative paths become longer, and the water particles encounter the buckets too early. The mean discharge received increases, and the buckets may be flooded. The relative speeds are increased, increasing the losses.

The Pelton turbines do not stand important head variations at constant speed [103].

Chapter 5

Rotating free surface flows

5.1 Fundamental equations of fluid mechanics

A fluid motion is described by a set of 3 equations, *i.e.* (i) the conservation of mass, (ii) the Momentum conservation, and (iii) the energy conservation.

Conservation of mass

Since the total amount of fluid in a control volume V is conserved, it can be written:

$$\frac{d}{dt}\int_V \rho dV = 0. \tag{5.1}$$

Using the Reynolds transport theorem [96], Eq.5.1 leads to:

$$\int_V \Big(\frac{\partial \rho}{\partial t} + \overrightarrow{\nabla} \cdot (\rho \overrightarrow{c})\Big) dV = 0. \tag{5.2}$$

Since Eq.5.2 must apply even to an infinitesimal volume of control, one obtains:

$$\frac{\partial \rho}{\partial t} + \overrightarrow{\nabla} \cdot (\rho \overrightarrow{c}) = 0 \tag{5.3}$$

or

$$\frac{D\rho}{Dt} + \rho \overrightarrow{\nabla} \cdot \overrightarrow{c} = 0. \tag{5.4}$$

Momentum conservation

In applying Newton's second law of motion to a finite, extended mass of fluid, the external resultant force is equated to the rate of change of resultant momentum which is calculated for a mass of fluid consisting of the same fluid particles. Thus,

$$\frac{d}{dt}\int_V \overrightarrow{c} \rho dV = \int_V \rho \overrightarrow{F} dV + \int_S \overline{\overline{\tau}} \cdot \overrightarrow{n} dS, \tag{5.5}$$

where $\overrightarrow{F}$ is the body force per unit volume acting on the fluid, $\overline{\overline{\tau}}$ is the stress tensor, S is the surface of control enclosing V, and $\overrightarrow{n}$ is the unit outward normal to the area element dS. Using the Reynolds transport theorem, Eq.5.5 becomes:

$$\int_V \Big(\frac{\partial}{\partial t}(\rho \overrightarrow{c}) + \overrightarrow{\nabla} \cdot (rho \overrightarrow{c} \overrightarrow{c})\Big) dV = \int_V \rho \overrightarrow{F} dV + \int_S \overline{\overline{\tau}} \cdot \overrightarrow{n} dS. \tag{5.6}$$

Using Green's theorem and Eq.5.3, Eq.5.6 becomes:

$$\rho\Big(\frac{\partial\vec{c}}{\partial t}+\vec{c}\cdot\vec{\nabla}\vec{c}\Big)=\rho\vec{F}+\vec{\nabla}\cdot\bar{\bar{\tau}}. \tag{5.7}$$

The terms of the stress tensor stem from the pressure and the viscous terms, and can be rewritten as:

$$\bar{\bar{\tau}}=p\,\vec{\vec{I}}+\mu\,\vec{c}\otimes\vec{c}. \tag{5.8}$$

The Momentum equation, Eq.5.7 then becomes the Navier-Stokes equation:

$$\frac{\partial\vec{c}}{\partial t}+\vec{c}\cdot\vec{\nabla}\vec{c}=-\frac{1}{\rho}\overrightarrow{\nabla p}+\nu\nabla^2\vec{c}+\vec{f}. \tag{5.9}$$

Energy conservation

Let consider the energy balance for the fluid in volume V. Work is done on this mass of fluid by both body and surface forces, and heat may also be transferred across the surface of control S. Some of this work done and heat transferred shows up as an increase in the kinetic energy energy of the fluid, and the reminder shows up as an increase in the internal energy of the fluid, according to the first law of thermodynamics.
The equation expressing the first law of thermodynamics is then:

$$\frac{d}{dt}\int_V\rho\Big(e+\frac{1}{2}\vec{c}^{\,2}+U\Big)dV=\frac{DQ}{Dt}-\frac{DW}{Dt}, \tag{5.10}$$

where e is the internal energy of the fluid per unit mass, U is the potential energy of the fluid in a conservative body-force field $\vec{f}=-\vec{\nabla}U$, Q is the heat transfer to the system, and W the work delivery from the system. Using the Reynolds transport theorem, the continuity equation, Eq.5.3, and after some algebraic manipulation, the conservation of energy finally becomes:

$$\rho\bigg(\frac{\partial}{\partial t}\Big(e+\frac{1}{2}\vec{c}^{\,2}+U\Big)+\vec{c}\cdot\vec{\nabla}\Big(e+\frac{1}{2}\vec{c}^{\,2}+U\Big)\bigg)=\frac{Dq}{Dt}-\frac{Dw}{Dt}. \tag{5.11}$$

5.1.1 Surface tension

Surface tension is a consequence of intermolecular cohesive forces. When 1 or 2 media in contact in a liquid phase, work must be done on a molecule approaching the interface from the interior of the liquid because this molecule experiences an unbalanced cohesive force directed away from the interface. The resultant of the tensile forces acting on a portion of the interface containing element dS is given by:

$$\overrightarrow{f_{ST}}=-\sigma\oint\vec{n}\times d\vec{x}, \tag{5.12}$$

where σ is the surface tension coefficient, and $d\vec{x}$ is the line element of the closed curve bounding the portion of the interface.

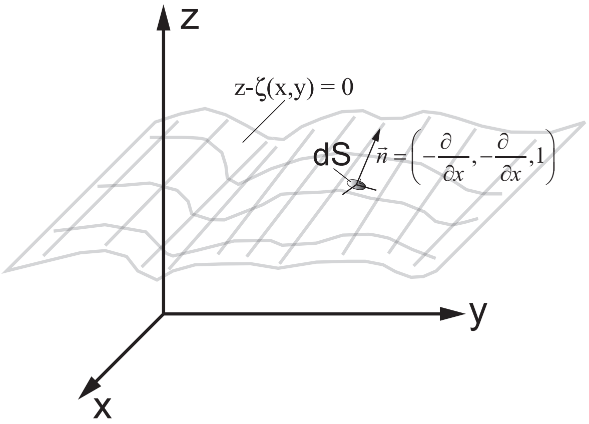
z
z-ζ(x,y) = 0
dS
$\vec{n} = \left(-\frac{\partial}{\partial x}, -\frac{\partial}{\partial x}, 1\right)$
y
x

Figure 5.1: surface tension.

The resultant is a force parallel to the local normal to surface element dS, and is of magnitude:

$$\overrightarrow{f_{ST}} = -\sigma \oint \Big(-\frac{\partial \zeta}{\partial x} dy + \frac{\partial \zeta}{\partial y} dx \Big) = \sigma \Big(\frac{\partial^2}{\partial x^2} + \frac{\partial^2}{\partial y^2} \Big) dS. \tag{5.13}$$

Equation 5.13 can be approximated as:

$$\overrightarrow{f_{ST}} \approx \sigma \Big(\frac{\partial^2 \zeta}{\partial x^2} + \frac{\partial^2 \zeta}{\partial y^2} \Big) dS. \tag{5.14}$$

The surface tension force acting on a curve bounding the interface element is dynamically equivalent to a pressure at dS on the interface of magnitude:

$$p_{ST} \approx \sigma \Big(\frac{1}{R_1} + \frac{1}{R_2} \Big) \delta_{12}, \tag{5.15}$$

where R_1 and R_2 are the principal radii of curvature at any given point of the surface, and the term δ_{12} is called the interface delta function; it is zero away from the interface, thereby ensuring that the surface tension force is active only near the interface.
The surface tension can be introduced in the Navier-Stokes Momentum equation and considered as a pressure [99].

5.2 Rotating flows

The dominance of rotation induced forces, *i.e.* the Coriolis and centrifugal forces, in a rotating flow can lead to interesting consequences. In general, rotation imparts some kind of rigidity to the flow, but also confers a certain elasticity on the fluid that makes possible the propagation of waves [62], [99].

5.2.1 Governing equations

When the motion of a uniformly rotating free-surface fluid is referred to a frame of reference that rotates with the fluid, the equation of motion of the fluid is changed only by the addition of an apparent body force:

$$\frac{\partial \vec{w}}{\partial t}+\vec{w}\cdot\vec{\nabla}\vec{w}=-\frac{1}{\rho}\vec{\nabla}p+\nu\nabla^2\vec{w}-\vec{\omega}\times(\vec{\omega}\times\vec{r})-2\vec{\omega}\times\vec{w}+\vec{\nabla}\sigma\left(\frac{1}{R_1}+\frac{1}{R_2}\right)\delta_{12}+\vec{g}, \quad (5.16)$$

where $\vec{\omega}$ is the angular velocity of the fluid. The centrifugal force $\vec{\omega}\times(\vec{\omega}\times\vec{r})$ only plays a significant role when the density ρ is nonuniform. On the other hand, if ρ is uniform, the centrifugal force is conservative and is equivalent to an effective radial pressure gradient and may be transformed away by incorporating this effective pressure in the actual pressure. The effects of rotation are then only contained in the term $2\vec{\omega}\times\vec{w}$, called the Coriolis force. The Coriolis force does not work on the fluid but acts to change the direction of velocity of the latter.

5.2.2 Dimensionless form

Equation 5.16 can be rendered dimensionless by introducing the following non-dimensional variables:

$x'=\frac{x}{L}$; $w'=\frac{w}{C}$; $t'=t\frac{C}{L}$;

$y'=\frac{y}{L}$; $p'=\frac{p}{\rho C^2}$; $r'=\frac{r}{L}$;

$z'=\frac{z}{L}$; $\nabla'=\nabla\cdot L$; $\omega'=\frac{\omega}{\Omega}$;

where L, C, and Ω are respectively a reference length, velocity and angular velocity. The Momentum equation can therefore be be rewritten in the following fashion by replacing the dimensional variables:

$$\begin{aligned}&\rho\frac{\partial(\vec{w'}C)}{\partial(t'\frac{L}{C})}+\rho\vec{w'}C\cdot\frac{1}{L}\vec{\nabla'}\vec{w'}C=-\frac{1}{L}\vec{\nabla'}(p'\rho C^2)+\frac{\mu}{L^2}\nabla'^2(\vec{w'}C)-\\&\rho\Omega\vec{\omega'}\times(\Omega\vec{\omega}'\times\vec{r'}L)-2\rho\Omega\vec{\omega'}\times\vec{w'}C+\vec{\nabla'}\frac{\sigma}{L^2}\left(\frac{1}{R'_1}+\frac{1}{R'_2}\right)\delta_{12}+\rho\vec{g}\end{aligned} \quad (5.17)$$

Rearranging the terms and multiplying both sides of Eq.5.17 by $\frac{L}{\rho C^2}$ yields to:

$$\begin{aligned}&\frac{\partial\vec{w'}}{\partial t}+\vec{w'}\vec{\nabla'}\vec{w'}=-\vec{\nabla'}p+\frac{\mu}{\rho CL}\nabla'^2\vec{w'}-\\&\frac{\Omega^2}{C^2}L^2\vec{\omega'}\times(\vec{\omega'}\times\vec{r'})-2\frac{\Omega L}{C}(\vec{\omega'}\times\vec{w'})+\vec{\nabla'}\frac{\sigma}{L^2\rho C^2}\left(\frac{1}{R'_1}+\frac{1}{R'_2}\right)\delta_{12}+\frac{L}{C^2}\vec{g}\end{aligned} \quad (5.18)$$

A series of remarkable non-dimensional numbers can be isolated from Eq.5.18. The dimensionless form of the Navier-Stokes Momentum conservation equation can hence be rewritten as:

$$\begin{aligned}&\frac{\partial\vec{w'}}{\partial t}+\vec{w'}\cdot\vec{\nabla'}\vec{w'}=-\vec{\nabla'}p'+\frac{1}{Re}\nabla'^2\vec{w'}-\frac{1}{Ro^2}\vec{\omega'}\times(\vec{\omega'}\times\vec{r'})\\&-\frac{2}{Ro}(\vec{\omega'}\times\vec{w'})+\frac{1}{We}\vec{\nabla'}(\frac{1}{R'_1}+\frac{1}{R'_2})\delta_{12}+\frac{1}{Fr}\vec{i_z}\end{aligned} \quad (5.19)$$

Reynolds number

The Reynolds number compares the magnitude of the inertia forces to the viscous forces.

$$Re = \frac{CL}{\nu} \tag{5.20}$$

Froude number

The Froude number measures the importance of the inertia forces relative to the gravity.

$$Fr = \sqrt{\frac{C^2}{gL}} \tag{5.21}$$

Weber number

The Weber number is the ratio between the inertia forces and the surface tension forces.

$$We = \frac{L\rho C^2}{\sigma} \tag{5.22}$$

Rossby number

The Rossby number measures the importance of the nonlinear convective acceleration term relative to the Coriolis term. For small Rossby number flows, like the steady large-scale circulations of the atmosphere and oceans, the inertia forces are negligible [99].

$$Ro = \frac{C}{L\Omega} \tag{5.23}$$

5.2.3 Step-up procedure

The reduced-scale tests are traditionally performed under the Froude similarity, because this ensures the same behavior of the water sheet flow leaving the machine on the model as on the prototype [115], [18]. As mentioned in section 2.1, this did not provide satisfactory results. This is the reason why a scaling-up procedure of the efficiency tests, intended to permit to conduct test campaigns on reduced scale models with a great deal of confidence and accuracy, has been developed from some of the above dimensionless numbers. Grein [30] identified from Buckingham's theorem the dimensionless numbers related to the main sources of losses in Pelton turbines. Then, based on a large number of homologous tests performed on reduced-scale and full-size machines, the so-called step-up formula was developed. The step-up is formulated so that the Froude similitude generally yields to positive step-up, as shown by Eq.5.24. The accuracy of the prediction is easier for well performing machines [93].

$$\Delta\eta = \eta_{proto} - \eta_{mod} = 5.7(1 - C_{Fr}^{0.3})\frac{\varphi_{B_2}^2}{\psi_1} + (1.95 \cdot 10^{-6} C_{We} + 10^{-8} C_{Re}^2)\frac{1}{\varphi_{B_2}^2/\psi_1} \tag{5.24}$$

where the coefficients C_{Fr}, C_{We}, and C_{Re} are defined as:

$$C_{Fr} = \frac{Fr_p}{Fr_M} \tag{5.25}$$

$$C_{We} = \frac{We_p}{We_M} \tag{5.26}$$

$$C_{Re} = \frac{Re_p}{Re_M} \tag{5.27}$$

Chapter 6

Physical models

6.1 Foreword

In multi-phase or multi-component flows, the presence of interfacial surfaces introduces significant difficulties in the mathematical and physical formulation of the problem [51]. From the mathematical point of view, a multi-phase flow can be considered as a field which is divided into single phase regions separated by moving boundaries. The differential balance holds for each subregion, however, it cannot be applied to the set of these sub-regions in the normal sense without violating the conditions of continuity.
From a physical point of view, the difficulties encountered in deriving the field and constitutive equations stem from the presence of the interface and from the fact that both the steady state and dynamic characteristics of dispersed two-phase flow systems depend upon the structure of the flow.

6.2 Multi-Fluid Models

The 2-Fluid Model, often called Euler-Euler model, is formulated by considering each phase separately. Thus, the model is expressed in terms of 2 sets of conservation equations describing the balance of masses, momenta and energies for each phase. However, since the averaged fields of one phase are not independent of the other phase, interaction terms must be introduced in the balance equations, *i.e.* mass, momentum and energy transfers to the n^{th} phase from the interfaces. Consequently 6 differential field equations with interfacial conditions describe the macroscopic 2-phase flow system.
In the 2-Fluid Model formulations, the transfer processes of each phase are expressed by their own balance equations. This model is highly complex not only in terms of the number of field equations but also in terms of the necessary number of constitutive equations.
The advantage of 2-Fluid Model lies within the fact that it can take into account the dynamic interactions between the phases. This is accomplished by using momentum equations for each phase and 2 independent velocity fields in the formulation. On the other hand the constitutive equations should be highly accurate, since the equations of the 2 phases are completely independent and the interaction terms modulates the degree of coupling between the phases [51].

Continuity equation

The 2-Fluid Model is characterized by 2 independent velocity fields for each phase. The most common choice is the mass-weighted mean phase velocities $\overrightarrow{C_n}$. The suitable form of the continuity equation is:

$$\frac{\partial \alpha_n \rho_n}{\partial t} + \vec{\nabla} \cdot (\alpha_n \rho_n \vec{C}_n) = \Gamma_n \tag{6.1}$$

with the interfacial mass transfer condition:

$$\sum_{n=1}^{2} \Gamma_n = 0 \tag{6.2}$$

where Γ_n represents the rate of production of the n^{th} phase mass from the phase changes at the interfaces and α_n is the local volume fraction . The sum of the volume fractions of the n phases must therefore be:

$$\sum_{n=1}^{2} \alpha_n = 1 \tag{6.3}$$

Momentum conservation

The conservation of Momentum is expressed by 2 Momentum equations (one for each phase), such as:

$$\frac{\partial}{\partial t}(\alpha_n \rho_n \vec{C}_n) + \alpha_n \rho_n (\vec{C}_n \cdot \vec{\nabla})\vec{C}_n = -\vec{\nabla}(\alpha_n p_n) + \vec{\nabla} \cdot (\alpha_n \bar{\bar{\tau}}_n + \alpha_n \bar{\bar{\tau}}_{t,n} + \vec{M}_n) + \vec{f} \tag{6.4}$$

The Momentum equation for each phase features an interfacial source term $\vec{M}_n$ that couples the motions of the 2 phases. The interfacial transfer condition has the form:

$$\sum_{n=1}^{2} \vec{M}_n = \vec{M}_m \tag{6.5}$$

and :

$$\vec{M}_m = 2R_{21}\sigma\vec{\nabla}\alpha_2 + \vec{M}_m^R, \tag{6.6}$$

where R_{21} denotes the average mean curvature of the interfaces, σ the surface tension coefficient , and $\vec{M}_m^R$ takes into account the effect of changes in the mean curvature. Finally, the Momentum equation can be written as :

$$\begin{aligned} &\frac{\partial}{\partial t}(\alpha_n \rho_n \vec{C}_n) + \alpha_n \rho_n (\vec{C}_n \cdot \vec{\nabla})\vec{C}_n = \\ &\qquad -\vec{\nabla}\alpha_n p_n + (p_{ni} - p_n)\vec{\nabla}\alpha_n + \vec{f} \\ &\qquad +\vec{\nabla} \cdot (\alpha_n \bar{\bar{\tau}}_{t,n} + \alpha_n \bar{\bar{\tau}}_n) + (\vec{C}_{ni} - \vec{C}_n)\Gamma_n + \vec{M}_n^d \end{aligned} \tag{6.7}$$

where Γ_n is the mass production rate, p_{ni} and $\vec{C}_{ni}$ the pressure and velocity of the n^{th} phase at interface i. The term $\vec{M}_n^d$ represents the total diffusion forces.

Constitutive conservation

In the previous formulations, the number of dependent variables exceeds those of the field equations, thus the balance equations with proper boundary conditions are insufficient to solve the problem. Consequently it is necessary to supplement them with various constitutive equations, usually of 4 types, *i.e.* (i) state, (ii) mechanical, (iii) energetic and (iv) turbulent, defining different classes of idealized fluids.

The constitutive equations of state express the fluid proprieties like density $\rho_n(T_n, p_n)$, enthalpy $h_n(T_n, p_n)$ and surface tension $S(T_n)$ as functions of thermodynamic properties.

In a mechanical point of view, the most used one is the linearly Navier-Stokes viscous flow is the most commonly used. The constitutive equation is of the form:

$$\tau_n = \mu_n \left[\nabla\vec{C_n} + \left(\nabla\vec{C_n}\right)^T\right] - \left(\tfrac{2}{3}\mu_n - \lambda_n\right)\left(\nabla\cdot\vec{C_n}\right)\bar{\bar{I}}$$

The contact heat transfer is expressed by the heat flux vector $\vec{q_n}$, while the energetic constitutive equation specifies the nature and mechanism of the contact energy transfer. Most fluids are assumed to behave according to the generalized Fourier's law of heat conduction.

The difficulties encountered in writing the constitutive equations for turbulent fluxes even in single phase flow are considerable. The formulations of the turbulent stress tensor are usually the same as for homogeneous mixtures.

6.3 Homogeneous Models

The basic concept of the so-called Mixture Model, also referred as Diffusion Model is to consider the mixture as a whole. This formulation is simpler than the 2-Fluid Model, however it requires some coarse assumptions involving some of the important characteristics of 2-phase flows to be lost.

The most important aspect of the diffusion model is the reduction in the total number of field and constitutive equations required. The system is expressed in terms of 3 field equations: (i) mixture continuity, (ii) Momentum conservation and (iii) energy conservation. These 3 macroscopic mixture conservation equations are supplemented by a diffusion equation which takes into account for the concentration, *i.e.* volume fraction change [51]. This approach is appropriate to mixtures, where the dynamic of the 2 components is locally closely coupled and the whole system is resolved in a macroscopic point of view. If the system does not include phase changes, *i.e.* negligible drift or diffusion of mass, the system can be simplified and is called 2-Phase Homogeneous Model.

Continuity equation

The mixture continuity equation can be written as follows:

$$\frac{\partial\rho_m}{\partial t} + \vec{\nabla}\cdot(\rho_m\vec{C_m}) = 0 \tag{6.8}$$

It presents exactly the same form as the single-phase continuity equation without internal discontinuities, where the mixture quantities are defined as:

$$\rho_m = \sum_{n=1}^{2}\rho_n\alpha_n \tag{6.9}$$

$$\vec{C}_m = \sum_{n=1}^{2} \frac{\rho_n \vec{C}_n}{\rho_m} \tag{6.10}$$

$$p_m = \sum_{n=1}^{2} p_n \alpha_n \tag{6.11}$$

Diffusion equation

The diffusion equation, which expresses the change in concentration α_n (i.e. the mixture density ρ_m), is derived as:

$$\frac{\partial \alpha_n \rho_n}{\partial t} + \vec{\nabla} \cdot (\alpha_n \rho_n \vec{C}_m) = \Gamma_n - \nabla \cdot \left(\alpha_n \rho_n \vec{C}_{12} \right) \tag{6.12}$$

where Γ_n accounts for the mass transfer at the interface, and the second right hand term is the diffusion flux term, since the convective flux are expressed by the velocity of the mixture center of mass. It should be noticed that in Eq.6.12, the diffusion terms are explicitly written as the development is based on the mixture center of mass.
In the case where the relation is expressed through the velocities of the center of mass of each phase, C_n, the equation will be:

$$\frac{\partial \alpha_n \rho_n}{\partial t} + \vec{\nabla} \cdot (\alpha_n \rho_n \vec{C}_n) = \Gamma_n \tag{6.13}$$

If the system is phase change controlled (negligible drift or diffusion of mass in the diffusion equation), *i.e.* the relative motion between the 2 phases is negligible or not taken into account, the model is simplified and called Homogeneous Model. The diffusion equation in this case reduces to ($C_{12} \sim 0$):

$$\frac{\partial \alpha_n \rho_n}{\partial t} + \vec{\nabla} \cdot (\alpha_n \rho_n \vec{C}_m) = \Gamma_n \tag{6.14}$$

On the other hand, when the effects of the relative motions between 2 phases are taken into account by the drift velocity, $\vec{C}_{12} \neq 0$, the model is referred as Drift Model .

Momentum equation

The general formulation of the conservation of Momentum exhibits the same form as in the single phase theory for the whole mixture:

$$\frac{\partial}{\partial t}(\rho_m \vec{C}_m) + \rho_m (\vec{C}_m \cdot \vec{\nabla}) \vec{C}_m = -\vec{\nabla}(p_m) + \vec{\nabla}(\bar{\bar{\tau}} + \bar{\bar{\tau}}_t) + \vec{M}_m + \vec{f} \tag{6.15}$$

$\vec{M}_m$ is the interfacial momentum source and the surface tension term is neglected. There is no direct terms in the mixture momentum equation.

6.3.1 Brackbill's surface tension model

The surface tension force is modelled as a volume force concentrated at the interface, rather than a surface force. The surface tension force $\overrightarrow{F_{12}}$ between a primary fluid 1, the liquid phase, and a secondary fluid 2, the gaseous phase, is given by [10]:

$$\overrightarrow{F_{12}} = \overrightarrow{f_{12}}\delta_{12} \tag{6.16}$$

Where

$$\overrightarrow{f_{12}} = -\sigma\kappa\overrightarrow{n_{12}} + \overrightarrow{\nabla}_s\sigma_{12} \tag{6.17}$$

and

$$\delta_{12} = \begin{cases} 1, & r_{12} \equiv 0 \\ 0, & r_{12} > 0 \end{cases} \tag{6.18}$$

The 2 terms summed on the right hand side of Eq. 6.17 reflect the normal and tangential components of the surface tension force. The normal component stems from the interface curvature and the tangential component from variations in the surface tension coefficient σ. The term δ_{12} is called the interface delta function; it is zero away from the interface, thereby ensuring that the surface tension force is active only near the interface.

6.4 Turbulent homogeneous flow formulation

A turbulent flow is by definition unsteady. The velocity vector varies randomly in terms of direction and magnitude, and the flow contains a large number of eddies of different sizes. The Reynolds decomposition, *i.e.* Reynolds Stress Averaging, allows describing the turbulent motion as the sum of an average velocity and a fluctuating velocity. Any velocity component u can therefore be written as:

$$u = \overline{u} + u', \tag{6.19}$$

where $\overline{u}$ is the average value and u' the fluctuating value. Applying this principle to the Momentum equation, Eq.5.9, yields to:

$$\rho\frac{\partial\overrightarrow{c}}{\partial t} + \rho(\overrightarrow{c}\cdot\overrightarrow{\nabla})\overrightarrow{c} = -\overrightarrow{\nabla}(p + \rho g z) + \mu\overrightarrow{\nabla}^2\overrightarrow{c} + \overrightarrow{\nabla}\cdot\overline{\overline{\tau}}_t \tag{6.20}$$

Equation 6.20 is known as Reynolds equation. $\overline{\overline{\tau_t}}$ is the Reynolds stress tensor which is expressed as a function of the correlation tensor between 2 fluctuating components of velocity vector $\overrightarrow{c}'$, such that:

$$\overline{\overline{\tau}}_t = -\rho\overline{\overrightarrow{c}'\otimes\overrightarrow{c}'} = -\rho\begin{pmatrix} \overline{u'^2} & \overline{u'v'} & \overline{u'w'} \\ \overline{v'u'} & \overline{v'^2} & \overline{v'w'} \\ \overline{w'u'} & \overline{w'v'} & \overline{w'^2} \end{pmatrix} \tag{6.21}$$

The Reynolds stress tensor is symmetrical. The Reynolds equation eventually features 10 unknowns, *i.e* the 3 velocity components, the pressure and the 6 components of the Reynolds tensor.

The complexity of the turbulence and its random characteristics, obligate to use a simple formulation for the extra stresses. That is the reason why the multiphase turbulence formulations are simplified to homogeneous formulations, meaning that the transport equations for the turbulence are limited to that of the whole fluid mixture.

6.4.1 Zero-equation models

Prandtl proposed to take into account the average shear as reference scale and introduced the turbulent mixing length, l. The Reynolds stress tensor can therefore be expressed as:

$$-\overline{\rho c_i' c_j'} = \rho l^2 \left(\frac{\partial \overline{c_i}}{\partial x_j} \right)^2 \tag{6.22}$$

Prandtl assumed that the velocity scale C was equal to the product of the average velocity field with the mixing length l:

$$C = \left| \frac{\partial \overline{c_i}}{\partial x_j} \right| \tag{6.23}$$

Boussinesq defined the turbulent viscosity coefficient μ_t, assuming the average velocity field and the Reynolds tensor components to be proportionally related. Therefore,

$$\mu_t = l^2 \left| \frac{d\overline{c_i}}{dx_j} \right| \tag{6.24}$$

Only one unknown, independent of the fluid properties, remains: the mixing length, l. More details can be found in [94].

6.4.2 k-ε models

Based on semi-empirical equations, the standard or original k-ε model (Jones and Launder 1972, Launder and Spalding, 1974) features 2 equations, one for the turbulent kinetic energy, k, and one for the rate of viscous dissipation, ε [112]. The velocity and the length scale are assumed to be:

$$C \sim \sqrt{k} \qquad\qquad L \sim \frac{k^{\frac{2}{3}}}{\varepsilon} \tag{6.25}$$

With the Prandtl-Kolmogorov analogy, the eddy viscosity is specified as:

$$\mu_t = Constant\ \rho C L = \rho C_\mu \frac{k^2}{\varepsilon} \tag{6.26}$$

relating the variables k and ε via a dimensionless constant C_μ.
The model uses the following transport equations:
(i) Turbulence Kinetic Energy:

$$\frac{\partial \rho k}{\partial t} + \frac{\partial \rho C_j k}{\partial x_j} = \frac{\partial}{\partial x_j}((\mu + \frac{\mu_t}{\sigma_k})\frac{\partial k}{\partial x_j}) + \tau_{ij}\frac{\partial C_i}{\partial x_j} - \rho\varepsilon \tag{6.27}$$

(ii) Dissipation Rate:

$$\frac{\partial \rho \varepsilon}{\partial t} + \frac{\partial \rho C_j \varepsilon}{\partial x_j} = \frac{\partial}{\partial x_j}\left((\mu + \frac{\mu_t}{\sigma_\varepsilon})\frac{\partial \varepsilon}{\partial x_j}\right) + \frac{\varepsilon}{k}\left(C_{\varepsilon 1}\tau_{ij}\frac{\partial C_i}{\partial x_j} - C_{\varepsilon 2}\rho\varepsilon\right) \tag{6.28}$$

.

The model contains 5 adjustable constants derived from experiments:

$C_\mu = 0.09$; $\sigma_k = 1.00$; $\sigma_\varepsilon = 1.30$; $C_{1\varepsilon} = 1.44$; $C_{2\varepsilon} = 1.92$.
The Reynolds stress tensor is computed using an extended Boussinesq relationship, Eq.6.24:

$$-\rho C_i' C_j' = \mu_t \left(\frac{\partial C_i}{\partial x_j} + \frac{\partial C_j}{\partial x_i} \right) - \frac{2}{3} \rho k \delta_{ij} \tag{6.29}$$

with the following auxiliary relations :

$$\omega = \frac{\varepsilon}{C_\mu k} \qquad L_t = C_\mu \frac{k^{3/2}}{\varepsilon}. \tag{6.30}$$

6.4.3 k-ω models

One of the advantages of the k-ω formulation is the near wall treatment for low-Reynolds number computations. The model does not involve the complex non-linear damping functions required for the k-ε model and is therefore more accurate and more robust. The k-ω model assumes that the eddy viscosity is linked to the turbulence kinetic energy and turbulent frequency via the relation:

$$\mu_t = \rho \frac{k}{\omega} \tag{6.31}$$

The standard (original) k-ω model [119] solves 2 transport equations, one for the turbulent kinetic energy k, and one for the specific dissipation rate ω (rate of dissipation per unit of turbulence kinetic energy, often called turbulent frequency) and the stress tensor is computed from the eddy-viscosity concept.

Turbulence Kinetic Energy:

$$\frac{\partial \rho k}{\partial t} + \frac{\partial \rho C_j k}{\partial x_j} = \frac{\partial}{\partial x_j} \left((\mu + \sigma^* \mu_t) \frac{\partial k}{\partial x_j} \right) + \tau_{ij} \frac{\partial C_i}{\partial x_j} - \beta^* \rho k \omega \tag{6.32}$$

Specific Dissipation Rate:

$$\frac{\partial \rho \omega}{\partial t} + \frac{\partial \rho C_j \omega}{\partial x_j} = \frac{\partial}{\partial x_j} \left((\mu + \sigma \mu_t) \frac{\partial \omega}{\partial x_j} \right) + \frac{\omega}{k} \left(\alpha \tau_{ij} \frac{\partial C_i}{\partial x_j} - \beta \rho k \omega \right) \tag{6.33}$$

Closure Coefficients :

$\alpha = 5/9$; $\beta = 3/40$; $\beta^* = 9/100$; $\sigma = 1/2$; $\sigma^* = 1/2$.

Auxiliary Relations :

$$\varepsilon = \beta^* \omega k \qquad L_t = \frac{k^{1/2}}{\omega} \tag{6.34}$$

6.4.4 SST models

A problem with the original k-ω model is its strong sensitivity to free-stream conditions [89]. In order to solve the problem, a blending between the k-ω model near the surface and the k-ε model in the outer region was developed by Menter [74].

The model called Shear Stress Transport model (SST) solves the problem by multiplying the k-ω equations by blending function (F_1), and the transformed Launder-Spalding k-ε equations by $(1 - F_1)$, such as:

Turbulence Kinetic Energy:

$$\frac{\partial \rho k}{\partial t} + \frac{\partial \rho C_j k}{\partial x_j} = \frac{\partial}{\partial x_j}\left((\mu + \frac{\mu_t}{\sigma_{k3}})\frac{\partial k}{\partial x_j}\right) + \tau_{ij}\frac{\partial C_i}{\partial x_j} - \beta^* \rho k \omega \tag{6.35}$$

Specific Dissipation Rate:

$$\begin{aligned}\rho\frac{\partial \omega}{\partial t} + \rho C_j \frac{\partial \omega}{\partial x_j} &= \frac{\partial}{\partial x_j}\left((\mu + \frac{\mu_t}{\sigma_{\omega 3}})\frac{\partial \omega}{\partial x_j}\right) + \frac{\omega}{k}\left(\alpha_3 \tau_{ij}\frac{\partial C_i}{\partial x_j} - \beta_3 \rho k \omega\right)\\ &+ (1 - F_1) 2\rho \frac{1}{\omega \sigma_{\omega 2}}\frac{\partial k}{\partial x_j}\frac{\partial \omega}{\partial x_j}\end{aligned} \tag{6.36}$$

where the coefficients of the model are a linear combination of the corresponding coefficients of the k-ω and modified k-ε models ($\Phi = F_1 \Phi_{k\omega} + (1 - F_1)\Phi_{k\varepsilon}$).

Closure coefficients :

k-ω:	$\alpha_1 = 5/9$;	$\beta_1 = 3/40$;	$\sigma_{k1} = 2$;	$\sigma_{\omega 1} = 2$;	$\beta^* = 9/100$;
k-ε:	$\alpha_2 = 0.44$;	$\beta_2 = 0.0828$;	$\sigma_{k2} = 1$;	$\sigma_{\omega 2} = 1/0.856$;	$C_\mu = 0.09$;

The model combines the advantages of the Wilcox k-ω and the Launder-Spalding k-ε model, but still fails to properly predict the onset and amount of flow separation from smooth surfaces due to the over-prediction of the eddy-viscosity (the transport of the turbulent shear stress not properly taken into account). The proper transport behavior can be obtained by a limiter added to the formulation of the eddy-viscosity:

$$\mu_t = \rho \frac{k}{\max(\omega, S F_2)} \tag{6.37}$$

F_2 is a blending function, which restricts the limiter to the wall boundary layer, as the underlying assumptions are not correct for free shear flows. S is an invariant measure of the strain rate.

The choice of the blending functions F_1 and F_2 are critical to the success of the method. Their formulation is based on the distance to the nearest surface and on the flow variables. The model accounts for the transport of the turbulent shear stress and should provide more accurate predictions of the onset and the amount of flow separation under adverse pressure gradients.

6.5 Turbulent multifluid flow formulation

With a multifluid approach, the logical modelling of turbulence would imply developing separate sets of equations defining each phase separately. The complexity of this approach conducts major researchers to deal with classical homogeneous turbulence formulation. However some researchers developed the idea of modifying the classical 2-equation turbulence models. Vaidyanathan [109] and Senocak [98] proposed a non-equilibrium k-ε model, based on the correction of the model coefficients to fit the experimental data based on optimization techniques. The differences between the computational and experimental results are used to assess the model accuracy. Reboud *et al.* [92], [21] have introduced an artificial compressibility in the classical incompressible k-ε model. The idea is to avoid the high diffusivity of the numerical model, caused by the addition of the artificial viscosity (μ_t). The model assumes a low and non linear turbulent viscosity on the multiphasic media, expressed as:

$$\mu_t = f(\rho) C_\mu \frac{k^2}{\varepsilon} \tag{6.38}$$

where $f(\rho)$ is a power function as:

$$f(\rho) = \rho_v + \left(\frac{\rho_v - \rho_m}{\rho_l - \rho_v} \right)^n (\rho_v - \rho_l) \qquad n \gg 1 \tag{6.39}$$

6.5.1 Reynolds Stress Turbulence Models

The Reynolds stress equation models (RSM), also called second-order or second-momentum closure models are based on transport equations for all the components of the Reynolds stress tensor and the dissipation rate. These models, which originate from Launder (1975), do not use the eddy viscosity hypothesis but solve an equation for the transport of Reynolds stresses in the fluid (algebraic equations for the Algebraic-RSM (ASM) and individual differential equations for each Reynolds stress component for the original RSM). The modelling of stress anisotropy, *i.e.* directional effects of the Reynolds stress field, makes Reynolds stress models more suitable for solving complex flows problems. The exact differential equations describing the Reynolds-stress tensor $-\rho\overline{C_i' C_j'}$ are:

$$\frac{\partial \rho \tau_{ij}}{\partial t} + \frac{\partial \rho C_k \tau_{ij}}{\partial x_k} = -P_{ij} + \varepsilon_{ij} - \Pi_{ij} + \frac{\partial}{\partial x_k} \left[\mu \frac{\partial \tau_{ij}}{\partial x_k} + C_{ijk} \right] \tag{6.40}$$

where

$$P_{ij} = \tau_{ik} \frac{\partial C_j}{\partial x_k} + \tau_{jk} \frac{\partial C_i}{\partial x_k} \tag{6.41}$$

$$\varepsilon_{ij} = \overline{2\mu \frac{\partial C_i'}{\partial x_k} \frac{\partial C_j'}{\partial x_k}} \tag{6.42}$$

$$C_{ijk} = \overline{\rho C_i' C_j' C_k'} + \overline{p' C_i'} \delta_{jk} + \overline{p' C_j'} \delta_{ik} \tag{6.43}$$

$$\Pi_{ij} = \overline{p' \left(\frac{\partial C_i'}{\partial x_j} + \frac{\partial C_j'}{\partial x_i} \right)} \tag{6.44}$$

are respectively the production, dissipation, turbulent transport and pressure-strain correlation tensors, which should be modelled to close the system of equations.

Reynolds stress-ω Turbulence Model

The Reynolds Stress-ω turbulence model is a Reynolds stress model based on the ω-equation (instead of ε-equation). The advantage is similar to that of the k-ω model allowing an accurate near wall treatment. The equations for the Reynolds stresses can be written as: Reynolds-Stress Tensor (6 differential equations):

$$\frac{\partial \rho \tau_{ij}}{\partial t} + \frac{\partial \rho C_k \tau_{ij}}{\partial x_k} = -P_{ij} + \varepsilon_{ij} - \Pi_{ij} + \frac{\partial}{\partial x_k}\left[\mu \frac{\partial \tau_{ij}}{\partial x_k} + C_{ijk}\right] \tag{6.45}$$

Specific Dissipation Rate :

$$\rho \frac{\partial \omega}{\partial t} + \rho \bar{C}_j \frac{\partial \omega}{\partial x_j} = \frac{\partial}{\partial x_k}\left((\mu + \sigma \mu_t)\frac{\partial \omega}{\partial x_k}\right) + \frac{\omega}{k}(\alpha \tau_{ij}\frac{\partial C_i}{\partial x_j} - \beta \rho k[\omega + \hat{\xi}\sqrt{2\Omega_{mn}\Omega_{mn}}]) \tag{6.46}$$

Auxiliary Closure Relations :

$$\mu_t = \rho \frac{k}{\omega} \qquad \varepsilon = \beta^* \omega k \tag{6.47}$$

$$P_{ij} = \tau_{ik}\frac{\partial C_j}{\partial x_k} + \tau_{jk}\frac{\partial C_i}{\partial x_k} \qquad D_{ij} = \tau_{ik}\frac{\partial C_k}{\partial x_j} + \tau_{jk}\frac{\partial C_k}{\partial x_i} \tag{6.48}$$

$$\begin{aligned}\Pi_{ij} = {} & \beta^* C_1 \omega \left(\tau_{ij} + \frac{2}{3}\rho k \delta_{ij}\sigma\right) - \hat{\alpha}\left(P_{ij} + \frac{2}{3}P\delta_{ij}\sigma\right) \\ & -\hat{\beta}\left(D_{ij} + \frac{2}{3}P\delta_{ij}\sigma\right) - \hat{\gamma}\rho k\left(S_{ij} + \frac{1}{3}S_{kk}\delta_{ij}\sigma\right)\end{aligned} \tag{6.49}$$

Closure coefficients :

$\alpha = 4/5;$	$\beta = 3/40;$	$\beta^* = 9/100;$	$\sigma = 1/2;$	$\sigma^* = 1/2;$
$\hat{\alpha} = 42/55;$	$\hat{\beta} = 6/55;$	$\hat{\gamma} = 1/4;$	$\hat{\xi} = 1;$	
$C_1 = 1 + 4(1 - e/k)^3/2;$				

Chapter 7

Main definitions

7.1 Duty cycle and angular datum definitions

The duty cycle of any bucket j of the runner can be defined as the arc out of bucket j rotation circle where it sees water transiting on its surface. The duty cycle ranges from the first encounter of bucket j tip with the upper generator of the jet to the evacuation of the last water particle stemming from the lower generator of the jet, *i.e.* arc AB on Fig.7.1. The exact angular position of point A is depending on the jet diameter, *i.e.* φ_{B_2} and point B by the head, *i.e.* ψ_1. Moreover, the jet boundary is difficult to experimentally determine with accuracy. An univocal angular datum is hence needed. Bucket j datum is set as the angular position where the virtual point located on bucket j splitter on the circle of diameter D_1 intersects the jet axis, see Fig.7.1. The angular positions of bucket j, θ_j, preceding the datum are negative, while the angular positions succeeding to the datum are positive.

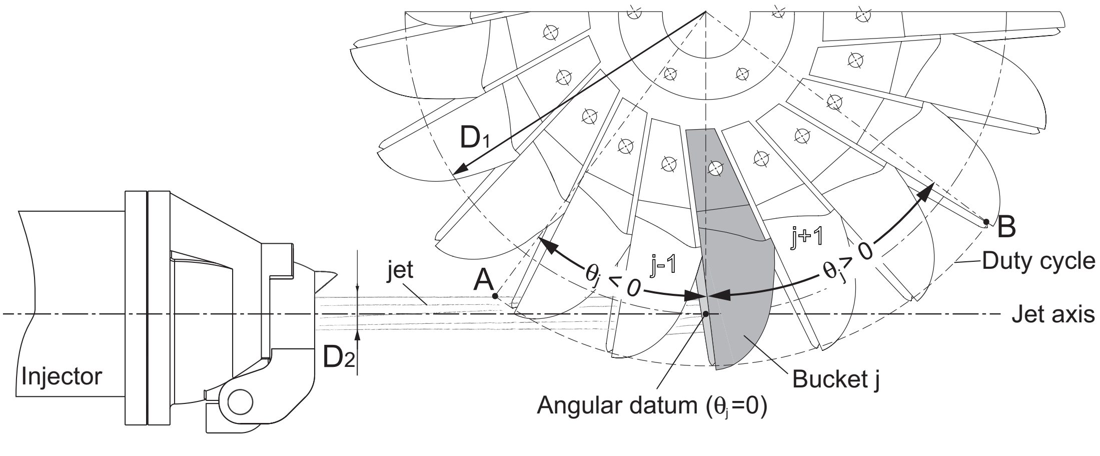

Figure 7.1: Bucket angular datum definition.

7.2 Non-dimensionalization of pressure

The pressure signals amplitude, be them the result of computations or measured ones, are made dimensionless by the introduction of the pressure coefficient Cp, defined as:

$$Cp = \frac{p - p_{ref}}{\rho g H} \tag{7.1}$$

where p_{ref} is a reference pressure, *i.e.* the atmospheric pressure for the experimental pressure measurements and any reference set for the computations, and H is the test head.

7.3 Non-dimensionalization of water thickness

The water film thickness in the buckets, referred as t, is rendered non-dimensional by the theoretical contracted jet diameter of the considered operating point k, calculated from the discharge conditions, D_{2_k}.

$$t' = \frac{t}{D_{2_k}} \tag{7.2}$$

Part II

INVESTIGATION TOOLS

Chapter 8

Experimental facilities

8.1 Test rig

All the measurements are carried out on the horizontal test rig of VA Tech Hydro SA, located in Vevey, Switzerland, see Fig.8.1. The test rig is suited for single- or twin-injector machines, and is equipped with 3 pumps, that can be operated either separately, in parallel or in series. The first one is powered by a $500kW$ asynchronous motor, while the 2 others are driven by DC motors, developing each $200kW$, fed by thyristors rectifier units. The rotational speed can thus be adjusted over a large band. Table 8.1 summarizes the main characteristics of the test rig. The facility is equipped with a torquemeter, and hydraulic

Table 8.1: VA Tech horizontal axis Pelton turbine test rig characteristics.

$P_{t_{max}}$ $[kW]$	H_{max} $[m]$	Q_{max} $[m^3 s^{-1}]$	Torquemeter limit $[kW]$
940	250	0.11	132

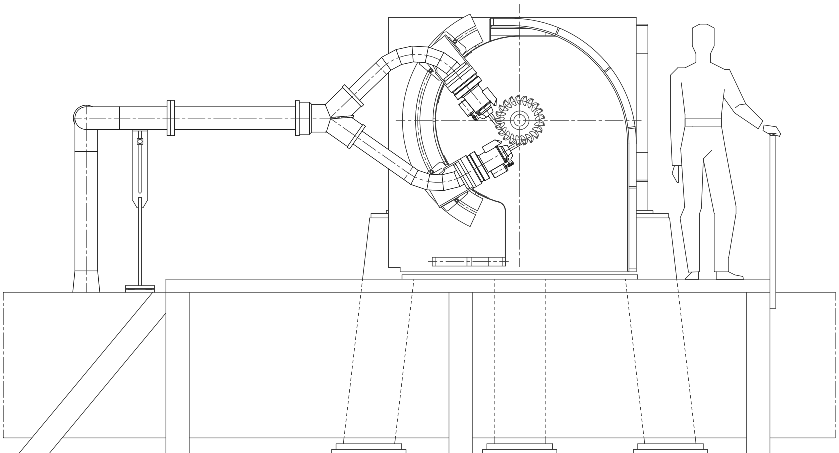

Figure 8.1: The Pelton test rig of VA Tech Hydro SA.

controlled injector needles. The equipment allowing setting the operating conditions, monitoring and measuring the relevant data is located in a control room adjacent to the test rig. The facility is fitted with a large plexiglas window allowing observing the runner and injector.

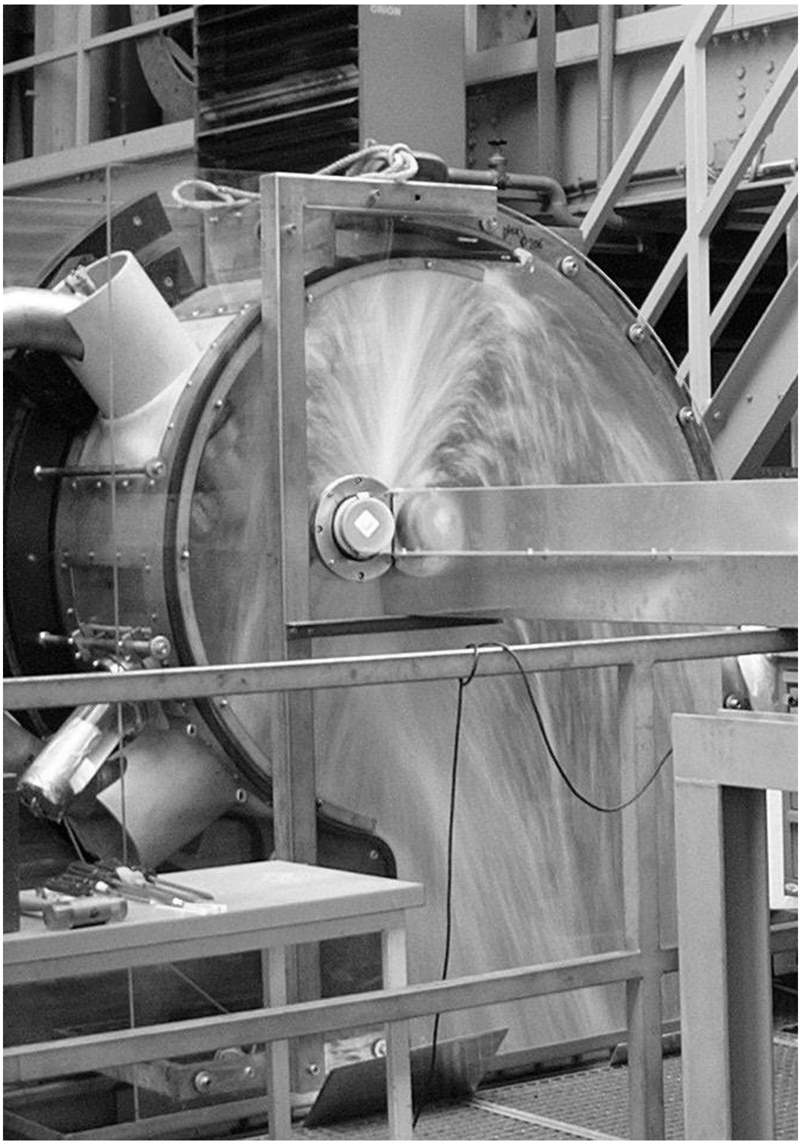

Figure 8.2: Test rig casing and plexiglas window.

Chapter 9

Onboard pressure measurements

9.1 Measurement tools

9.1.1 Piezo-resistive pressure transducers

Piezo-resistive sensors are designed for dynamic and static pressure measurements purposes. The pressure sensitive elements are piezo-resistive chips made of micro-machined Silicon, mounted in a Wheatstone bridge, as schematized by Fig.9.1. The active face of the sensor is made of a waterproof membrane of high stiffness. Piezo-resistive gauges are placed on the periphery of the membrane in traction and compression zones. When a pressure is applied on the membrane, the deformation of the latter is transmitted to the gauges, inducing a disequilibrium in the Wheatstone bridge, and thus a variation of the sensor output voltage. The main characteristics of the Unisensor AG transducers chosen for the bucket instrumentation are summarized by Table 9.1.

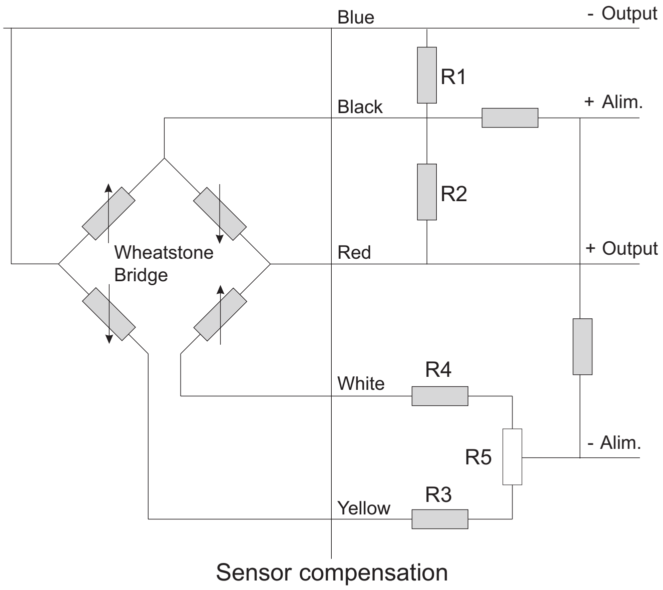
Blue
- Output
R1
Black
+ Alim.
R2
Wheatstone Bridge
Red
+ Output
White
R4
R5
- Alim.
Yellow
R3
Sensor compensation

Figure 9.1: Wheatstone bridge of a piezo-resistive sensor.

Table 9.1: Sensors characteristics.

D_{ext} $[mm]$	Thickness $[mm]$	$D_{membrane}$ $[mm]$	Linear Range $[bar]$	Bandwidth $[kHz]$	Linearity $[\%error]$
3	0.9	0.9	0...7	25	< 0.5

9.1.2 Instrumented shaft

An instrumented shaft has been developed at the LMH for onboard measurement purposes. Up to 32 channels, be them pressure sensors, strain gauges, or any measurement device generating a variable voltage output, can be acquired simultaneously. The onboard electronic for signal conditioning is made of 32 preamplifiers and anti-aliasing filters. Amplification factors may be selected from 1 to 10^3. The conditioning equipment is connected to 8 4-channel acquisition boards, fitted with 12-bit A/D converters. The sample frequency ranges $100Hz...20kHz$ while the memory storage capability is of $64k$-sample per channel [26]. Figure 9.2 shows the main organs of the instrumented shaft. A host PC computer is used for monitoring, control, and data transfer via an ArcNet(Attached Resource Computer Network) communication network. External communication and power supply are achieved with a 5-channel slip ring (HBM5K5). The system is capable of transferring up to 1.5 $Mbits$ per second. The synchronization of the data sampling process of the active boards is performed through a master-slave scheme. The slave boards are armed first, and then the master board is armed in turn. Once the master is triggered by the onboard tachometer signal, it outputs a TTL signal to trigger the onboard slave modules. All active modules are synchronously triggered within 5 μs, see Fig.9.3.

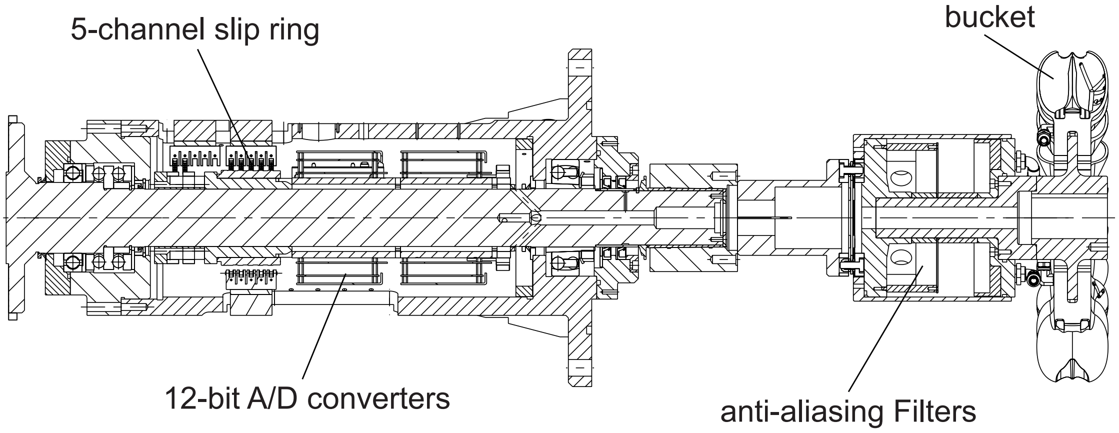

Figure 9.2: Instrumented shaft main organs.

9.2 Instrumented runner

The buckets to be instrumented with pressure transducers are made of bronze instead of epoxy polymer.

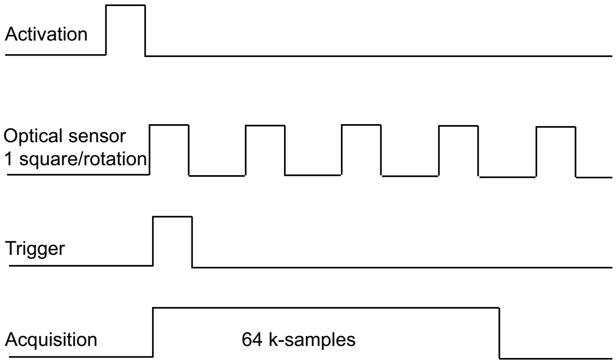
Activation
Optical sensor
1 square/rotation
Trigger
Acquisition
64 k-samples

Figure 9.3: Synchronization diagram of the instrumented shaft.

9.2.1 Sensors location and distribution

The 3 buckets are equipped with 43 sensors, distributed as summarized by Table 9.2 and illustrated by Fig.9.4. The sensors are distributed so as to cover most of the bucket inner surface, while not generating geometric alterations on either side of the bucket. CAM-CAD tools are used not only to check the locations of the sensors but also to design the wiring passages.

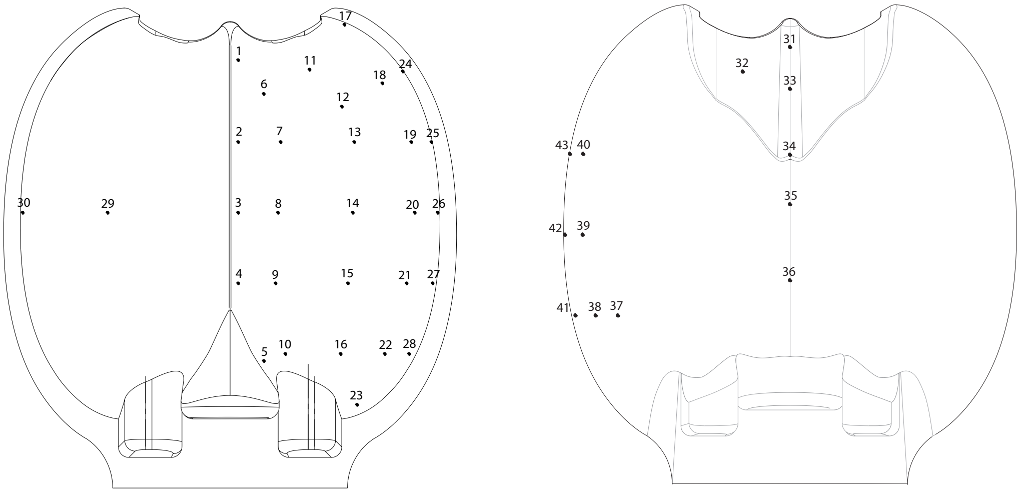
17
1
11
24
18
6
12
2
7
13
19
25
30
29
3
8
14
20
26
4
9
15
21
27
5
10
16
22
28
23
31
32
33
43
40
34
35
42
39
36
41
38
37

(a) Inner surface. (b) Backside.

Figure 9.4: Location of the 43 pressure sensors.

Table 9.2: Sensors distribution.

Location	Inner surface	Symmetry	Backside	Side
Sensors ♯	30	2	6	7

- **Redundant locations**. 2 transducers are added to check the symmetry of the flow.

(i) in a region of expected high amplitudes of pressure, to enhance the accuracy of the symmetry comparison, (ii) near the outer edge, close to the main stream outflow.

- **Backside**. A total of 6 sensors are placed on the backside, 5 of which on the longitudinal line of symmetry of the bucket in order to monitor the behavior of the cut jet portion.
- **Side**. Inasmuch the runner is designed to suffer from outflow heeling, a group of 6 sensors are located on the outer edge. They are also intended to measure the ventilation flow of air around the runner.

9.2.2 Machining

The whole manufacturing process of the instrumented buckets is modelled by CAM-CAD tools, *i.e* the machining process, the tools trajectories, and change of tools. A 5-axis numerical drill permits producing almost finished buckets, including the sensor lodgings and wiring grooves, Fig.9.5(a).

9.2.3 Transducers installation

The installation procedure is performed by Unisensor AG using their well mastered vacuum technique, while the wiring is made by the LMH staff, Fig.9.5(b). The wires are glued in the bucket grooves, a layer of a waterproof polymer resin is applied, and finally the original geometry is reconstituted with mastic and by polishing. A transducer test rig is built to check the wirings and verify the response of the sensors upon application of static pressure. The test is repeated at each step of the assembly process.

9.2.4 Final assembly

The different elements of the runner, *i.e.* the epoxy resin and bronze buckets, the flask, and the electronic housing are assembled by the LMH staff, see Fig.9.5(c). The finish resin polymer is applied by the VATech Kriens staff. The last step involves the final wiring and the installation of the electronic components, as portrayed by Fig.9.5(d).

9.3 Calibration procedures

9.3.1 Static calibration

The purpose of static calibration is to check the sensitivity, repeatability, and the hysteresis error of the sensors.

Procedure

The pressure sensors static calibration is performed by installing the instrumented runner in a pressurized vessel connected to the pneumatic network of the laboratory. A pressure regulator permits to set and keep the desired pressure in the vessel. The static pressure is increased by 0.5-*bar* steps until equalizing the pneumatic network pressure, *i.e.* 6 *bar*.

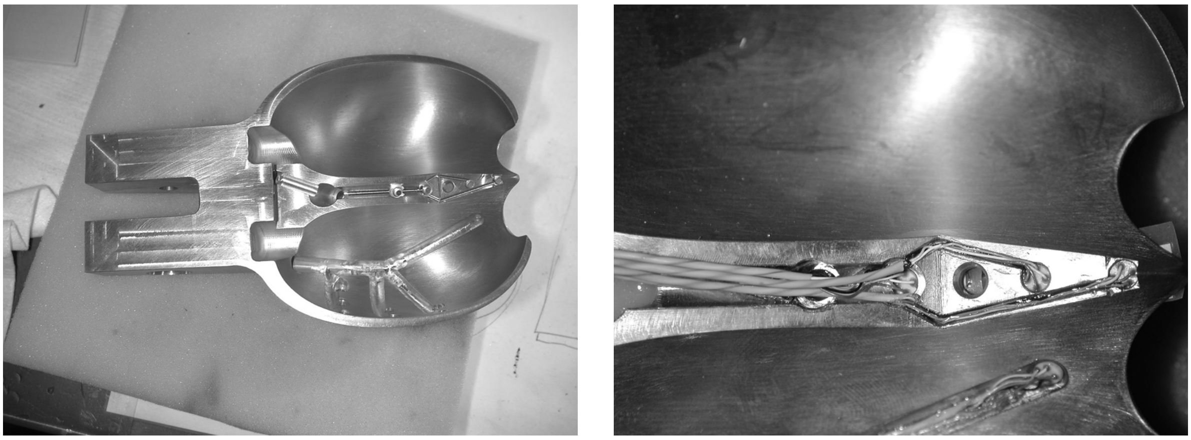

(a) Milled bronze bucket. (b) Wiring procedure.

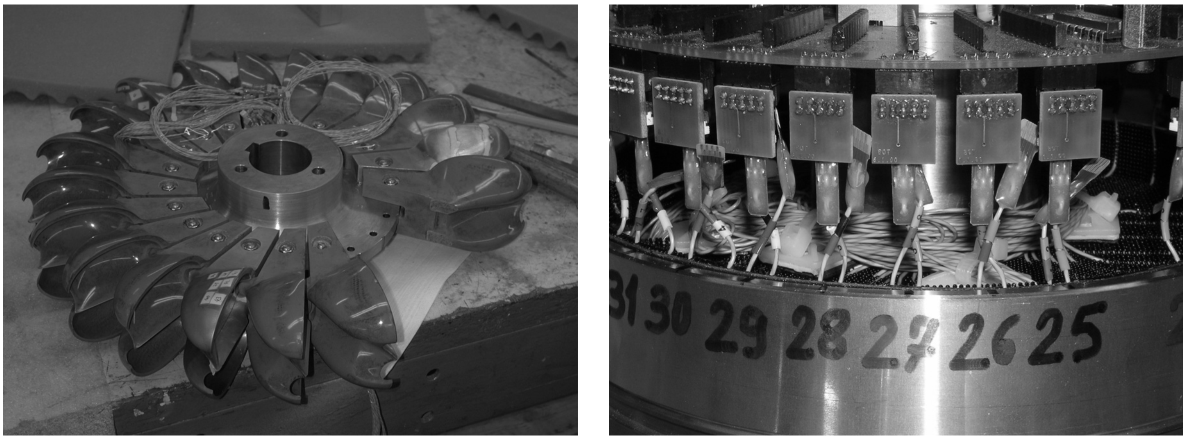

(c) Runner assembly. (d) Electronic components final wiring.

Figure 9.5: Instrumented runner construction.

It is then decreased by 1-*bar* steps to check for the hysteresis error of the sensors. The sensors outputs are collected by the instrumented shaft. The voltages are averaged and compared to a high precision reference transducer. The reference pressure transducer Huber main characteristics are given in Table 9.3.

Table 9.3: Huber characteristics.

Measurement Range [*bar*]	Sensitivity [%]
0...16	0.03

Calibration curves

The static calibration procedure permits plotting the pressure as a function of the output voltage for each sensor. A linear regression method is used to determine the slope of the regression line, which is in fact the inverse of the sensor sensitivity. The regression curve equation for sensor l is:

$$P_{cal} = mU_l + b, \tag{9.1}$$

where m is the slope, U_l the output voltage and b the intersection with the y-axis. The slope m and the intersection b are respectively given by:

$$m = \frac{N \sum P_{ca} U_l - \sum (P_{cal})(\sum U_l)}{N \sum U_l^2 - (\sum U_l)^2} \tag{9.2}$$

$$b = \frac{\sum P_{cal} U_l^2 - (\sum P_{cal} U_i)(\sum U_l)}{N \sum U_l^2 - (\sum U_l^2)} \tag{9.3}$$

with N the total number of data. The error ϵ represents the difference between the pressure obtained from the sensors and the pressure measured by the reference:

$$\epsilon = \frac{P_{ref} - P_{cal}}{P_{ref,N} - P_{ref,0}} \tag{9.4}$$

Figure 9.6 shows the calibration curves and error curves obtained for 4 representative sensors. An excellent linear response is observed, and the maximum error is found to lie within 0.75% of the measurement range for all the 43 sensors. The dispersion observed in the sensors population is most likely caused by the silicone compound volume which varies for each sensor.

9.3.2 Dynamic calibration

The dynamic calibration of the sensors is carried on in a large vessel with a spark generator device. This device allows discharging up to 50 J electric energy between 2 immersed electrodes within 10 μs. An explosive growth of a vapor bubble occurs, followed by the collapse of the bubble, generating strong shock waves. The resulting pressure pulse excites the pressure transducer in a large frequency band. A reference pressure transducer (Kistler 701) of known characteristics is located close to the tested sensor for frequency estimation purposes. The results show a transfer function close to 1 and an excellent coherence for a bandwidth spreading 150...5000 Hz [86].

9.3.3 Data reduction

The pressure measurements are phase averaged from 200 to 350 runner rotations depending on the test head and synchronized from the tachometric signal.

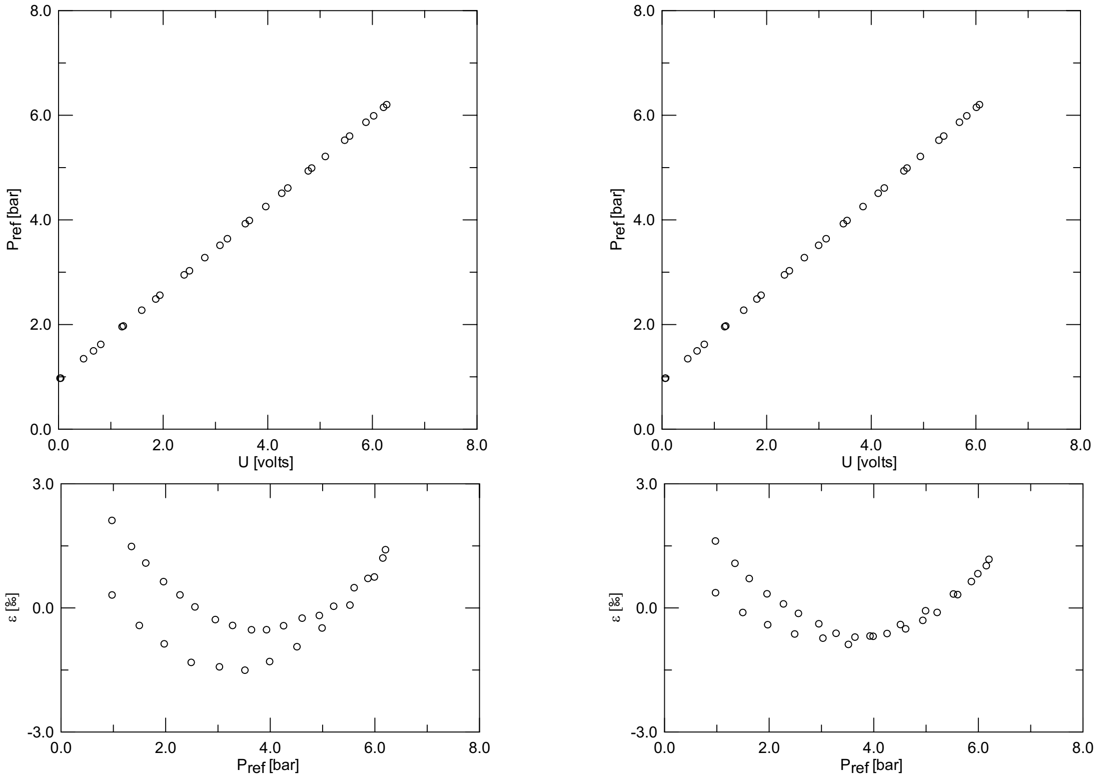

(a) Sensor 1. (b) Sensor 6.

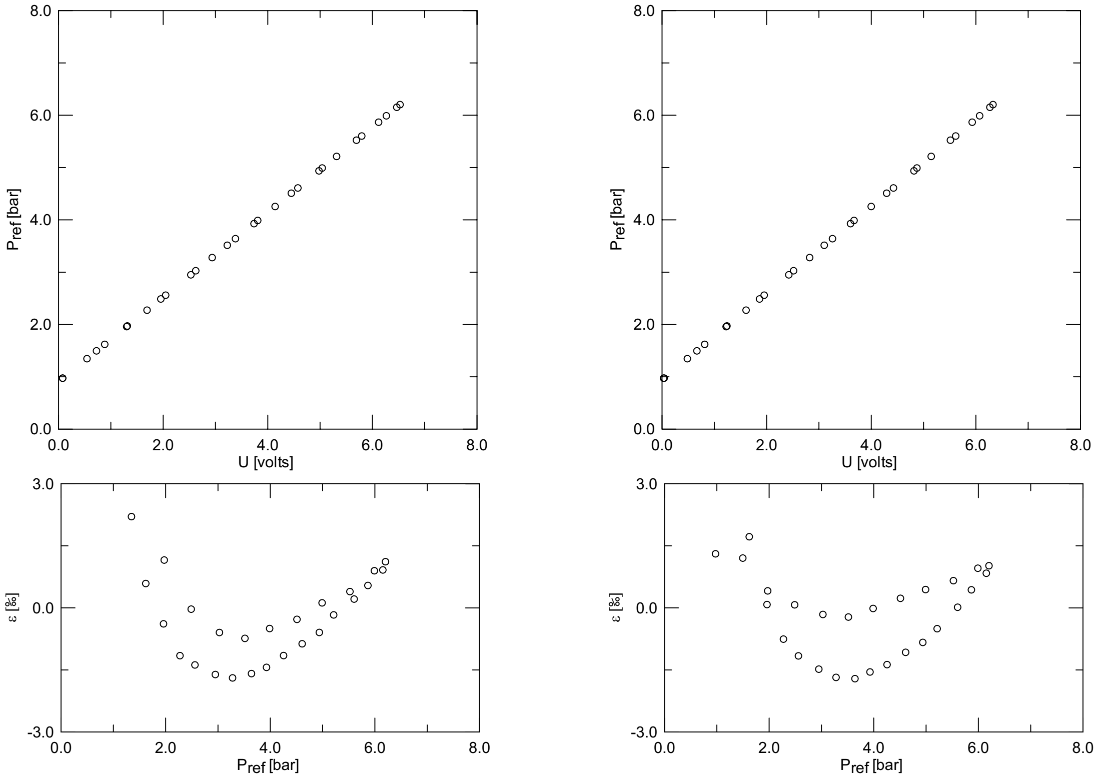

(c) Sensor 32. (d) Sensor 41.

Figure 9.6: Calibration curves and relative errors obtained for 4 sensors.

Chapter 10

Flow visualizations

10.1 Requirements

To overcome the difficulties inherent to the observation of the flow in the buckets, some requirements are to be followed, regarding optics, photographic equipment, and lighting systems.

10.1.1 Optical requirements

The optical devices to be used must permit avoiding the shortcomings of the approaches chosen so far [64]. There are 6 requirements: (i) the optical system dimensions are to be compact enough so as not to disturb the flow around the runner. The water sheets leaving the runner should under no circumstances be deviated back against the runner. (ii) It should permit a close observation of the subject. (iii) The field of view must offer a large depth without need for focusing, enabling to follow the evolution of flow structures likely to be convected by the mean stream. (iv) The image distortions are to be kept to the minimum to avoid heavy post-processing of the images. Very short focal lengths like fish-eye lenses are not considered a solution for this reason. (v) The luminosity must remain acceptable for performing high-speed photography. (vi) The system has to be waterproof, and equipped with a lens wiping system to prevent the droplets present in the atmosphere surrounding the turbine to stick on it and reduce the visibility.

10.1.2 Exposure time requirements

To freeze the motion observed, the exposure duration should be chosen so that the blur distance due to motion does not exceed 1/30 of the characteristic length of the feature to be photographed [25]. The required exposure time is expressed as:

$$t_{exp} = \frac{d_{blur}}{c} \tag{10.1}$$

where d_{blur} is the blur distance due to motion, and c the velocity of motion.

10.1.3 Lighting requirements

The duration of a flashlight, τ_{flash}, is conventionally obtained by measuring with a photosensitive detector and displaying on a cathode-ray tube oscilloscope the time between 1/3 peak values of light on the rising and falling portions of the light-time curve. Light-time outputs are determined by integrating the light curve to obtain the lamp output in Candela-seconds or Beam-Candela-seconds (BCPS) [25]. The most significant number describing the photographic ability of a flash unit is the guide factor, defined as a function of the output of a particular flash system. The guide factor is expressed as the product of the lamp-to-subject distance D by the camera lens aperture A for a satisfactory photograph. In terms of light output (BCPS) and film sensitivity (ASA) speed s, the guide factor becomes:

$$DA = \sqrt{BCPS\frac{s}{k}} \tag{10.2}$$

with $k \simeq 160...270$. Using a high-speed camera and a long duration flash unit of high output, exceeding the output and exposure time required, the maximum number of frames that can be taken during a single flash pulse is expressed as

$$N_{frames} = \frac{(BCPS)_{lamp}}{(BCPS)_{required}} \tag{10.3}$$

The maximum shutter speed achievable, neglecting the inter-frame time interval is therefore:

$$t_{shutter} = \frac{\tau_{flash}}{N_{frames}} \tag{10.4}$$

10.2 Observation tools

10.2.1 Borescopes

The optical requirements presented in section 10.1.1 match those of medical imagery. Indeed, modern medical techniques call for direct observation of bodily cavities with non-invasive devices. A large depth of sight is of primary importance. The optical industry developed over the last 50 years a range of endoscopes of different lengths and diameters, rigid or flexible. Their excellent optical properties provide clear and undistorted images, and a large depth of sight. Endoscopes meet more and more industrial applications, notably for jet engine or complex structures inspections without need for dismantling. Karl Storz so-called borescopes, *i.e.* rigid endoscopes, are chosen for the flow visualizations in the Pelton turbine, Fig.10.1.

10.2.2 High speed camera

A high-speed Photron Ultima Fastcam APX is chosen as image acquisition device. It is fitted with a 10-*bit* CMOS sensor, which sensitivity rating is approximately 4800 ISO/ASA at $0dB$ gain. Table 10.1 resumes the technical data of the camera. The system is made of one processor and a camera head linked by a pair of $5m$ flexible cables. The frame

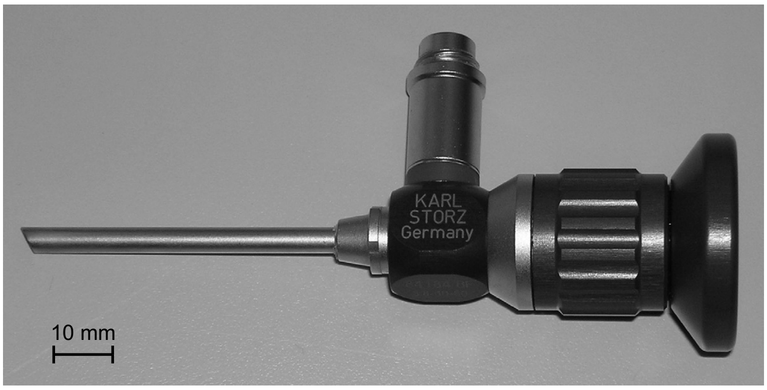

Figure 10.1: Karl Storz 3.8 mm diameter borescope.

Table 10.1: High-speed camera specifications.

Shutter speed $[\mu s]$	Frame rate $[fps]$	max resolution $[pixels]$
4...1670	$1 - 12 \cdot 10^3$	1024×1024

rate goes up to $2 \cdot 10^3 fps$ at full resolution and up to $120 \cdot 10^3 fps$ at reduced resolution. The buffer memory of the camera enables storing up to $8GB$ of images. Triggering and synchronization is achieved via positive or negative TTL $5V$ p-p. Interchangeable F-mount standard is fitted to the camera head, allowing using the whole Nikkor series of lenses.

10.2.3 Lighting systems

Two independent Cordin mod.309 flash units are chosen as light sources. They provide a square wave pulse at a brightness 1000 times that of sunlight. The Xenon flash produces light that is spectrally balanced throughout the visible range. The technical data of the Cordin mod.309 flashlamps is presented by Table 10.2.

Table 10.2: Flashlamps specifications.

Peak light output $[Beam - Candela \cdot s]$	Electric energy $[J]$	Jitter time $[\mu s]$	Rise time $[\mu s]$	Flash duration $[ms]$
2400	1875	2	< 10	$0.5 - 11$

10.3 Onboard flow visualizations

10.3.1 Endoscope location

A $3.8mm$ diameter borescope is chosen for the onboard visualizations. The equivalent aperture is $f/11$. Its location, as shown by Fig.10.2(a), is defined using CAM-CAD tools, with the distal lens is at the root of one half bucket. An observation grid is drawn on the bucket inner surface. This choice is made for the following reasons: (i) no water is to be expected during normal operation, as Pelton's modification to Knight's original impulse turbine was to avoid water flowing towards the flange [22]. (ii) The mounting is non-intrusive. (iii) The field of observation is not obstructed by the splitter, Fig.10.2(b). (iv) The distal lens is oriented so that the radial acceleration prevents droplets to stick on it, and is periodically treated with a rain repellent solution.

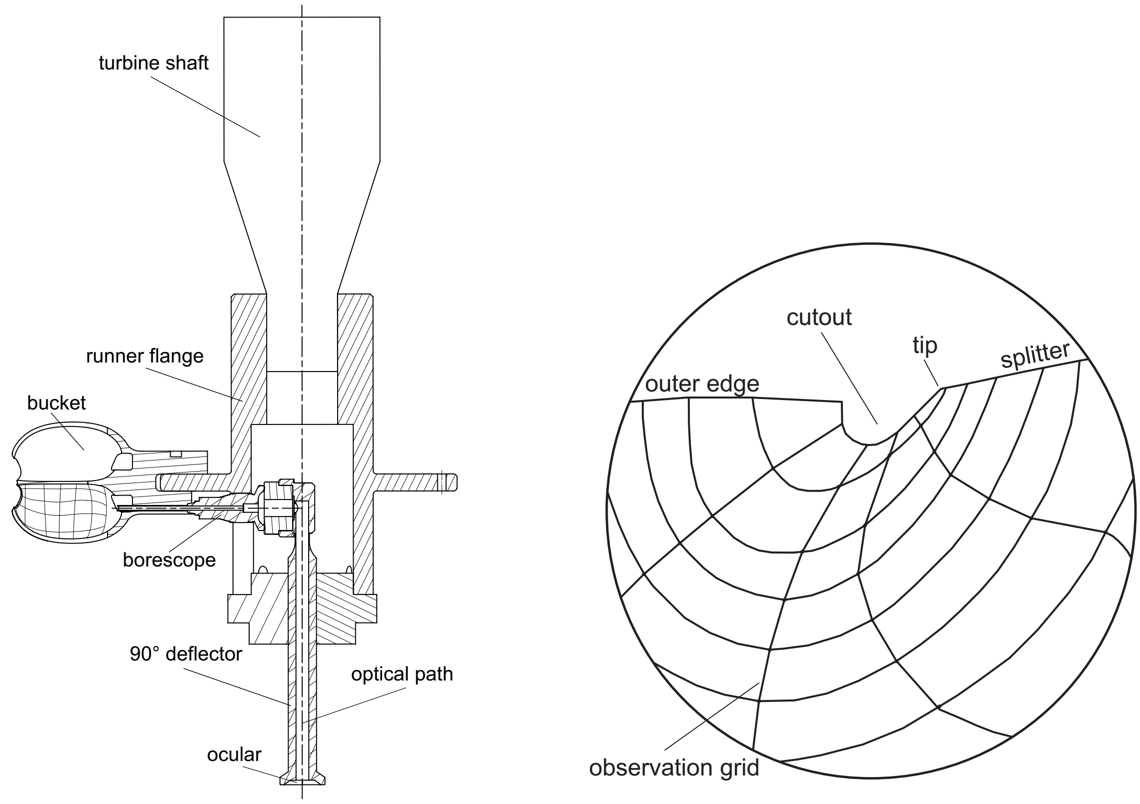

(a) Onboard endoscope location and assembly. (b) Field of observation.

Figure 10.2: Onboard endoscope location and field of observation.

10.3.2 Setup

Apparatus

The camera head and the processor are kept outside the rotating parts of the test rig. The observation frames of the endoscope are transmitted via a 90° optical deflector passing through the runner rotation axis, and protruding outside the test rig window, as shown by Fig.10.3(a). The high-speed camera, equipped with a 55mm Micro-Nikkor lens, is mounted on a 4-degree-of-freedom moveable support. The lens axis is aligned on the deflector axis by means of micrometric screws, Fig.10.3(c). The advantages of the approaches are (i) no communication problems between the camera head and processor; (ii) no electronic component in rotation; (iii) no mass unbalance of rotating parts. The flashlights are installed in waterproof housings that are mounted as close as achievable to the runner, on movable supports. They are oriented so as to avoid shadows in the observation area, Fig.10.3(b).

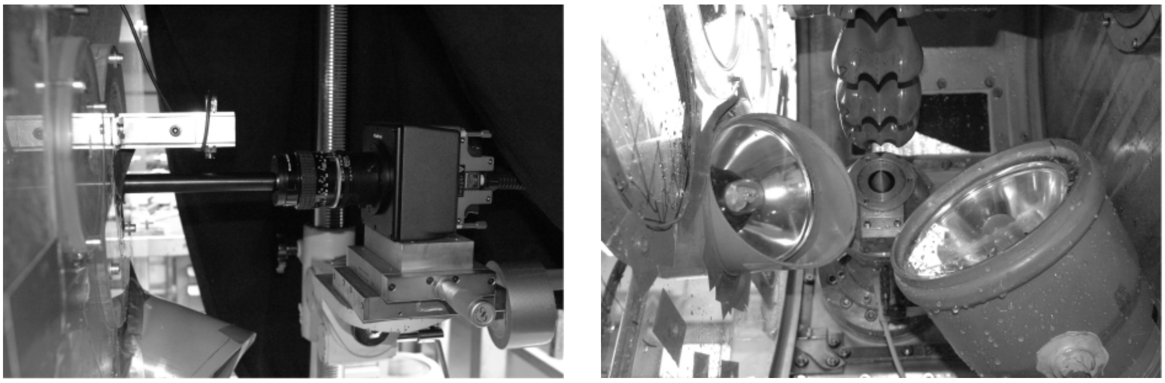

(a) Camera aligned with the deflector. (b) Waterproof flashlights housings.

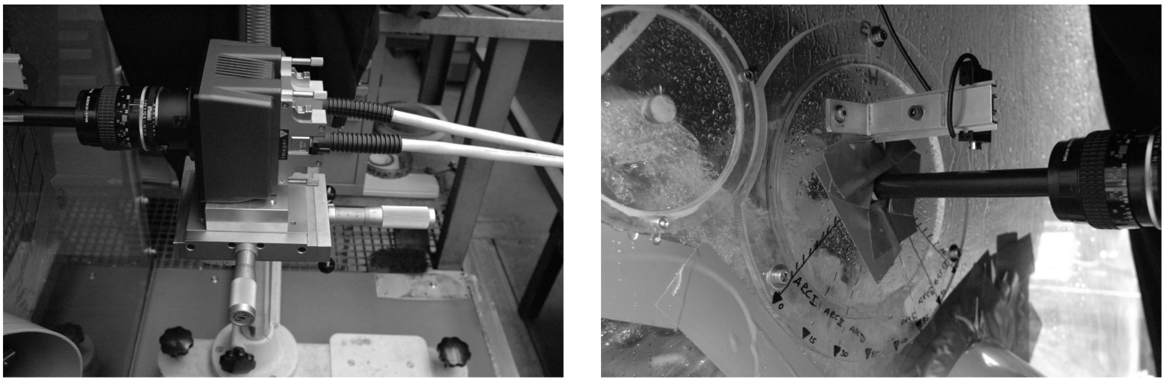

(c) 4-degree-of-freedom camera support. (d) Optical deflector and optical encoder.

Figure 10.3: Experimental setup for the onboard visualizations.

Frame rate and exposure time

The required BCPS is determined according to the procedure defined in section 10.1.3. The ideal shutter speed is between 5 and $10\mu s$ depending on the value of constant k in Eqn.10.2. To keep the resolution at the acceptable value of 512×512 $pixels$, the frame rate is limited to $6000fps$. With a flash duration set to $6ms$, the number of valid frames recorded is 35. Even if the light source and camera capabilities allow measuring a complete bucket duty cycle, the non-moving assembly of the lighting system claims for a division of the duty cycle in overlapping subcycles to maintain adequate lighting conditions.

10.3.3 Trigger chain

An optical encoder is fitted on the deflector, see Fig.10.3(d), giving a $+5V$ TTL pulse at each runner rotation. The TTL signal is sent via an adjustable delay line unit set to fire the camera and the flash units synchronously at the desired runner angular position. The trigger signal is released upon manual activation of the delay line unit. The camera delay and flashlights jitter are short enough to be neglected, as they are of O($30ns$). Figure 10.4 schematizes the trigger chain.

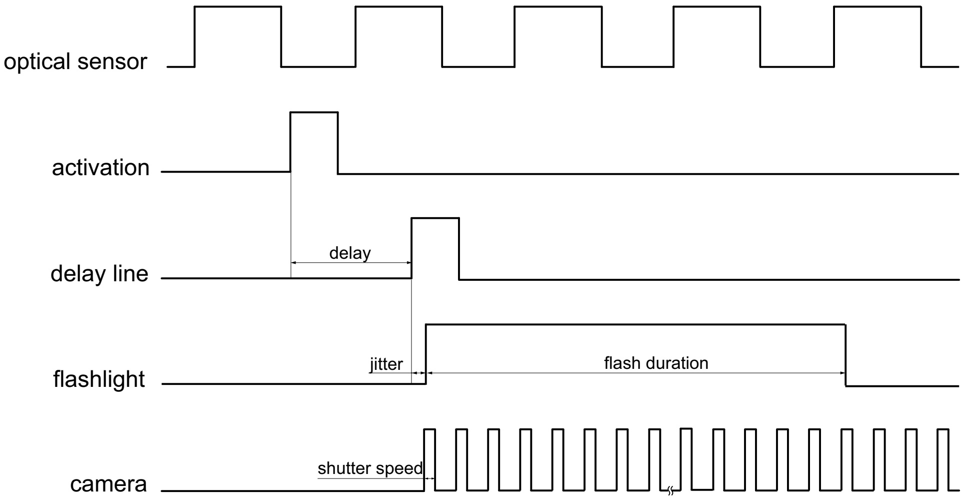

Figure 10.4: Trigger chain for the onboard visualizations.

10.3.4 Images processing

The images captured by the camera inside the turbine bucket suffer 2 major limitations: (i) the image contrast and luminosity vary depending on the angular position of the bucket; (ii) the field of view rotates as the endoscope rotates with the turbine. To make possible and simple the analysis of the water sheet movement inside the bucket, a sequence of frames with a steady point of view is required. A semi-automated process is set up to transform the raw video images output by the endoscopic camera in a specific test run into a high quality sequence of images.

The image processing splits in 5 steps: (i) Montage of the frames stemming from the subsequent subcycles; (ii) File names and formats adjustment for the subsequent steps, contrast and luminosity enhancement and de-rotation of the images. This step is not sufficient to produce a steady image along the whole bucket duty cycle because of the precession of the optical deflector due to mechanical tolerances. (iii) Manual marking of the image center and viewing aperture of the endoscope on selected images in the sequence. (iv) Manual interpolation of the collected positions on the whole image sequence to center the endoscope view aperture. To enhance the resulting image quality a mask is applied to remove everything outside the endoscope aperture. (v) Assembly of the individual frames into a standard AVI formatted movie file.

10.4 External flow visualizations

10.4.1 Positions of observation

The flow in the absolute frame of reference is surveyed using a $10mm$ diameter borescope. The borescope ocular is bound to the same Nikkor $55mm$ lens as for the external visualization, while the camera head is mounted on a light tripod. The distal lens of the endoscope is fitted with a pneumatic wiping system able to blow the droplets away, see Fig.10.5. A total of 6 endoscope locations are tested, as shown by Fig.10.6 and Fig.10.7. Configurations (1) to (3) focus on the early stages of jet-bucket interaction with different

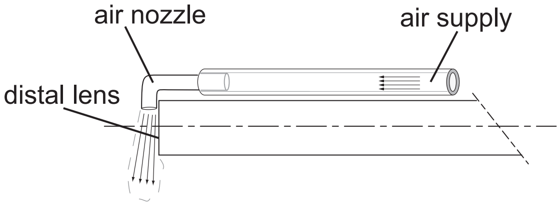

Figure 10.5: Distal lens wiping system.

angles of view. Configuration (4) is a view from the side of the jet being cut by the bucket. In configuration (5) the endoscope is oriented along the injector to provide a wider view of the flow. Configuration (6) is an observation of the jet itself at the outlet of the injector.

10.4.2 Trigger chain, frame rate and exposure time

The trigger chain operates on the same principle as the for the onboard visualizations. Different frame rates are set according to the various configurations and to the phenomena to be investigated. The resolution of the frames is by default kept to the maximum of the capabilities of the camera. Table 10.3 summaries the measurement conditions for configuration (1) to (6).

Table 10.3: Frame rates and exposure time.

Configuration $[-]$	Frame rate $[Frame/s \cdot 10^3]$	Shutter speed $[\mu s]$	Resolution $[pixels \times pixels]$
1	6	5	512 × 512
	12.5	4	512 × 256
2	6	4	512 × 512
	15	4	1024 × 128
3	15	4	1024 × 128
	50	4	256 × 64
	87.6	4	256 × 32
4	6	4	512 × 512
	4	4	1024 × 512
5	6	4	512 × 512
	4	4	1024 × 512
6	6	5	512 × 512

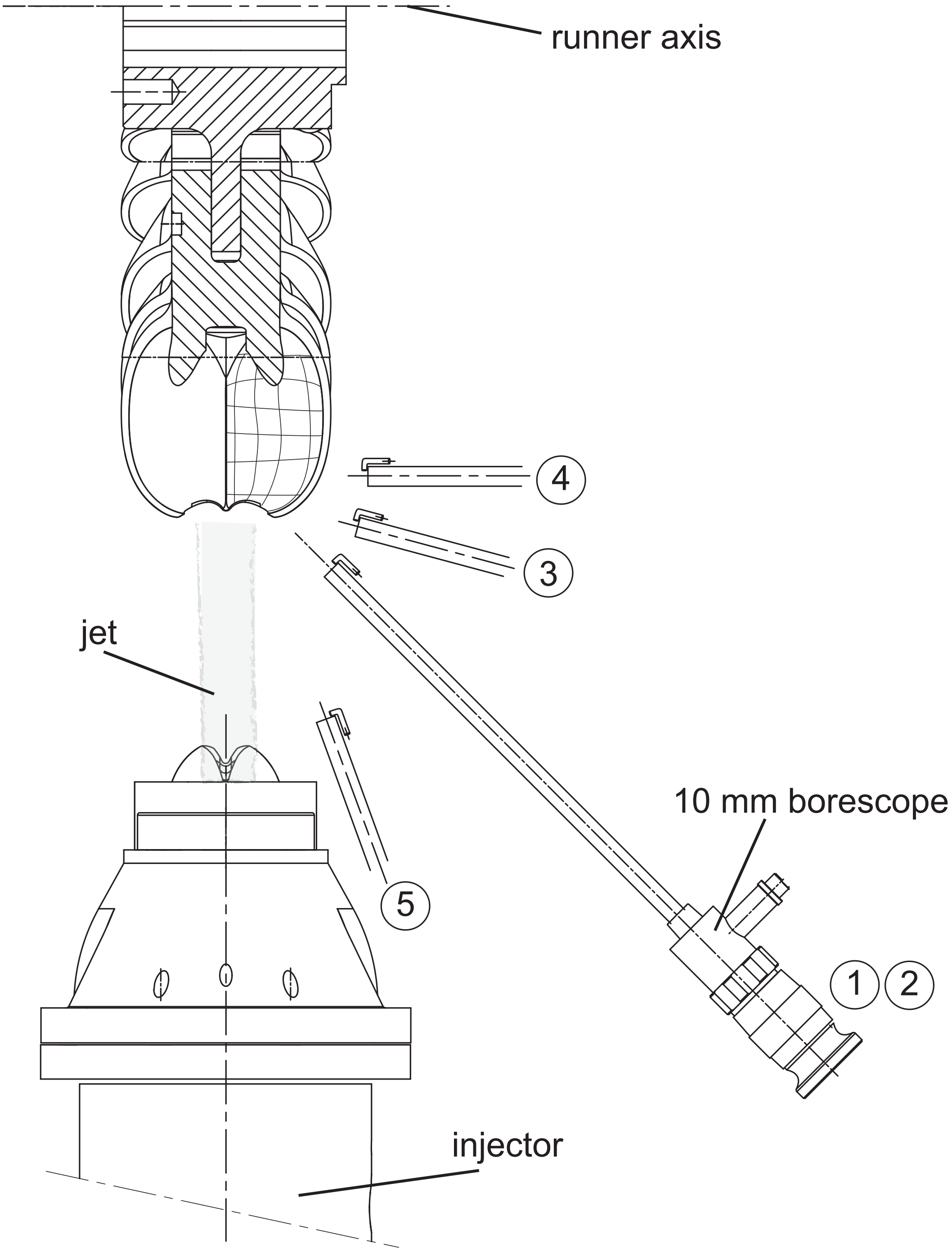
runner axis
4
3
jet
10 mm borescope
5
1
2
injector

Figure 10.6: External visualization configuration, frontal view.

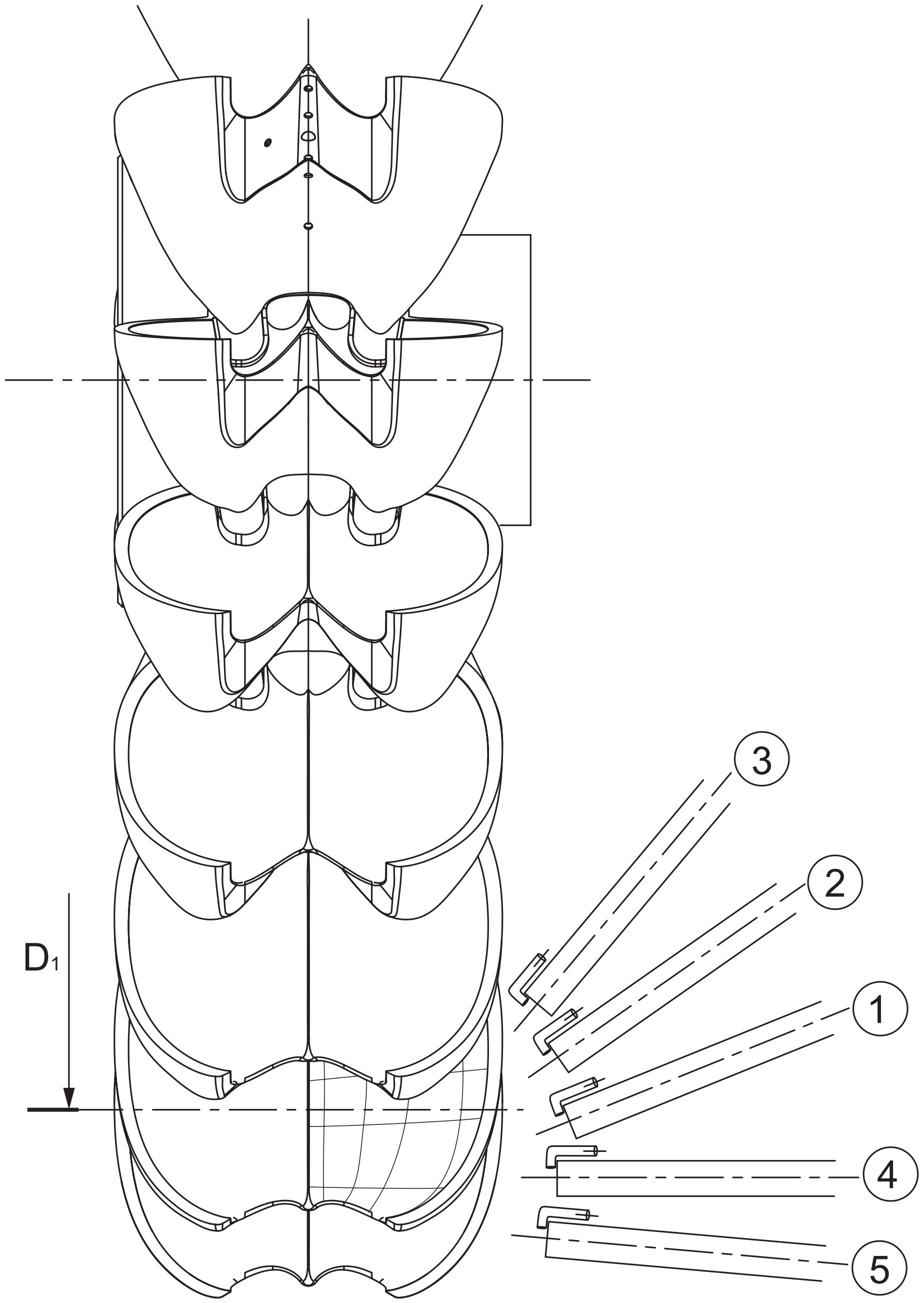

Figure 10.7: External visualization configuration, top view.

Chapter 11

Water film thickness measurements

11.1 Water thickness by refraction

The water film induces an apparent displacement of the observation grid due to the optical refraction, as schematized by Fig.11.1. By comparing 2 images, *i.e.* with and without water films on the inner surface, it is possible to extract the values of the observation angles and from that the value of the apparent displacement of the grid points. Assuming that (i) the endoscope distal lens reduces to a single geometric point, and (ii) that the air-water interface is locally parallel to the bucket surface, the problem can be reduced to a $2D$ problem, as represented by Fig.11.2.

The Sine Theorem expressed in triangle ARR' yields to:

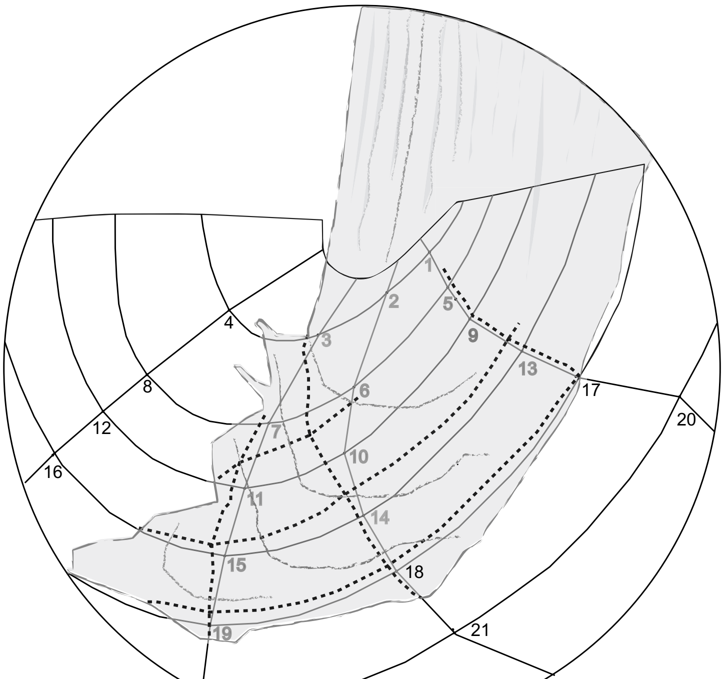

Figure 11.1: Apparent grid displacement. Continuous line: actual grid. Dashed line: apparent grid.

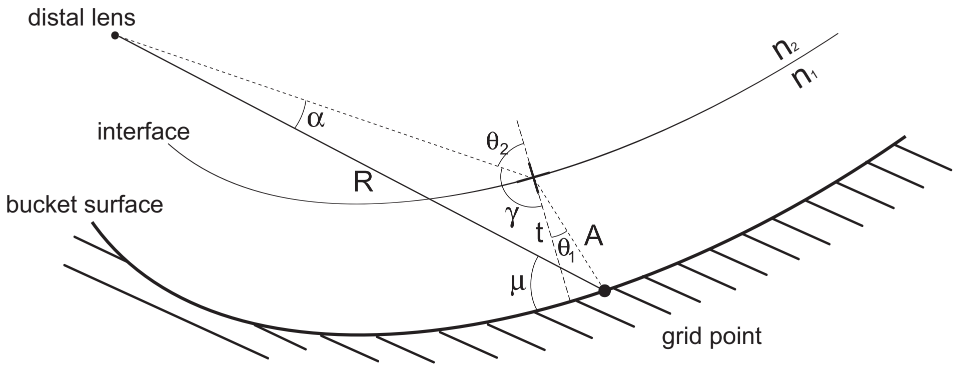

Figure 11.2: Simplified optical model.

$$\frac{A}{\sin\alpha} = \frac{R}{\sin\gamma} \tag{11.1}$$

Observing Fig.11.2, the angle γ is determined as:

$$\gamma = (\frac{\pi}{2} - \theta_2) + (\frac{\pi}{2} + \theta_1) \tag{11.2}$$

$$\Rightarrow \sin\gamma = \sin(\theta_2 - \theta_1) \tag{11.3}$$

From the sketch, the refraction angle in air, θ_2, can be expressed as a function of the apparent angular displacement α:

$$\theta_2 = \alpha - \mu + \frac{\pi}{2} \tag{11.4}$$

The refraction angles θ_1 and θ_2 are related through Snell's law [54]:

$$n_1 \sin\theta_1 = n_2 \sin\theta_2 \tag{11.5}$$

From Fig.11.2, A can be substituted for the sought water film thickness t:

$$t = \frac{A}{\cos\theta_1} \tag{11.6}$$

The water film thickness is therefore simply expressed as:

$$t = \frac{R\cos\theta_1}{\sin(\theta_2 - \theta_1)} \sin\alpha \tag{11.7}$$

11.2 Processing technique

The values of the variables R and μ for each grid point are obtained from the CAM-CAD $3D$ model of the bucket fitted with the onboard borescope, while the value of α must be deduced from the observation frames. In order to reduce the errors due to the mechanical imperfections, a common datum is chosen for the dry reference frame and the subsequent wet frames. The apparent displacement vector of point j can be calculated from that datum. Knowing the angular arc between adjacent grid points, it is possible to obtain the apparent displacement angle of grid point j, α_j, by interpolation, as schematized by Fig.11.3:

$$\alpha_j = \frac{\Delta y^2 + \Delta z^2}{\sqrt{(y_{j+1} - y_j)^2 + (z_{j+1} - z_j)^2}} (\mu_{j+1} - \mu_j). \tag{11.8}$$

The water film thickness t can then be obtained from Eq.11.4 and Eq.11.7.

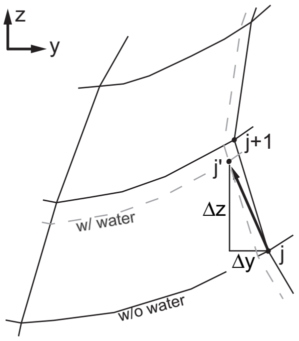

Figure 11.3: Apparent grid interpolation.

11.3 Validation test

In order to assess the validity of the method, a simple test is carried out. A plastic bowl is partially filled with a series of known volumes of water. An observation grid of known dimensions is drawn on the bottom of the bowl, see Fig.11.4. The water thickness is then

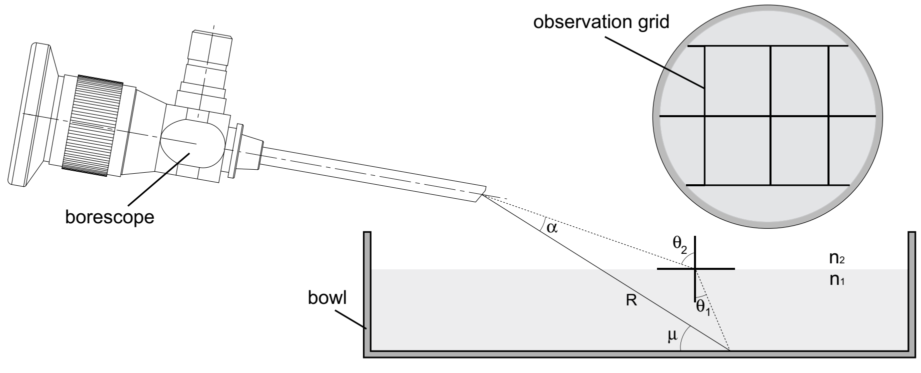

Figure 11.4: Thickness measurement validation test setup.

measured with the technique described in section 11.1. Photographs are shot through the same borescope as for the onboard visualizations, using a still camera and ambient light. Figure 11.5 is a comparison of the thickness value obtained from the volume and the refraction measurement. The relative error is within 8% of the measured value.

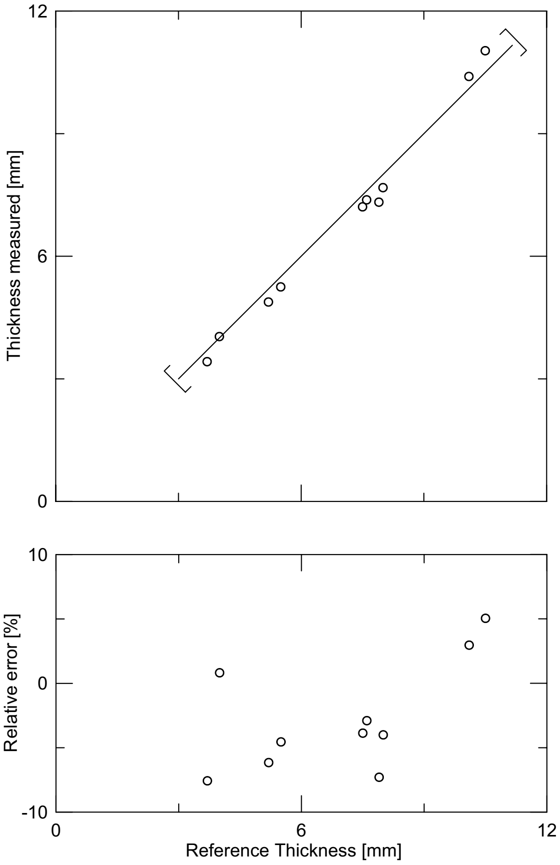

Figure 11.5: Thickness measured by refraction vs. reference thickness.

11.4 Error estimation and propagation

The total uncertainty of the water thickness values obtained must be determined. As expressed by Eq.11.7, the water thickness t is a function of 4 variables. Some of the variables are dependent on the others, as θ_1 which is related to θ_2 through Snell's law. t is therefore a function of the following primary variables:

$$t = f(R, \theta_2, \alpha, \mu) \tag{11.9}$$

The total error, determined according to the procedure described in Appendix B, is expressed as:

$$\Delta t = |\Delta R \frac{\partial t}{\partial R}| + |\Delta \theta_2 \frac{\partial t}{\partial \theta_2}| + |\Delta \alpha \frac{\partial t}{\partial \alpha}| + |\Delta \mu \frac{\partial t}{\partial \mu}| \tag{11.10}$$

ΔR is the error on the distance between the endoscope distal lens and the considered gird point j. ΔR is function of the accuracy of the grid points coordinates, assuming that the lens suffers no position error.

$$\Delta R = |\Delta y_j \frac{\partial R}{\partial y_j}| + |\Delta z_j \frac{\partial R}{\partial z_j}| \tag{11.11}$$

$\Delta\alpha$ is the error on the apparent displacement angle α. From Eq.11.8, the error $\Delta\alpha$ becomes:

$$\begin{aligned}\Delta\alpha = {} & |\Delta(\Delta y)\frac{\partial\alpha}{\partial(\Delta y)}| + |\Delta(\Delta z)\frac{\partial\alpha}{\partial(\Delta z)}| + |\Delta y_{j+1}\frac{\partial\alpha}{\partial y_{j+1}}| + |\Delta y_j\frac{\partial\alpha}{\partial y_j}| \\ & + |\Delta z_{j+1}\frac{\partial\alpha}{\partial z_{j+1}}| + |\Delta z_j\frac{\partial\alpha}{\partial z_j}| + |\Delta\mu_{j+1}\frac{\partial\alpha}{\partial\mu_{j+1}}| + |\Delta\mu_j\frac{\partial\alpha}{\partial\mu_j}| \end{aligned} \tag{11.12}$$

The error $\Delta\theta_1$ is directly dependent upon the error on $\Delta\theta_2$, which is a function of the angles α and μ.

Table 11.1 summarizes the uncertainties estimated for the primary variables y, z, R and μ. The error is assumed to grow by 0.1% for each subsequent frame along the bucket duty cycle. Figure 11.6 shows the evolution of the absolute error $\epsilon_{t_j} = \Delta t_j / D_2$ for 4 grid points. The maximum error can account for 7.5% of D_2 for grid point 4. It appears that the grid points that are far from the borescope distal lens, *i.e.* with the smaller value of angle μ, suffer the larger error. This is the reason why grid points 1, 2, 3, 5 and 6 are rejected for the film thickness determination. Most of the grid points located on the splitter side, *i.e.* points 5, 9 and 13, are rejected because the main assumptions made for the film thickness measurement are false in this area. Indeed, this region is fed by the still cylindrical jet that prevents an unequivocal processing of the observation grid points.

Table 11.1: Uncertainties on the primary variables.

Δy	Δz	ΔR	$\Delta\mu$
$\mp 0.5mm$	$\mp 0.5mm$	$\mp 1.5mm$	$\mp 0.5°$

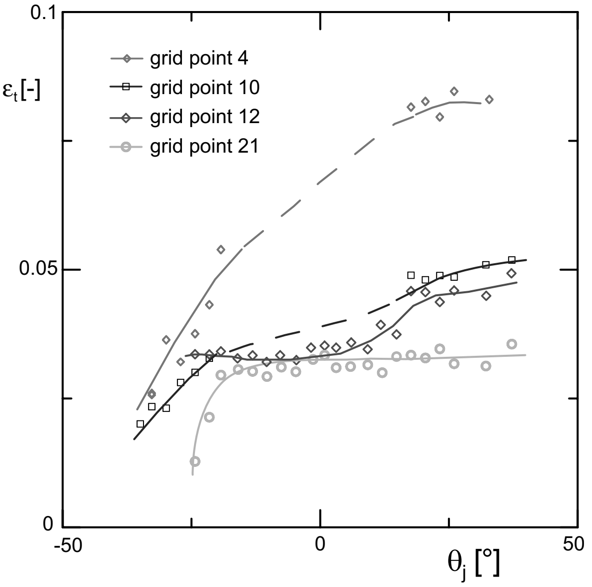

Figure 11.6: Film thickness error evolution.

Chapter 12

Numerical approaches

12.1 setup

The simulations are performed with the CFX-10 commercial code. The 2-Phase Homogeneous and the 2-Fluid Models are used to simulate the operation of the test runner for $OP1$ ($\psi_1/\psi_1^{\wedge} = 0.89$ and $\varphi_{B_2}/\varphi_{B_2}^{\wedge} = 1.07$) at the $20m$ test head. The results obtained are compared with the experimental data in terms of (i) pressure distribution, (ii) water film thickness, and (iii) flow patterns in the buckets.

12.1.1 Discretization

Two sizes of meshes are used for the simulations: (i) for the physical models comparison purposes, the same spatial discretization is chosen. The mesh is refined on the buckets inner surface and backsides. (ii) For analyzing the flow and a performing a detailed comparison with the experimental data, a more refined mesh is created, *i.e* with more mesh elements in the regions of the outer edges and on the sides of the buckets to accurately simulate the discharge flow and the outflow heeling.

The computational domain is divided in 2 sub-domains, *i.e.* a stator with a dummy injector and a rotor with the runner, linked with a transient rotor-stator sliding interface. By assuming periodic flow, one-third of the runner is simulated, *i.e.* 7 buckets, see Fig.12.2. Unstructured meshes composed of tetrahedral, Hexahedral, and Pyramidal elements, see Fig.12.1, are used. The characteristics of the meshes are summarized in Table 12.1 and 12.2.

The continuity and Momentum conservation equations are discretized using a high-resolution upwind scheme with the physical advection terms weighted by a gradient-dependent blend factor, providing a good trade-off between diffusion and dispersion. A second-order backward Euler scheme is used for the transient terms.

Table 12.1: Mesh dimensions, model comparison.

	Stator	Rotor	Total
Number of elements (k)	144.024	5558.040	699.064
Number of nodes (k)	27.488	1008.680	1036.168

Table 12.2: Mesh dimensions, detailed simulation.

	Stator	Rotor	Total
Number of elements (k)	384.491	6071.037	6455.528
Number of nodes (k)	403.102	2434.354	2837.456

12.1.2 Boundary conditions

Figure 12.2 depicts the computational domain and the boundary conditions applied. The incoming jet is assumed to be ideal, with a constant velocity profile determined from the specific energy and discharge conditions, and the flow relative to the splitter to be symmetrical. The turbulence is taken into account using a shear-stress model, *i.e.* SST turbulence model with a standard wall function. Indeed, previous investigations [87] showed that the standard k-ε turbulence model provides unsatisfactory results for the bucket regions where the flow undergoes high shear stresses, such as the splitter sides and the cutout. The turbulence intensity is set to 5% and the length scale equal to $1/10^{th}$ of $B_2/2$. The walls are treated as smooth walls. No casing is taken into account, the outlet boundaries are set as openings with constant pressure. The specific details of the 2-Fluid Model are provided by Table 12.3.

Table 12.3: Specifications of the Mixture Model.

Interface length scale	1 mm
Momentum Transfer	Drag coefficient
Mass Transfer	none

12.1.3 Initial conditions

An uniform velocity of $0m/s$ is imposed in the whole domain, with the same turbulence data as for the inlet condition. The 2 sub-domains are filled with air. The time step corresponds to 0.5° of rotation of the runner.

12.2 Quality check

The simulations are run until the RMS residuals for the Momentum equations reduce below 10^{-5}, and the bucket and runner torques become periodic. The mass flow conservation through the domain is checked as well.

12.2.1 Mesh dependency

In order to check the mesh influence on the solution, 4 different meshes with an increasing number of elements are tested. The RMS value of the absolute grid solution error on the

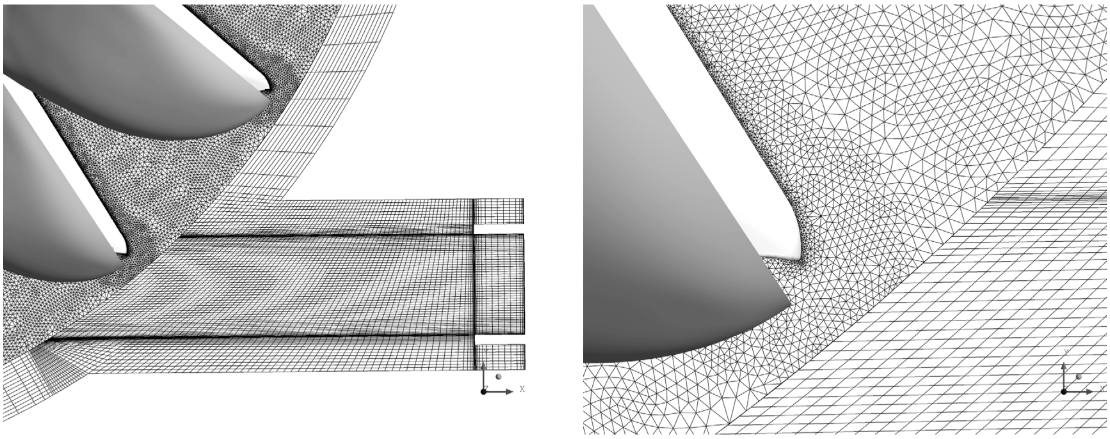

(a) Mesh refinement around the jet. (b) Detail on the plane of symmetry.

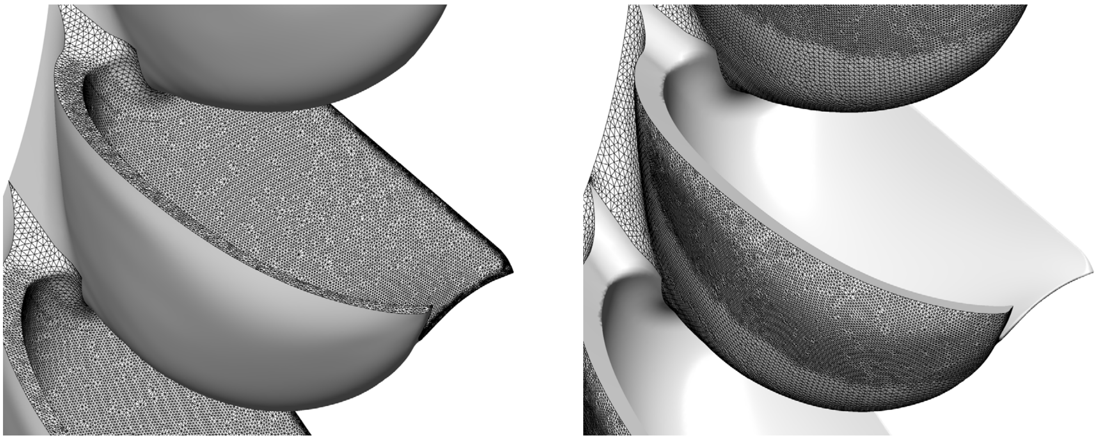

(c) Mesh of the inner surface. (d) Mesh of the outer surface.

Figure 12.1: Unstructured meshes used for the numerical simulations.

calculated pressure signal for 5 different monitoring points spread on the bucket inner surface is determined, see Eq.12.1, and plotted in Fig.12.3.

$$RMS = \sqrt{\frac{1}{N}\sum_{i=1}^{N}\left(\frac{f_{fine_i} - f_{k_i}}{f_{fine_i}}\right)^2}, \tag{12.1}$$

where f_{fine_i} is the solution on the finest grid and f_k the solution for coarse grid k. The subscript i refers to the time step, and N is the total number of time steps.

12.3 Discussion of the results

12.3.1 Pressure distribution

The 18 sensors located on the inner surface are spread into the 5 zones displayed in Fig.14.14 [88], [87], [66]. The experimental signals are represented by the phase-averaged value augmented or cut by the standard deviation, see Fig.12.5 and 12.6.

- **Zone** 1. The results obtained from both models are very close. The timing does

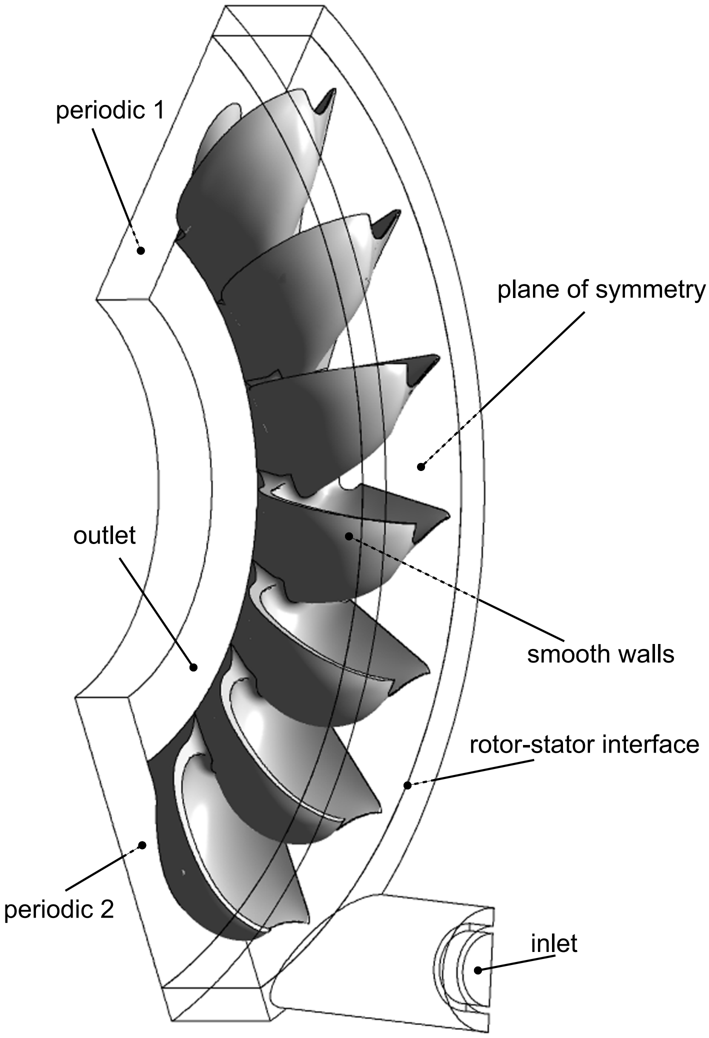

Figure 12.2: Computational domain and boundary conditions applied.

not match the experiments well, as the CFD signals lead the experimental signal by about 4°. The amplitudes are nevertheless well predicted.

- **Zone** 2. The pressure signals in zone 2 are in very good accordance between the measurements and the simulation: the predicted rise and decay times, signal phases, and signal periods match very well the experimental data. The timing is better predicted by the 2-Phase Homogeneous Model than by the 2-Fluid Model, whose signal exhibits a 3° delay. However, the latter is more accurate in terms of amplitude and identifies the pressure peaks recorded.
- **Zone** 3. The results are less accurate in the aft portion of this zone, especially in terms of amplitude with errors in excess of 50%.
- **Zone** 4. Both Models underpredict the signal amplitude by at least 15%, while the decay slopes are accurately simulated. The 2-Fluid Model predicts small peaks of pressure at the initial rise of the signals that do not arise in the measurements

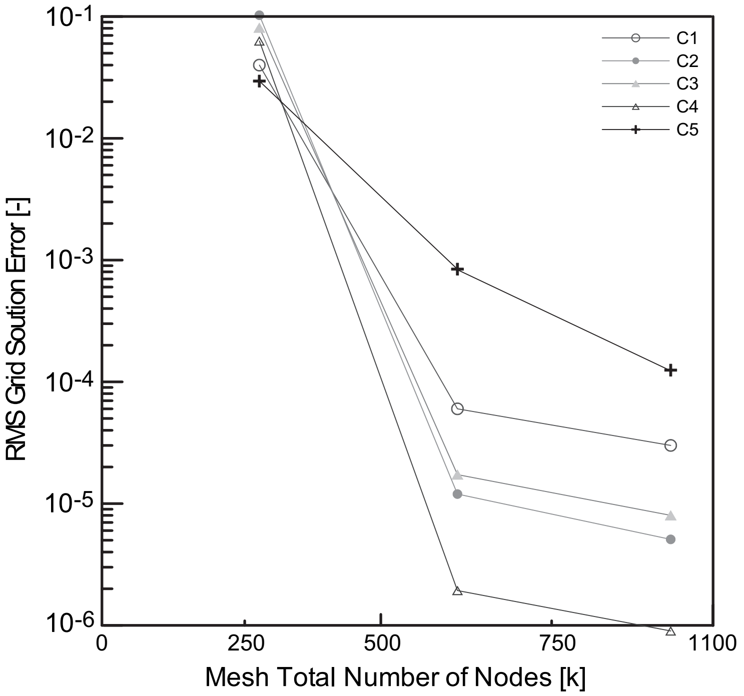

Figure 12.3: Mesh dependency.

(sensors 26 and 28).

- **Zone** 5. In this region, the timing is adequate for both models, while the amplitude predicted by the 2-Phase Homogeneous Model is significantly too low, with errors up to 42% for sensor 17.

- **Backside**. The pressure distribution close to the tip, *i.e.* sensors 31 and 32, is fairly predicted by both models, with the timing and rise slopes more accurate for the 2-Fluid Model. On the other hand, the pressure signals of the aft sensors is much better predicted by the 2-Fluid than by the 2-Phase Homogeneous Model. For sensor 34, neither the timing nor the amplitude are adequately predicted by the 2-Phase Homogeneous Model, with errors accounting respectively for $\sim 7^\circ$ and 89%, while the 2-Fluid Model underpredicts the depression by 41%.

- **Lateral edges**. The initial pressure increase is adequately predicted by the 2-Fluid Model in terms of amplitude and signal rise, even if the duration is over-estimated for sensor 40. The durations obtained from the 2-Phase Homogeneous Model are up to 3 times that of the measurements.

12.3.2 Water film thickness

Figure 12.7 provides a comparison of the water film thickness obtained from the 2 numerical models with the measurements.

The overall agreement is good, the amplitudes being comparable for most of the grid points, with the exception of points 14 and 15, where the 2-Phase Homogeneous Model

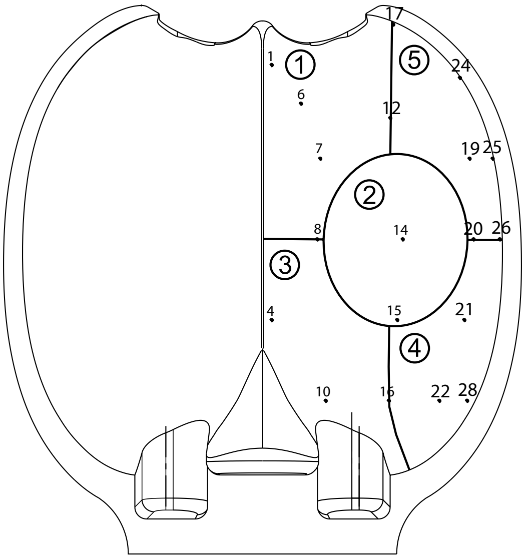

Figure 12.4: Bucket zones.

exhibits overestimated film thicknesses in the vicinity of $\theta_j = 0°$. These exaggerated amplitudes coincide with the passage of fragments of the cut jet over the grid points. Indeed, the 2-Phase Homogeneous Models overestimates the size of the jet fragments.

On the other hand, the water film spread rate is underestimated by both models, as witnessed by the signals obtained for grid points 4 and 8. The lag accounts for about $\sim 7.5°$. It is also remarkable that the period of the signals predicted by the 2-Phase Homogeneous Model are longer. This phenomenon is more visible for the grid points that are reached later in the duty cycle, as grid points 18, 19, or 21, and is most probably linked with the higher numerical diffusion of the latter.

12.3.3 Flow Patterns

Figure 12.8 and Fig.12.9 show the relative flow patterns obtained from the 2 CFD models, represented by the $\alpha = 0.5$ isosurface and as observed by the onboard borescope.

- **Inflow**. The timing matches the experiments well, while the shape of the jet front differs between the models; The 2-Fluid Model predicts well the rolled up splay crown shape displayed by the jet front, see $\theta_j = -35°$, and the jet lateral spread at the moment of impact, see $\theta_j = -30°$. The 2-Phase Homogeneous Model is not capable of predicting this phenomenon because of the assumption of shared velocity profiles between air and water .

- **Flow development**. The initial spread rate of the water film match well the observations for both models, see $\theta_j = -20°...-2°$. The film fronts reach the outer edge of the bucket at the same moment.

- **Jet separation**. The jet detachment process differs: the enlargement of the jet, see $\theta_j = -5°$, is better modelled by the 2-Phase Homogenous Model. The formation of the lobe, $\theta_j = -2°...3°$, however, resembles the observations well for both models. The last stages of the feeding process are convincing for neither model. The

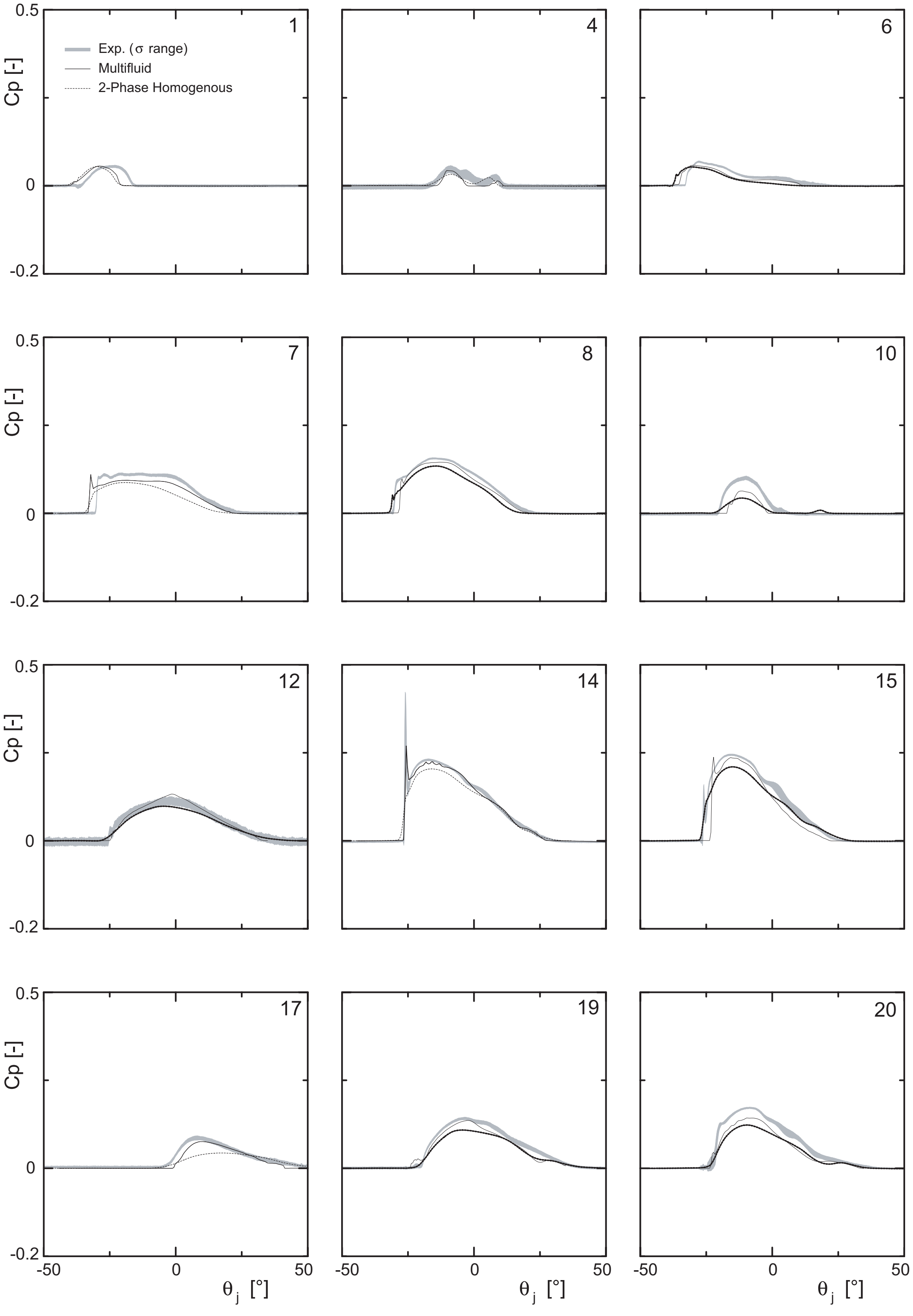

Figure 12.5: Comparison of the pressure coefficients, part I.

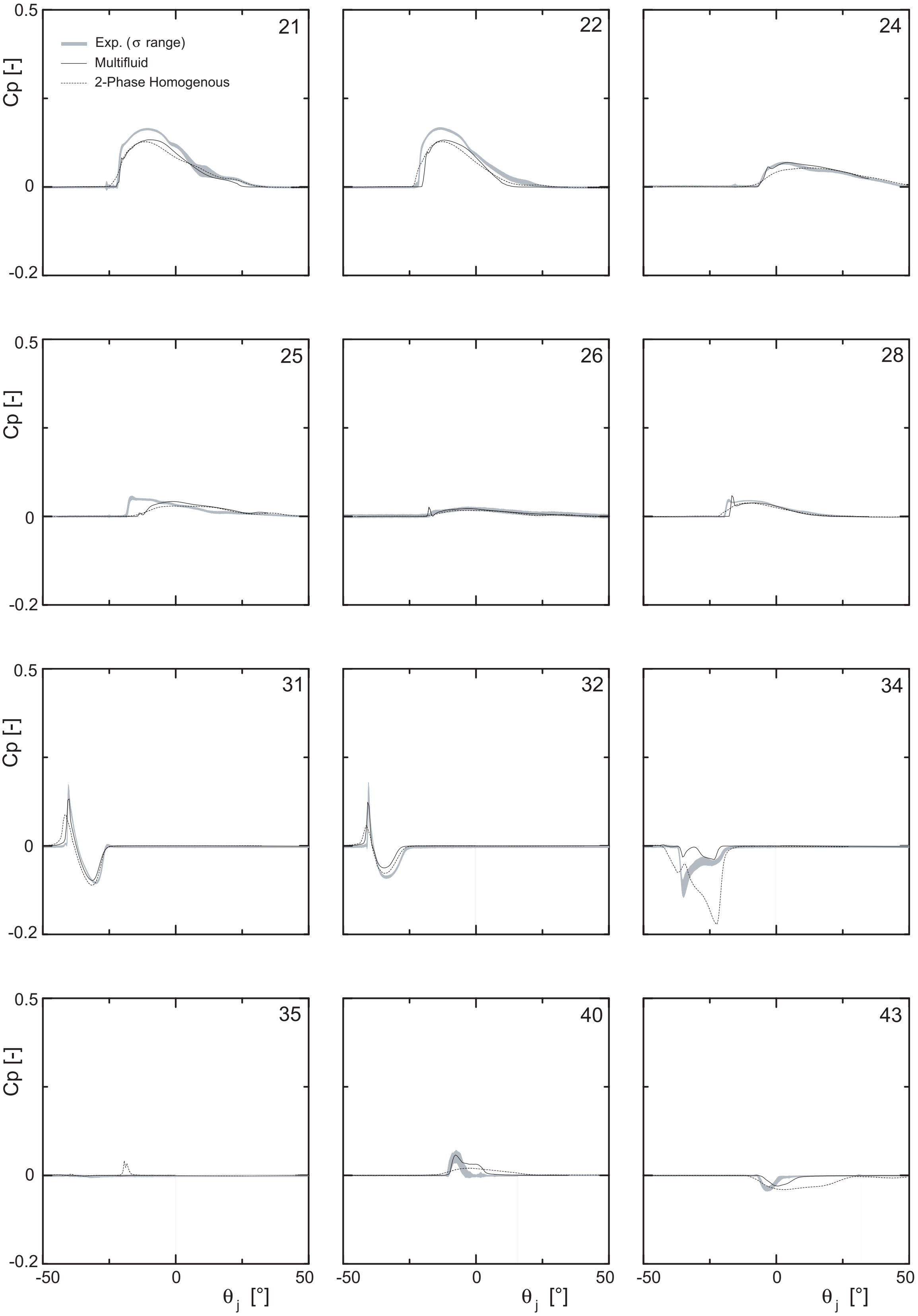

Figure 12.6: Comparison of the pressure coefficients, part II.

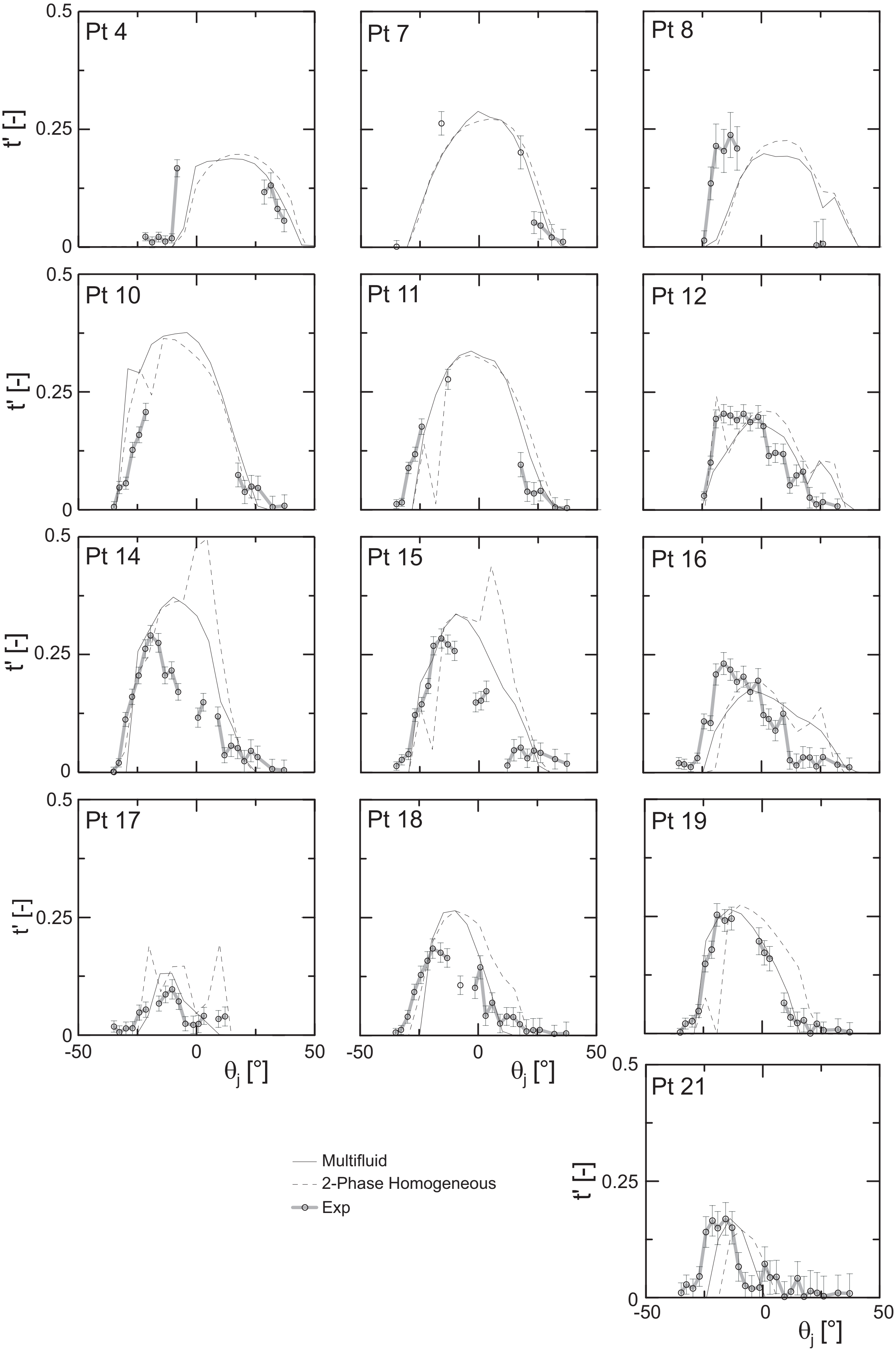

Figure 12.7: Comparison of the water film thickness.

predicted enlargement is not sufficient and the flow still impinges on the splitter of the bucket, while in reality it breaks up in a series of threads and filaments, that continue to catch up for the inner surface of bucket j later in the duty cycle.

- **End of cycle**. The secondary flow throughout the cutout, see $\theta_j = 13°...23°$, is closer to the observations for the 2-Fluid Model, while it is barely not visible for the 2-Phase Homogenous Model. Also, the evacuating flow continuity breaks up earlier with the latter, see $\theta_j = 33°$.

12.3.4 Most suited numerical Model

Globally, the 2-Phase Homogenous Model presents an accuracy that decreases with time. The zones that are reached at the beginning of the duty cycle are better predicted than the zones reached by the flow at the end of the cycle. The amplitudes become underestimated, while the timing remain in good accordance with the measurements. The pressure on the backside is poorly simulated, with both the timing and the amplitude far from the measured data.

The 2-Fluid Model, on the other hand, shows an accuracy that remains constant along the duty cycle. Despite that the timing presents some discrepancies with the experimental results, leading the measurements in the early stages of the cycle, the flow perturbations, visible in the experimental signals from the high standard-deviations of the pressure signals, are well captured.

From the previous considerations, it clearly appears that the 2-Fluid Model globally outperforms the 2-Phase Homogenous Model, because it encompasses more physics than the latter. This is the reason why for the subsequent analysis of the bucket flow only the simulations made with the 2-Fluid Model on the finer mesh will be treated.

θ_j [°]	2-Phase H.	Mixture	Experimental
-40	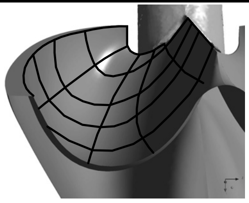	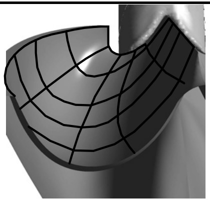	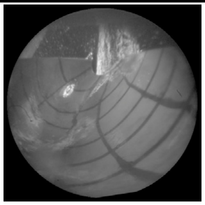
-35	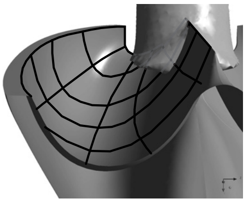	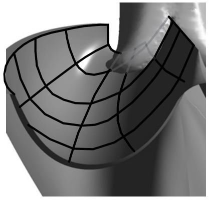	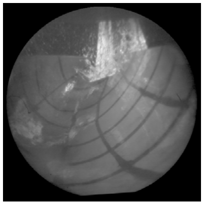
-30	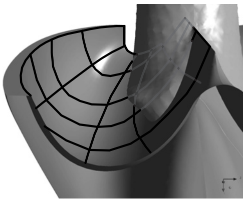	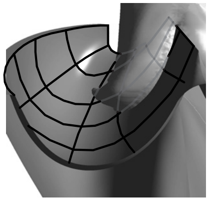	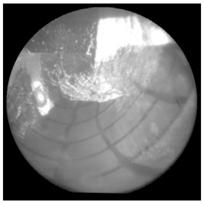
-25	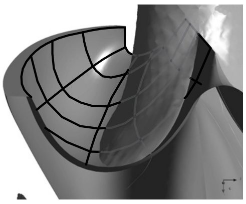	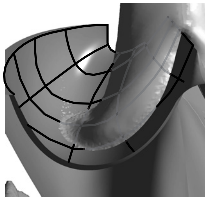	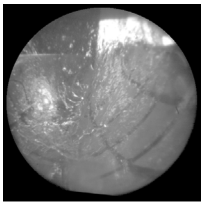
-20	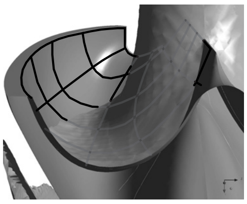	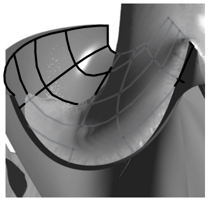	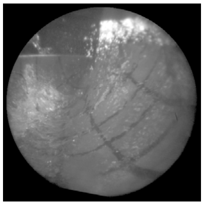
-15	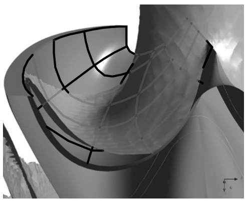	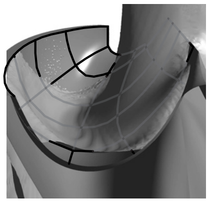	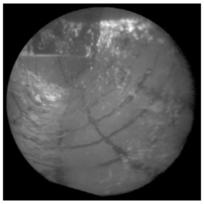
-10	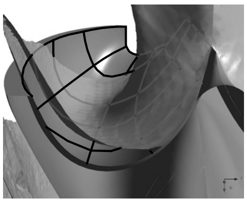	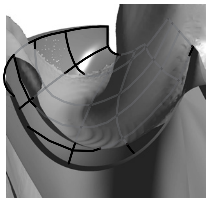	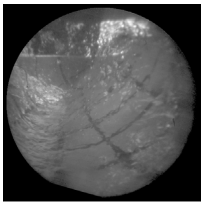
-5	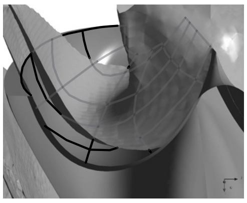	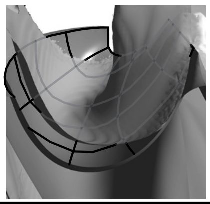	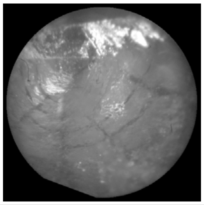

Figure 12.8: Comparison of the relative flow patterns, part I.

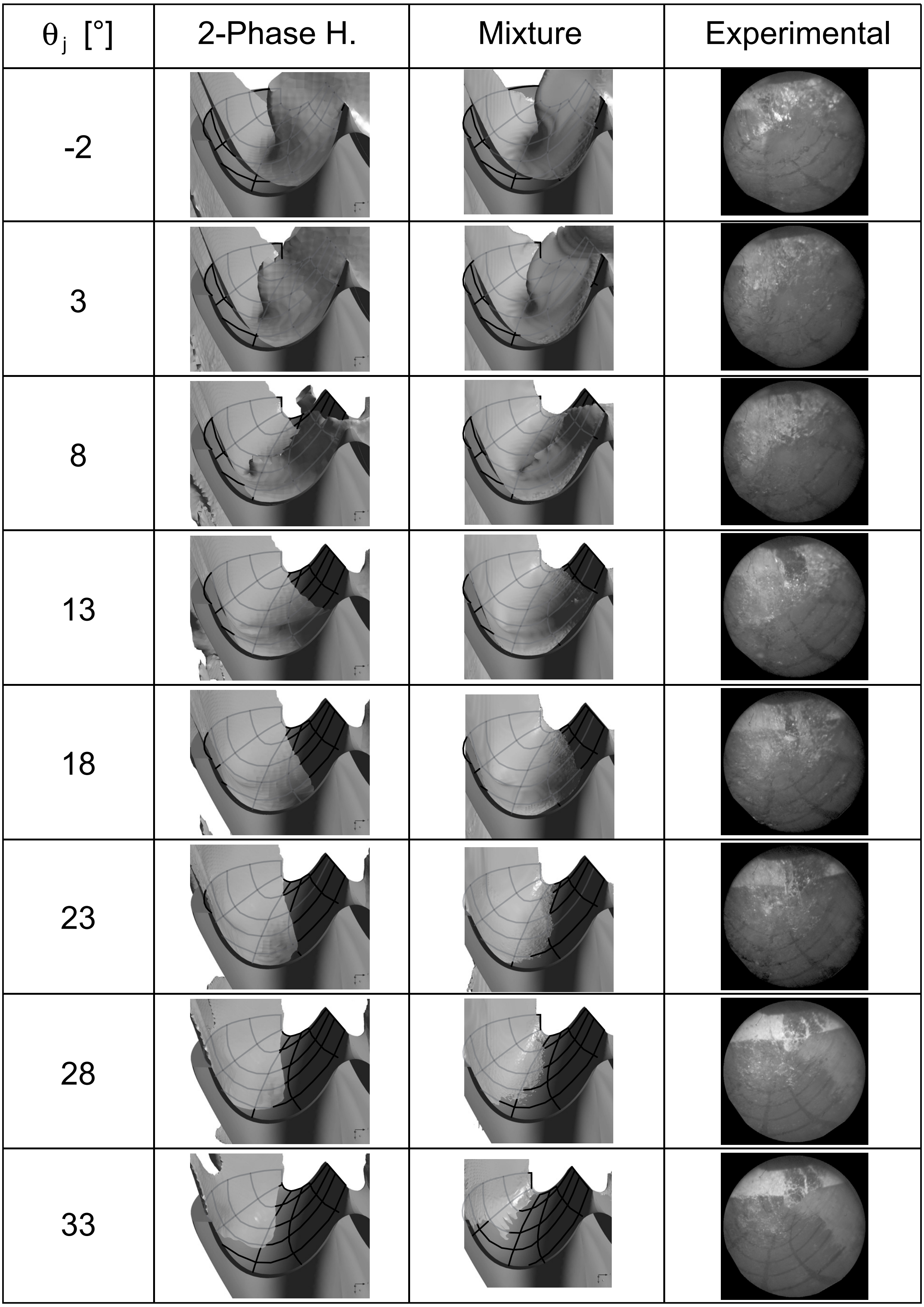
θj [°]
2-Phase H.
Mixture
Experimental
-2
3
8
13
18
23
28
33

Figure 12.9: Comparison of the relative flow patterns, part II.

Part III

RESULTS AND ANALYSIS

Chapter 13

Bucket duty cycle

13.1 Description

The flow sequence of bucket j duty cycle is divided in 6 steps, see Fig.13.1 [7], [88], [87]. The description of the relative flow sequences is performed according to Fig.13.2 and 13.3 for the higher jet diameters, with varying energy coefficients, and to Fig.13.4 and Fig.13.5 for different jet diameters with constant energy coefficients.
The observations from the absolute frame of reference are featured by Fig.13.6 and 13.7 for the external observations.

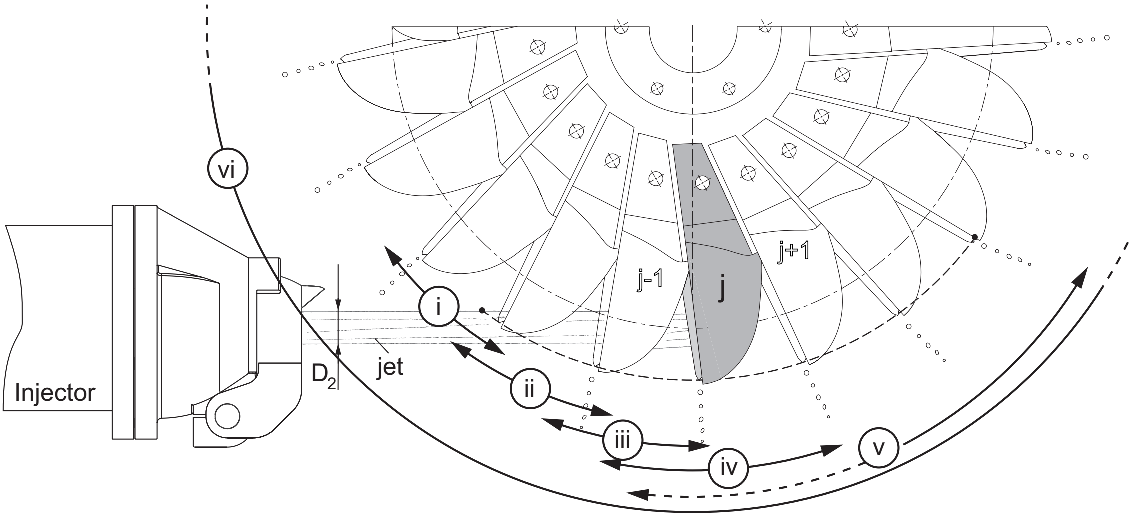

Figure 13.1: Duty cycle sequence

(i) Approach of the tip to the jet ($\theta_j < -40°$). Beside appearing striated and rippled, the jet surface exhibits perturbations, detail a, and a series of convected impact craters, detail b, Fig.13.6.

(ii) Initial feeding process. ($\theta_j = -40°...-10°$). Once the tip and the cutout lips are in contact with the jet upper surface, the jet starts to separate in 2 branches, *i.e.* the upper one, that flows in bucket j, and the lower one that continues to feed bucket $j+1$.

The image sequence show an outburst of the jet, and the appearance of a splay crown of water threads on the upper side, detail c, and a radial splashing water adhering to some extend to the ribs on the backside, detail d, animated by almost the same velocity as the jet. The jet front and the splay crown, detail c, fly over bucket j and impinge on it later in the cycle, at $\theta_j \sim -17°$ for OP1 and $\theta_j \sim -23°$ for OP14. Immediately after the impact, the onset of foam, detail e, is clearly visible. At this point the jet is already partially cut by bucket $j-1$. Thereafter, the flow evolves into the expected film flow, detail f, moving first slightly towards the root and then laterally towards the outer edge. The outflow process, detail g, starts at $\theta_j \sim -10°$. For the higher values of ψ_1, the flow reaches the bucket root, drowning the distal lens of the onboard borescope.

(iii) Entire separation of the jet ($\theta_j = -10°...0°$). At this point the impinging main flow feeds bucket j mainly normally to the splitter. The now entirely separated portion of the jet remains attached to bucket $j-1$ backside far in the duty cycle, as predicted by Lowy [69] and observed by Bachmann [7]. In addition, it seems to be deflected against bucket $j-1$ backside. The deformations it displays match well the predictions made by Lowy [69]: the cross-section of the jet is crescent-shaped, concave against bucket $j-1$ backside. The cross-section consists of 2 different flows: the core, detail h, practically filled with liquid and the spray, which consists of numerous single separated water threads, detail i. The resulting section is much larger than the original jet diameter, and impinges not only on the splitter but also on the established water sheets, detail f. The water sheet for OP14 exhibits a tumescence, detail $f1$, that appears around $\theta_j = -13°$ and becomes larger at $\theta_j = -4°$.

(iv) Last stage of inflow ($\theta_j = 0°...15°$). The last threads and droplets of the distorted and disintegrated end of the jet, detail i, enter bucket j partially on the bottom surface and partially on the lateral edges next to the cutout. Some of the water escapes bucket j directly through the cutout in a radial direction, detail j, even for very low discharges, see OP14, Fig.13.5.

(v) Last stage of outflow ($\theta_j = 15°...50°$). The water sheet presents a corrugated surface as it is not fed anymore, detail k. The outflow sheet remains fully developed late in the duty cycle, and becomes thinner and thinner until it breaks up, detail m, at first near the root and then towards the front. The end of the outflow process shows a significant stratification of the flow: the sheet appears to slide film by film, detail n.

(vi) Series of droplets ($\theta_j = -50°...\infty$). The outflow never comes to an end. A line of droplets, detail l, is visible along the entire runner periphery. The droplets are released from the outer edge tips, on the external side of the cutout, and from the splitter tip.

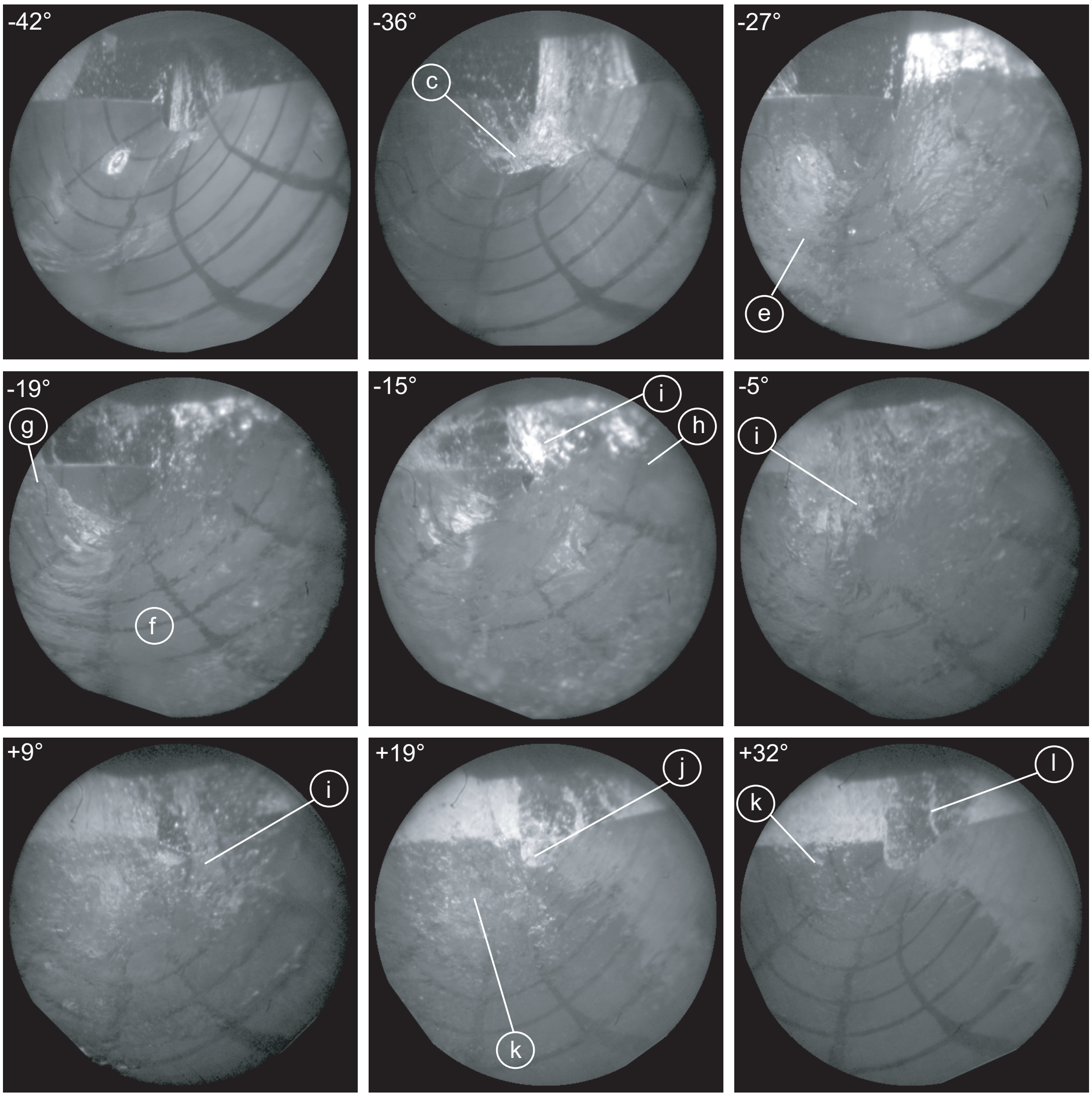
-42°
-36°
c
-27°
e
-19°
g
f
-15°
i
h
-5°
i
+9°
i
+19°
j
k
+32°
k
l

Figure 13.2: Bucket onboard film sequence, OP1, $\psi_1/\psi_1^\wedge = 0.89$, $\varphi_{B_2}/\varphi_{B_2}^\wedge = 1.07$.

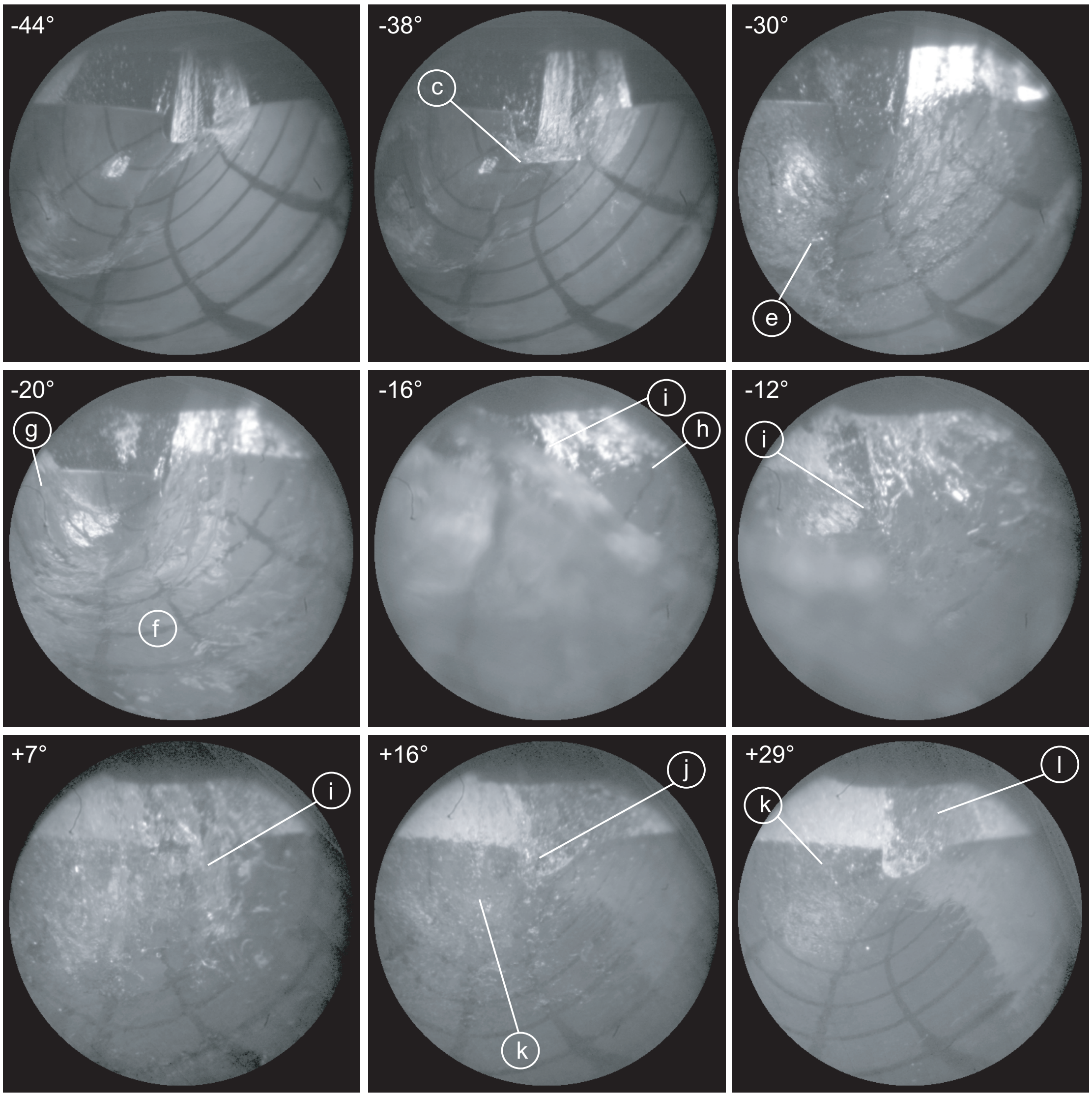
-44°
-38°
c
-30°
e
-20°
g
f
-16°
i
h
-12°
i
+7°
i
+16°
j
k
+29°
k
l

Figure 13.3: Bucket onboard film sequence, OP3, $\psi_1/\psi_1^{\wedge} = 1.07$, $\varphi_{B_2}/\varphi_{B_2}^{\wedge} = 1.20$.

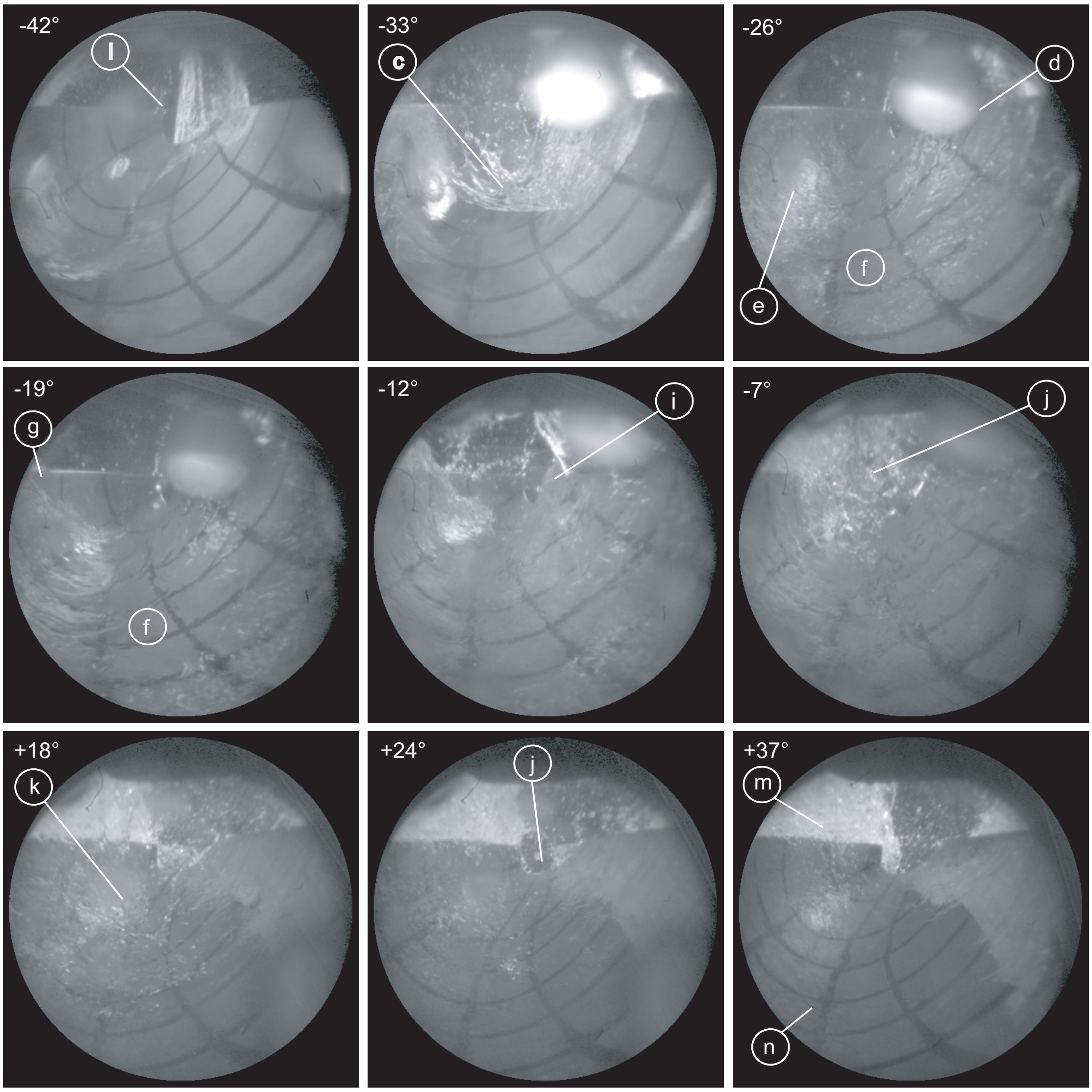
-42°
l
-33°
c
-26°
d
e
f
-19°
g
f
-12°
i
-7°
j
+18°
k
+24°
j
+37°
m
n

Figure 13.4: Bucket onboard film sequence, OP5, $\psi_1/\psi_1^{\wedge} = 1.00$, $\varphi_{B_2}/\varphi_{B_2}^{\wedge} = 0.95$.

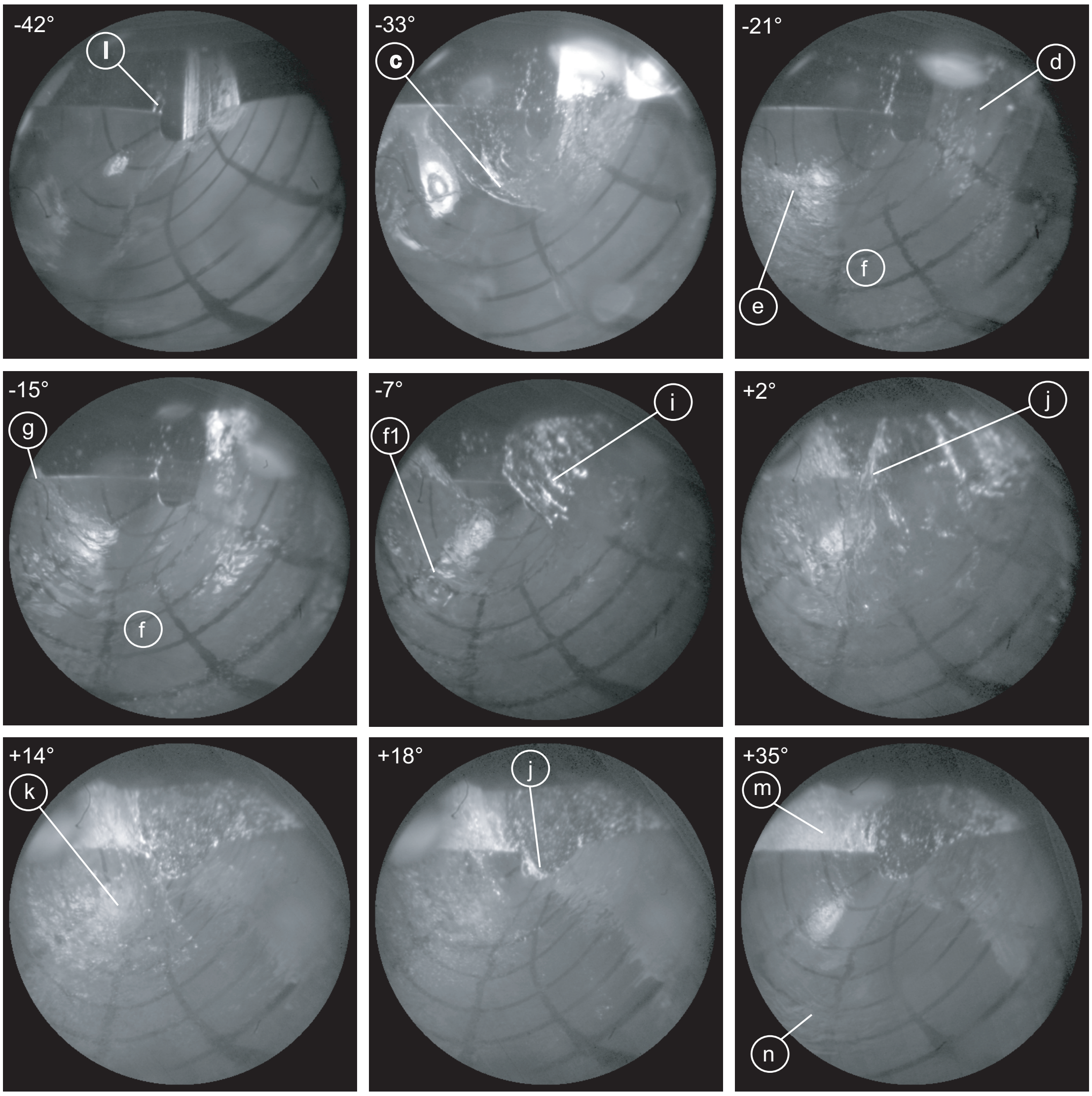
-42°
l
-33°
c
-21°
d
e
f
-15°
g
f
-7°
f1
i
+2°
j
+14°
k
+18°
j
+35°
m
n

Figure 13.5: Bucket onboard film sequence, OP14, $\psi_1/\psi_1^\wedge = 1.000$, $\varphi_{B_2}/\varphi_{B_2}^\wedge = 0.54$.

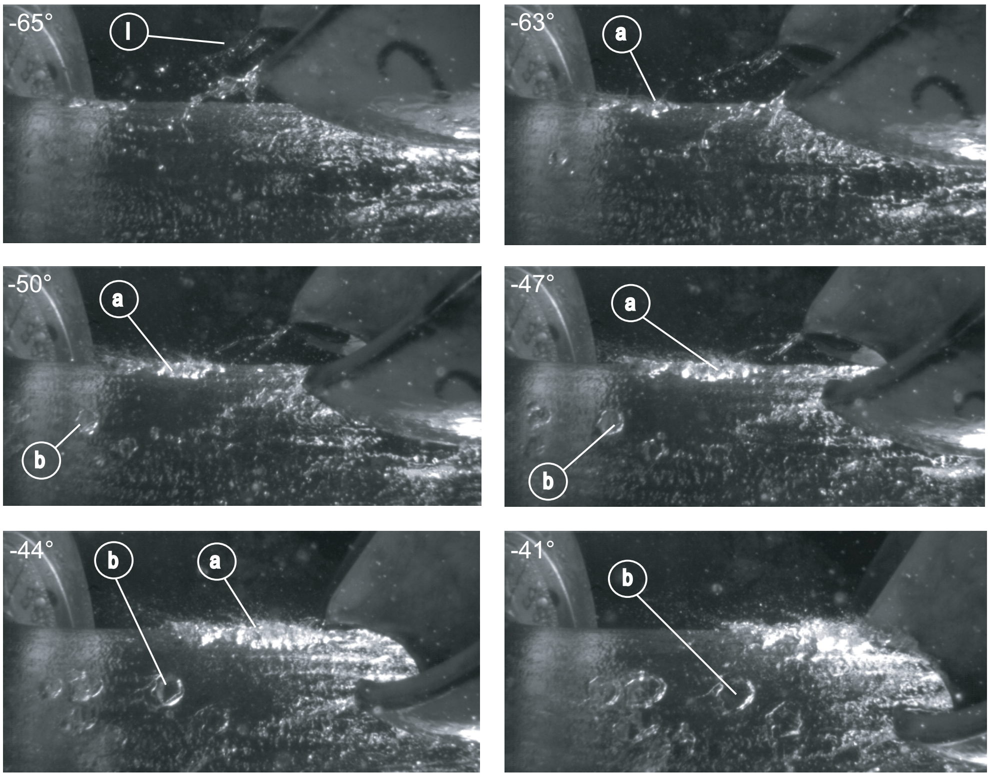
-65°
I
-63°
a
-50°
a
b
-47°
a
b
-44°
b
a
-41°
b

Figure 13.6: Jet surface perturbation by droplets impact, OP1, $\psi_1/\psi_1^\wedge = 0.89$, $\varphi_{B_2}/\varphi_{B_2}^\wedge = 1.07$.

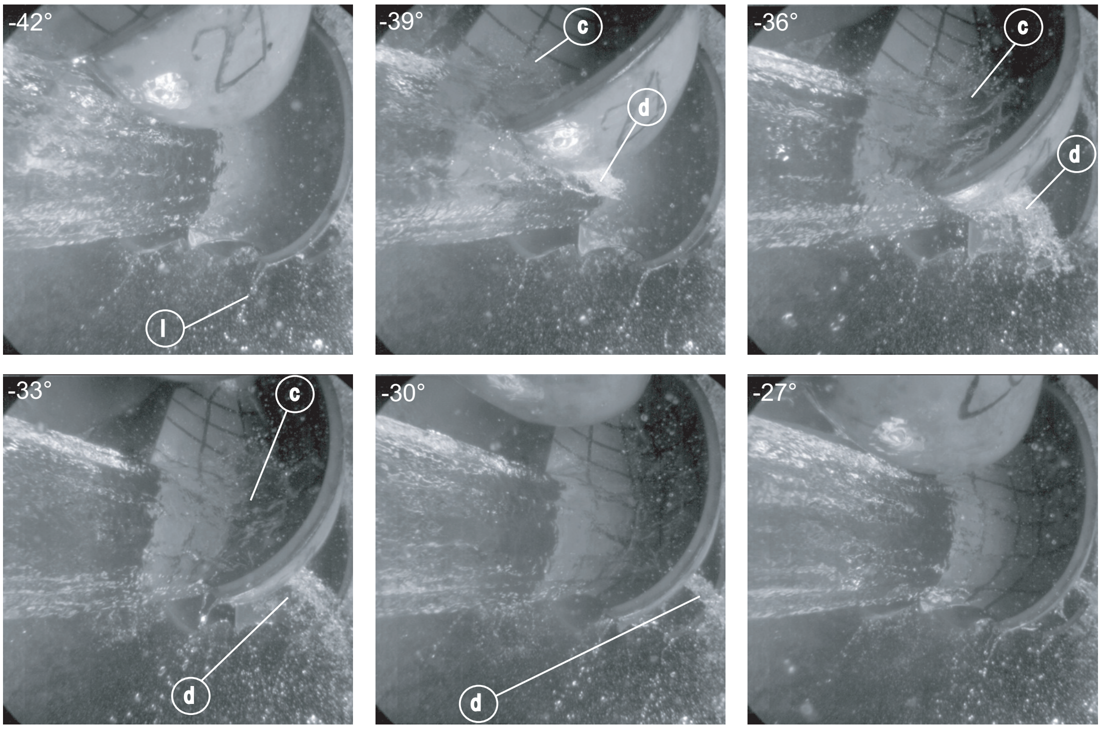
-42°
I
-39°
c
d
-36°
c
d
-33°
c
d
-30°
d
-27°

Figure 13.7: Bucket external observation, OP1, $\psi_1/\psi_1^\wedge = 0.89$, $\varphi_{B_2}/\varphi_{B_2}^\wedge = 1.07$.

Chapter 14

Inlet flow

14.1 Impact of the bucket tip on the jet surface

As defined in section 7.1, bucket j duty cycle is assumed to start when the splitter tip impacts the jet upper generator. Figure 14.1 is a view of the first instant of contact as seen by the external borescope in configuration 4. The interaction zone moves then on the cutout lips, first close to the tip and then more and more laterally. The early stages of the interaction were never observed in details, nor was the nature of the physics involved studied so far [87]. The fact that some prototype machines and even reduced scale models display erosion damages [29], [15], [16], indicates that high pressures occur in the contact area, as displayed by Fig.14.2. Cavitation is usually chosen as explanation, but nothing is presented to backup this assumption [29]. Numerical results show a counter-pressure at

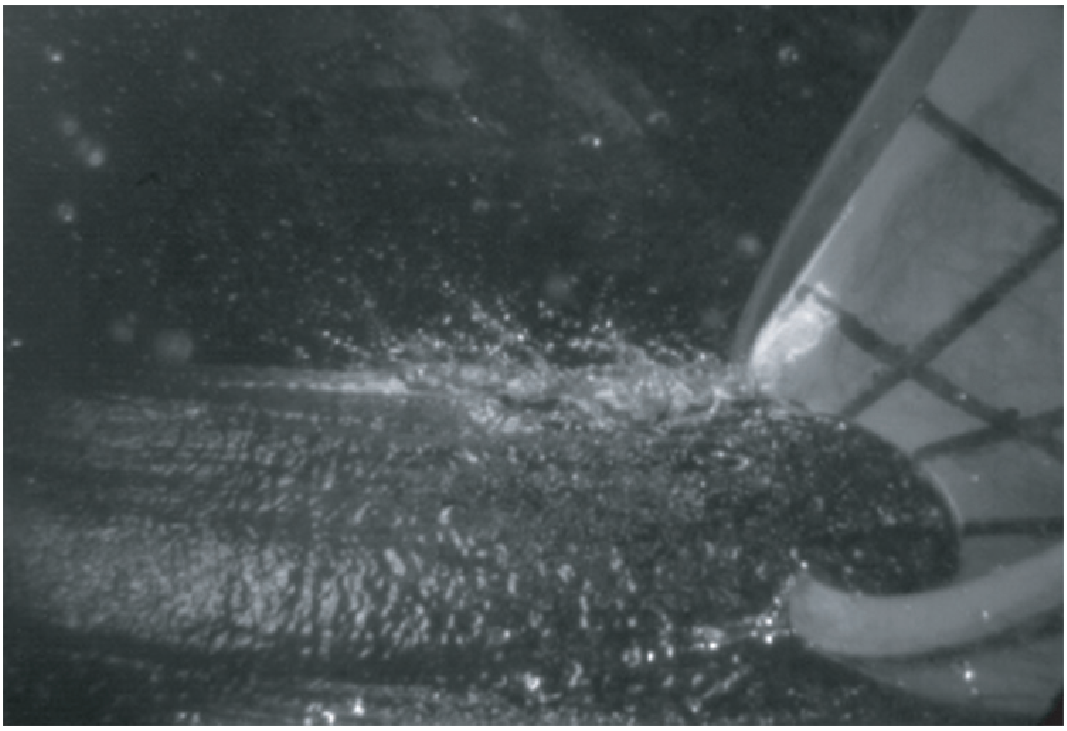

Figure 14.1: Initial jet/bucket contact.

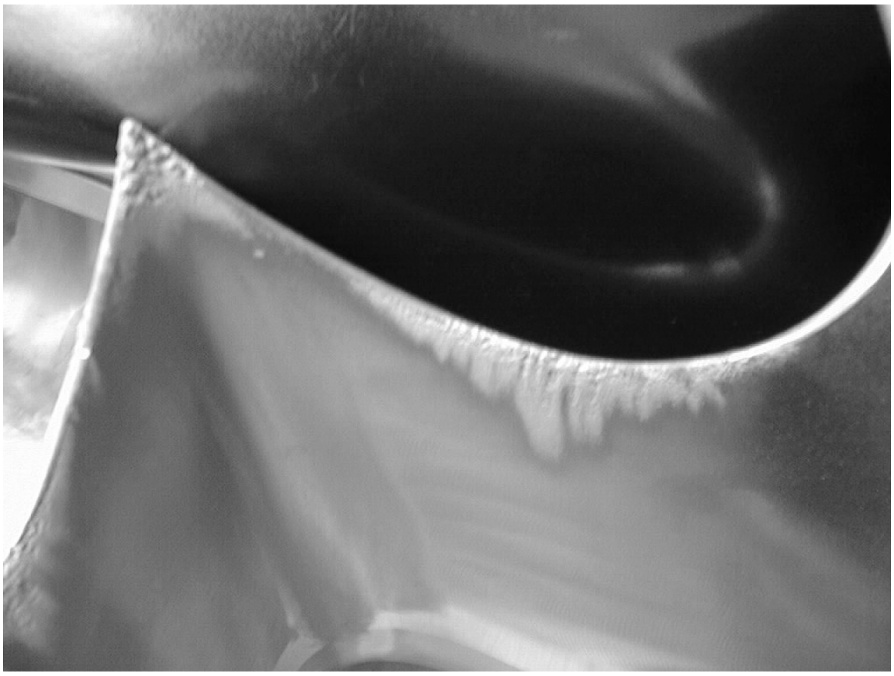

Figure 14.2: Erosion damages in the cutout area of a prototype turbine.

the beginning of the contact, but the amplitudes are well below that capable of generating erosion damages on steel buckets.

14.1.1 Approach

Since no pressure sensor is mounted directly in the tip, a theoretical approach is carried out to estimate the pressure amplitudes during the initial impact: (i) a kinematic study is performed to determine the local speeds and angles of attack at the instant of impact; (ii) by the light of Appendix C, the local Mach numbers of the edges of the contact area are estimated; (iii) the transient pressure amplitudes are estimated using a simplified hydroacoustic model.

14.1.2 $2D$ simplification: kinematic study

The case is reduced to a $2D$ problem. The jet is assumed to be $2D$, and a longitudinal cut along bucket j symmetry plane is considered. The jet is animated by the absolute velocity $\overrightarrow{C}$, while bucket j tip moves with the peripheral velocity $\overrightarrow{U_b}$. The first contact between bucket j tip and the jet upper generator occurs with relative velocity $\overrightarrow{W}$, Fig.14.3. In the relative frame of reference, the jet is assumed to be a semi-infinite plane of water [101], and that the bucket tip is a $2D$ wedge moving in translation at velocity $\overrightarrow{W}$, see Fig.14.4. The angle of impact of the tip, γ, must now be determined.

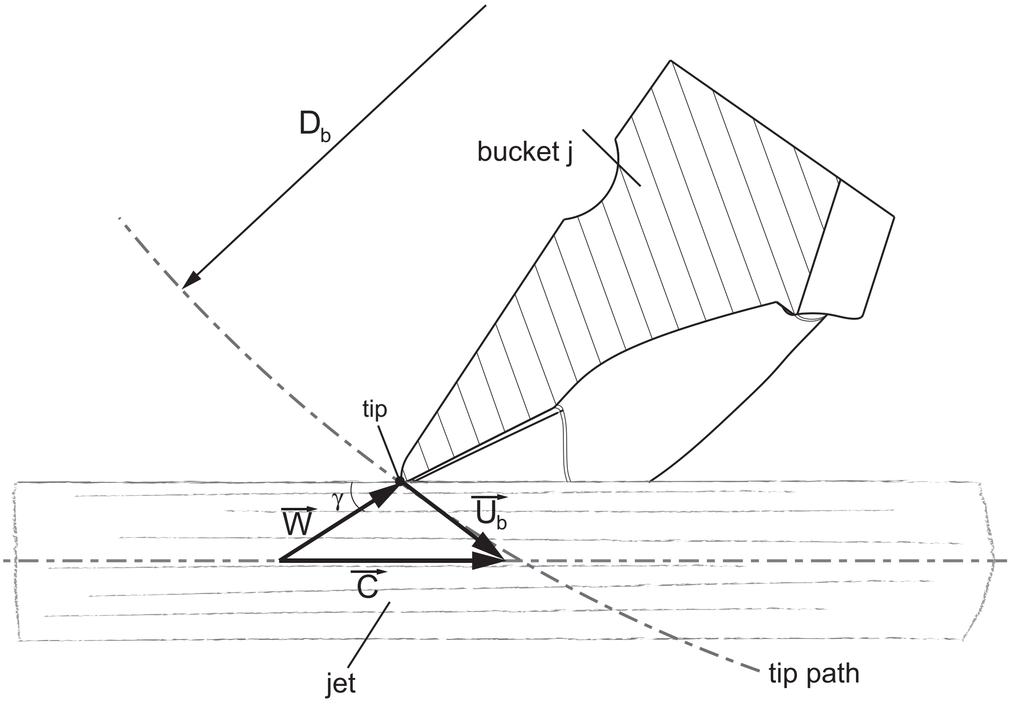

Figure 14.3: $2D$ velocity triangle at the instant of impact.

Impact angle of impact

The position of bucket j tip in a fixed frame of reference, which origin coincides with the center of rotation of the runner, see Fig.14.5, is given by:

$$\begin{cases} x_b(t) = \dfrac{D_b}{2}\cos(\omega t + \omega t_0) \\ z_b(t) = \dfrac{D_b}{2}\sin(\omega t + \omega t_0) \end{cases} \tag{14.1}$$

ωt_0 is the arc between the datum and the first contact point A, see Fig.7.1 and is given

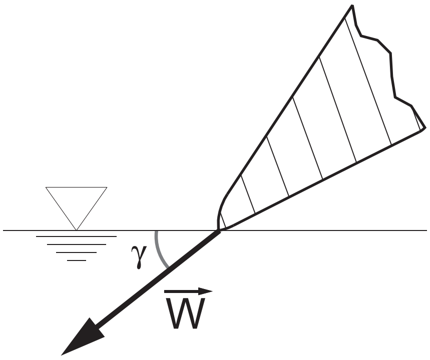

Figure 14.4: $2D$ wedge impact on a water surface.

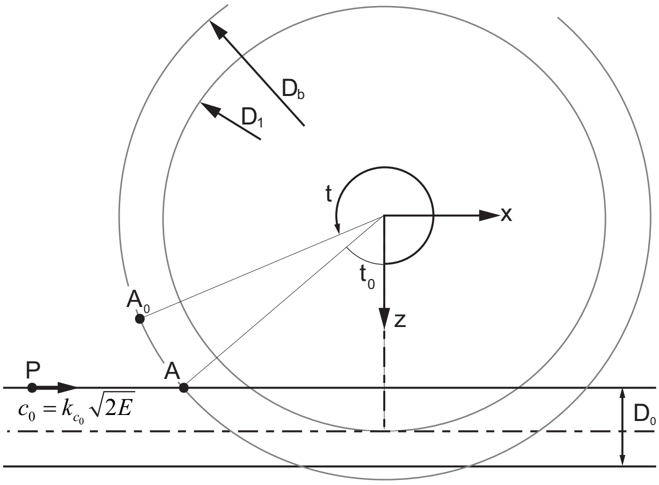

Figure 14.5: Kinematic path of the tip.

by

$$\omega t_0 = \arccos(\frac{D_1 - D_2}{D_b}). \tag{14.2}$$

The velocity of bucket j tip is obtained by deriving Eq.14.1:

$$\begin{cases} U_{x_b} = \dfrac{dx_b(t)}{dt} = \dfrac{D_b}{2}\sin(\omega t + \omega t_0) \cdot \omega \\ U_{z_b} = \dfrac{dz_b(t)}{dt} = -\dfrac{D_b}{2}\cos(\omega t + \omega t_0) \cdot \omega. \end{cases} \tag{14.3}$$

Let now consider the jet of diameter D_2 oriented parallel to the x-axis. Let P be the water particle travelling on the jet upper generator at constant velocity $C = k_{c_0}\sqrt{2E}$, that is to encounter bucket j tip at position A. Particle P position is given by:

$$\begin{cases} x_p(t) = k_{c_0}\sqrt{2E} \cdot t \\ z_p(t) = \dfrac{D_1 - D_2}{2} \end{cases} \tag{14.4}$$

and its velocity is:

$$\begin{cases} C_{x_p} = \dfrac{dx_p(t)}{dt} = k_{c_0}\sqrt{2E} \\ C_{z_p} = \dfrac{z_p(t)}{dt} = 0. \end{cases} \tag{14.5}$$

The relative velocity components of particle P with respect to bucket j tip is, as defined by the velocity triangle ($\overrightarrow{W} = \overrightarrow{C} - \overrightarrow{U}$), at the instant of impact, t_0:

$$\begin{cases} W_{x_p} = k_{c_0}\sqrt{2E} - \dfrac{D_b}{2}\sin(\omega t_0 + \omega t_0) \cdot \omega \\ W_{z_p} = \dfrac{D_b}{2}\cos(\omega t_0 + \omega t_0) \cdot \omega \end{cases} \tag{14.6}$$

The relative angle of impact of the tip is expressed as:

$$\gamma = \arctan(\frac{W_{z_p}}{W_{x_p}}) + \rho. \tag{14.7}$$

ρ is the angle of setting of bucket j, and is given by, see Fig.14.6:

$$\rho = \arcsin(\frac{2r}{D_b}). \tag{14.8}$$

Introducing the massic energy coefficient ψ_1, the expression for the impact angle of attack

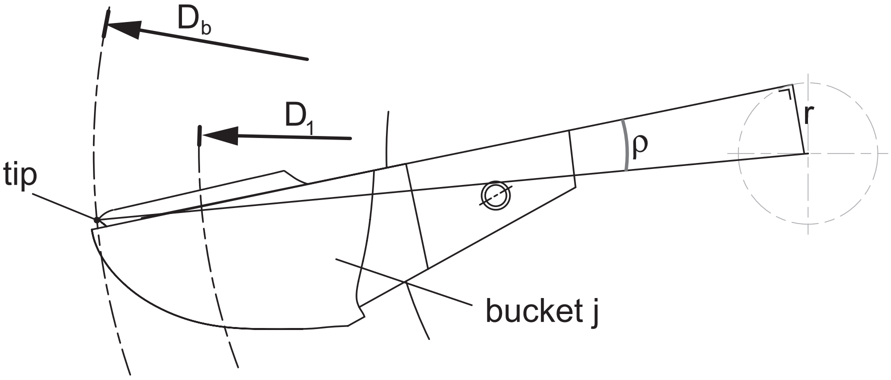

Figure 14.6: Bucket angle of setting definition.

γ becomes:

$$\gamma = \text{arccot}\left(\frac{D_1 - D_2}{\psi_1^{1/2} k_{c_0} - \frac{D_b}{D_1}\sqrt{1 - \left(\frac{D_1 - D_2}{D_b}\right)^2}}\right) \tag{14.9}$$

The angle γ is function of 3 parameters: $\gamma = \gamma(\psi_1, D_2, k_{c_0})$. Figure 14.7 displays the evolution of γ with respect to ψ_1 and D_2. It can be seen that the influence of D_2 is negligible.

14.1.3 Impact problem formulation

The problem is now reduced to that of the impact of a rigid body onto the surface of a semi-infinite fluid. It is assumed that the normal component of the impact speed, W_z, is small compared to a, the speed of sound in the liquid, *i.e.* the entry Mach number is less than unity. It is usually assumed that under the condition $W_z/a < 1$, the fluid could be treated as incompressible. This is correct if the body is not too blunt. For a blunt body the area of contact between the fluid and the solid expands rapidly. The velocity W_{z_e} of the boundary of the contact area is of the order of $W_z/\tan\kappa$, where κ is the typical slope of the wedge [101], which in turn depends on the bucket tip geometric angle β, Fig.14.8:

$$\kappa = \gamma - \beta. \tag{14.10}$$

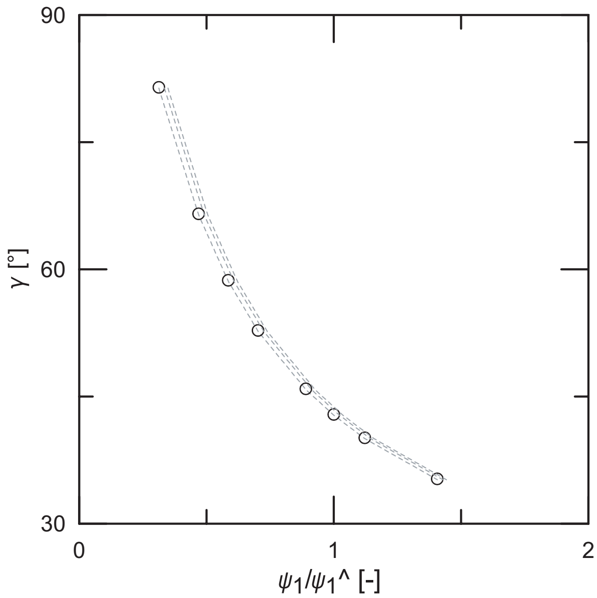

Figure 14.7: Variation of the angle of attack γ with respect to ψ_1 and D_2.

If W_{z_e} is larger than the local speed of sound a, the action of the body on the fluid corresponds to a loaded area which expands supersonically with respect to the fluid. Hence the compressibility of the fluid must be considered to obtain realistic results. Defining an edge Mach number, $M_e = W_{z_e}/a$, it may be anticipated that the fluid must be treated as compressible whenever $M_e \approx 1$. The following analysis will therefore be limited to the initial moments of impact when κ is small and the penetration of the bucket into the jet is small. Assuming furthermore that changes in density within the fluid are small justifies the use of the acoustic equations for the fluid. The fluid is assumed inviscid and at rest initially, the motion of the fluid during impact is irrotational and a velocity potential χ exists such that the velocity $\overrightarrow{W}$ is:

$$\overrightarrow{W} = \overrightarrow{\nabla}\chi, \tag{14.11}$$

where χ satisfies the wave equation

$$\nabla^2\chi = \frac{1}{a^2}\frac{\partial^2\chi}{\partial t^2}. \tag{14.12}$$

The initial conditions of no motion and zero pressure in the fluid are:

$$\left\{\begin{array}{l} \chi = 0 \\ \dfrac{\partial\chi}{\partial t} = 0 \end{array}\right\} \text{at t} = 0 \tag{14.13}$$

The impact problem for a rigid wedge of arbitrary angle is a case for which analogous solutions are available in the supersonic flow literature [101]. These cases are treated by the theory of conical fields. The $2D$ bucket tip is considered a wedge of semivertex angle β moving in the z-direction with a constant speed W_z. Figure 14.8 shows the geometry of the reduced impact problem. The boundary conditions are:

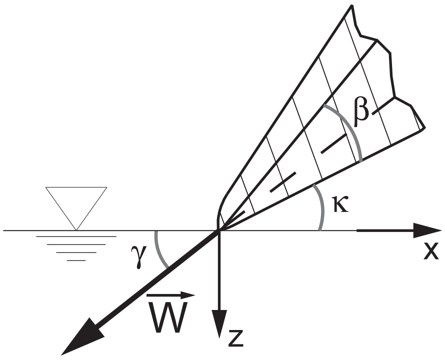

Figure 14.8: Configuration of wedge at the instant of impact.

$$\begin{cases} \frac{\partial \chi}{\partial z}(x,0,t) = W_z = W \sin\kappa \qquad x < W_z t \cot\kappa \\ \chi(x, z=0, t) = 0 \qquad x > W_z t \cot\kappa \end{cases} \tag{14.14}$$

The width of the wetted surface of the wedge as a function of time is shown in the $(x-t)$-plane as the grayed region in Fig.14.9. The line $x = V_1 t$ is the trace of the intersection of the wedge and the free-surface. The velocity of the intersection is:

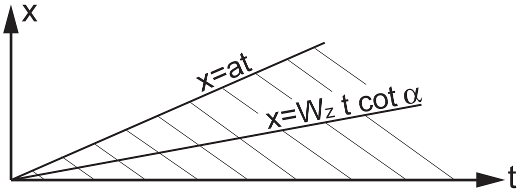

Figure 14.9: Wetted surface of wedge in $(x-t)$-plane.

$$V_1 = W_z \cot\kappa, \tag{14.15}$$

and the edge Mach number is defined as:

$$M_1 = \frac{V_1}{a}. \tag{14.16}$$

The edge Mach number will be called supersonic or subsonic depending on whether it is greater or less than unity. Equation 14.12 is hyperbolic and therefore is a characteristic cone in a x, z, t-space given by

$$at - \sqrt{x^2 + \ z^2} = 0. \tag{14.17}$$

The intersection of this characteristic cone with the plane $z = 0$ is

$$x = at \tag{14.18}$$

and the case of supersonic and subsonic edge numbers corresponds to the traces of the wetted surface in Fig.14.9 lying outside or inside the characteristic cone. From the results presented in Appendix C, the local speed of sound in the jet periphery is likely to be as low as $40 m/s$. The resulting edge Mach number for different operating conditions and different test heads are represented in Fig.14.10(a). These edge Mach number are called supersonic or subsonic depending on whether they are greater or less than unity.

14.1.4 Impact problem solution

The compressibility has to be taken into account for edge Mach numbers above 0.25 [101], [28], [55]. The solution of Eq.14.12 is similar to the problem of a plane subsonic wing at an angle of attack. The numerical solution results are plotted in Fig.14.10(b). The pressures are divided by $\rho a W$, the pressure that would de developed in a $1D$ impact case with impact velocity W. The length are divided by the instantaneous width of the side of the impacting wedge. Each curve represents a different Mach number. The impact pressure can reach up to $3\rho a W_z$ [28]. The real amplitude is function of the air diffusion in the jet, *i.e.* the jet spread. The protuberances and craters visible on the jet surface, Fig.14.11, that are convected by the flow dramatically modify the impact conditions, both in terms of geometry (area of contact) and air diffusion. The edge Mach number is increased and thus the pressure amplitudes reach most certainly higher values than determined from the hydroacoustic model.

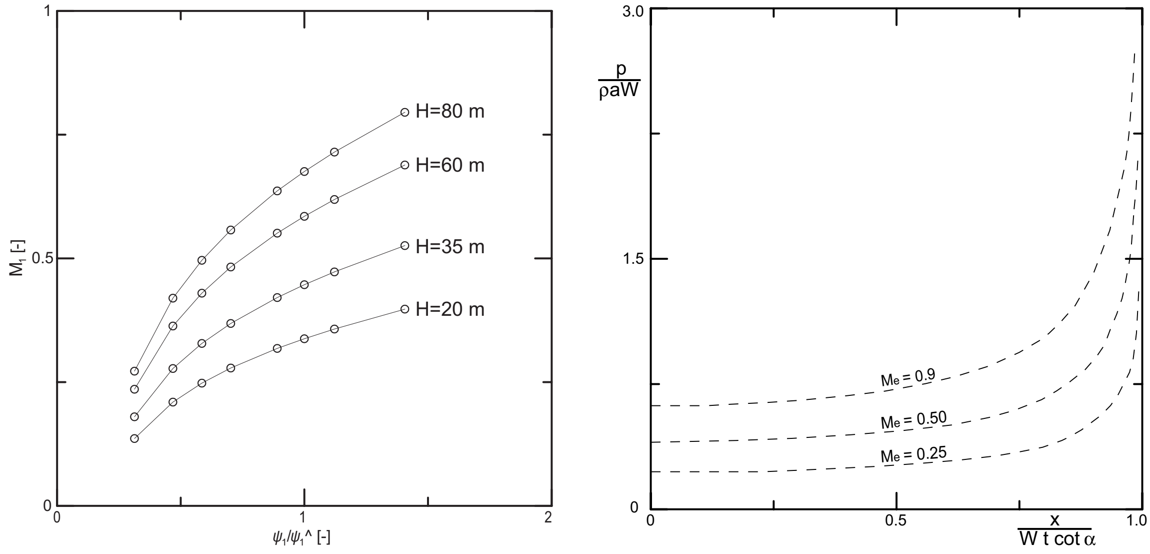

(a) Edge Mach number variation.

(b) Pressure on the wedge.

Figure 14.10: Impact problem solution.

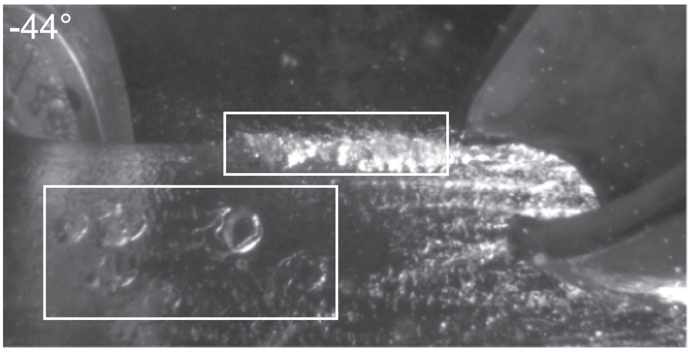

Figure 14.11: Jet surface protuberances and craters convected.

14.1.5 Spillway effect

As an aftermath of the impact of the cutout, the jet surface bursts, and the cut section expands radially from the jet axis and forms a splay crown, detail c on Fig.13.2, 13.3 and 13.7. The conjunction of 2 phenomena explain the jet outburst: (i) The compression waves are released across the free surface, generating an outward radial flow of liquid [55]. (ii) The cutout lips form an obstacle that the flow has to go round, thus prolonging the normal to the jet velocity component generated by the impact. All sequences clearly indicate that the front of the cut jet does not follow bucket j surface, but overflies it due the longitudinal curvature of the latter. The water threads forming the splay crown are caused by the surface tension force and their backwards curved shape to their drag that is significantly higher than that of the smoother jet surface. In fact, the cutout lips appears to act like a spillway, as illustrated by Fig.14.12, inducing a significant aeration process in the jet front [17].

14.2 Jet impact and waterhammer

All previous pressure measurements campaigns conducted on Pelton runners show the presence of peaks of pressure in the central region of the buckets [15], [16], [66]. The pressure signals recorded in that area exhibit the same shape: a pulse of high amplitude, with the amplitude exceeding by far the maximum of the remaining portion of the signal. No satisfactory explanation has been provided so far. The phenomenon was attributed to a stagnation point with the formation of a re-entrant micro jet [66], while other studies [16] concluded that it could be related to rain erosion, induced by the repetitive impact of water droplets escaped from the jet. The pulse amplitude is not related to the ambient pressure in the turbine casing [15]. Moreover, prototype machines and sometimes reduced scale models exhibit erosion damages in that region, attesting the existence of very high pressures, Fig.14.13. On the other hand, no numerical simulation so far is able to adequately predict the peak and its amplitude, as as stated in chapter 12.

14.2.1 Zone delimitation

As far as the test runner is concerned, 3 sensors present a similar pulse of pressure. The area that undergoes high transient pressures can thus be delimited. Figure 14.14 shows the 3 sensors locations, the zone delimitation, and the related pressure signals. It is remarkable that the standard-deviation band at the moment of the pulses is significantly thicker than for the remaining of the signals. The maxima envelope show an amplitude much higher than the phase-averaged value, while the minima envelope does not show any peak at all. Sensor 14, located in the center of the zone features 3 remarkable characteristics: (1) it exhibits the highest amplitude, (2) its signal is the first to rise, although it is located beyond sensor 13, and (3) it is located almost exactly on D_1.

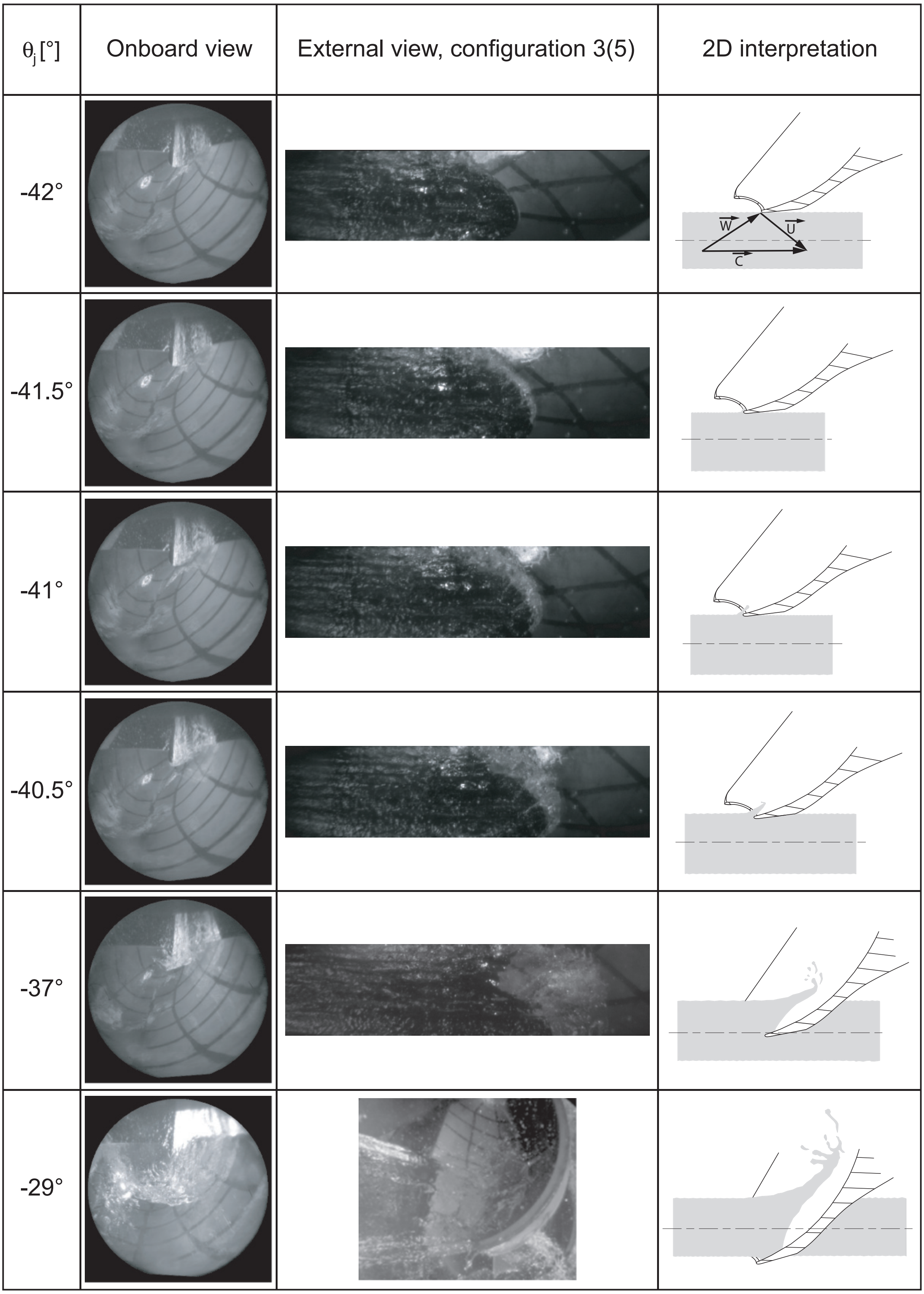
θ_j [°]
Onboard view
External view, configuration 3(5)
2D interpretation
-42°
-41.5°
-41°
-40.5°
-37°
-29°
$\vec{W}$
$\vec{U}$
$\vec{C}$

Figure 14.12: Spillway effect during the jet cut.

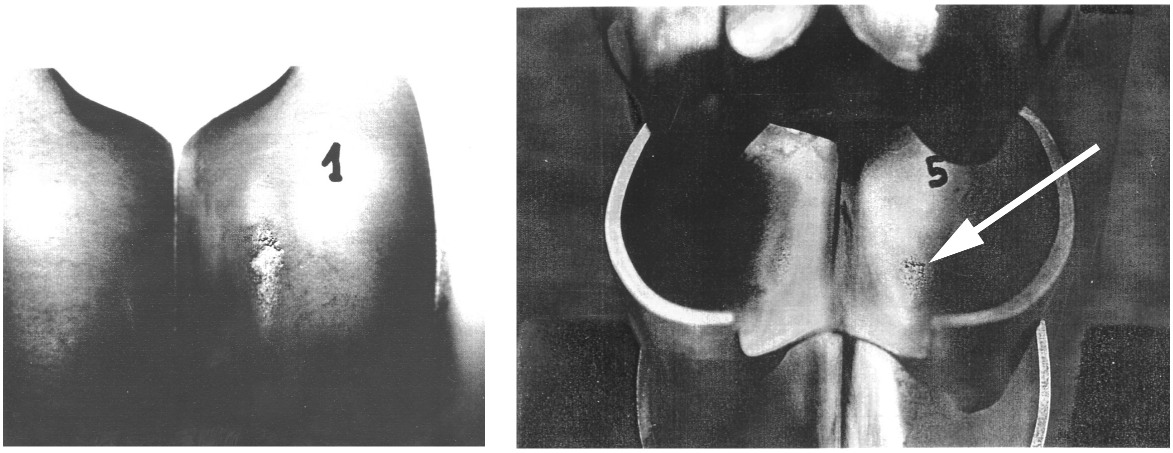

Figure 14.13: Erosion damages in reduced scale models [15].

14.2.2 Peak of pressure versus operating conditions and head

Figure 14.15 show the evolution of the maximum pressure coefficient as a function of (a) ψ_1, (b) φ_{B_2} and (c) of the relative head, H', respectively, defined as:

$$H' = \frac{(\omega D_1)^2}{8g} \tag{14.19}$$

The pulse amplitude clearly appears to be related to ψ_1, *i.e.* to the angle of attack at the instant of impact. It is remarkable that for $\psi_1/\psi_1^{\wedge} = 0.6 - 0.8$, the pressure coefficient reaches 1.4 times the value corresponding to the steady-state stagnation point of the jet impinging on the bucket with the runner blocked. In the normal operating range, the highest value is reached for $\psi_1/\psi_1^{\wedge} = 0.89$. The variation of the peak pressure coefficient with respect to φ_{B_2} shows that it increases quasi linearly with the jet diameter, *i.e.* the needle stroke. It is maximum for the largest openings. The amplitude of the peak, expressed in *bar* evolutes in $\sqrt{H'}$, showing that the pressure pulse can not be not a simple stagnation point, but has a compressible origin. However it is difficult to draw definite conclusions since the signal is under-sampled [66]. Indeed, the peak is only defined by 2 or 3 samples.

From the previous considerations, focus is made on OP1 ($\psi_1/\psi_1^{\wedge} = 0.89$ and $\varphi_{B2}/\varphi_{B_2}^{\wedge} = 1.07$) and on sensor 14.

14.2.3 Impact pressure theory

During the early stages of the impact of a liquid jet on a plane, assumed to be a rigid solid, it is found that compressive effects are dominant owing to the rapid rate at which the contact area between the liquid and the solid increases. A very high compressive stress is thus generated in the vicinity of the area of contact for times of the order of microseconds, and this is followed by outward radial flow of liquid at high speed [55]. The initial, momentary high-compressive stresses on impact arise because the liquid behaves compressible, as it remains non-deformed until release waves from the circumference of the jet reach its center [57]. Once a steady-state flow of water across the impact surface has been achieved, the ordinary hydrodynamic pressure at the stagnation point remains,

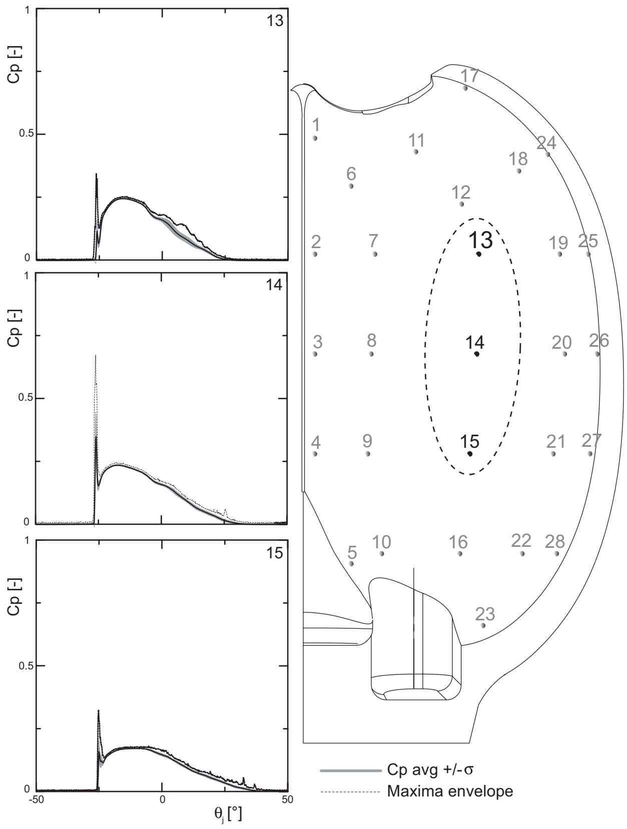

Figure 14.14: Zone with high pressure peaks, $\varphi_{B_2}/\varphi_{B_2}^{\wedge} = 1.12$, $\psi_1/\psi_1^{\wedge} = 0.89$, $H = 20m$.

$P = \frac{1}{2}\rho C^2$, where C is the normal impact speed of the jet [42]. The radial flow is generated by the relaxation of the pressure wave across the free surface. Several investigations concerning the initial pressure have been conducted, both experimentally and theoretically. Cook [19] showed that it can be represented by the waterhammer equation, $P = \rho a C$, where a is the speed of compressive waves in the liquid. The work done by Heritage and Enever [42] using an integral representation technique to solve the wave equation, validated by the measurements made by Vickers and Johnson [55], indicates maximum pressure near the edge of the contact area and minimum pressure at the center, *i.e.* a ring of high pressure. The pressure amplitudes reached during these initial impact stages are depending on (i) the contact area edge expansion Mach number, (ii) the liquid density and (iii) the local speed of sound in the liquid. Indeed, as presented in Appendix C, the local speed of sound in a jet is function of the amount of air dissolved in the water [14]. According to the authors cited above, the maximum pressure amplitudes range from 2/3 at the jet center to $1.4 - 2.5$ times $\rho a C$ at its periphery.

14.2.4 Pressure signal and onboard visualization synchronization

The sequence of images taken by the onboard flow visualization system, Fig.14.16, confirms that the peak of pressure is related to the impact of the front of the jet, and more accurately to the impact of the splayed crown border, see frame 3: if the jet core impinges

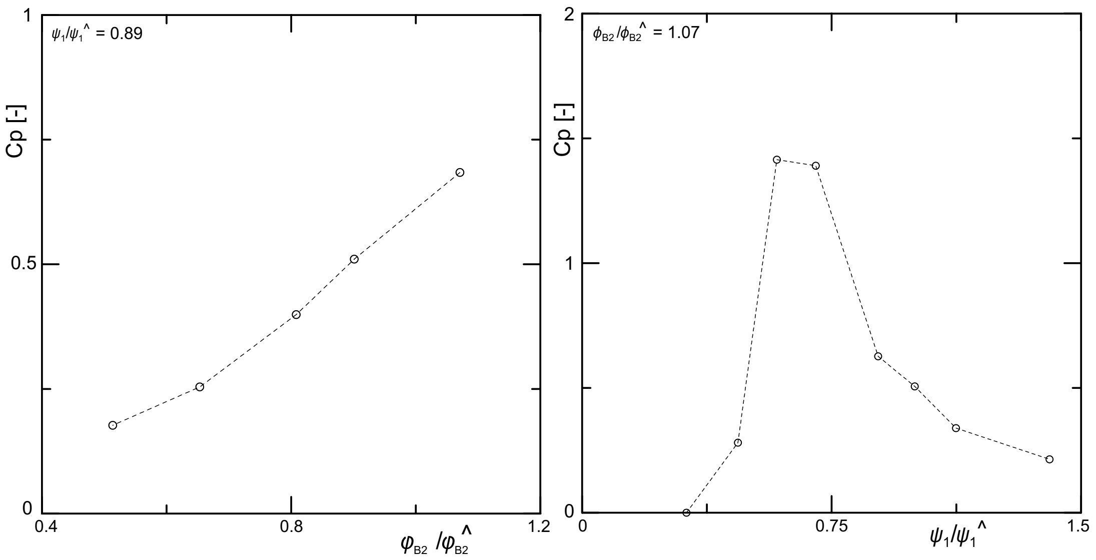

(a) Discharge coefficient

(b) Massic energy coefficient

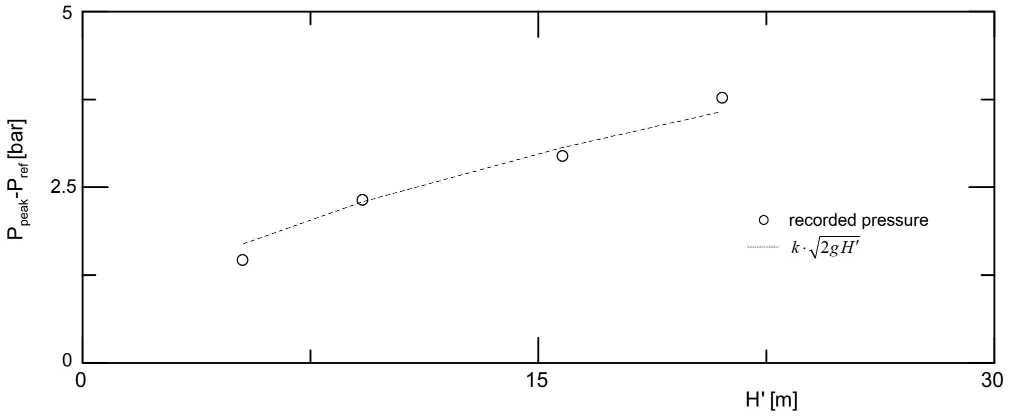

(c) Relative head

Figure 14.15: Pressure peak evolution with respect to φ_{B_2}, ψ_1, and H'.

on the splitter lateral edges, the crown, animated by the same velocity $\overrightarrow{W_1}$, impinges on the bucket bottom directly in the central region. Frames 3 and 4 show quasi no deformation of the incoming flow, while the pressure rise occurs. Frames 5 and 6 show the onset of foam, and the emergence of a small lateral flow moving fast towards the outer edge. This lateral flow can be observed on the subsequent frames 7 and 8, as it progresses across the bucket faster than the main water film boundary. Figure 14.17 schematizes the path of the lateral flow. If the pressure signal for sensor 14 provided by the numerical 2-Fluid Model does not adequately predict the amplitude of the pulse, it is remarkable that it exhibits an embryo of a peak at the same angular position as in the measurements. The presence of the peak in the simulation is probably caused by a numerical artefact. For time accurate calculations, compressible sub-iterations are introduced to fully recover the incompressible continuity equation at each real time step. The artificial compressibility should disappear upon total convergence of the computation [39], but this is difficult to obtain within fair computation times for all single time steps.

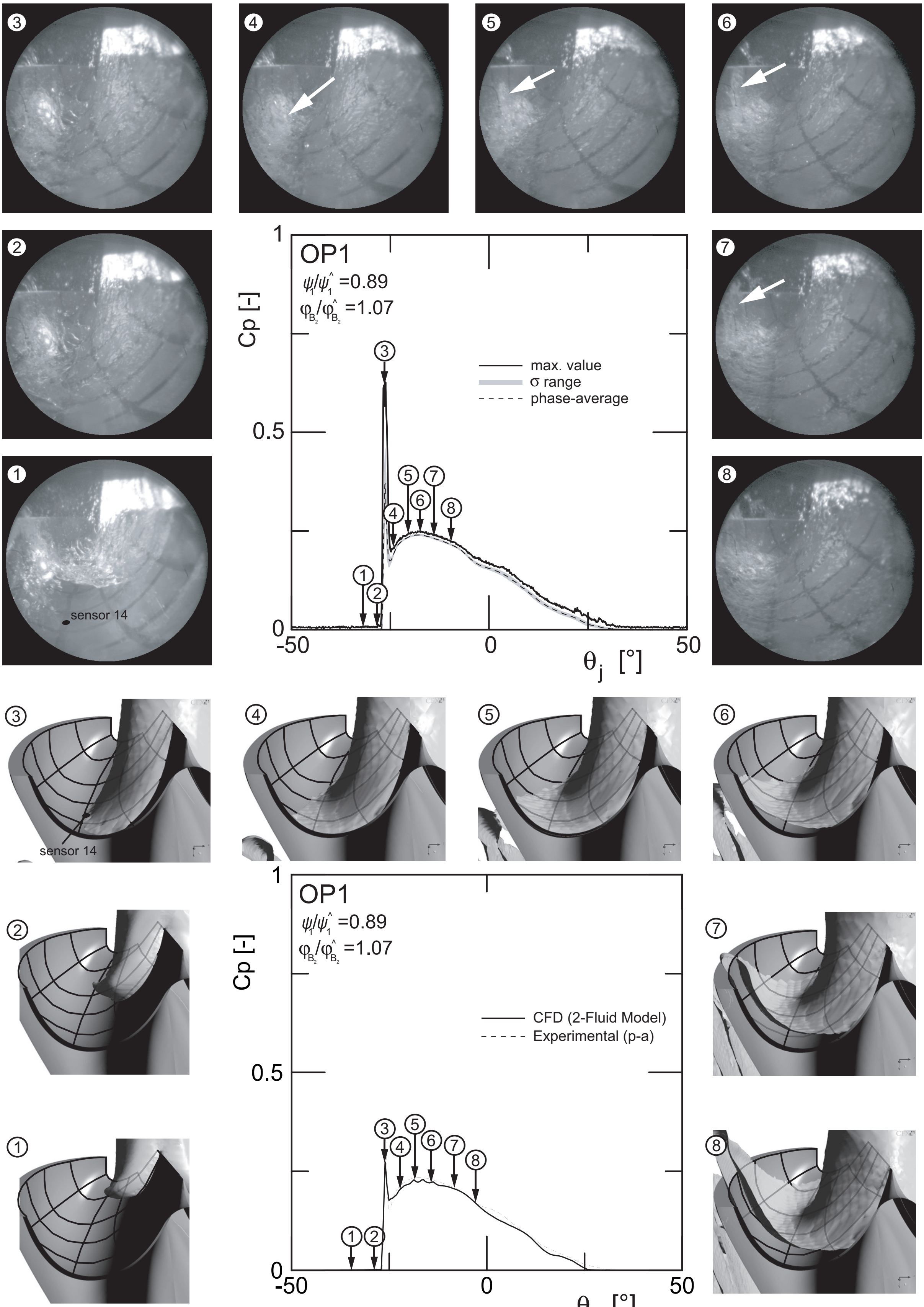

Figure 14.16: Sensor 14 during initial jet impact.

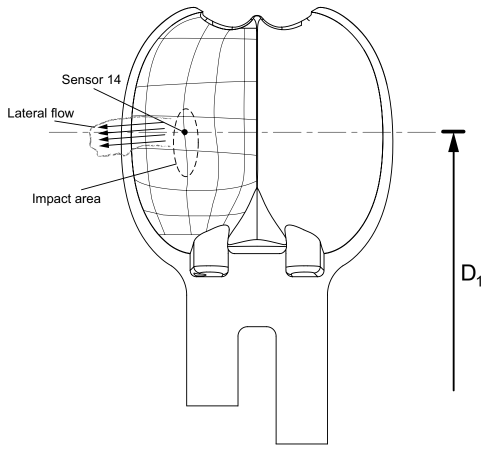

Figure 14.17: Path of the lateral flow.

14.2.5 Time constants

The pressure peak duration, well defined from the measurements, is between 80 and 100 μs, matching well the results obtained by Johnson *et al.* [55]. The time to the lateral flow is more difficult to estimate as the impact area is hidden by the foam during the initial moments of the lateral flow. However, from the film sequence, the time between the impact and the lateral flow can be estimated $\sim 500\ \mu s$, in good accordance with the estimation provided by the analytical model developed by Heritage *et al.* [42]. The lateral flow velocity can be deduced from the images sequence as well. From the observation grid drawn on the bucket surface and the frame rate, the flow velocity is estimated to be around 25 m/s, *i.e.* faster than the jet itself as it leaves the injector nozzle. The presence of the lateral flow confirms the hypothesis of compression waves in the jet front at the moment of impact on the bucket and most probably corresponds to the relaxation of the compression waves.

14.2.6 Peak real amplitude estimation

As aforementioned, the pressure pulse is under-sampled, so it is not trivial to retrieve its real amplitude. From the literature [55], [28], [42], it is known that the amplitude is $O(k\rho a W_1)$. The problem lies within the fact that the mixture density and local speed of sound are unknowns. As described in section 14.1, the cutout acts as a spillway, thus enhancing the jet aeration. The air volume fraction in the jet front can be expected to be significant [17], reducing the local speed of sound to very low values, see Appendix C. Assuming the energy stored in the peak to be partially converted into kinetic energy in the lateral flow, it can be written:

$$P_{pulse} = k_e \frac{1}{2} \rho_m W_{lateral}^2 = K \rho_m a_m W_1, \tag{14.20}$$

where k_e is a constant below unity.

The real impact condition can be retrieved from Appendix C. The procedure is illustrated step-by-step by Fig.14.18. Depending on the value of constant K, the real amplitude may reach up to 2 times the pressure of the equivalent point of stagnation with the runner blocked.

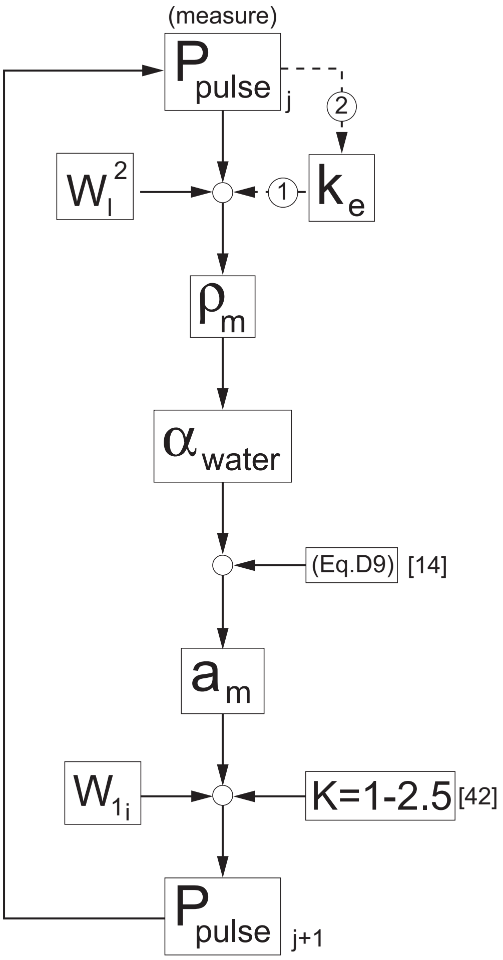
(measure)
P_pulse j
2
W_l^2
1
k_e
ρ_m
α_water
(Eq.D9) [14]
a_m
W_1i
K=1-2.5 [42]
P_pulse j+1

Figure 14.18: Impact peak determination procedure.

Chapter 15

Backside flow

15.1 Observations

As observed in section 13.1, the flow on the backsides of the buckets features 2 remarkable phenomena: (i) the onset of a radial splashing flow that adheres to the ribs, and (ii) the separated portion of the jet that remains attached to bucket j-1 backside far in the duty cycle. Different hypothesis have been formulated to explain the jet attachment. Bachmann [7] simply attributes the fact to the higher velocity of the jet particles that would generate a vacuum capable of sucking the water filaments on the wall.
The wall pressure measurements permits to monitor the pressure distribution evolution during the bucket duty cycle, and to precisely identify the geometric and angular positions where the jet separation occurs. They do actually show a significant depression on the backside area for the complete set of operating conditions measured, see Fig.15.1, 15.2, 15.3 and 15.4. It must be emphasized that sensors 31 and 33 ceased to transmit data during the tests conducted at $60m$ for OP3 ($\psi_1/\psi_1^{\wedge} = 1.12$ and $\varphi_{B_2}/\varphi_{B_2}^{\wedge} = 1.20$), respectively for OP9 ($\psi_1/\psi_1^{\wedge} = 1.12$ and $\varphi_{B_2}/\varphi_{B_2}^{\wedge} = 0.91$).

The backside flow study is to be treated in a similar fashion as the compressibility at the initial tip impact, section 14.1.

15.2 Kinematic problem

Examining the instantaneous velocity triangle at bucket tip location shows that at the beginning of the duty cycle the bucket backside resembles an hydrofoil at angle of attack α. The angle of attack α increases with time and with decreasing radii, *i.e.* α at tip is smaller than at the position D_1. The definition of α is given by:

$$\alpha = \operatorname{arccot}\left(\frac{D_1 - D_2}{\psi_1^{1/2} k_{c_0} - \frac{D_b}{D_1}\sqrt{1 - \left(\frac{D_1 - D_2}{D_b}\right)^2}}\right) - (\omega t_0 + \theta_j) + \rho, \tag{15.1}$$

and is a function of D_2, ψ_1, and θ_j. The variation of α during the first half of bucket j duty cycle is shown in Fig.15.5. The initial value of bucket j angle of attack α spreads on a wide range depending on the value of ψ_1. For normal operating conditions, *i.e.* $\psi_1 = 3.8...4.8$, α corresponds to that of an hydrofoil at high angle of attack ($\alpha \approx 15°$).

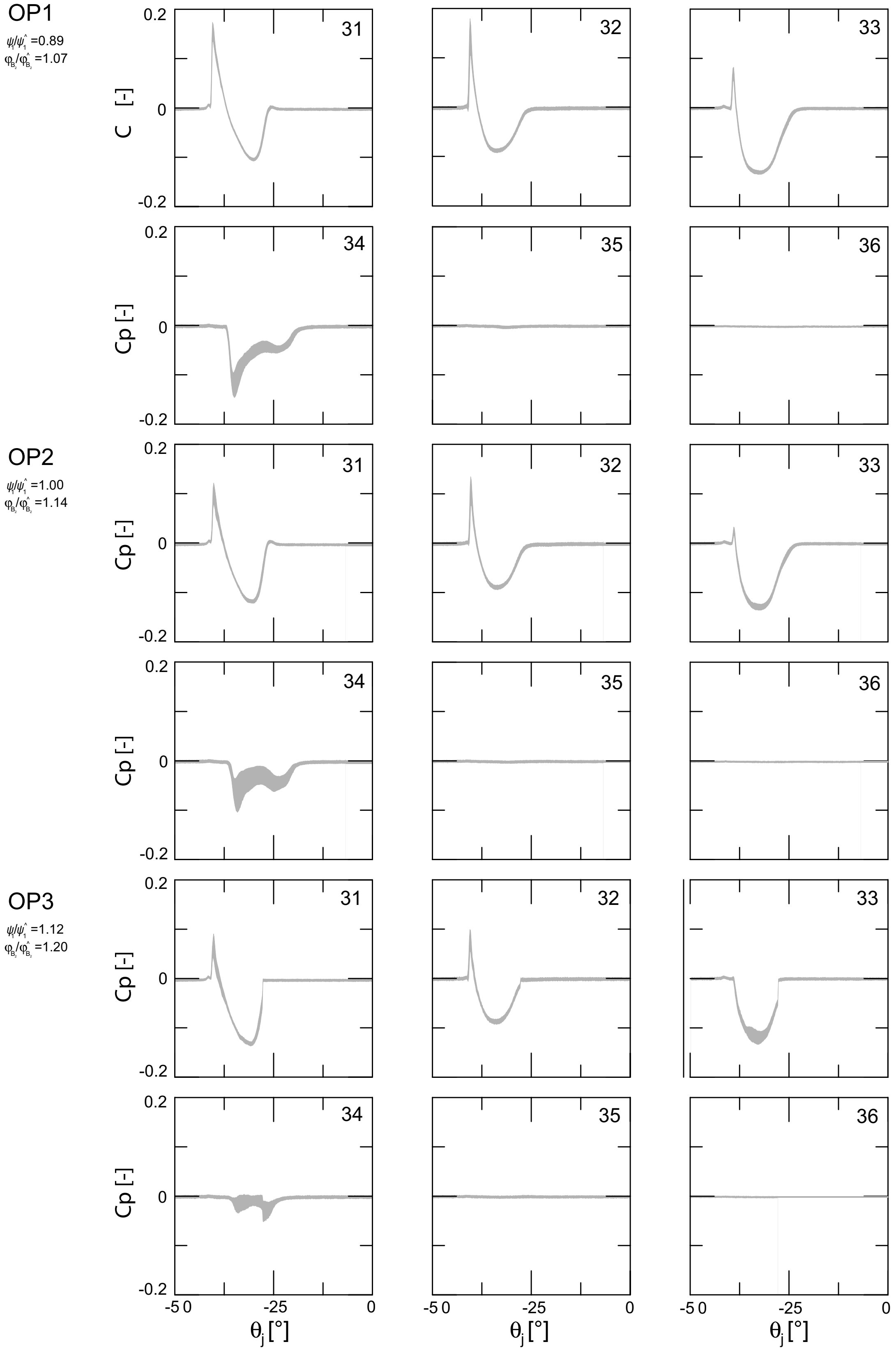

Figure 15.1: Backside pressure signals, $H = 20m$, $s/s^{\wedge} = 1.34$.

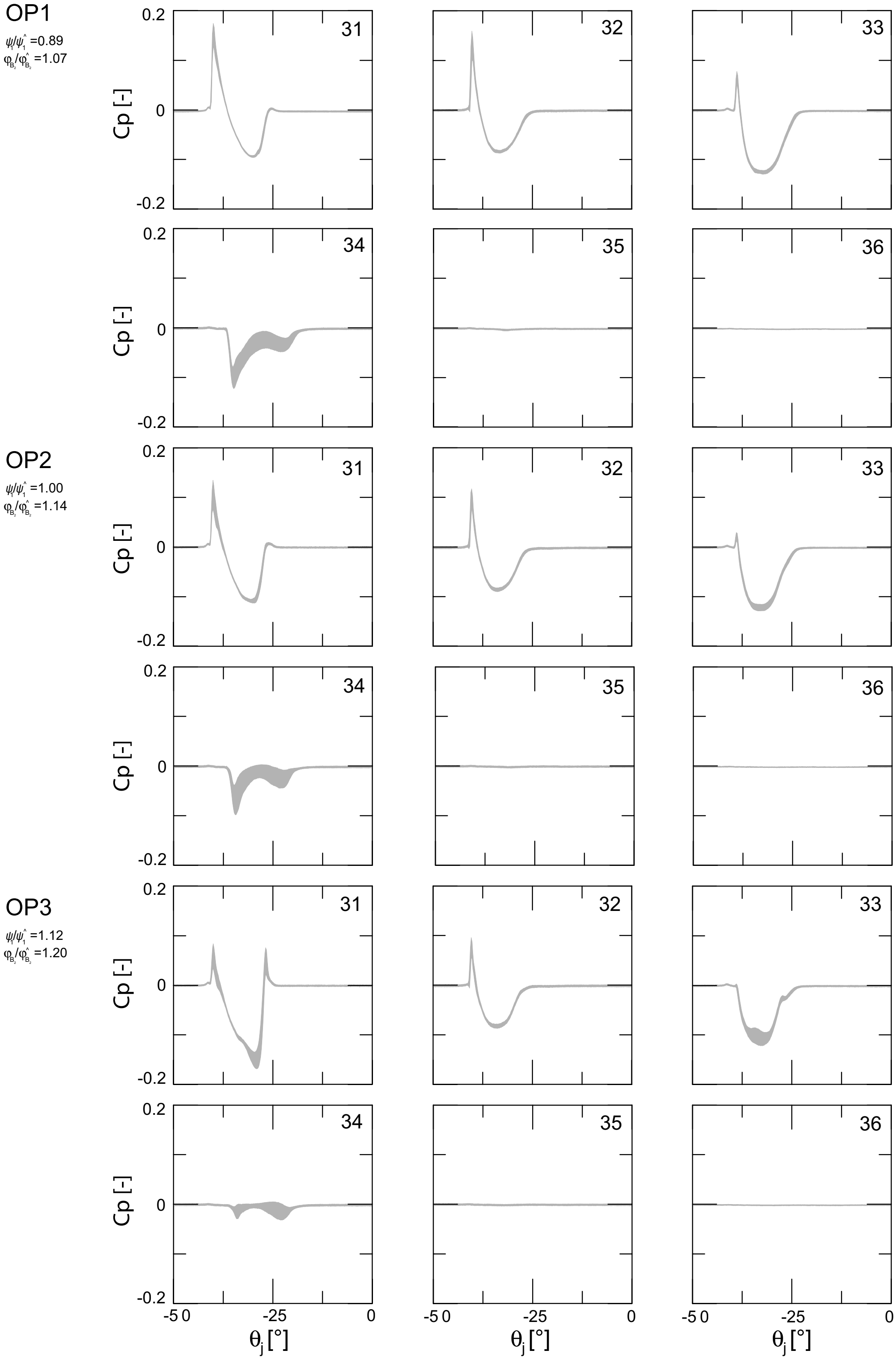

Figure 15.2: Backside pressure signals, $H = 35m$, $s/s^{\wedge} = 1.34$.

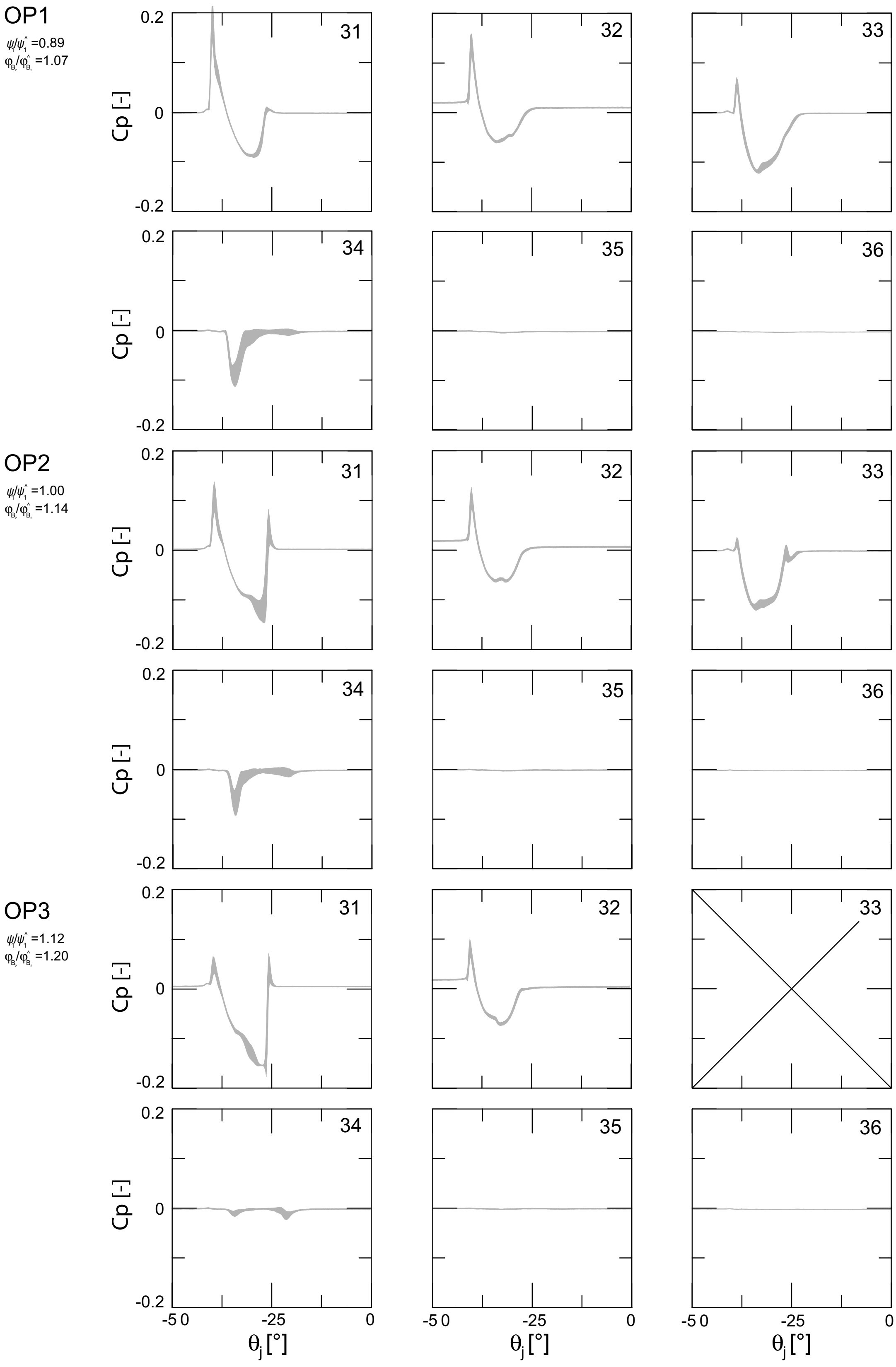

Figure 15.3: Backside pressure signals, $H = 60m$, $s/s^{\wedge} = 1.34$.

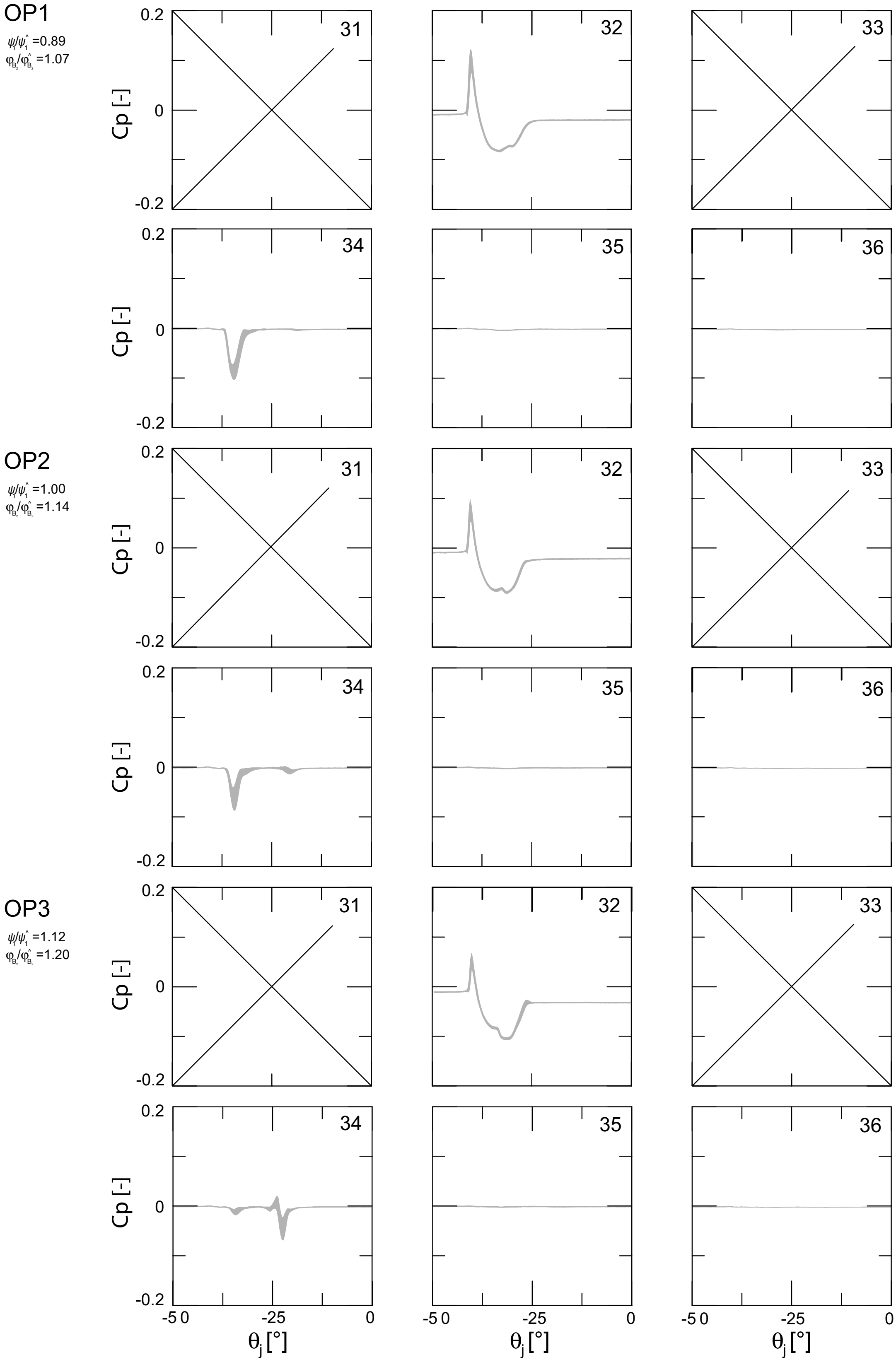

Figure 15.4: Backside pressure signals, $H = 80m$, $s/s^{\wedge} = 1.34$.

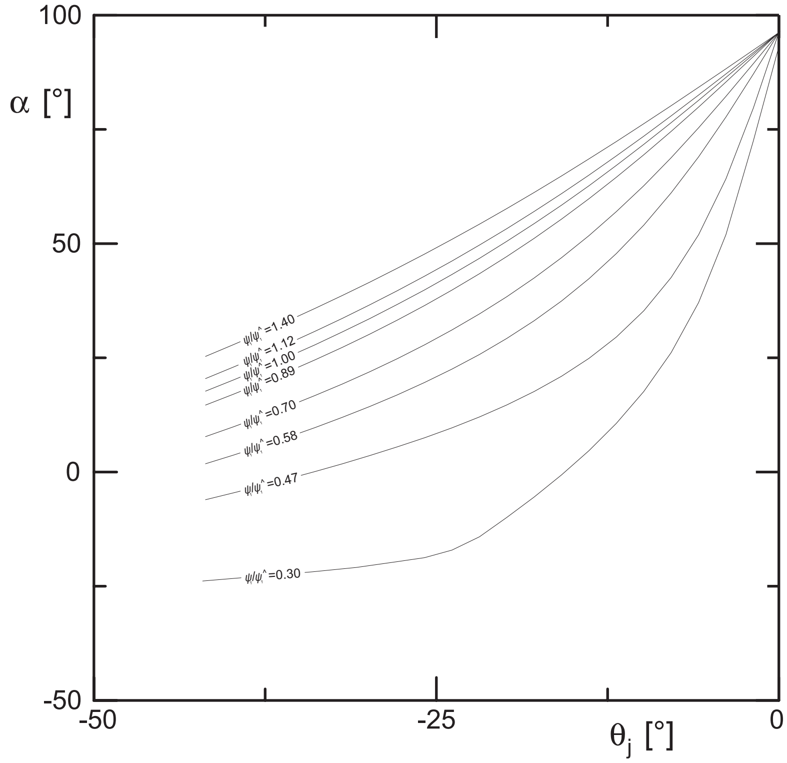

Figure 15.5: Evolution with respect to ψ_1 of bucket j relative angle of attack α along bucket j duty cycle.

15.3 Bucket hydrodynamic chord, BHC

The bucket backside is assumed to be a hydrofoil bounded by D_b and D_1. As a matter of fact, the pressure signals measured by sensors 35 and 36 show that no interaction occurs between the water and the bucket backside beyond D_1. The bucket hydrodynamic chord, referred as BHC, can thus be defined as:

$$BHC = \frac{D_b - D_1}{2}. \tag{15.2}$$

The position of pressure sensor l along the BHC can therefore expressed in terms of %BHC:

$$(BHC)_l = \frac{D_b - D_l}{D_b - D_1} \cdot 100 \quad [\%] \tag{15.3}$$

15.4 Influence of the test head

Figure 15.7, Fig. 15.8, and Fig.15.9 display the pressure distribution for a series of remarkable bucket angular position along bucket j radial plane of symmetry, *i.e.* cut *A-A* on Fig.15.6 for 20, 35, and 60m. The results obtained for 80m are not displayed as the data of sensors 31 and 33 are missing. Whatever the test head, the kinematic

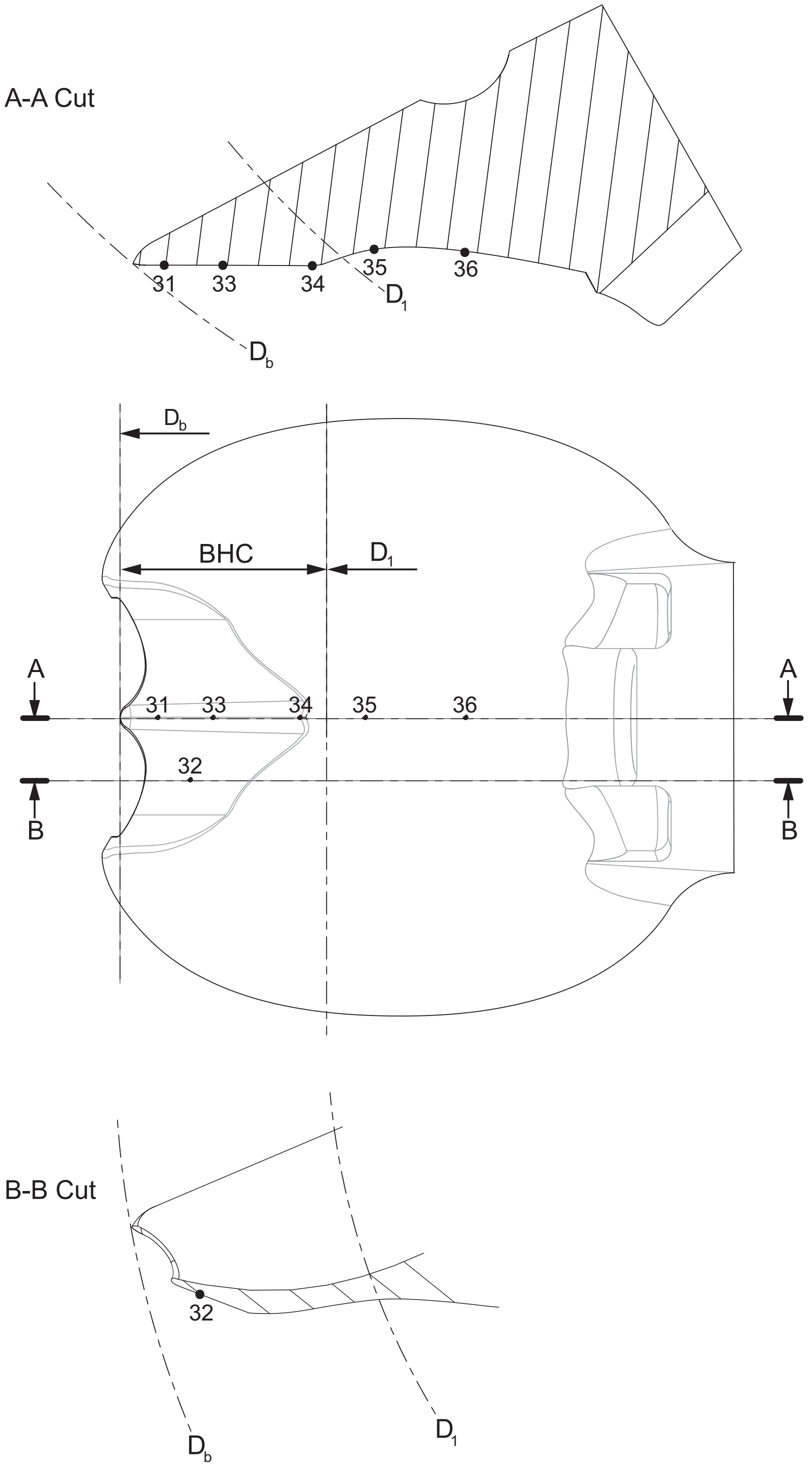
A-A Cut
31
33
34
35
36
D_1
D_b
D_b
BHC
D_1
A
A
31
33
34
35
36
32
B
B
B-B Cut
32
D_b
D_1

Figure 15.6: Definition of the Bucket Hydrodynamic Chord, BHC.

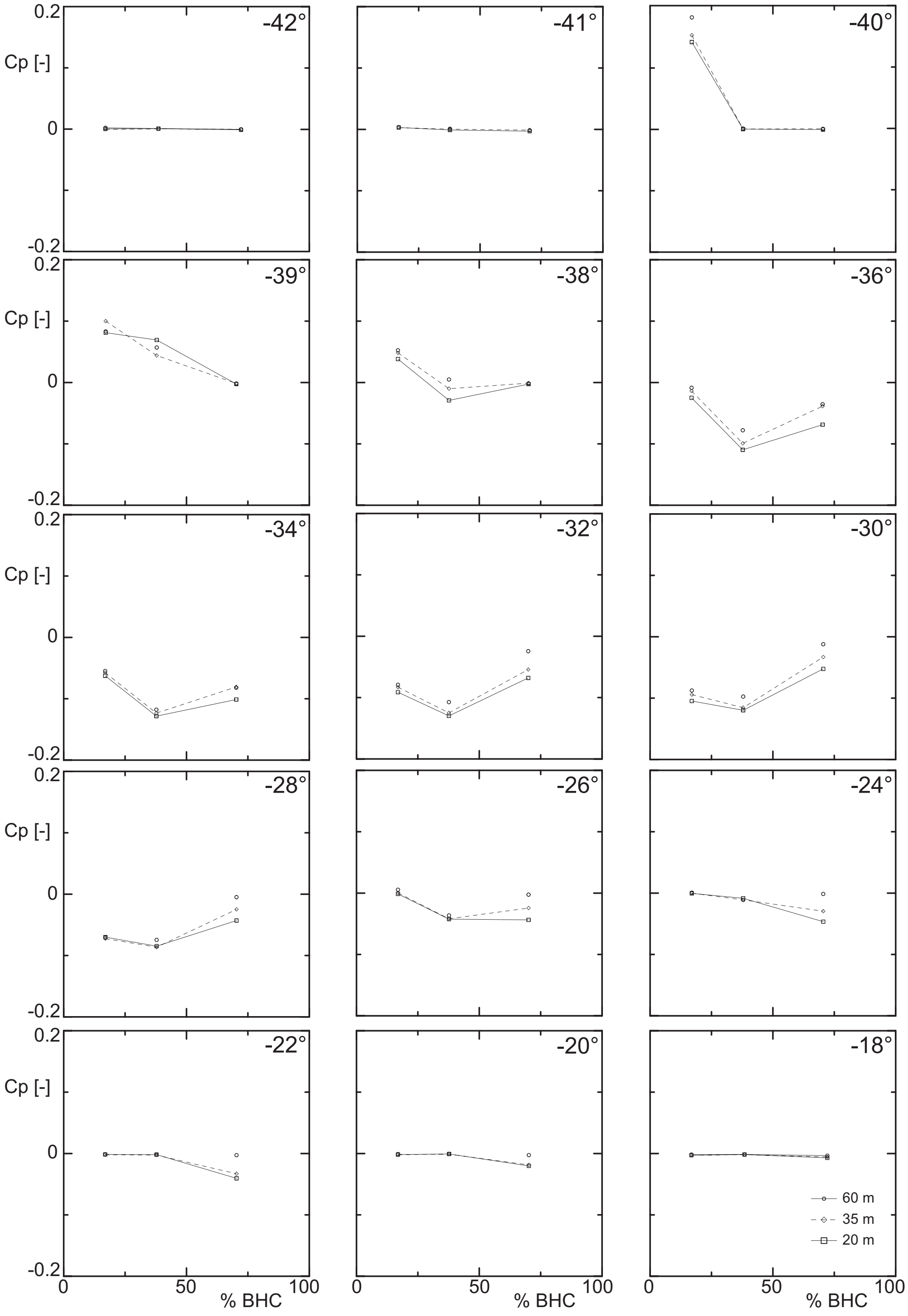

Figure 15.7: BHC pressure distribution, OP1($\psi_1/\psi_1^\wedge = 0.89$ and $\varphi_{B_2}/\varphi_{B_2}^\wedge = 1.07$).

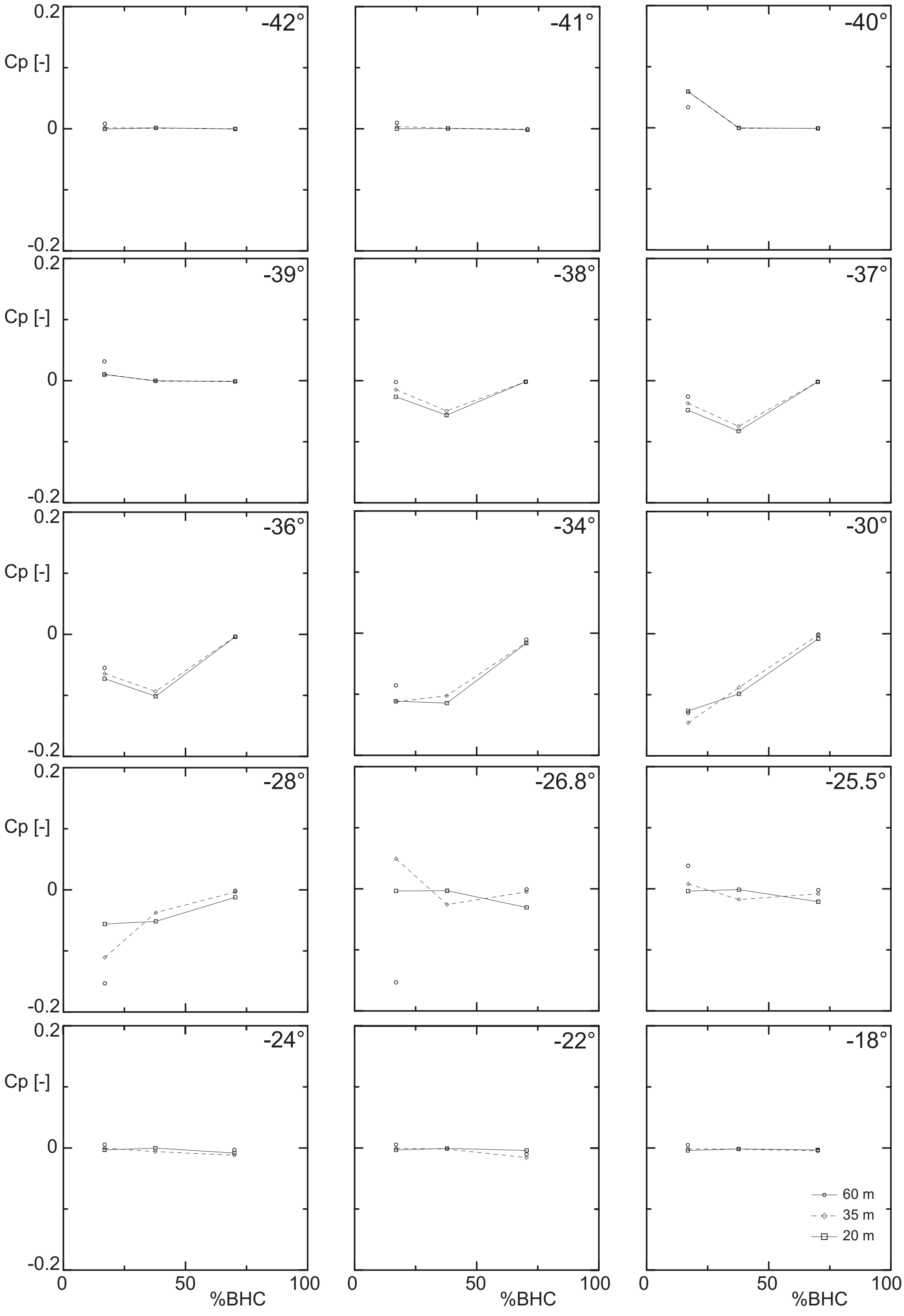

Figure 15.8: BHC pressure distribution, OP3($\psi_1/\psi_1^\wedge = 1.12$ and $\varphi_{B_2}/\varphi_{B_2}^\wedge = 1.20$).

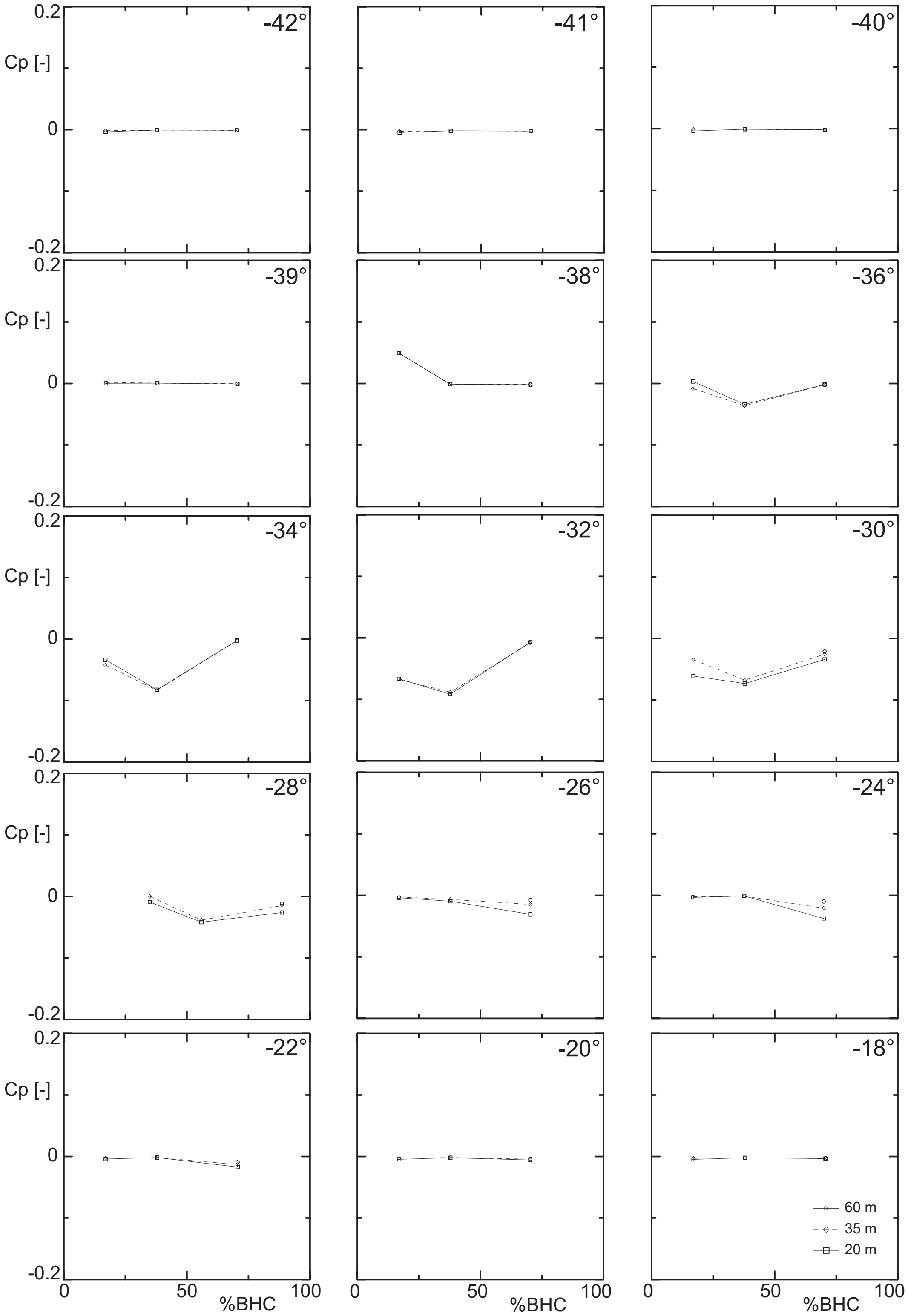

Figure 15.9: BHC pressure distribution, OP14($\psi_1/\psi_1^{\wedge} = 1.00$ and $\varphi_{B_2}/\varphi_{B_2}^{\wedge} = 0.54$)

similitude is assured by the same φ_{B_2}-ψ_1 condition, *i.e.* the velocity triangles at any location of the jet or runner are similar.

- Signal rise. The increase of pressure recorded at the beginning of the cycle occurs at the same angular position for the 3 heads, witnessing the kinematic similitude. The pressure increase is due to the passage of the front of the flow on the sensor. The water particles velocity in adjacent streamlines in the boundary layer is decreasing closer to the bucket surface, causing the shear forces to bend the fluid in the direction of the slower moving particles [99]. This in turn generates the apparition of successive stagnation points as the jet front is moving, see Fig.15.10.

- Depression build-up. After the initial pressure rise, the pressure coefficient values drop below ambient pressure. The depression continues to grow until $\theta_j = -32°$. The lower the test head, the lower the pressure coefficient. The jet is completely separated from the injector, *i.e.* bucket j tip skews the jet lower generator at $\theta_j \sim 30°$. The pressure distribution shows that sensor 34 has already regained the ambient pressure at $60m$ whereas it still exhibits a significant depression for the lower test heads. This tendency becomes more and more marked later in the cycle: if the complete jet separation occurs at $\theta_j = 25°$ for OP1 at $60m$, it only does 7° later for the 20 and $35m$ test heads and for positions of smaller radii. The same tendency appears for OP3 and OP13, even if the comparison is made more difficult by the loss of sensor 33.

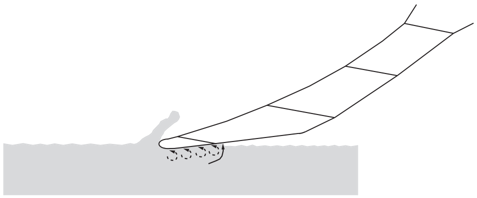

Figure 15.10: Successive stagnation points at jet front.

15.5 Effect of ventilation

An hypothesis is that the lower than atmospheric pressure in the volume between adjacent buckets would be sufficient to trigger the attachment of the upper jet generator filament. This explanation, however, suffers 2 shortcomings: (i) the rotation-induced pressure variation is extremely low, and for the sensors located in the region of jet attachment, positive for the lower test heads, see Fig.15.11; (ii) the centrifugal forces are several orders of magnitude higher.

15.6 Coanda effect

The backside area of the bucket acts as the suction side of a hydrofoil at high angle of attack under Coanda effect, see Appendix D. The flow that follows the bucket backside

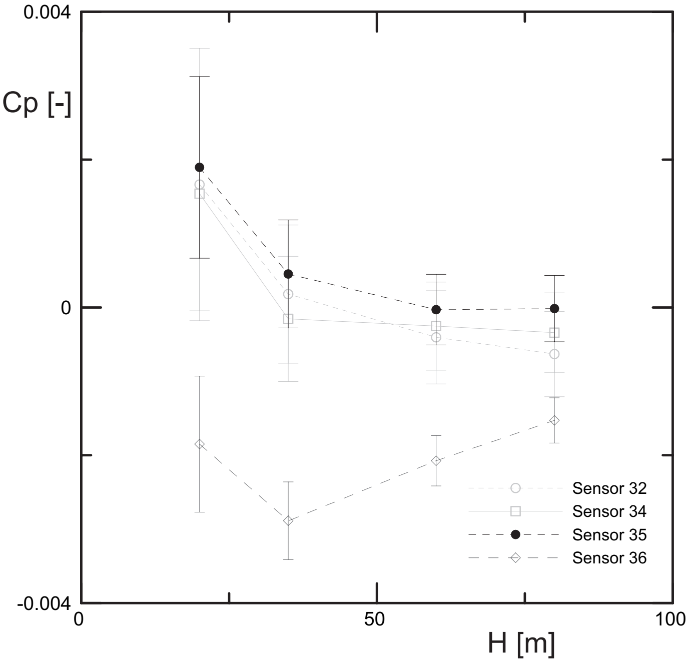

Figure 15.11: Rotation-induced pressure variation on the bucket backside.

wall curvature generates a pressure gradient across the boundary layer that is sufficient to suck the flow back towards the bucket surface, Fig.15.12(a). The same effect arises on the lateral ribs, Fig.15.12(b). The lateral effect is more intense than the longitudinal one, since the velocity involved is smaller and the curvature radii smaller. As the runner is rotating the angle of attack increases to values beyond the stall values of a normal hydrofoil ($\alpha \sim 15°$). Due to the Coanda effects, the angles of attack rise up to more 40° without separation, consistent with the experiences made by von Glahn [114] and Teodorescu [105]. This explanation is consistent with the jet disintegration process observed from

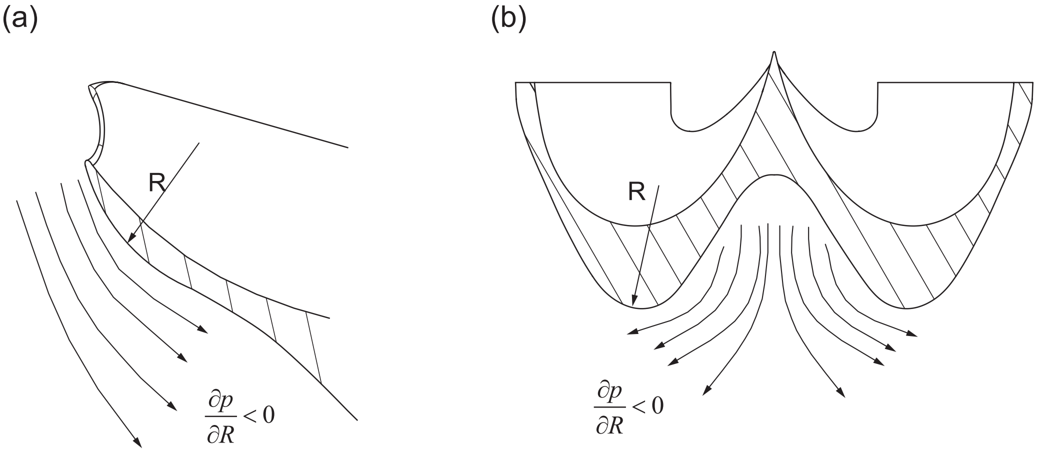
(a)
(b)
R
R
$\frac{\partial p}{\partial R} < 0$
$\frac{\partial p}{\partial R} < 0$

Figure 15.12: Coanda effect on the bucket backside. (a) Longitudinal effect; (b) transversal effect.

the onboard borescope, see Fig.15.12(b). The surface-tension and capillary forces become stronger relatively to the inertia forces for the higher angles of attack and the lower test heads. This would explain why the separation occurs later for the lower heads than it does for the higher ones. The separation of the liquid from the wall is the result of an instability of the air-liquid interface. Waves appear, with their fronts in the direction of the flow. Their amplitude may grow quickly and the film breaks up into separate jets and finally into separated water threads [120]. The jet disintegration and separation can therefore probably be predicted by looking at the respective evolution of Reynolds and Weber numbers.

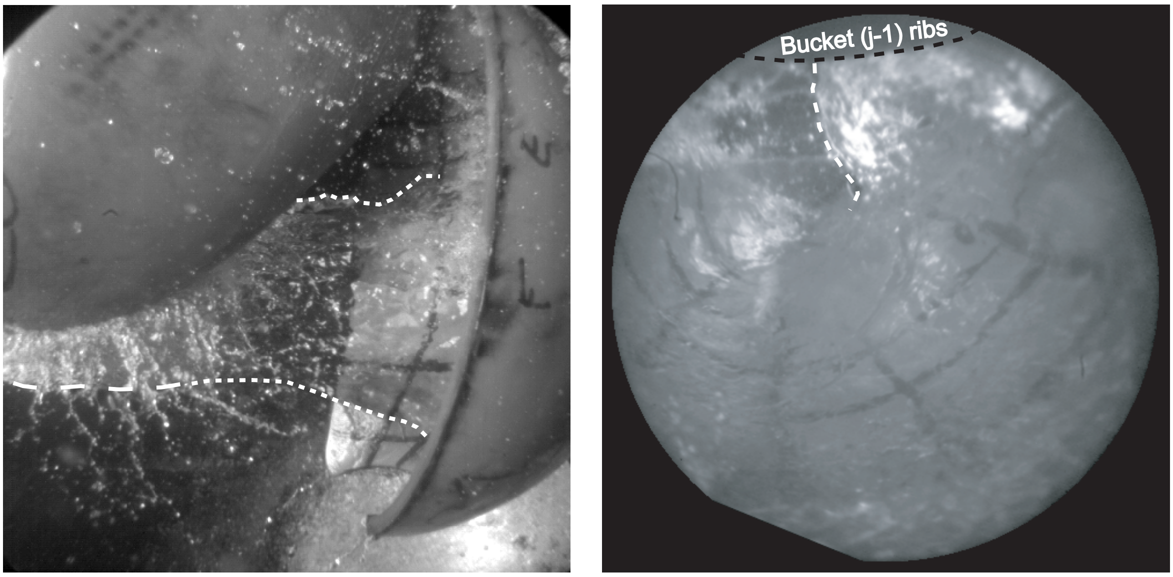

(a) Jet longitudinal deviation, $\theta_j = -34°$. (b) Jet lateral deviation, $\theta_j = -30°$.

Figure 15.13: Coanda effect observed, $OP1(\psi_1/\psi_1^{\wedge} = 0.89$ and $\varphi_{B_2}/\varphi_{B_2}^{\wedge} = 1.07)$.

15.7 Cavitation

Sensors 31 and 33 signals show a pressure bounce for the higher ψ_1 range with an amplitude increasing together with the test head, see Fig.15.1 to Fig.15.4. The signal shapes, with the depression followed by a steep rise resembles the signal recorded along hydrofoils under cavitating conditions. This would imply that the depression on the bucket backside leads to the onset of cavitation bubbles, and that the pressure bounce corresponds to the collapse of these bubbles. For test heads larger than $60m$, the pressure amplitudes exceed the resistance of the sensors, *i.e.* $15bar$, as proved by the destruction of sensors 31 and 33.

The theoretical cavitation inception condition is given by:

$$Cp < \sigma_i = \frac{p_v - p_{ref}}{\rho g H}. \tag{15.4}$$

As shown by table 15.1, this condition is not fulfilled even if the values of Cp are getting closer to σ_i for the higher test heads. Nevertheless, as stated by Brennen [14], the presence

Table 15.1: Minimum pressure coefficient recorded vs. theoretical cavitation inception condition, sensor 31.

H $[m]$	$\sigma_i(22°C)$ $[-]$	$\overline{Cp}$ $[-]$	Cp_{min} $[-]$	*Rebounce* ...
20	-0.485	-0.133	-0.144	*No*
35	-0.277	-0.150	-0.192	*Yes*
60	-0.161	-0.154	-0.158	*Yes*
80	-0.121	$-$	$-$	$-$

of germs in the flow yields to significantly higher values of σ_i. The air content of the water jet is significant, as discussed in Appendix C, explaining why cavitation occurs before the theoretical criteria σ_i is actually reached.

15.7.1 Erosion damages

To fully assess the hypothesis aforementioned, a microscopic survey of the bucket backside is performed. Most of the buckets present small pits in the backside region, see Fig.15.14. 2 different types of damages can be identified: (i) Flaws in the resin matrix, see photographs (a), (c), (e), and (f). Small pockets of air are trapped within the resin matrix during the manufacturing process. The cavitation impacts shatter the thin layer of resin that covers the air pockets that are closest to the surface, revealing the flaws. The presence of cracks, and the irregular shape of the boundaries attests the erosion-induced origin. (ii) Fragile break of the resin, see photographs (b) and (d). The cavitation impacts shatter the resin surface and rip out small volumes of material. The cracks that surround the impacts and their irregular shape are characteristic of fragile rupture [85].

15.8 Consequences on performances

The presence of the depression and the induced jet attachment have positive and detrimental effects on the efficiency of the bucket.

15.8.1 Backside torque

The Coanda effect leads to the creation of a lift force, and from that an angular Momentum in the sense of rotation, contributing to the runner torque [120], [105]. The torque generated can be estimated from the pressure distribution along the BHC, making the following assumptions: (i) The jet surface remains constant during the cut; (ii) the pressure amplitude decays laterally from the centerline at a rate than can be modelled by an analytical test function; (iii) bucket j center of pressure, BCP, is located at 50% BHC and does not move aft with increasing angles of attack.
Bucket j backside torque generated by the Coanda lift force is therefore expressed as:

$$\overrightarrow{T} = \overrightarrow{r_{BCP}} \times \int\int_S p(x) \cdot (1 - z^{\lambda})\, d\overrightarrow{S} \cdot \sin\left(\frac{\delta_{ribs}}{2}\right) \tag{15.5}$$

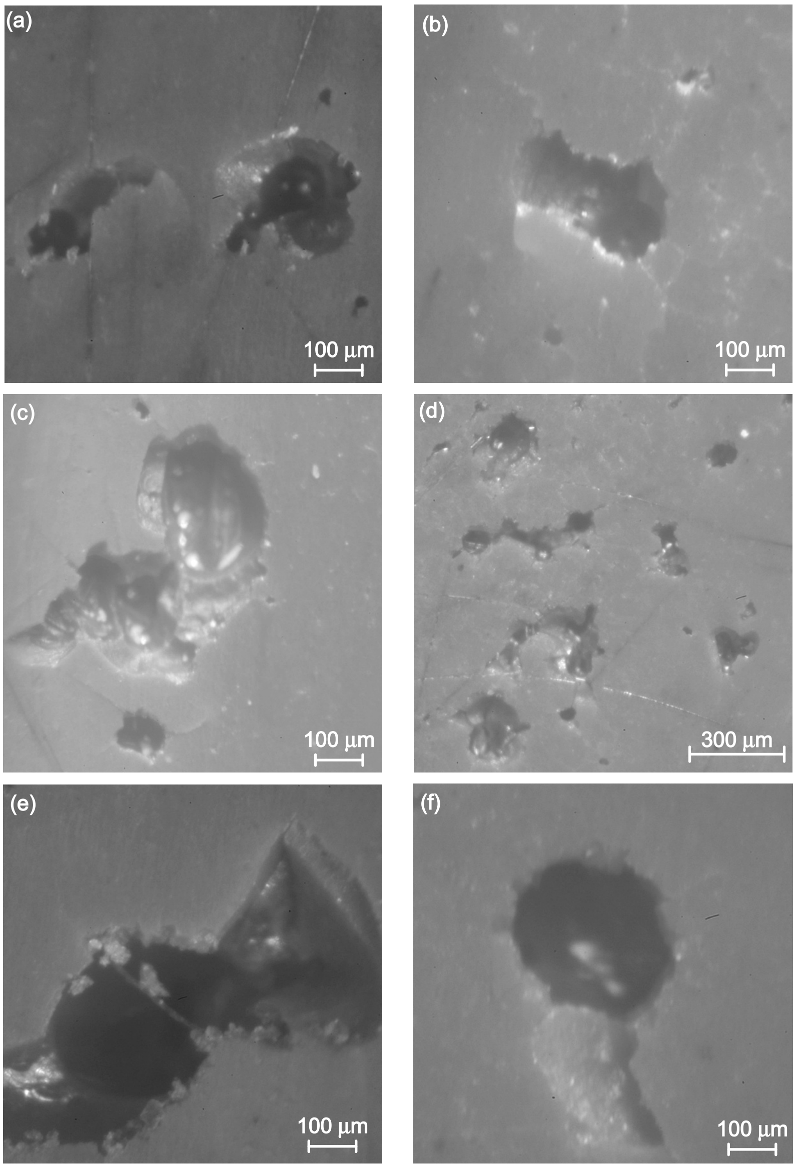

Figure 15.14: Erosion pits observed on the resin buckets.

where λ is the pressure amplitude lateral decay constant, and δ_{ribs} represents the angle formed by the bucket ribs, see Fig.15.15. The lateral decay constant λ is determined by making the assumption that the jet energy radially decrease in the same manner as the dynamic pressure measured in a Pitot tube experience [65]. The results obtained for OP1 for the 3 test heads are displayed by Fig.15.16. The relative amplitude of the counter-torque at the beginning of the duty cycle is equivalent for all the test heads. The positive torque contribution, however, appears to be higher for the lower test heads, as stated for the pressure distribution.

15.8.2 Jet deviation

Nevertheless, there are 2 aftermaths on the runner performance due to the jet deviation: (i) the cut portion of the jet impinges in bucket $j+1$ far from the intended region, *i.e.*

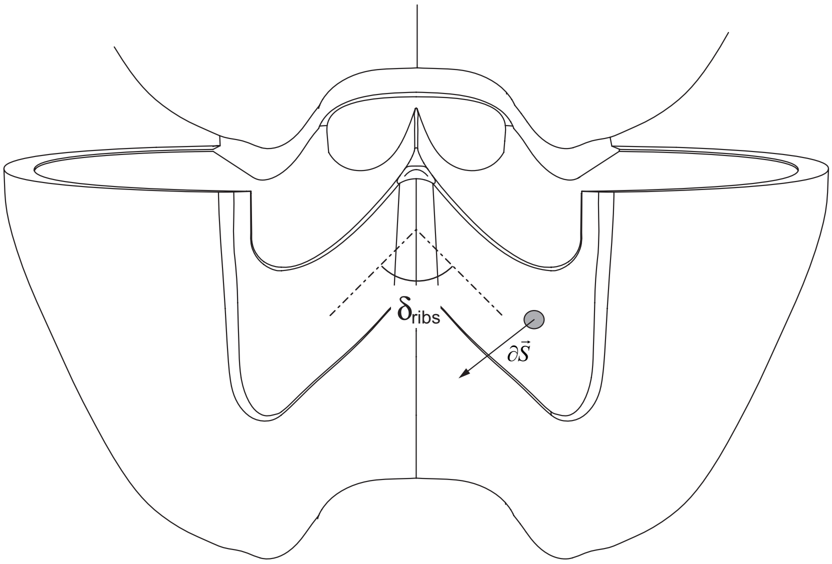

Figure 15.15: Bucket ribs angle δ_{ribs}.

nearer to the root, where the radius of action is smaller; (ii) the ribs make the jet larger, and thus the jet does not impinge on the splitter anymore, but rather in the bottom region of the bucket, generating a large level of mixing losses, see section 16.2.

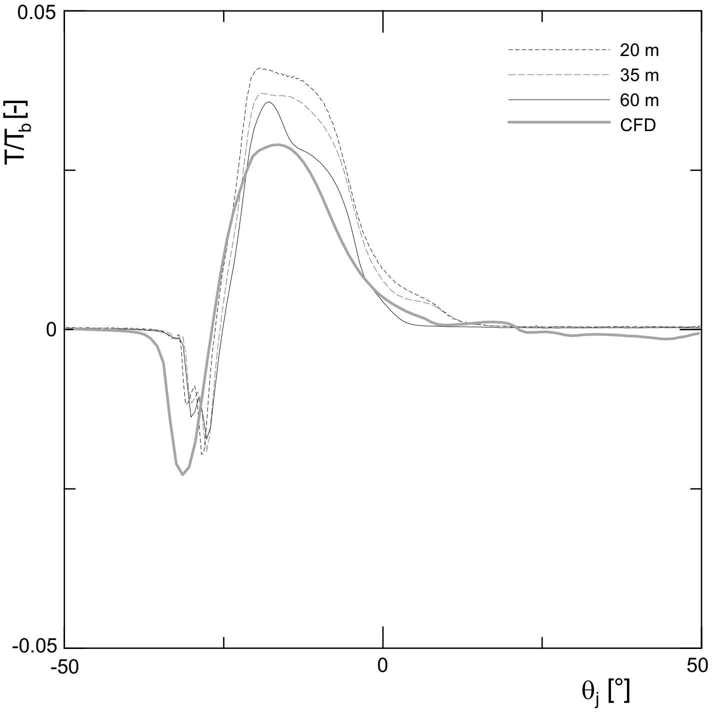

Figure 15.16: Experimental backside torque.

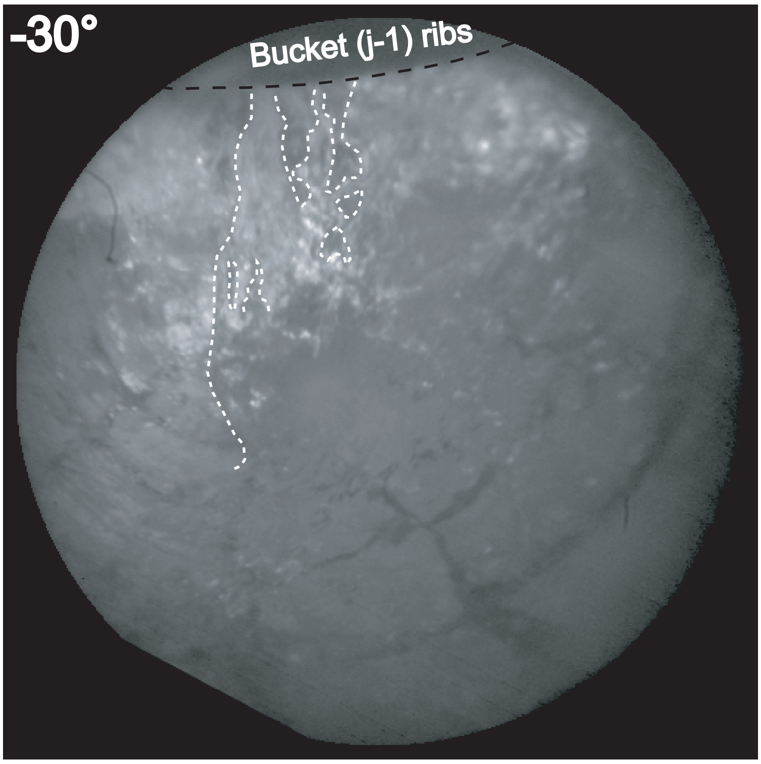

Figure 15.17: Fragmented jet impingement on the bottom surface of the bucket.

Chapter 16

Bucket Flow

16.1 Pressure and water film thickness signals

The discussion to follow refers to Fig.16.2, Fig.16.3, Fig.16.4, and Fig.16.5 for the wall pressure, and to Fig.16.6, Fig.16.7 and Fig.16.8 for the water film thickness. The 5 bucket zones [87], referred as zone 1 to 5, are defined as shown by Fig.16.1.

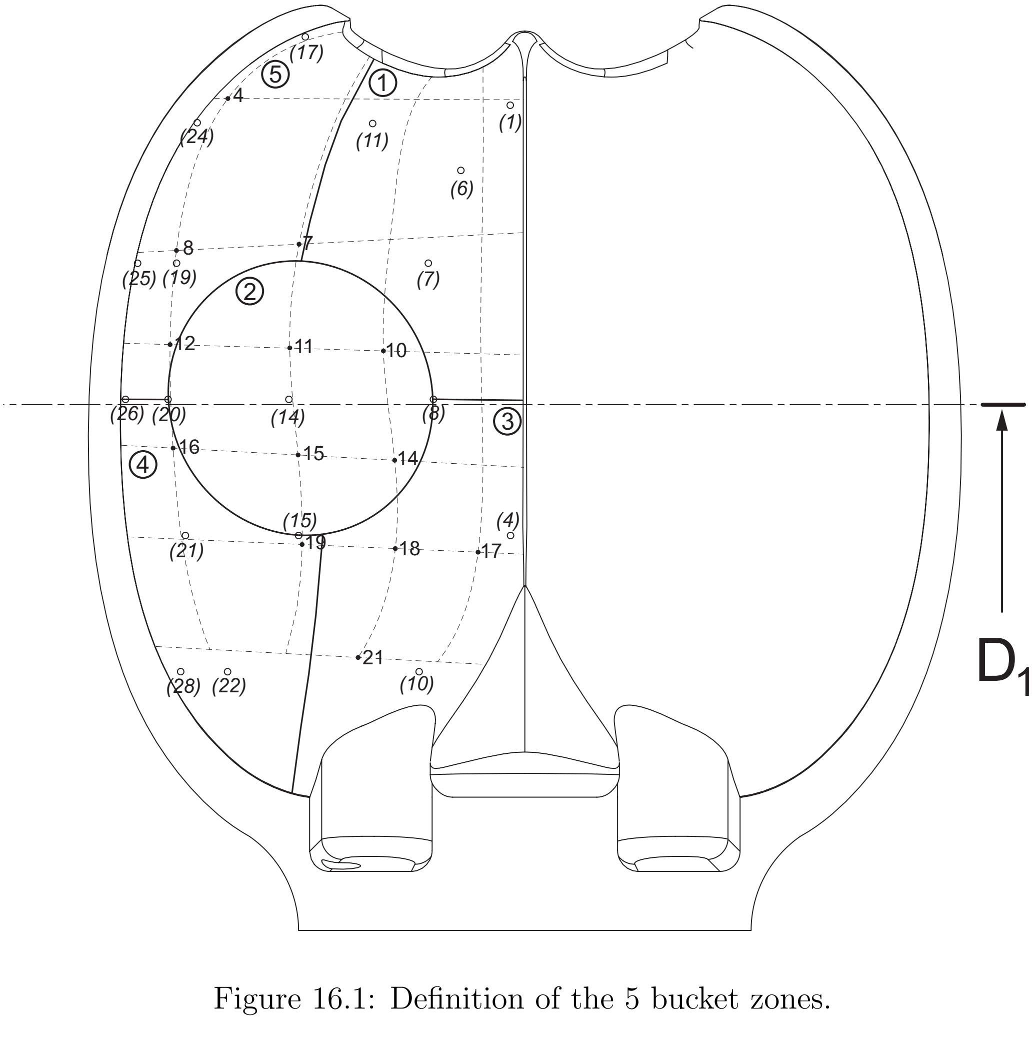
(17)
⑤
①
4
(1)
(24)
(11)
(6)
8
7
(25)
(19)
(7)
②
12
11
10
(26)
(20)
(14)
(8)
③
16
15
14
④
(15)
(4)
19
(21)
18
17
21
(28)
(22)
(10)
D_1

Figure 16.1: Definition of the 5 bucket zones.

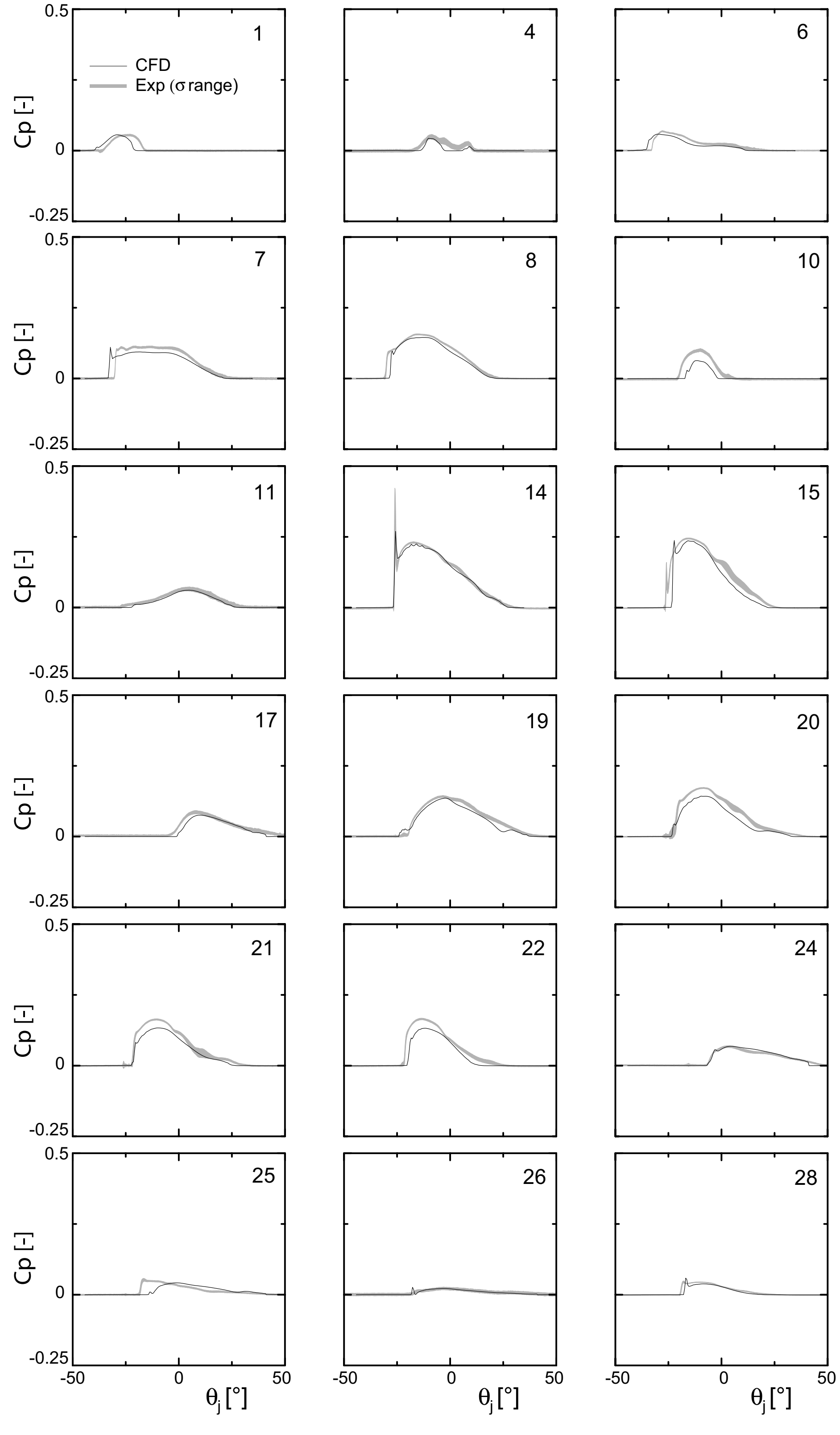

Figure 16.2: Pressure signals, OP1($\psi_1/\psi_1^\wedge = 0.89$, $\varphi_{B_2}/\varphi_{B_2}^\wedge = 1.07$).

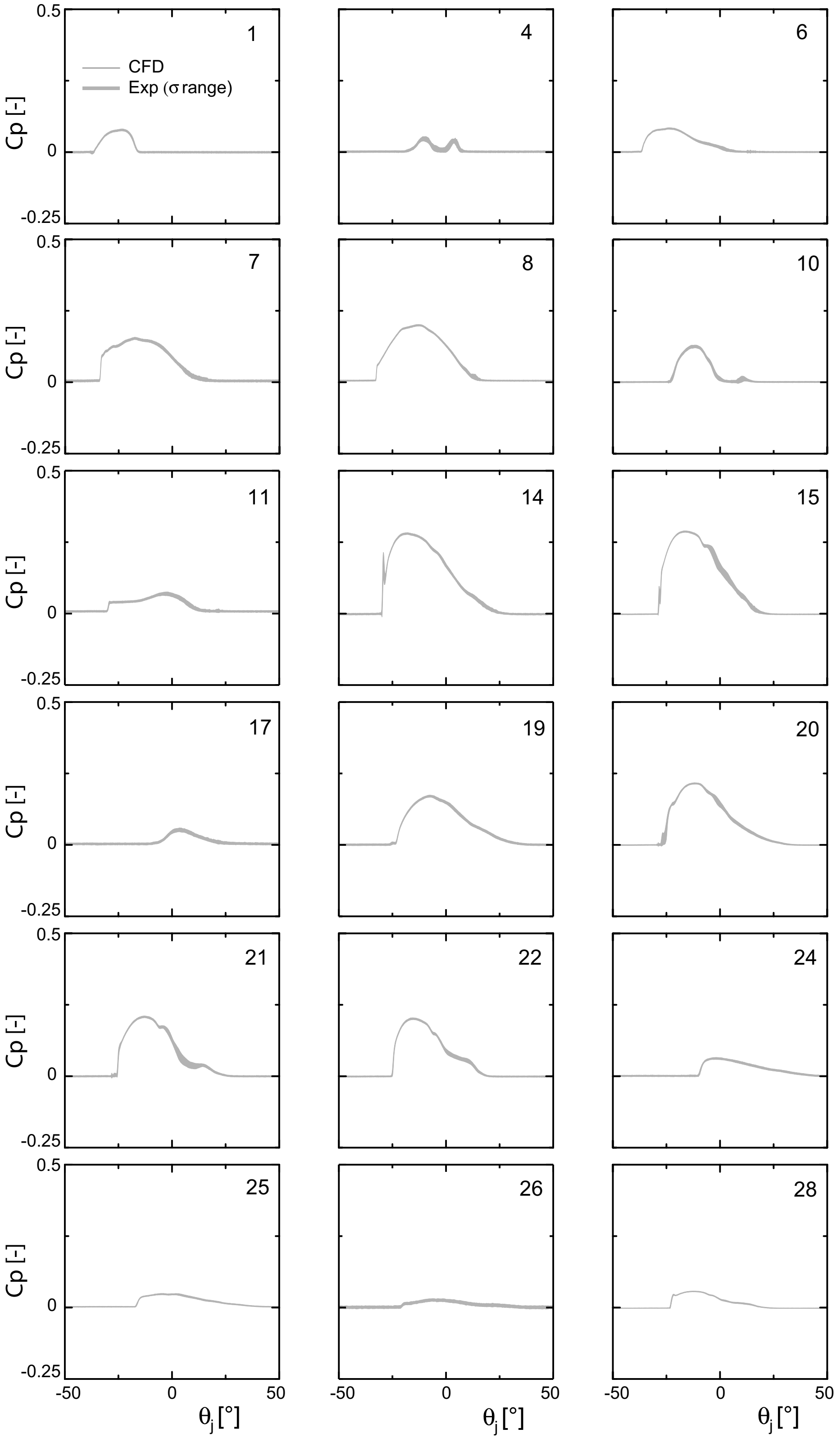

Figure 16.3: Pressure signals, OP3($\psi_1/\psi_1^\wedge = 1.07$, $\varphi_{B_2}/\varphi_{B_2}^\wedge = 1.20$).

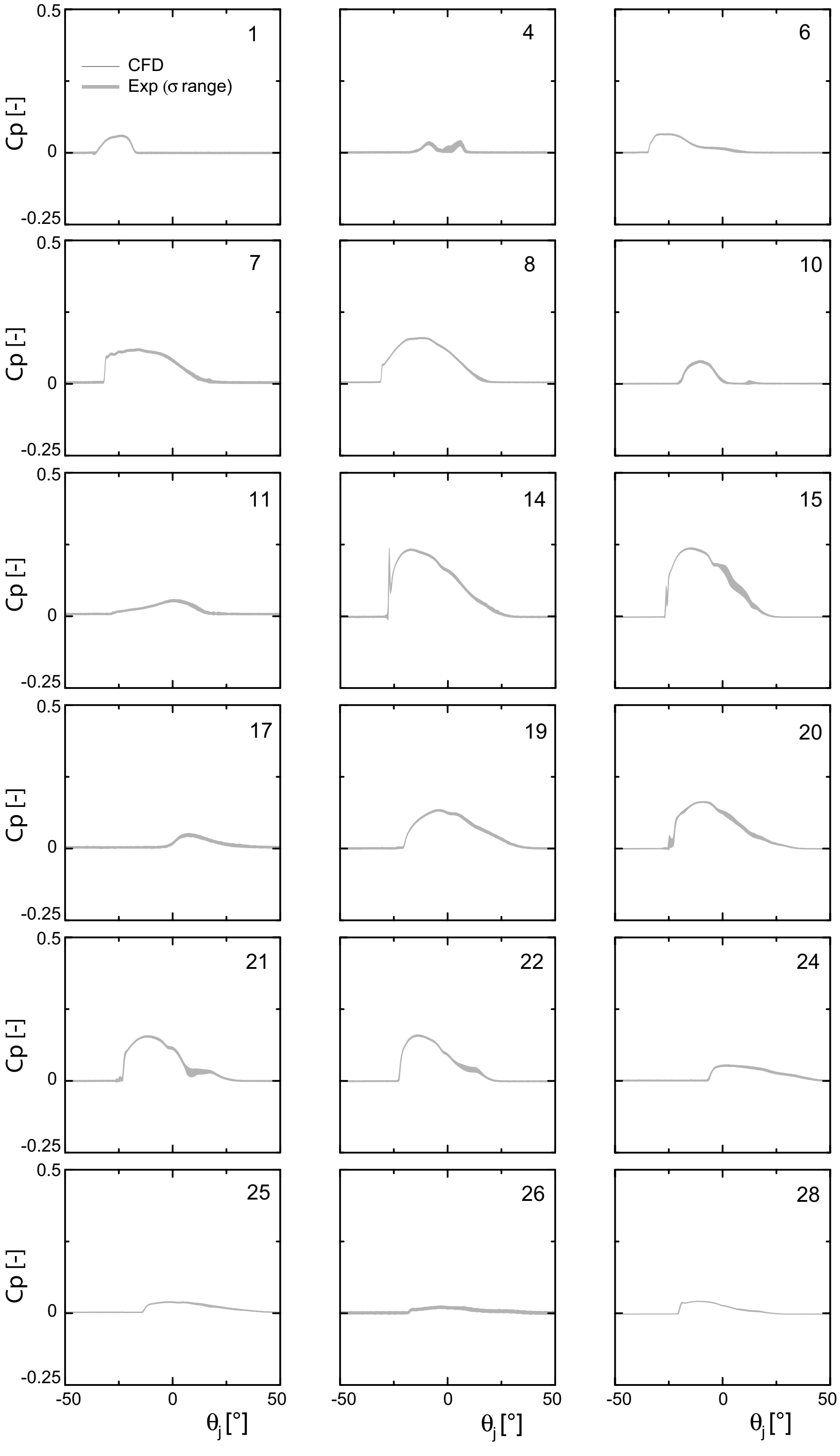

Figure 16.4: Pressure signals, OP5($\psi_1/\psi_1^\wedge = 1.00$, $\varphi_{B_2}/\varphi_{B_2}^\wedge = 0.95$).

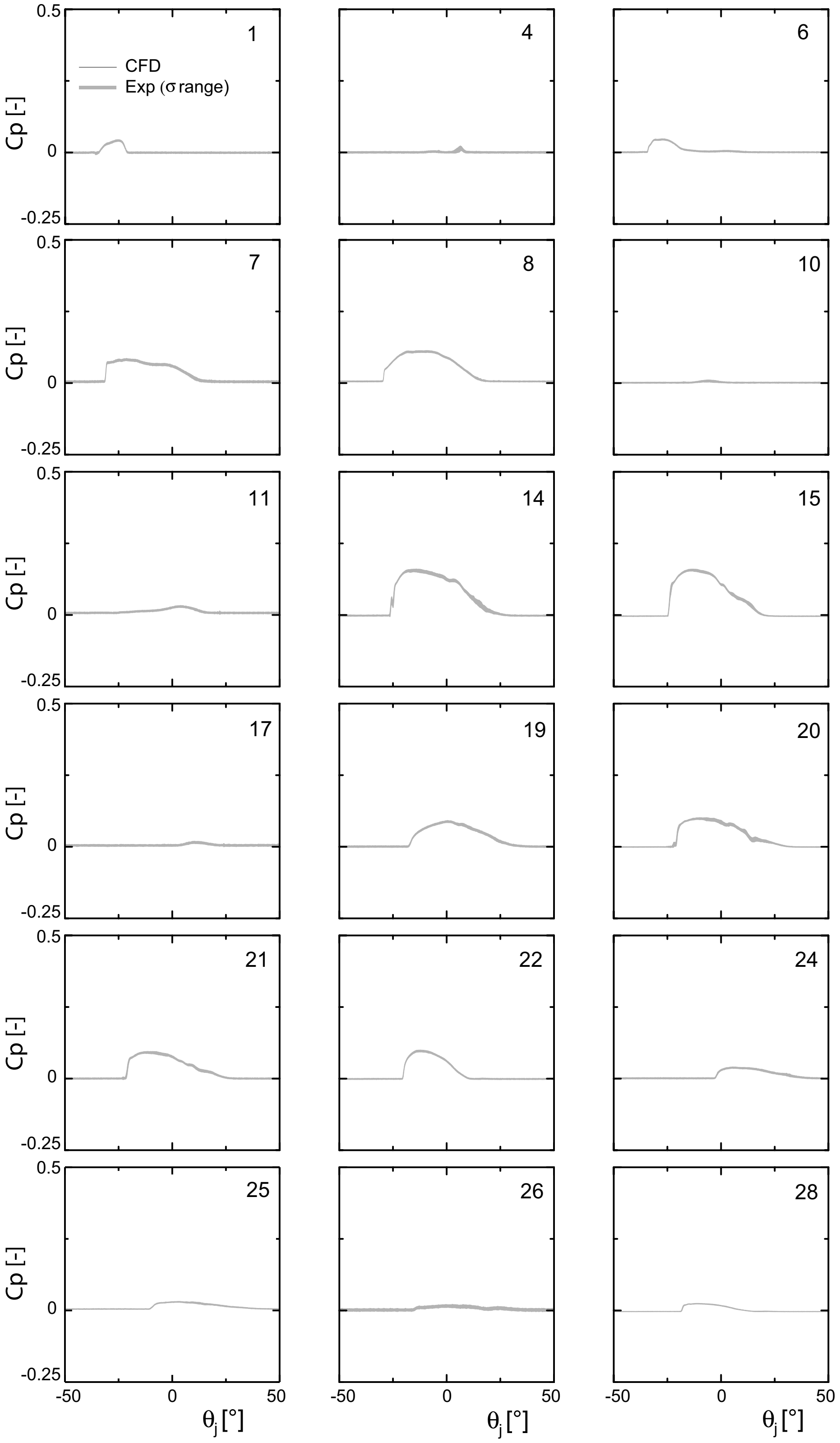

Figure 16.5: Pressure signals, OP14($\psi_1/\psi_1^\wedge = 1.000$, $\varphi_{B_2}/\varphi_{B_2}^\wedge = 0.54$).

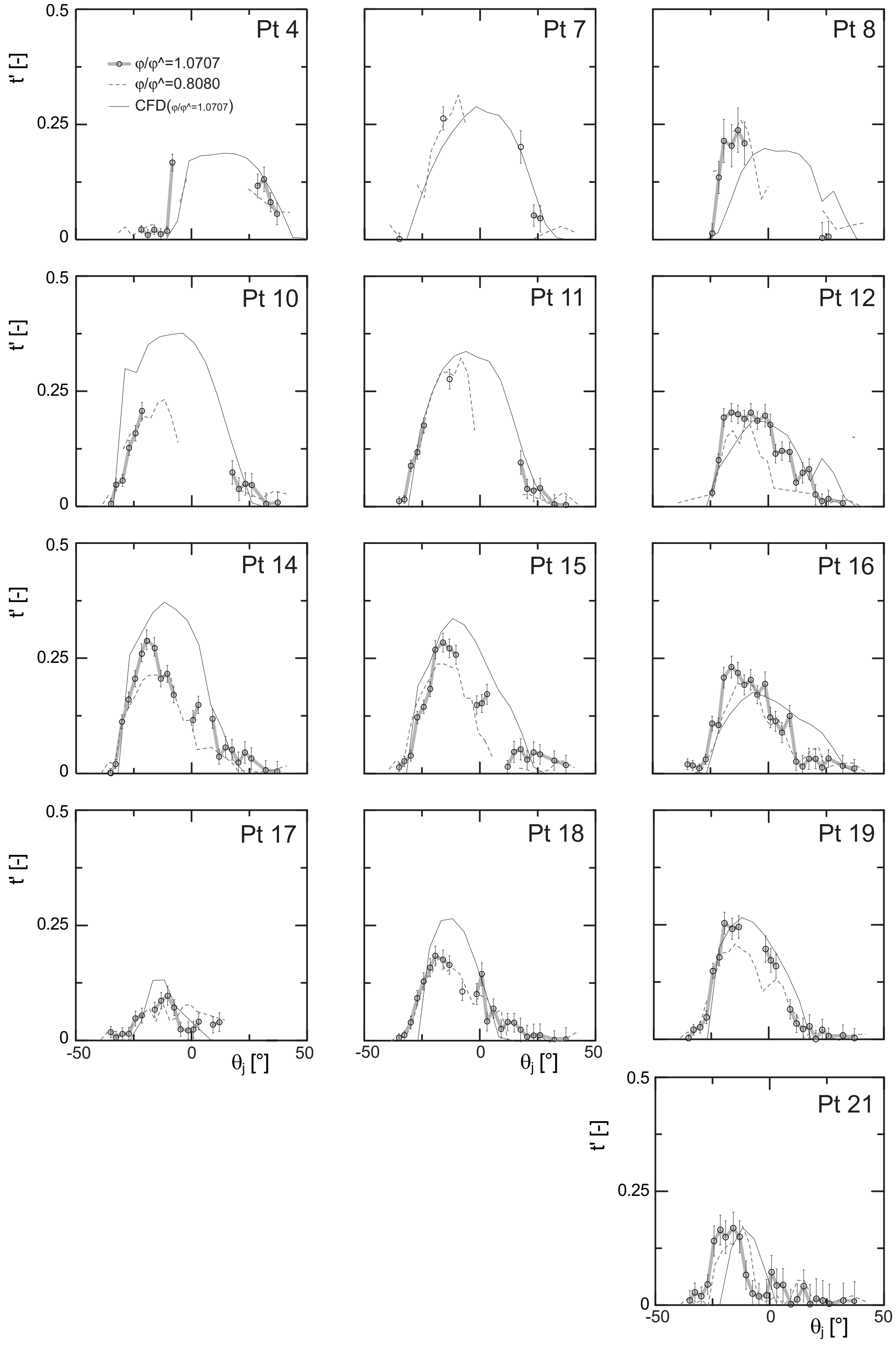

Figure 16.6: Water film thickness signal, $\psi_1/\psi_1^\wedge = 0.89$.

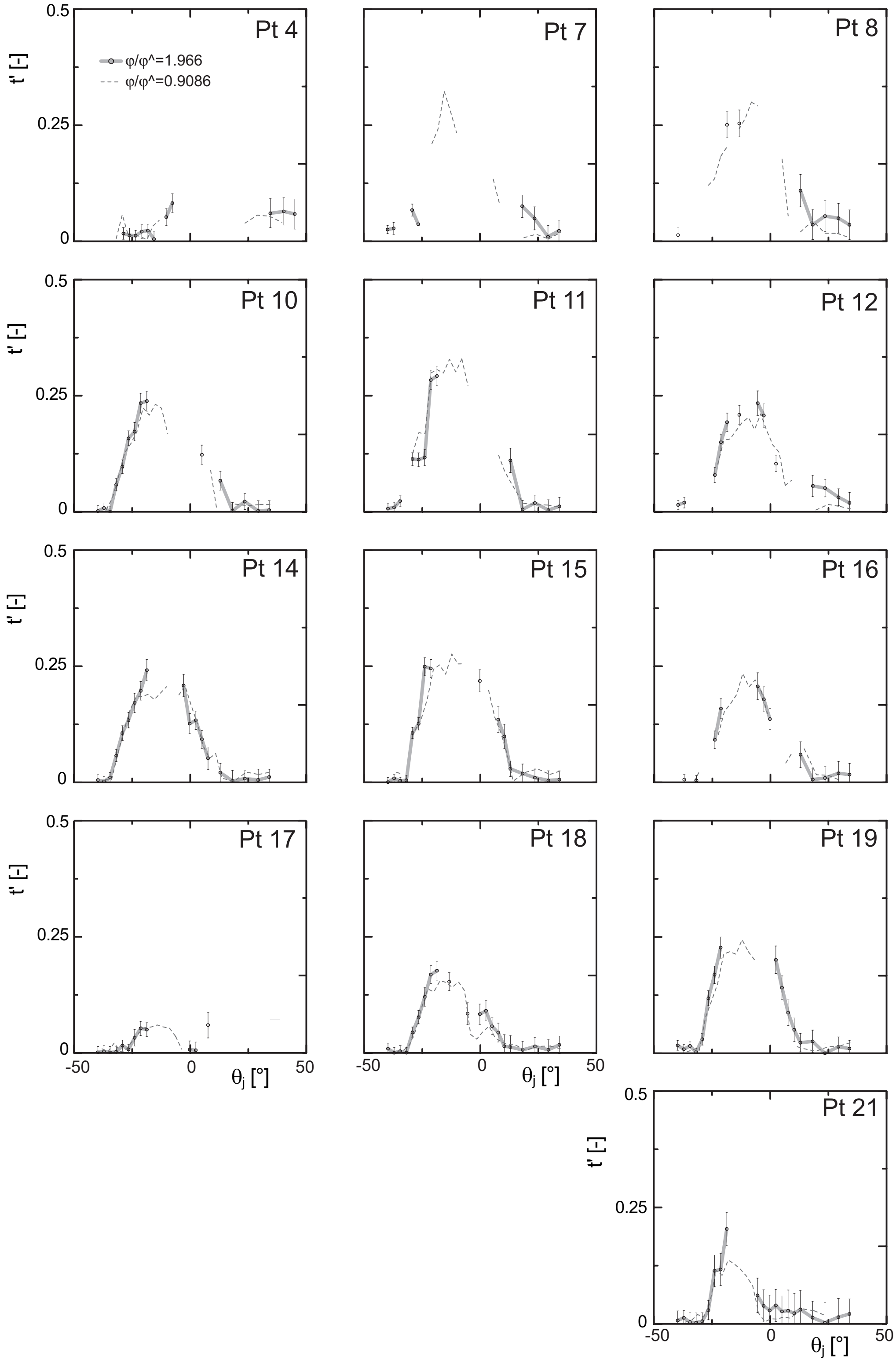

Figure 16.7: Water film thickness signal, $\psi_1/\psi_1^\wedge = 1.12$.

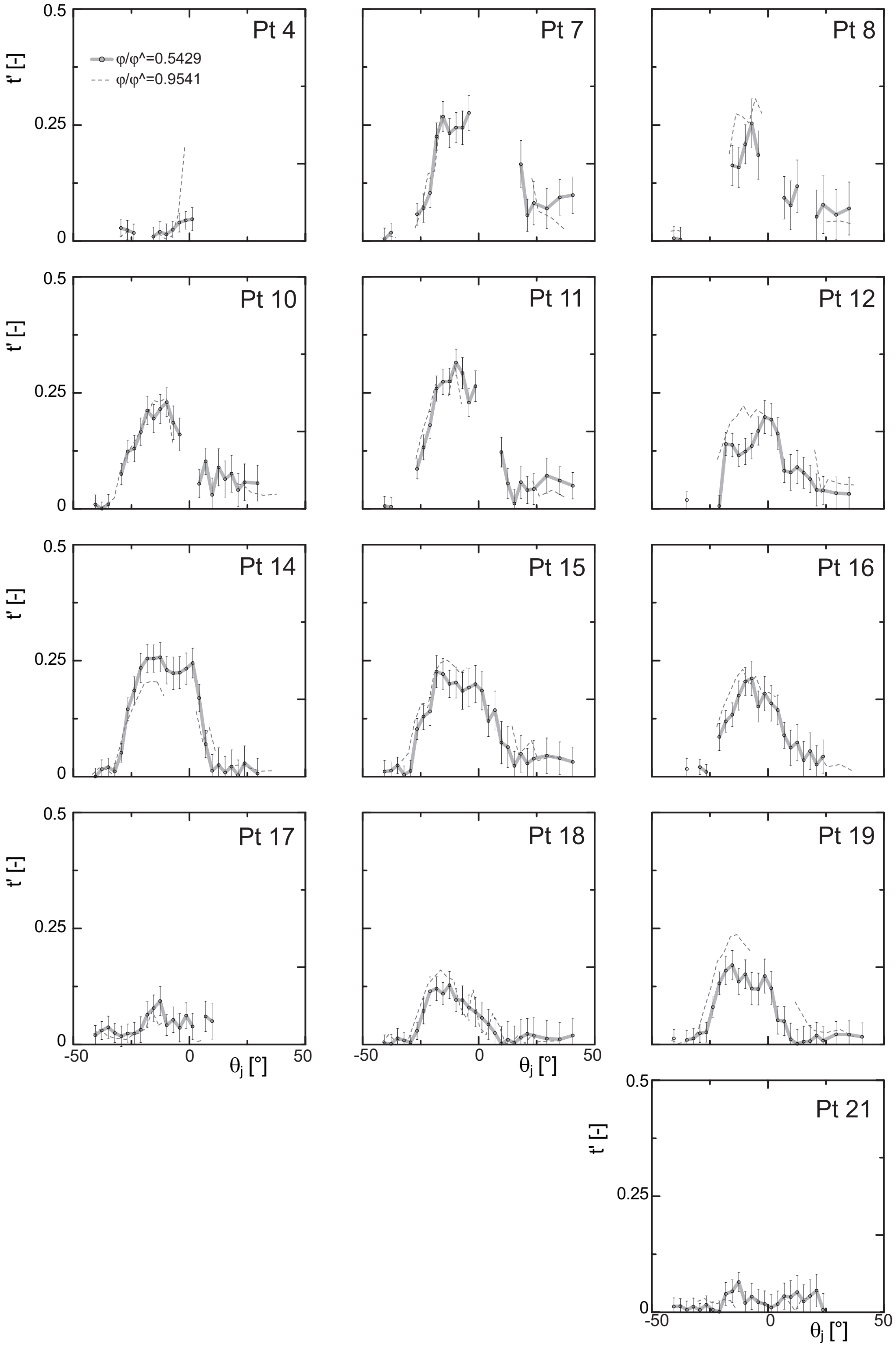

Figure 16.8: Water film thickness signal, $\psi_1/\psi_1^\wedge = 1.00$.

16.1.1 Zone 1

The water jet encounters bucket j in zone 1. The first peak of pressure recorded by the sensors is related to the passage of the front of the jet. The small standard deviation confirms the periodicity of the flow. The second peak, or plateau, visible on sensor 6 signal on the lower ψ_1 range, presents a non-periodic behavior, as shown by the high standard deviation value. Indeed, 3 phenomena that are visible from the observations are superposed: (i) As the jet is being cut by bucket $j+1$, its diameter increases, projecting more water particles on zone 1. (ii) The jet appears to bend toward the bucket j root as the cutting process of bucket $j+1$ starts, modifying its angle of attack relative to bucket j. (iii) If the flow moves backward in the direction of the bucket root at the beginning of the bucket duty cycle, then it flows toward the cutout, loading zone 1 again in the second half of the duty cycle.

16.1.2 Zone 2

The peak of pressure measured in zone 2 is treated in section 14.2. The jet fully feeds bucket j in zone 2 from $\theta_j \simeq -25°$ until $\theta_j \simeq -8°$, *i.e.*, the runner pitch. The measured signal remains quasi-steady during the pitch period. The flow fills almost the entire bucket helicoidally from zone 2. The signals account for 5/6 of the bucket duty cycle. The signal shrinks as the feeding process stops. Zone 2 is a focus region that receives water stemming from the whole feeding process. The numerical flow simulation results for that region are very accurate because the flow received in zone 2 is dominated by inertia effects and is not affected by the jet-bucket interaction. The short plateau, and the higher-than-average standard deviation at $\theta_j \sim 0°$ duty cycle, visible on the signals of sensors 14 and 15, are related to portions of the cut jet catching up to the bucket, and the transition from jet impact flow to a purely water film flow.

16.1.3 Zone 3

Zone 3 is where the end of the feeding process occurs. The signal rises are smoother because the front of the jet is not sharp anymore and is preceded by the water sheet already formed in zones 1 and 2. The measured signal for sensor 4 presents a double-peak around $\theta_j = 0°$, followed by a rapid drop of amplitude. This is related to the impingement of water threads stemming from the jet, as for zone 2. The delay in signal rise may be related to the jet enlargement at the moment of the jet cut stated previously, which is underestimated by the numerical simulation.

16.1.4 Zone 4

Zone 4 only receives water film flow and is at the beginning of the bucket outflow. The main discrepancies between the simulation and the measurement are the phase shift for sensor 22 and the lack of amplitude of the predicted signals. The predicted water film seems to exhibit a shorter period than the real one, arriving later and leaving the zone earlier. At $\theta_j \sim -24°$, zone 4 is still dry in the numerical flow simulation results, while the measured signal rise indicates that the water sheet already covers the aft region of the bucket. The lack of amplitude of the signals is related to the deformation and increase of the diameter caused by the Coanda effect on the bucket ribs.

16.1.5 Zone 5

The accuracy of the prediction is better than in zone 4 because zone 5 is less affected by the deformation and bending of the jet after its encounter with bucket $j+1$.

16.1.6 Analysis of the results

The main differences that can be stated from the comparison of the experiments and the simulations are as follows: (i) The actual feeding process is faster than predicted by the numerical flow simulation, with more water flowing towards the bucket root, and more water leaving the bucket from zone 4. (ii) The end of the feeding process arises earlier than predicted, between zones 2 and 3, as opposed to the numerical flow simulation, where it arises in zone 3. (iii) The jet enlargement and bending after its encounter with bucket $j+1$ is underestimated in the simulation. (iv) The flow distribution in the bucket: the flow in the buckets balances back and forth, flowing from zone 1 to zone 2 and from zone 2 to zones 3 to 5 in a counterclockwise pattern [7], [88]. The numerical flow simulation prediction seems to lead the measurements in the first portion of the duty cycle and to lag behind them in the second portion. The jet-cutting process modeling is related to the discrepancies observed.

16.2 Mixing losses

The bucket mixing losses can be divided in 3 main types: (i) unavoidable mixing losses related to the relative motion in the bucket; (ii) crossing of streamlines; (iii) flow interferences.

16.2.1 Mixing losses

The impact of the jet on the splitter and bucket surface takes place at different radial locations, thus every single water filament has a different angle of attack and a different velocity magnitude [118], Fig.16.9. The relations between the velocities in a moving system, for 2 points 1 and 2 at distinct locations, can be written as:

$$\frac{u_2^2 - u_1^2}{2g} + \frac{w_1^2 - w_2^2}{2g} = 0 \tag{16.1}$$

Equation 16.1 shows that the relative velocity in the rotating system changes in the same degree as the peripheral velocity.

However, 2 neighboring streamlines 1 and 2 are not independent. They represent a hydraulic continuity in which pressure transformations arise. Along streamline 1, the energy conservation can be written as:

$$E_1 = \frac{w_1^2 - u_1^2}{2g} + \frac{p}{\rho}, \tag{16.2}$$

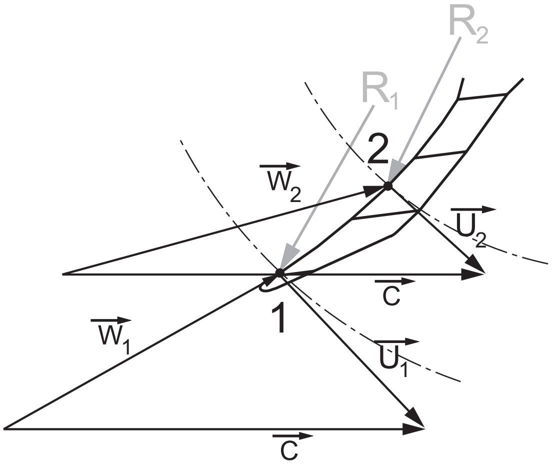

Figure 16.9: Relative velocity change with respect to the radial position.

where E_1 is a massic energy in the relative frame of reference that remains invariable for a closed system. It is therefore necessary that an exchange takes place between the various filaments on the bucket. The jet on the bucket does not represent in relative motion a hydraulic continuity with a uniform massic energy in every filament. The energy exchange is due to the fact that all filaments do not start with the same energy level in the relative frame of reference. The mixing loss itself consists in the appearance of a vortex motion between the water filaments with an equalization of the respective massic energies. These vortices can either grow up to macroscopic scales and become visible as a rolling wave at the front of the water film in the bucket, or trigger the apparition of cavitation [75]. The mixing losses can be exacerbated when the jet features macro-scale eddies generated by a curved piping system without fins [90].

16.2.2 Crossing of streamlines

The various water filaments, besides of having different massic energies in the relative frame, exhibit trajectories that vary in length. The encounter of 2 streamlines with paths working against each other generates a tumescence of the water film in the bucket. Figure 16.10 shows the sequence of appearance and disappearance of such a T-shaped tumescence close to the outer edge. The measured film thickness undulates while the pressure signal presents a larger standard-deviation. The tumescence is likely to be caused by the encounter of 2 streams, both originating from the splitter and working against each other [69]. One water filament flows towards the root, while the other is already moving towards the front, Fig.16.11.

16.2.3 Flow interferences

Flow interferences occur when water films of different massic energies encounter in the bucket, and are known as a cause of unsatisfactory performances on multi-jet machines - 'Falaise' effect [115]. Figure 16.12 portrays the sequence of interference between the established water film on the bucket surface and the impacting threads stemming from

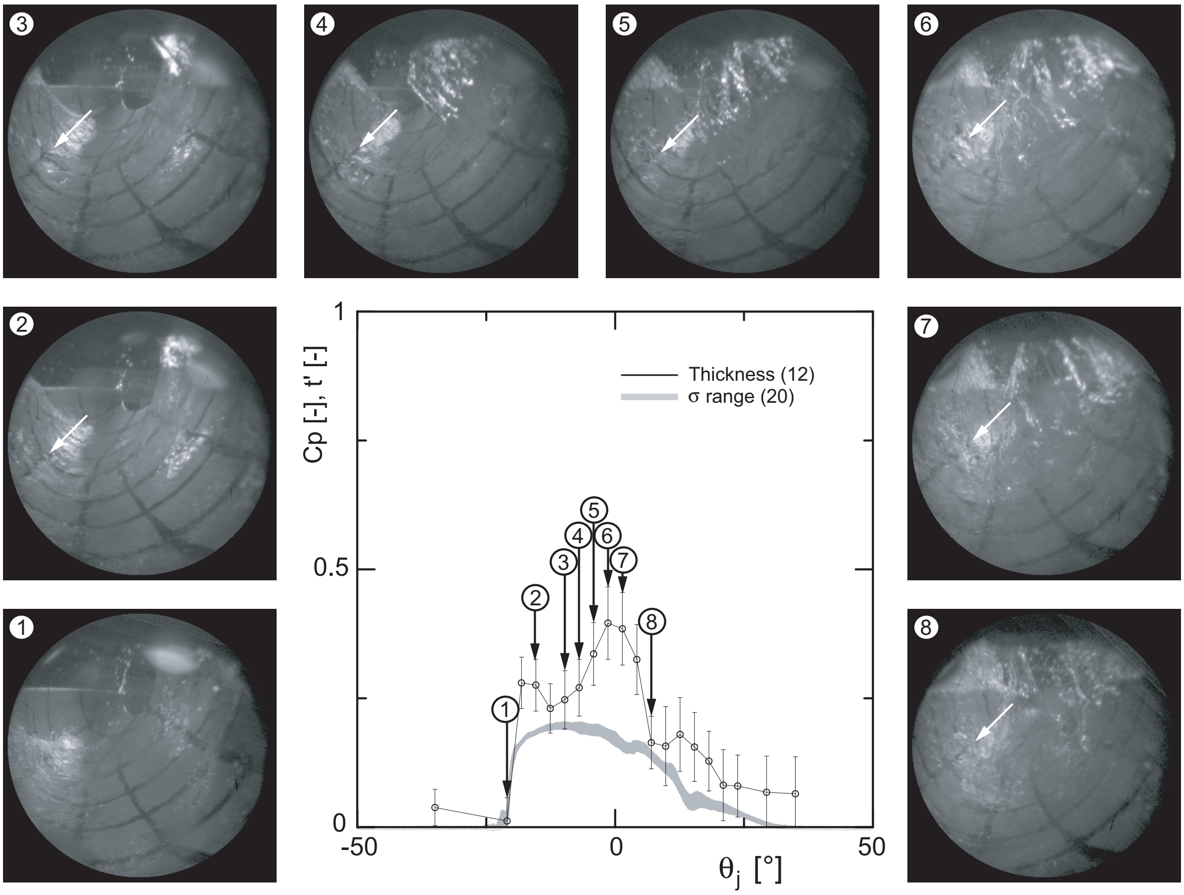

Figure 16.10: Crossing of streamlines.

the jet disintegration. The pressure signal in the zone displays a large standard-deviation, while recording of the film thickness perturbation is not possible.

16.3 Flow stratification

The last stages of the bucket discharge process exhibit a stratification of the flow. Different layers appear, diverging with angles in excess of 30°, Fig.16.13. The flow veers in the thinner layers, where the thickness is of the order of a few $1/10mm$. The cause of this phenomenon lies with the Coriolis acceleration variation caused by the runner rotation.

$$\overrightarrow{a_{Coriolis}} = 2\overrightarrow{\omega} \times \overrightarrow{w}(\overrightarrow{n}) \tag{16.3}$$

Provided that $\overrightarrow{w}(\overrightarrow{n})$ varies across the water film, so does the Coriolis acceleration in terms of intensity and direction. It acts in a stronger fashion in the main stream than in the thinner films. Indeed, the balance between the inertia, rotation-induced, viscous and surface tension forces is modified in the thinner films, the last ones becoming paramount. The velocity profiles across the water film must therefore be highly $3D$, as schematized by Fig. 16.14. The layer where the viscous forces outperform the Coriolis force are referred

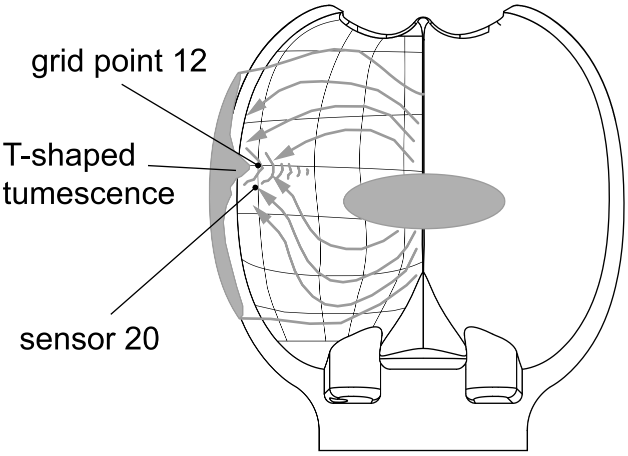

Figure 16.11: Formation of the T-shaped tumescence.

as the Ekman layer [24]. The definition of the Ekman layer is given by:

$$\delta_E = \sqrt{\frac{\nu}{2\Omega}} \approx 10^{-1} mm. \tag{16.4}$$

As can be stated, this value is independent on the relative flow velocity. The value obtained is in good accordance with the observations.

16.4 Draining-off

The ejection of the series of droplets, detail *l* in Fig.13.2, Fig.13.6 and Fig.13.7, is fed by the vapor-saturated atmosphere that prevails in the casing. The bucket surfaces act as a dew trap for the micro water droplets: the intersticial volume between the buckets is in depression due to the runner rotation. The droplets captured by the buckets then amalgamate until they form volumes of water heavy enough to be centrifuged.

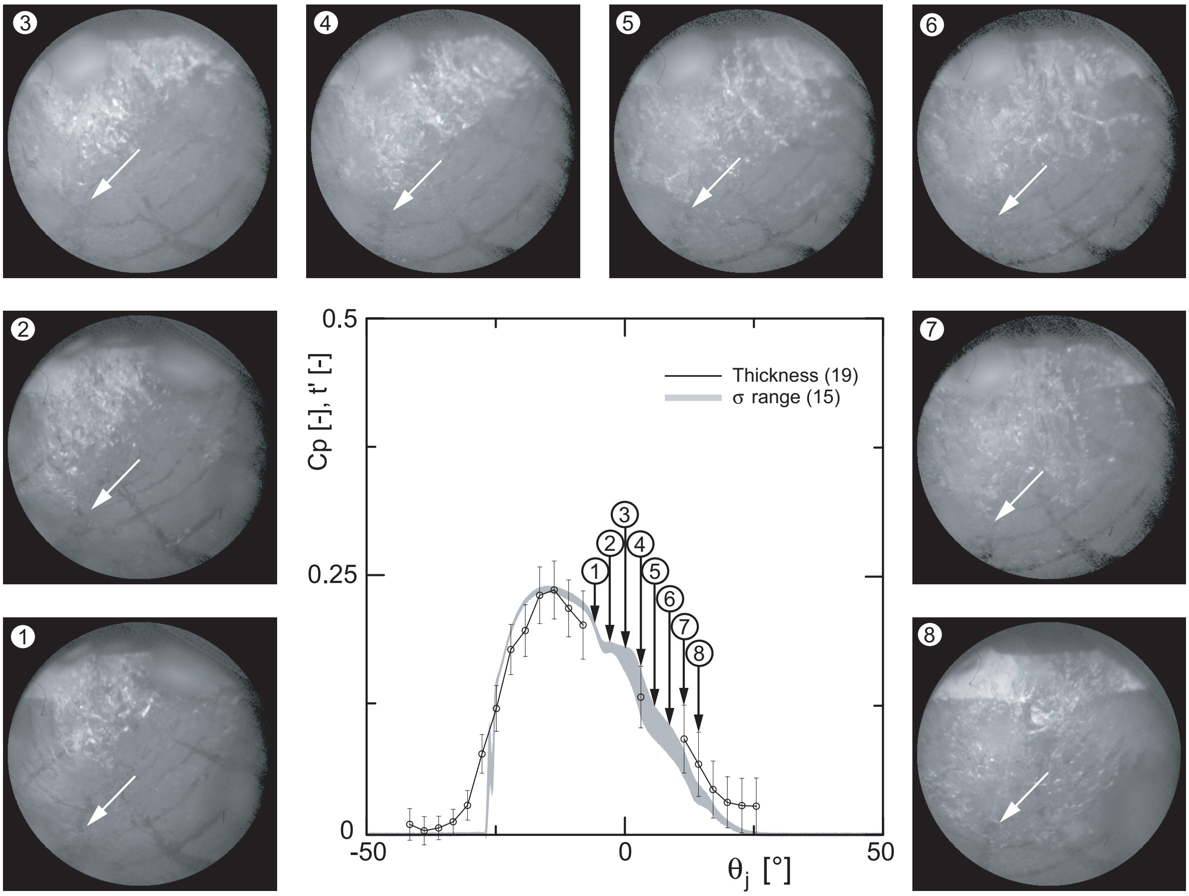

Figure 16.12: Interference mixing.

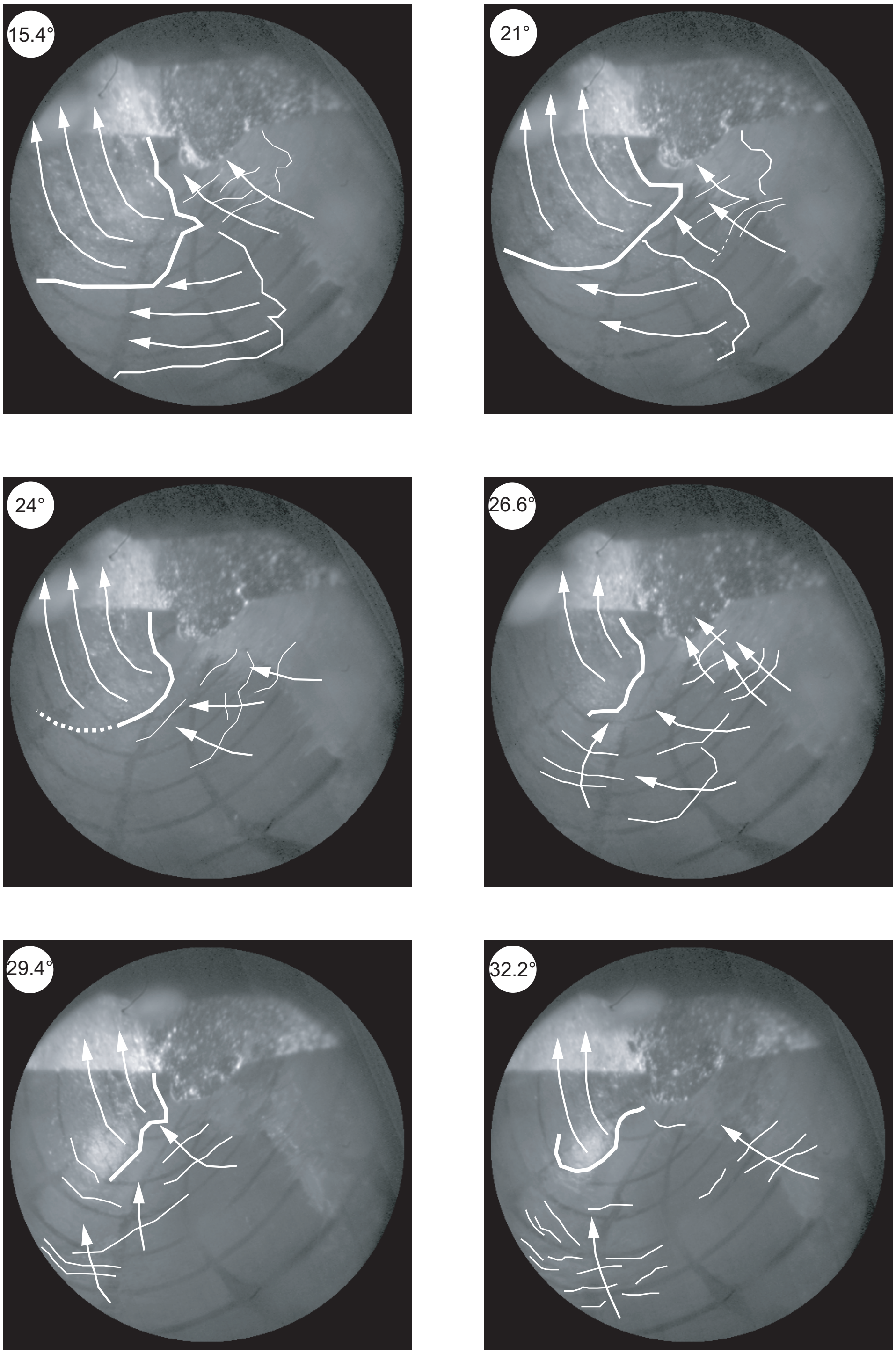
15.4°
21°
24°
26.6°
29.4°
32.2°

Figure 16.13: Flow stratification.

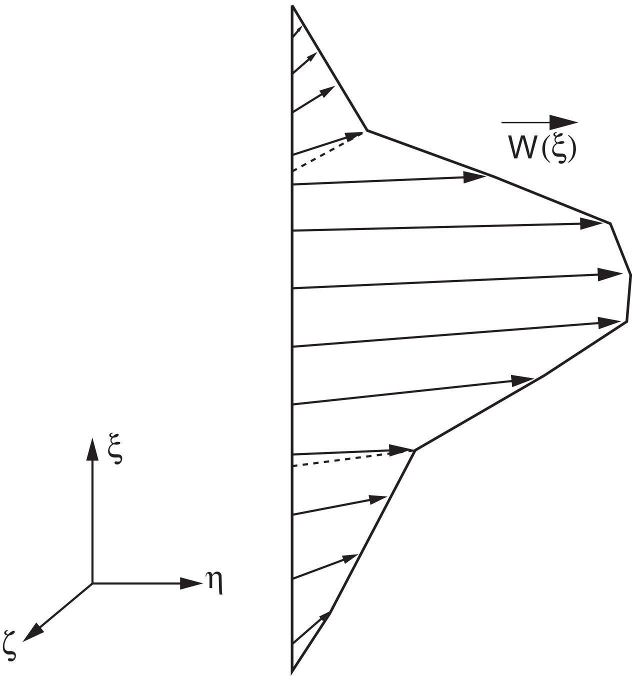
$\overrightarrow{W(\xi)}$
ξ
η
ζ

Figure 16.14: Velocity profile evolution.

Chapter 17

Outflow heeling

17.1 Lateral pressure distribution

The sensors located on the lateral sides of the buckets provide information about the outflow heeling phenomenon and how it influences the bucket performances. Figure 17.1, Fig.17.2, Fig.17.3 and Fig.17.4 show the pressure distribution for the 4 test heads. 3 zones can be defined, referred as frontal, central and aft areas, see Fig.17.5.

17.1.1 Frontal area

This is the region where most of the heeling occurs. For all the operating points considered, sensor 40, located in the lower portion of the area, records a positive pressure signal, while sensor 43, located in the upper portion, records a depression. The positive signal exhibits a large standard-deviation, while the negative signal is more periodic. It is remarkable that the pressure coefficient decreases for increasing heads.
This pressure distribution indicates that past the initial stagnation region, the flow goes round the bucket lateral face, what in turn generates a depression. The phenomenon resembles the Coanda effects present on the backside, as schematized by Fig.17.6.

17.1.2 Central area

Depending on the operating conditions, the heeling may or may not occur. As can be expected, it is more marked for the higher values of ψ_1. The signals are very short. The CFD signals predict a depression at the location of sensor 42 that does not exist. The cause of this error is difficult to assess. It could be related to an overestimation of the sheet thickness close to the outer edge due to numerical diffusion.

17.1.3 Aft area

Whatever the operating conditions, no heeling can be identified.

17.1.4 Consequences

Early researchers as Wagenbach [116], Tenot [104] and Lowy [69], suggest that a slight outflow heeling has no detrimental effect on the bucket performances, as smaller outflow

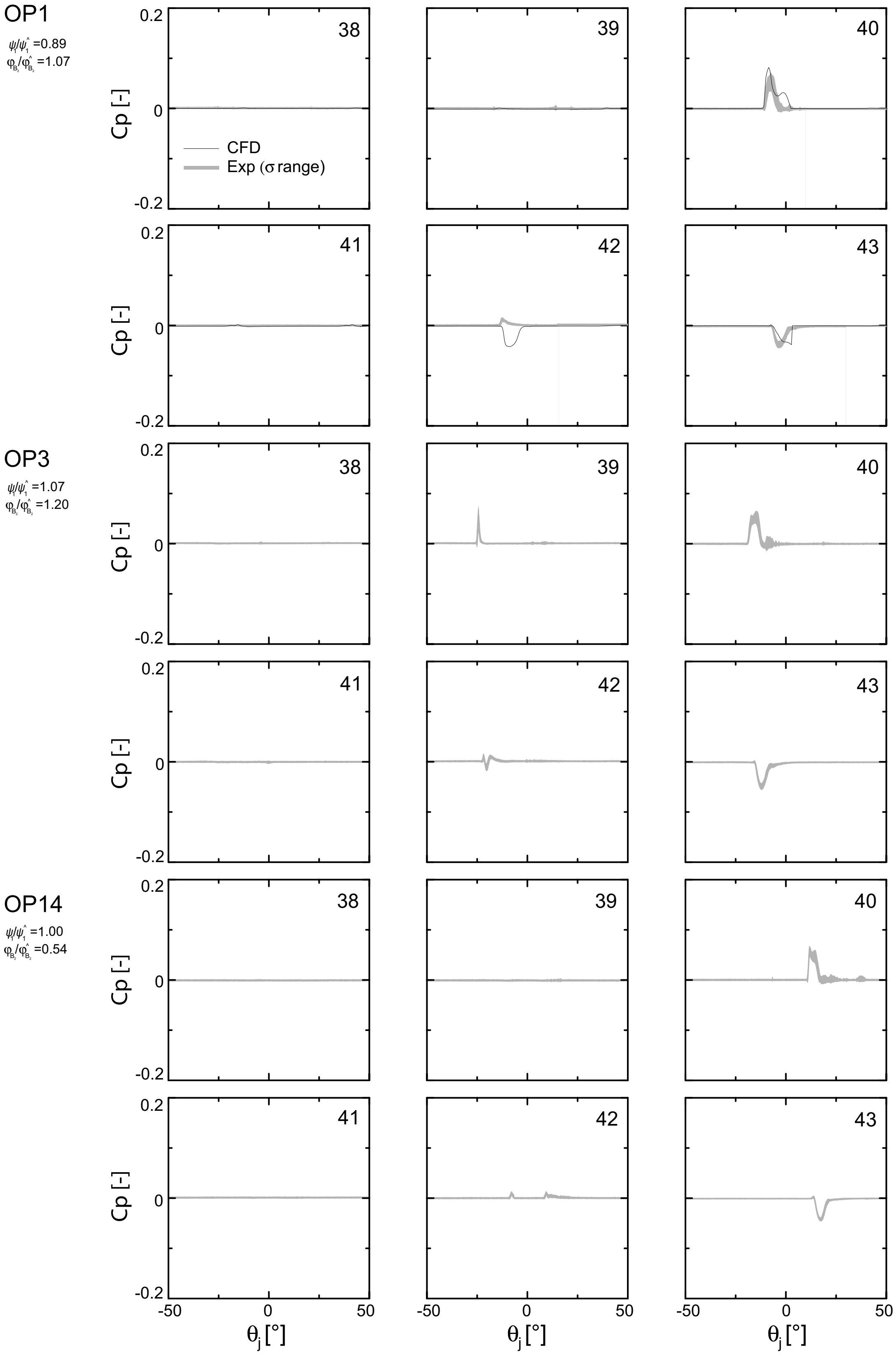

Figure 17.1: Lateral face pressure signals, $H = 20m$.

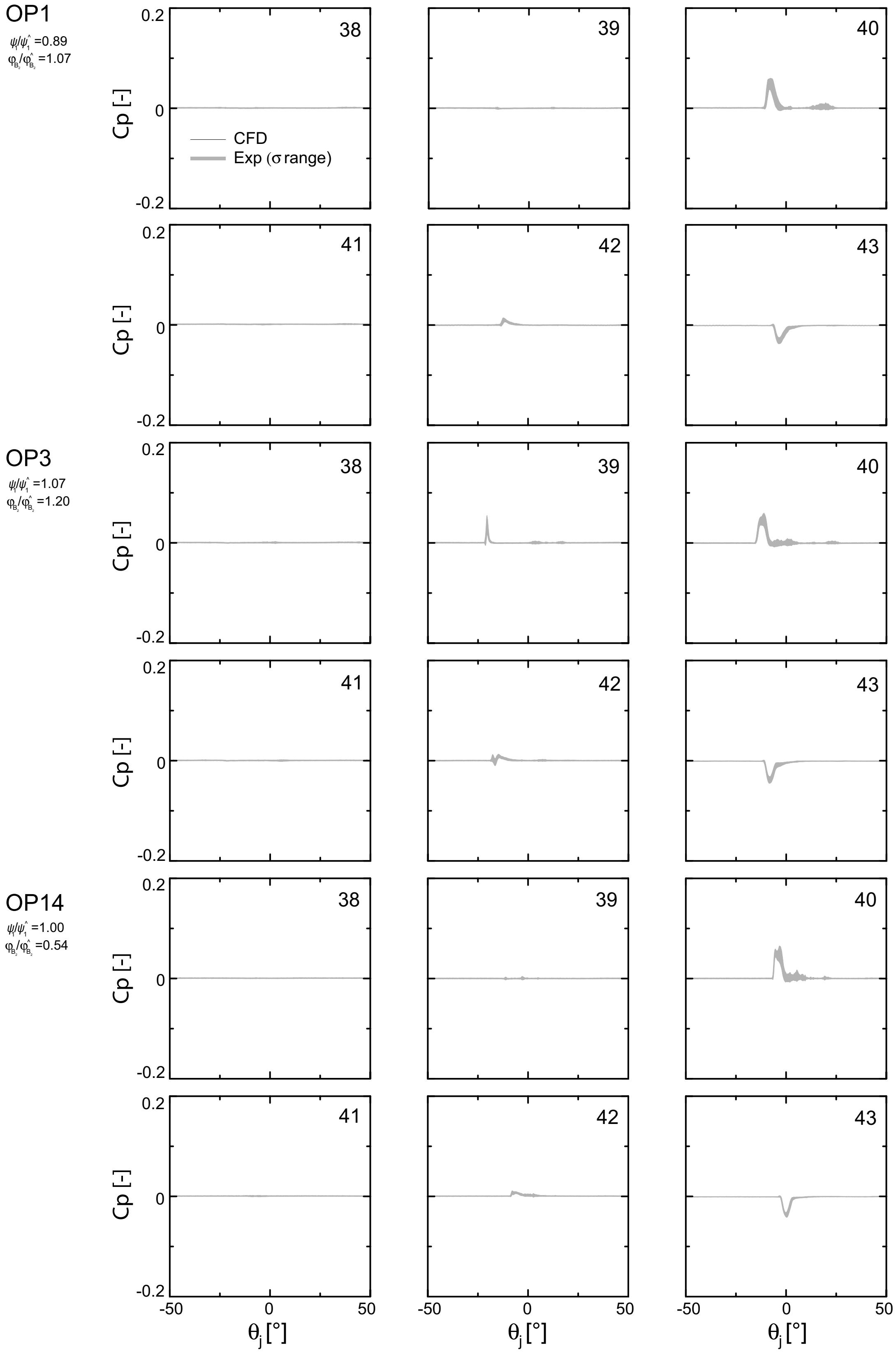

Figure 17.2: Lateral face pressure signals, $H = 35m$.

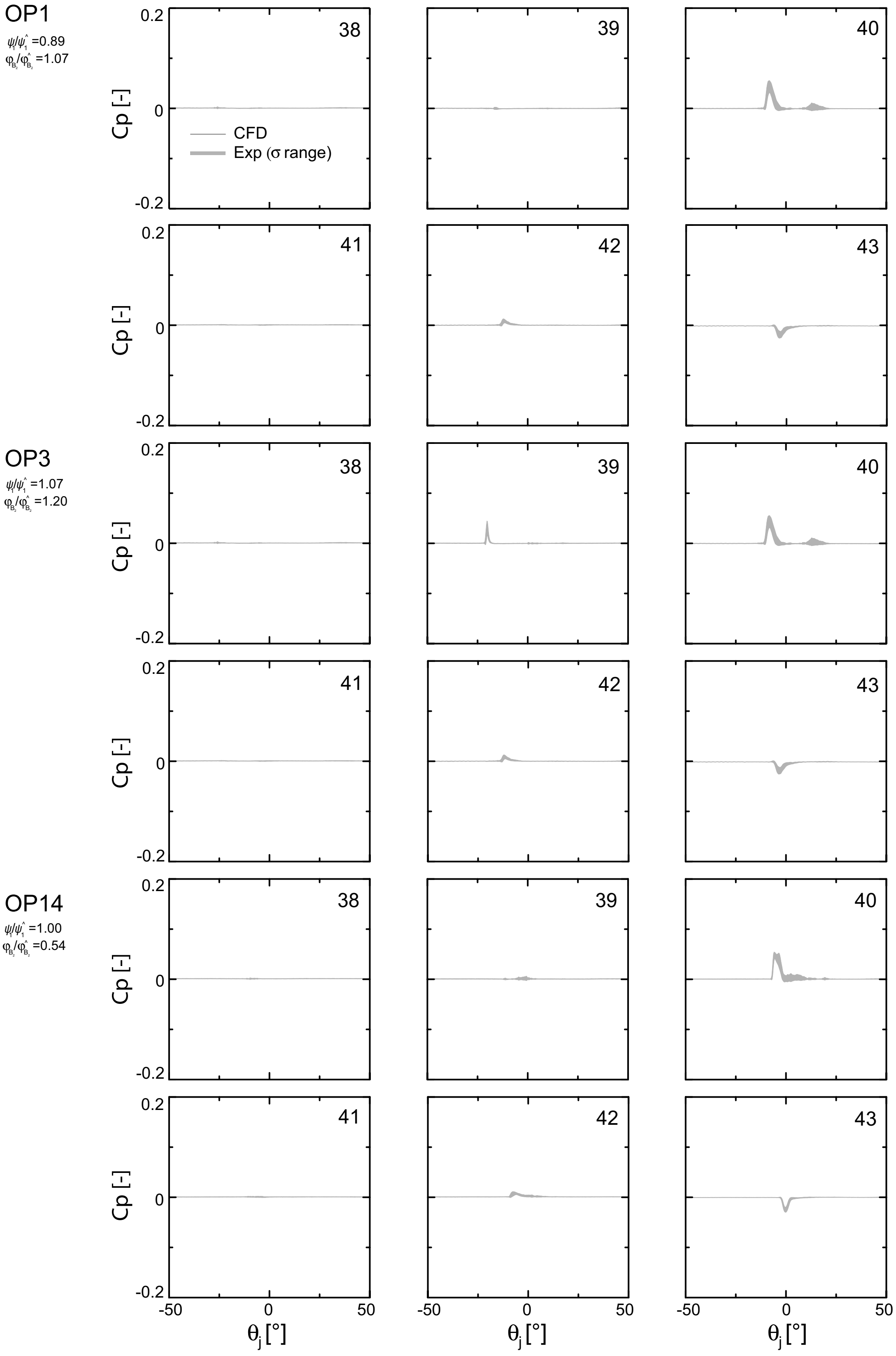

Figure 17.3: Lateral face pressure signals, $H = 60m$.

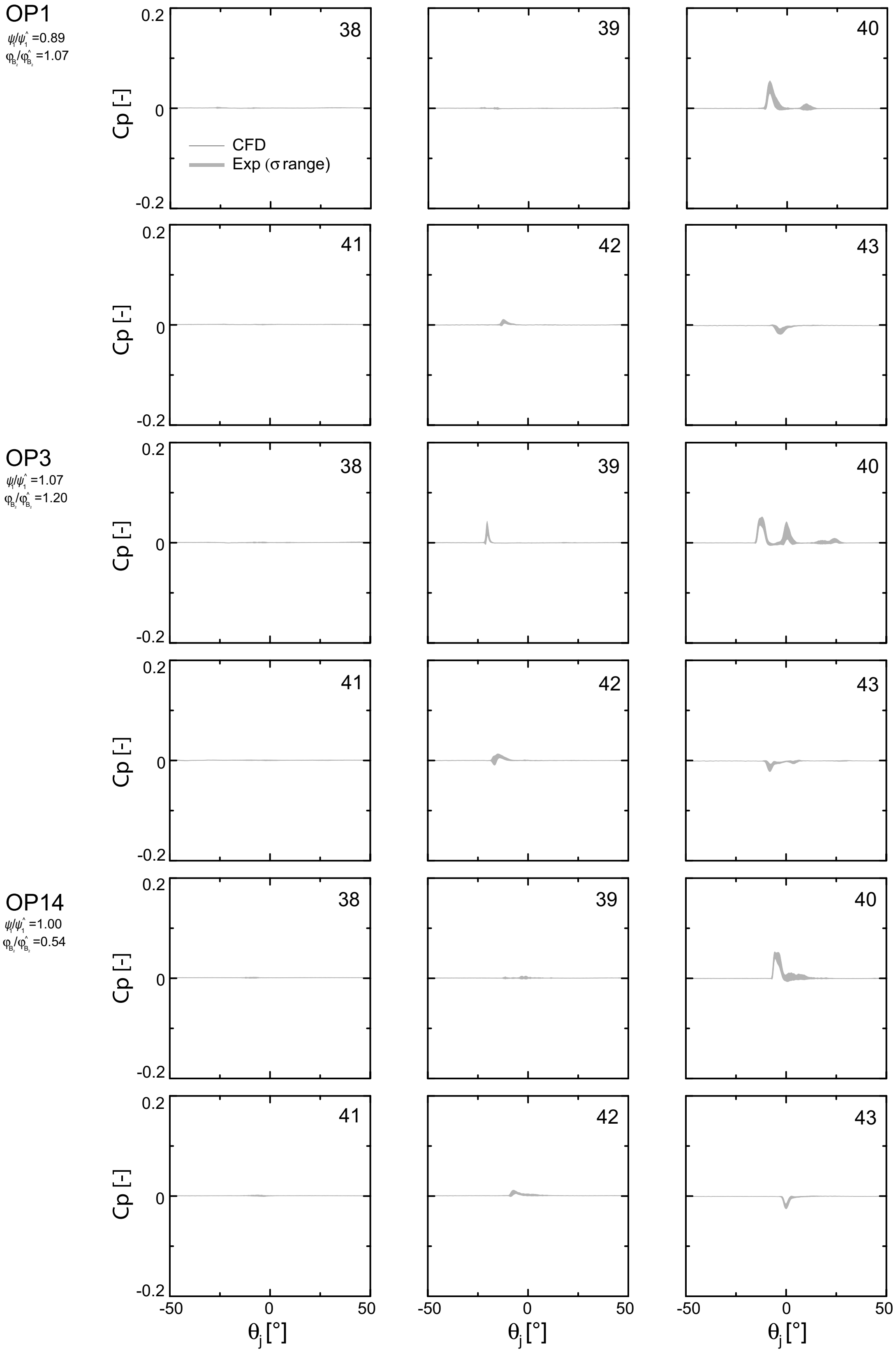

Figure 17.4: Lateral face pressure signals, $H = 80m$.

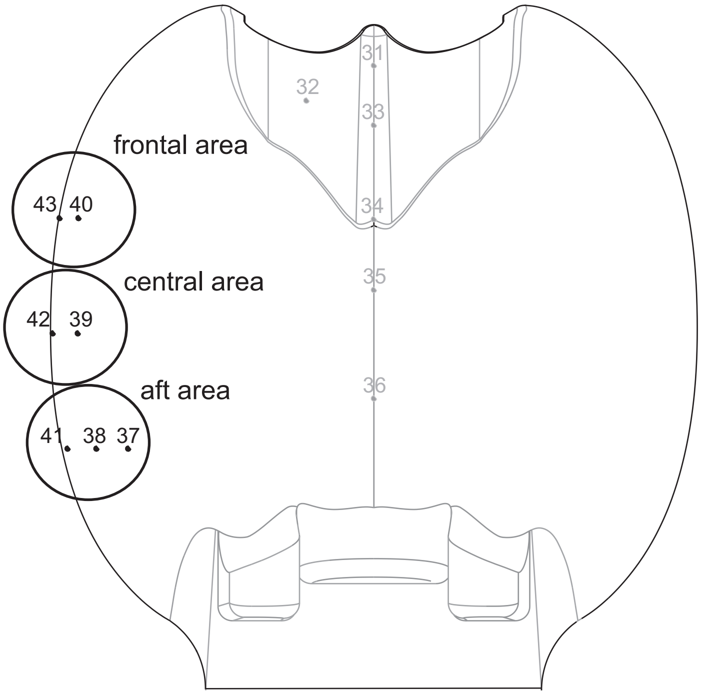
31
32
33
34
35
36
frontal area
43
40
central area
42
39
aft area
41
38
37

Figure 17.5: Lateral zones of the bucket.

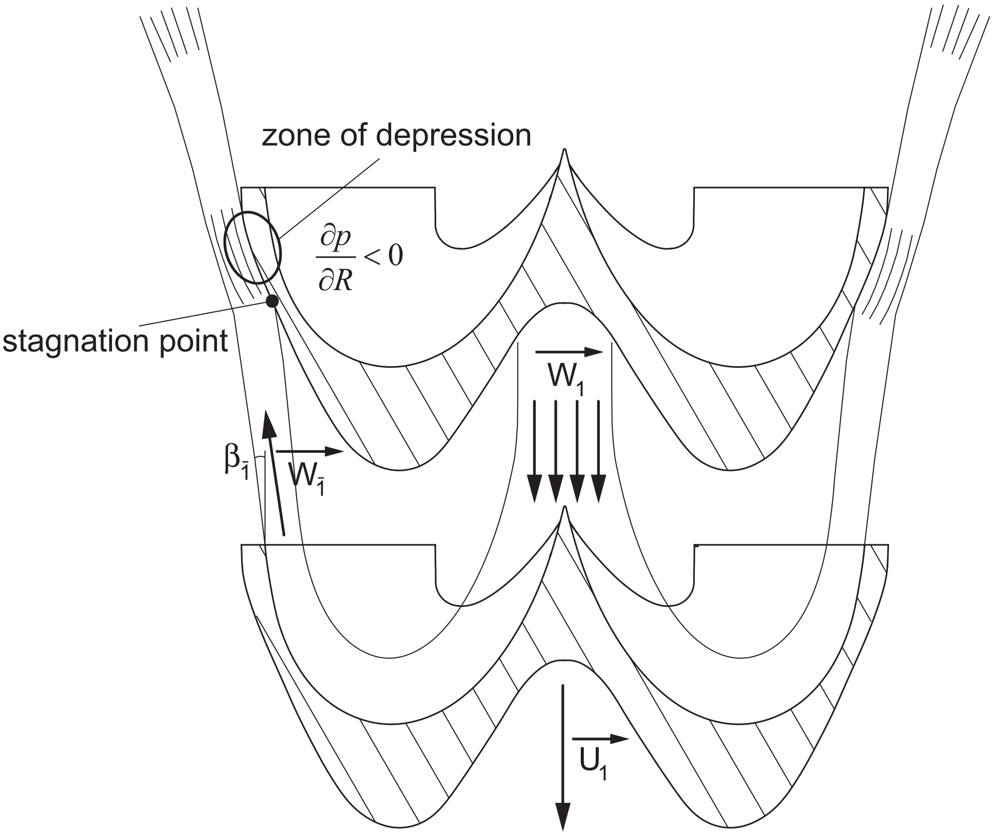
zone of depression
$\frac{\partial p}{\partial R} < 0$
stagnation point
$\vec{W}_1$
$\beta_{\bar{1}}$
$\vec{W}_{\bar{1}}$
$\vec{U}_1$

Figure 17.6: Outlet heeling, frontal area.

angles increase the bucket performances, except the risk of cavitation onset for the lower specific speed machines. Indeed, the depression generates a lift force that exhibits a slight component in the direction of rotation of the runner. That indicates that some outflow heeling acts positively on the runner efficiency by scavenging a portion of the kinetic energy otherwise lost in the water sheets.

Chapter 18

Power Budget

18.1 Local Power definition

The pressure field does not adequately show where the zones are that contribute the most to the bucket power build up. It is more relevant to investigate the bucket-power history to assess the effective Momentum transfer between the flow and the bucket. The critical criteria are as follows: (i) the bucket surface geometry, (ii) the radius of application of the driving force, (iii) the water remaining kinetic energy, and (iv) bucket angle of setting. To obtain the resultant instantaneous power produced by each zone from the location of the experimental pressure sensors, a $2D$-Delaunay triangulation is used, see Fig.18.1. The integration is performed by linearly averaging the values at the triangle vertices and multiplying the result by the triangle surface. The power, in turn, is determined from the projection on the local peripheral direction of the local surface normal pressure of each triangle area A_m that composes zone i, multiplied by the runner angular velocity, see Eq.18.1. The other components of the stress tensor are neglected.

$$P_i = \sum_{m=1}^{n} \overrightarrow{t_{i_m}} \cdot \overrightarrow{\omega} = \left[\sum_{m=1}^{n} \overrightarrow{r_{i_m}} \times \left(\int_{A_{i_m}} p_{i_m}(t) \overrightarrow{n_{i_k}} dA_{i_m} \right) \right] \cdot \overrightarrow{\omega} \tag{18.1}$$

The pressure field shows the regions that are the most loaded in terms of normal mechanical stress, but does not give real information about the energy transfer in the bucket.

18.2 Power distribution

The power contribution of the different bucket zones, see Fig.18.2, highlights the effective Momentum transfer between the flow and the bucket throughout the bucket duty cycle.
Zones 1 is the first to receive water particles at the beginning of the duty cycle. The power signal presents a plateau accounting for the duration of the full jet period.
Zone 2 contributes the most to the bucket power for all the operating points considered because this region experiences the direct impingement of the jet at the beginning of the bucket period, when the kinetic energy of the flow is at its maximum. Zone 2 contributions exhibit the longest and tallest pressure signal, lasting more than 2/3 of the bucket period, and accounts for more than 25% of the bucket power. Zone 2 can be considered as a focal region, which collects all the water particles transiting in the bucket. The flow received in

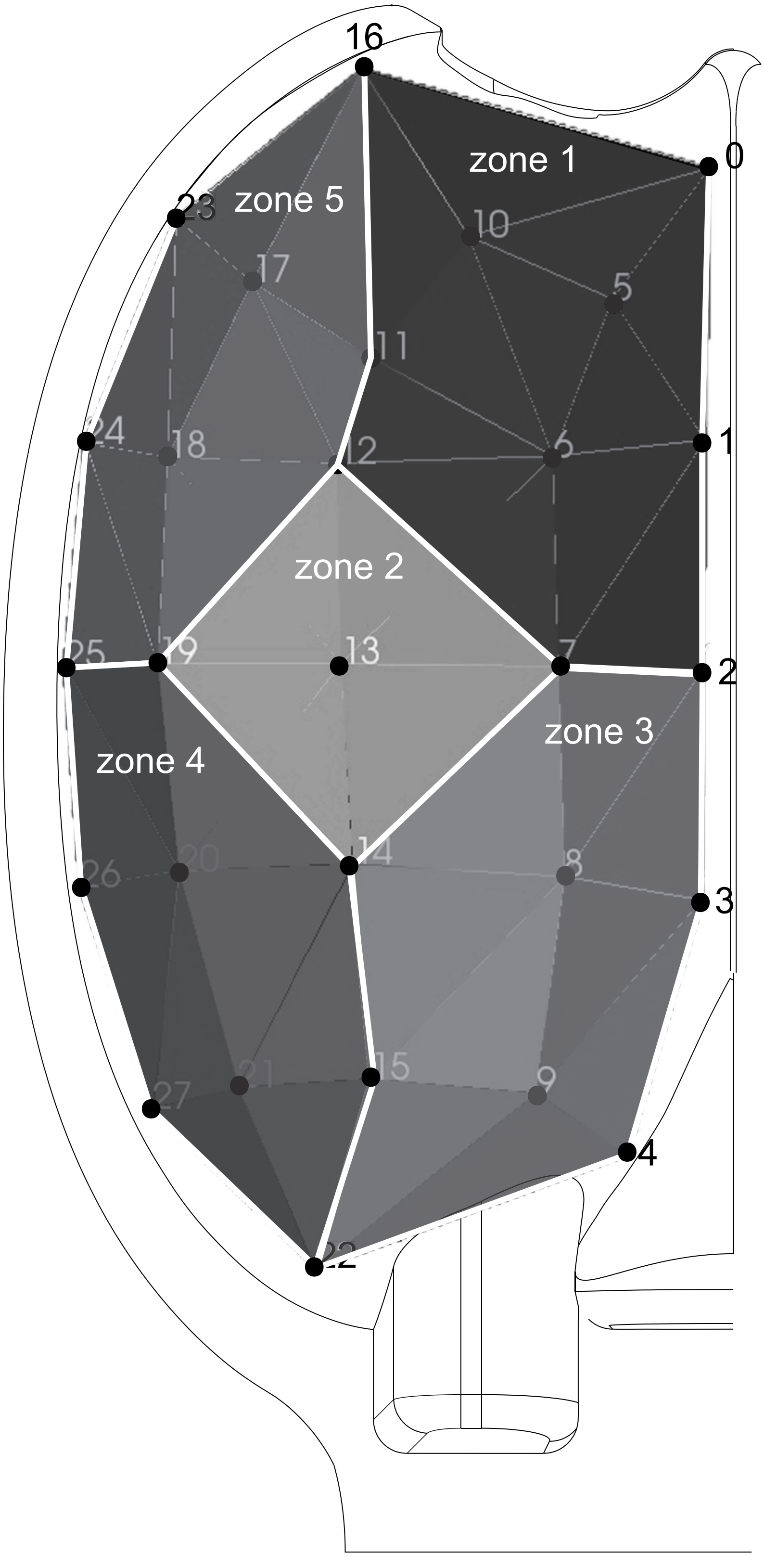
16
0
zone 1
23
zone 5
10
17
5
11
24
18
12
6
1
zone 2
25
19
13
7
2
zone 3
zone 4
26
20
14
8
3
15
21
27
9
4
22

Figure 18.1: Delaunay triangulation and definition of the bucket zones.

zone 2 during the full jet period is in accordance with the kinematical assumptions made to design the buckets. This explains why the classic design methods permit one to obtain machines of fair efficiency [87].

Zones 3 and 4 feature the shortest signals for all operating conditions. Zone 5 surpasses all the other regions in terms of power contribution duration, accounting for more than 2/3 of the bucket period. Its relative contribution is higher for the lower φ_{B_2} conditions. The bucket power rise present a series of steps, and for the lower ψ_1 operating points, a peak. The peak corresponds to the pressure peak generated by the impact of the jet front in zone 2 discussed in section 14.2. The relative effect of the impact on the bucket power is probably overstated by the Delaunay triangulation and integration procedure that tends to exaggerate the relative importance of the isolated sensors. The maximum power is reached between $\theta_j = -10°$ and $\theta_j = -9°$ when the contributions of zones 2-4 are closest to their respective maxima.

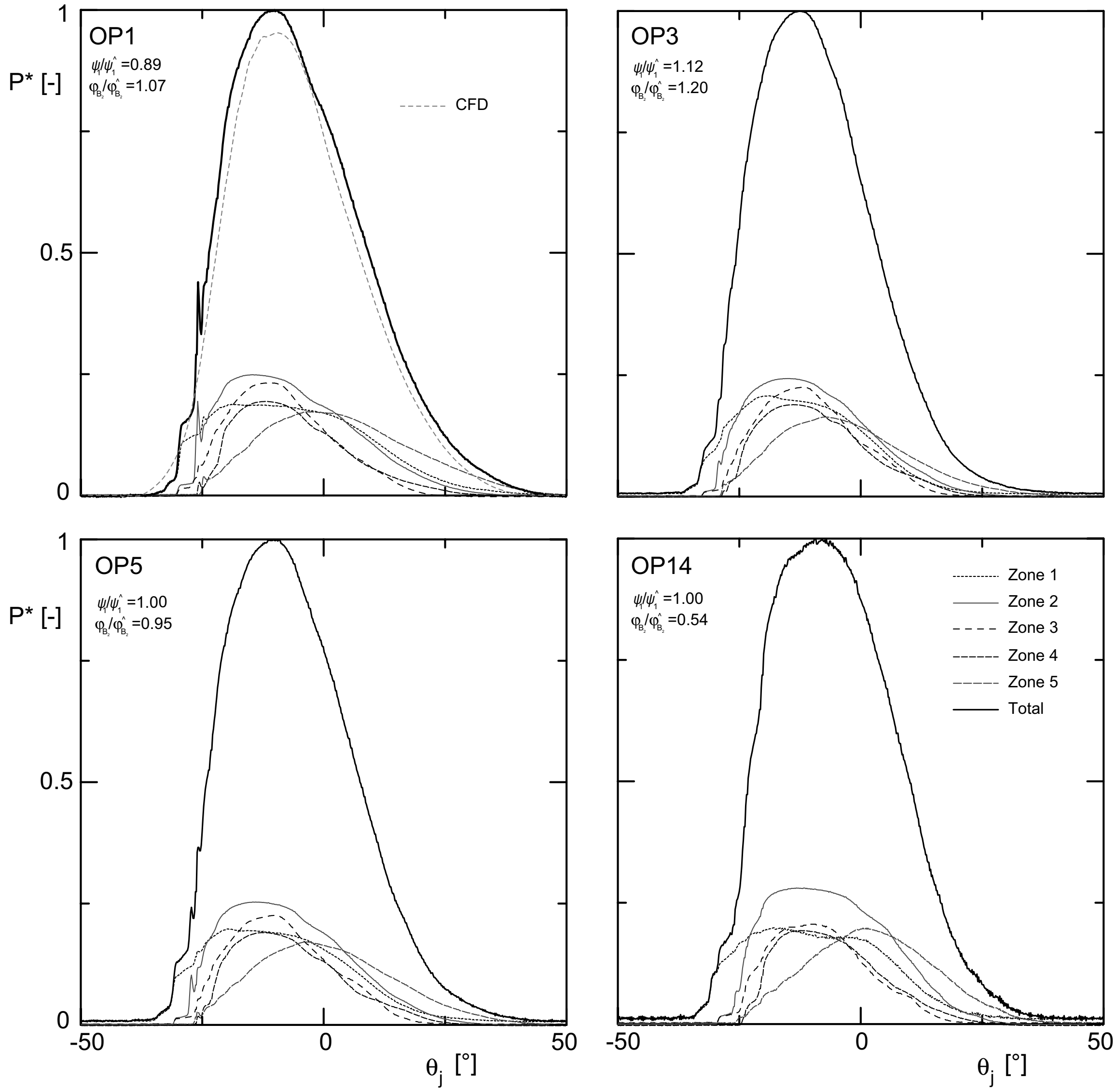

Figure 18.2: Bucket power distribution.

18.3 Bucket and runner power fluctuations

The runner power fluctuations can be determined by taking into account the backside contribution:

$$P_{runner}(\theta) = \sum_{j=1}^{z} \{P_{i_j}(\theta) + P_{b_j}(\theta)\}, \tag{18.2}$$

where P_i and P_b are respectively the power signal of the inner surface and backside. Figure 18.3 displays the power fluctuations of the runner for the 4 operating conditions under consideration. The signals obtained for the different operating conditions show significant fluctuations that are modulated by the flow conditions. The bucket passages into the jet are visible on the 4 signals. In a similar fashion, the impact pressure pulse,

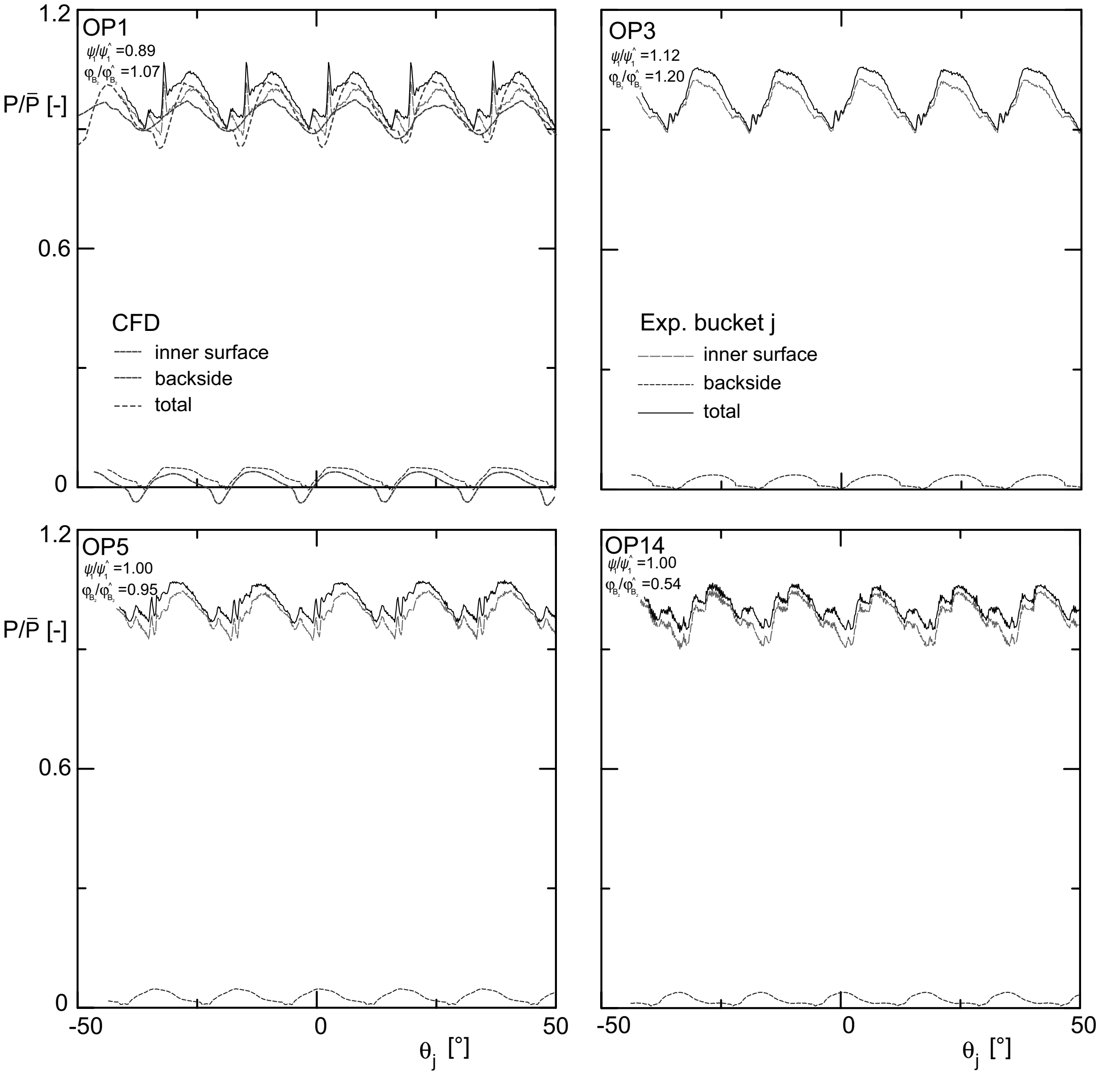

Figure 18.3: Runner power fluctuations.

typical of the lower ψ_1 operating conditions, generates a peak on the whole runner power that is absent from the higher ψ_1 operating conditions considered.
As discussed in section 15.2, the power signals obtained for the backside is essentially function of the ψ_1 regime. Indeed, the signal decays are steeper for the higher ψ_1 than for the other operating conditions, witnessing a neater separation of the jet due to the higher relative angle of attack.

18.3.1 Amplitude spectra

The power amplitude spectra of the runner is put into evidence using a Fast Fourier Transform (FFT). The result is shown by Fig.18.4. The harmonic contain is inversely proportional to the runner efficiency: the richer the harmonic contain, the less the runner efficiency. The cleanliness of the power signal closer to the best efficiency conditions contrasts with the large number of harmonic recorded for the lower efficiency operating condition. At the operation at the lower ψ_1 values, the impact pressure pulse energy induces a higher amplitude for the higher rank harmonics, see $\frac{f}{f_N \cdot z_b} = 9$. This would demonstrate the flow perturbations frequency is too high to excite an eigenfrequency of the runner or the hydro-alternator inasmuch the first harmonic is $O(\sim 200Hz)$.

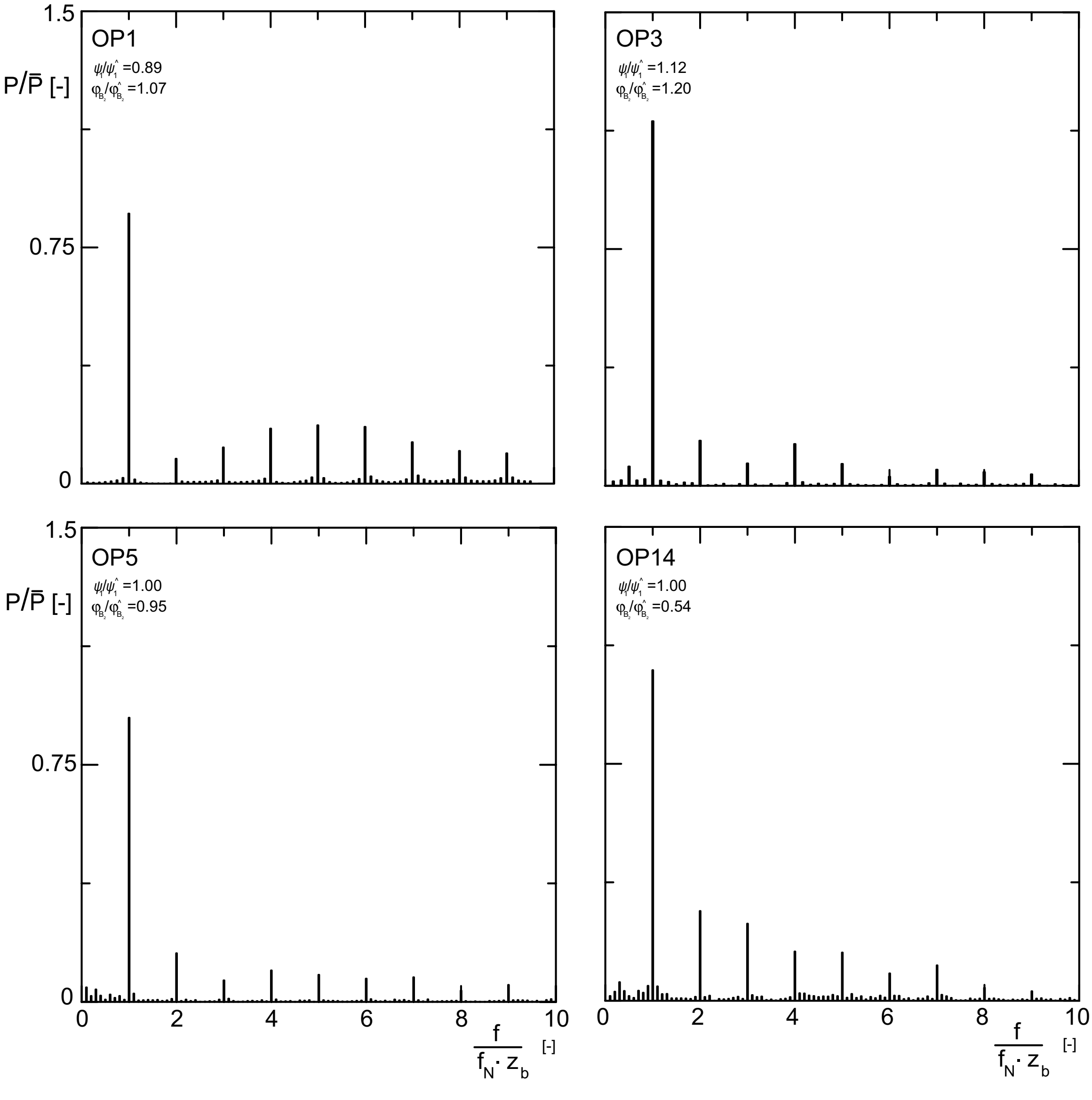

Figure 18.4: Runner power amplitude spectra.

Chapter 19

Momentum transfer

19.1 Energy balance

By integrating the zone power signals treated in section 18.2, the effective energy transfer occurring respectively on the 5 bucket zones and on the backside, and the percentage of the kinetic energy of the jet portion turbinated by each bucket, are highlighted. The energy received by bucket j zone i and backside under operation at condition k is expressed as:

$$(E_{i,j})_k = \frac{180 \cdot \omega_k}{\pi} \int_{(\theta_j)_0}^{(\theta_j)_\infty} (P_{i,j})_k \theta_j d\theta_j. \tag{19.1}$$

The result is rendered non-dimensional by the total hydraulic energy transformed by bucket j:

$$(E_j)_k = \frac{180 \cdot \omega_k}{\pi} \int_{(\theta_j)_0}^{(\theta_j)_\infty} (P_i)_k d\theta_j \tag{19.2}$$

The distribution of the effective energy transferred to bucket j is given in Fig.19.1. The transformed energy distribution reveals that up to 5% of the energy is received by the backside for the lower ψ_1 conditions considered. The energy distribution is modified by the operating conditions. With a lower jet diameter, most of the energy is converted in zone 2 and zone 1, while zones 3 and 4 contributions shrink below the contribution of zone 5. Close to the best efficiency, the contributions of zones 3, 4 and 5 appear more homogeneously spread.

19.2 Energy transfer mechanism

As discussed in chapter 4, the energy is transferred by deviating the flow in the bucket, using the principle expressed by Newton's second law.

The Momentum conservation equation expressed in integral form for the small fluid column V_l ceiling pressure sensor l, see Fig.19.2, can be written in the following manner, if

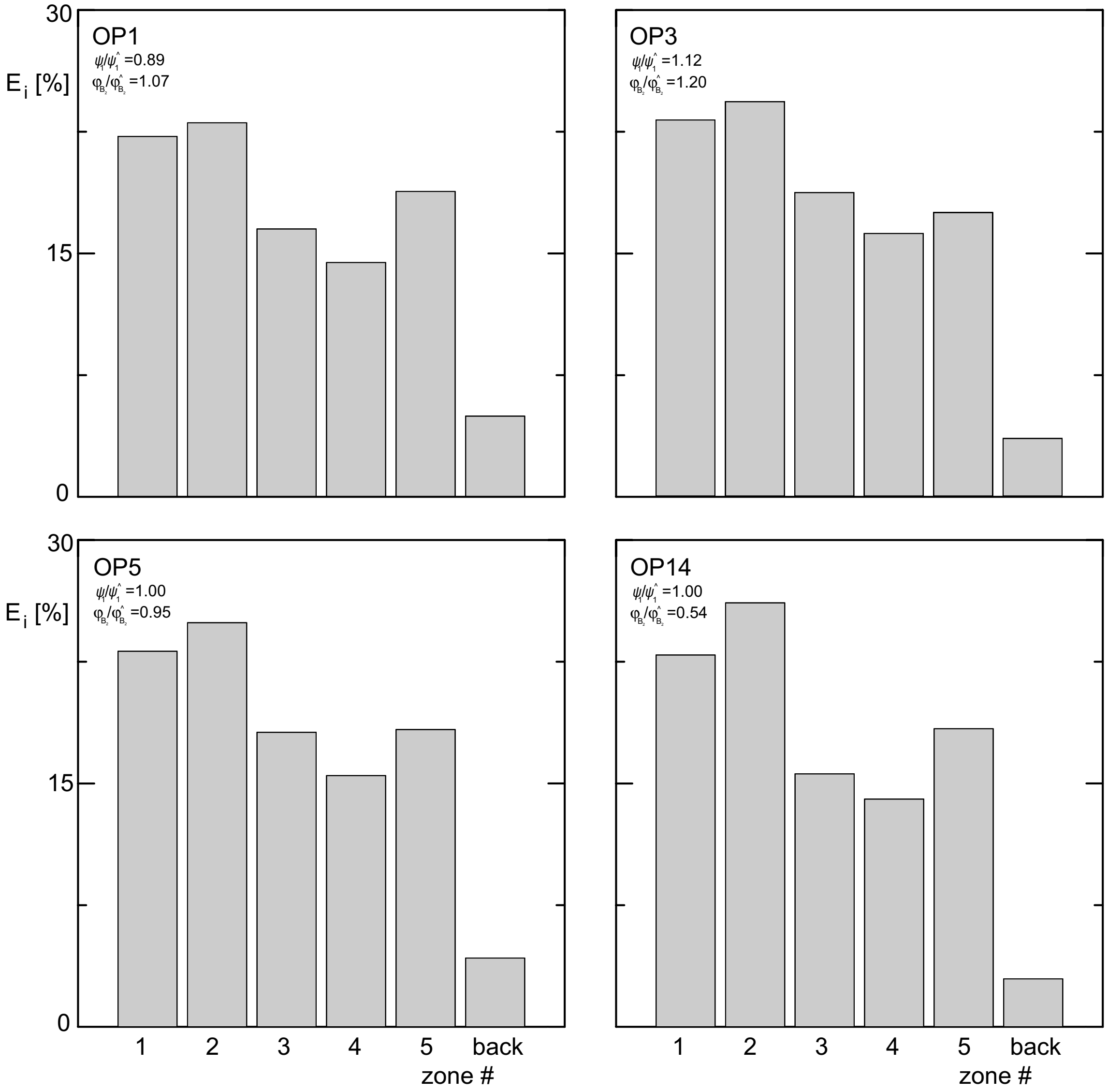

Figure 19.1: Bucket j energy distribution.

the flow is assumed to be accurately represented by successive steady state flow regimes:

$$\underbrace{\int\limits_{V_l} \rho \frac{\partial}{\partial t}(\overrightarrow{w}) dV}_{\rightarrow 0} + \underbrace{\int\limits_{S_l} \rho \overrightarrow{w}(\overrightarrow{w} \cdot \overrightarrow{n}) dS}_{deviation\ induced\ acceleration} = - \underbrace{\int\limits_{S_l} p \overrightarrow{n} dS}_{local\ driving\ force,\ \overrightarrow{F_{D_l}}} + \underbrace{\int\limits_{V_l} \rho \overrightarrow{g} dV}_{gravity} + \underbrace{\nu \int\limits_{S_l} \overrightarrow{\overrightarrow{\tau}} \cdot \overrightarrow{n} dS}_{viscous\ forces,\ \overrightarrow{F_{visc}}}$$
$$+ \underbrace{2\rho \int\limits_{V_l} (\overrightarrow{\omega} \times \overrightarrow{w} dV}_{Coriolis\ force,\ \overrightarrow{F_{Cor}}} + \underbrace{\rho \int\limits_{V_l} \overrightarrow{\omega} \times (\overrightarrow{\omega} \times \overrightarrow{r}) dV}_{Centrifugal\ force,\ \overrightarrow{F_{Cent}}} + \underbrace{\int\limits_{S_l} \sigma\left(\frac{1}{R_1} + \frac{1}{R_2}\right) \delta_{12} \overrightarrow{n} dS}_{surface\ tension\ force,\ \overrightarrow{F_\sigma}} \tag{19.3}$$

The driving force acting on sensor l surface then becomes:

$$\begin{aligned}\overrightarrow{F_{D_l}} = \rho \int\limits_{S_l} \overrightarrow{w}(\overrightarrow{w} \cdot \overrightarrow{n})dS - 2\rho \int\limits_{V_l} \overrightarrow{\omega} \times \overrightarrow{w}dV - \rho \int\limits_{V_l} \overrightarrow{\omega} \times (\omega \times \overrightarrow{r})dV - \rho \int\limits_{V_l} \overrightarrow{g}dV \\ - \nu \int\limits_{S_l} \overrightarrow{\overrightarrow{\tau}} \cdot \overrightarrow{n}dS - \int\limits_{S_k} \sigma(\frac{1}{R_1} + \frac{1}{R_2})\delta_{12}\overrightarrow{n}dS\end{aligned} \tag{19.4}$$

If the flow is globally dominated by the inertia and rotation-induced forces, depending on the angular instant of the duty cycle, the viscous and surface tension forces can become predominant, as seen in section 16.3. Nevertheless the driving force acting on sensor l at angular position θ_j can be accurately be approximated by:

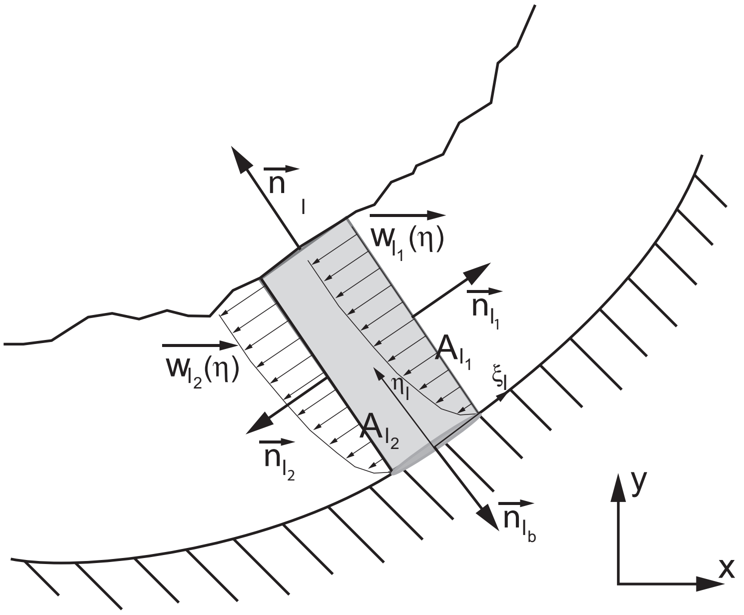

Figure 19.2: Sensor l volume of control.

$$\overrightarrow{F_{D_l}} \simeq \rho \int\limits_{S_l} \overrightarrow{w}(\overrightarrow{w} \cdot \overrightarrow{n})dS - 2\rho \int\limits_{V_l} \overrightarrow{\omega} \times \overrightarrow{w}dV - \rho \int\limits_{V_l} \overrightarrow{\omega} \times (\overrightarrow{\omega} \times \overrightarrow{r})dV. \tag{19.5}$$

19.2.1 Assessment test

Integrating Eq.19.5 on the volume of control situated at the location of pressure sensor 19 and film thickness measurement point 15 permits to assess the good agreement between the model and the measure during the main flow, while the accuracy decreases at the end of the duty cycle. The following assumptions are made: (i) the magnitude of the local relative speed is determined from the onboard observations; (ii) its direction is estimated from the observations; (iii) the sensor surface is square.

The results obtained for the 4 operating conditions investigated are displayed by Fig.19.3. The agreement between the local force calculated from the pressure measurement and the approximate Euler model is globally excellent. Figure 19.4 shows the evolution of the

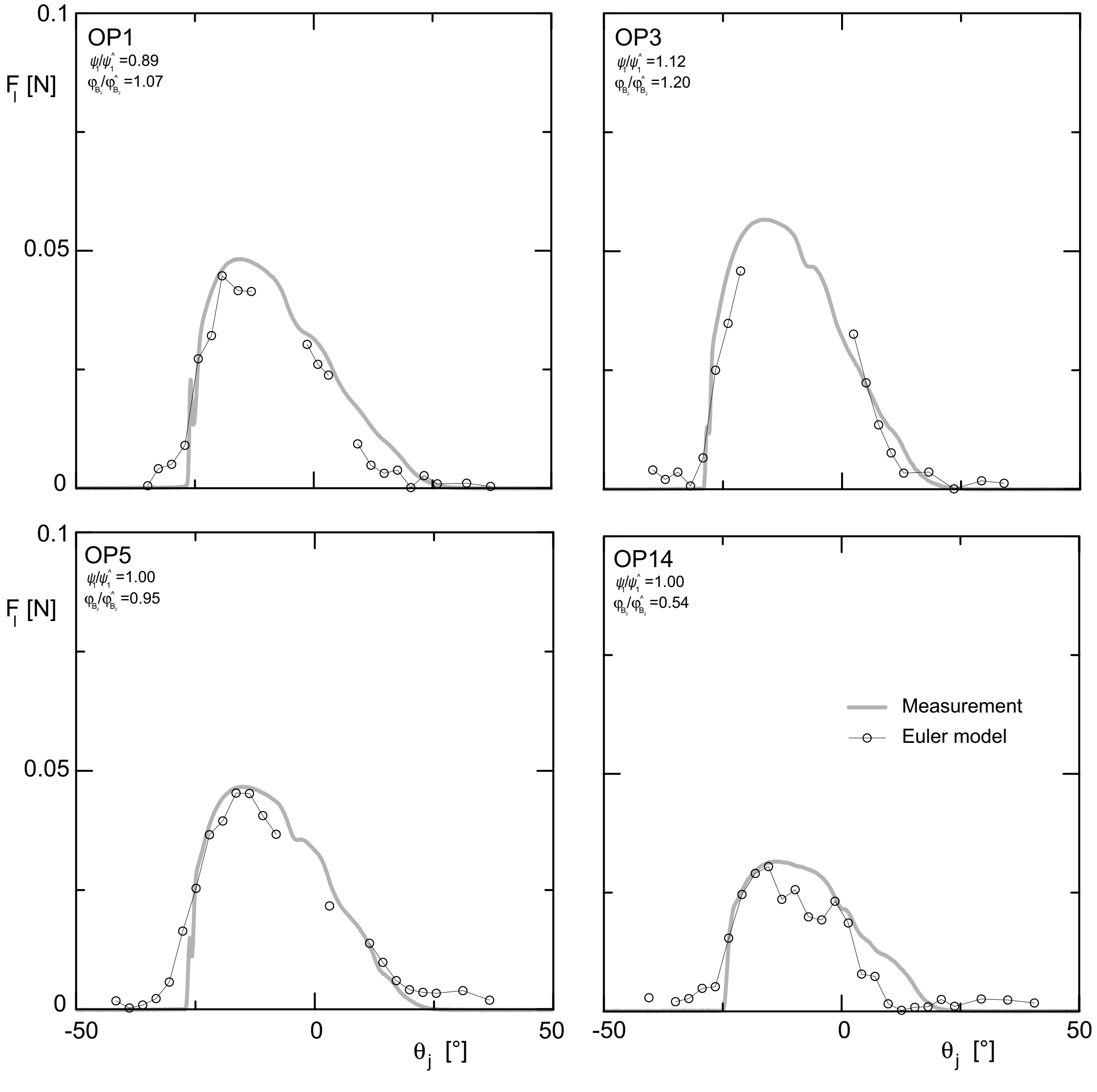

Figure 19.3: Euler Momentum transfer vs. force measurement, sensor 15.

magnitudes of the Coriolis, Centrifugal and surface tension forces throughout bucket j duty cycle. The main radii for the determination of the surface tension force are considered as $1/10th$ of the main bucket curvatures, *i.e.* $\frac{D_b-D_{root}}{2}$ and $\frac{B_2}{2}$ [117].

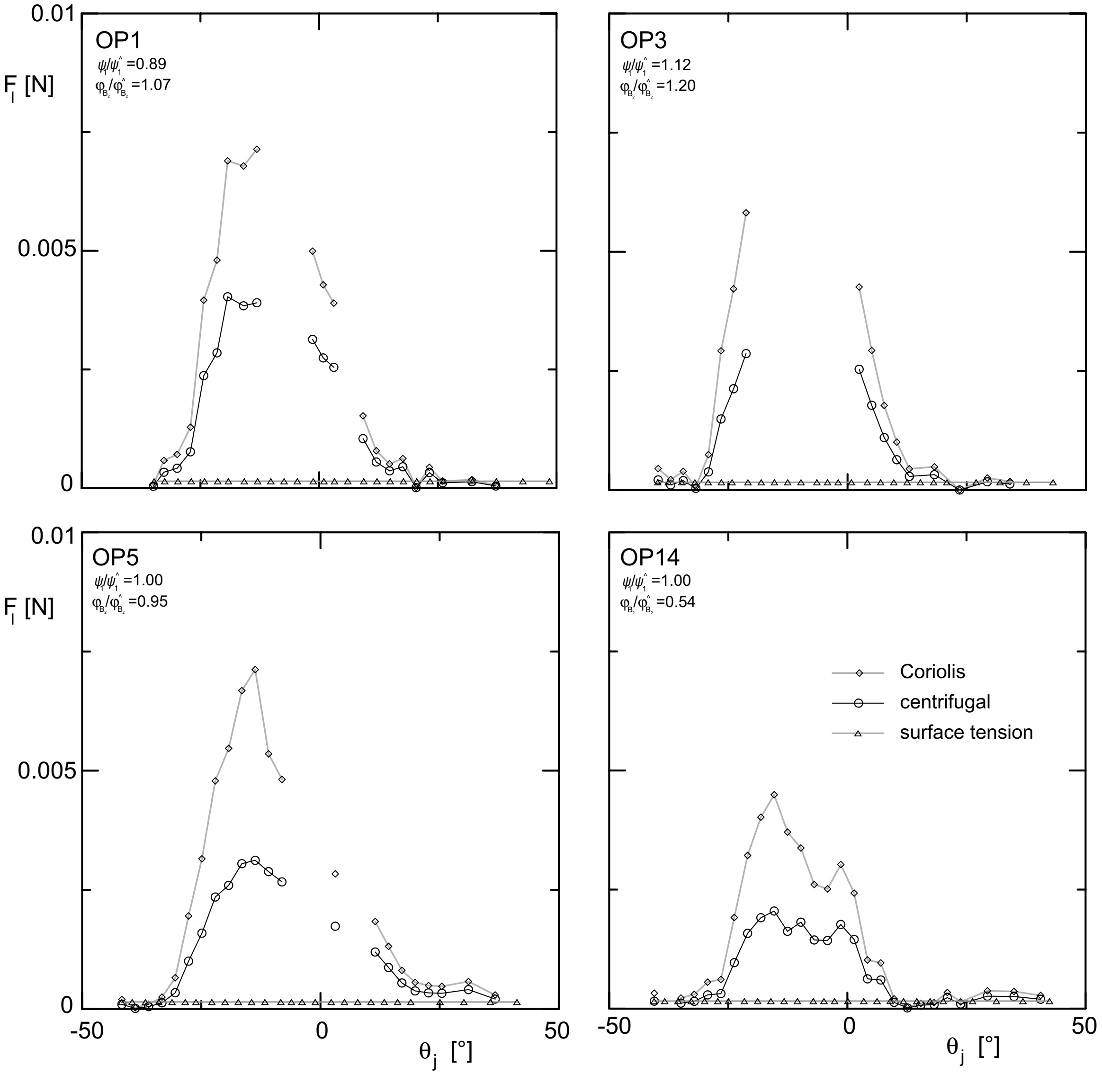

Figure 19.4: Force comparison, sensor 15.

SUMMARY AND CONCLUSION

Chapter 20

Summary and conclusion

20.1 Summary

In the framework of the present study, the transient free-surface flow in a rotating Pelton turbine bucket is thoroughly investigated with experimental approaches carried out in a rotating runner, *i.e.* (i) unsteady wall pressure measurements, (ii) flow visualizations, and (iii) water thickness measurements. The experiments are completed by transient numerical simulations.

20.1.1 Investigation tools

The unsteady pressure measurements are performed by installing 43 piezo-electric pressure sensors in machined buckets made of bronze. The pressure sensors are distributed so that to cover uniformly the inner surface (*i.e.* also along the splitter and in the cutout region), the backside and the lateral sides of the buckets. The LMH instrumented shaft permits the simultaneous recording of the signals of the sensors. The static calibration procedure demonstrate the excellent linearity of the sensors, their high degree of repeatability, and their small error ($\epsilon < 1\%$) in comparison with the reference instrument.

In order to perform high-speed onboard flow visualizations, a $3.8mm$ diameter borescope is fitted in the runner, with the distal lens located at the root of one half bucket. The high-speed camera itself, capable of recording up to $87'600$ frames per second, is kept outside the rotating parts of the Pelton test rig, the images being transmitted via a $90°$ optical deflector through the axis of the machine. The lighting is achieved by means of a pair of high-output xenon flashlights mounted in waterproof housings installed directly in the test rig casing, as close as possible to the runner. The flow observations are completed by a set of external visualizations carried out with a $10mm$ diameter borescope.

The water film thickness evolution in the bucket is determined by evaluating the apparent displacement of the observation grid by processing the images taken by the onboard visualization system. The apparent displacement is caused by the different indices of refraction of air and water.

Series of numerical simulations are made with increasing mesh sizes for 2 different numerical models, *i.e.* the 2-Phase Homogeneous Model and the 2-Fluid Model. The results obtained from both models are compared with the experimental data in terms of unsteady pressure, water film thickness, and water film topology. The 2-Fluid Model appears to provide the best results, while the 2-Phase Homogeneous Model is too dispersive. Indeed, the accuracy of the latter decreases significantly with the successive time steps.

20.1.2 Flow analysis

From the flow visualizations, the bucket duty cycle is divided in 6 steps. The main structures of interest are put into evidence for 4 different operating conditions.

The initial jet/bucket interaction, and more precisely the impact of the cutout lips on the jet boundary, is modelled by a $2D$ kinematical model. A hydroacoustical development show the possible occurrence of compressible effects at the initial moments of the impact, generating locally high pressure peaks, and thus erosion damages, and a lateral outburst of the jet.

Due to the lateral jet outburst, and the bucket longitudinal curvature, the bucket inner surface acts as a spillway. The jet front overflies the bucket, and forms a rear-facing splay crown, where a strong aeration process takes place.

The aerated splay crown is responsible for the apparition of a high-pressure pulse upon impact on the bucket inner surface, as showed by the synchronization of the pressure signals with the onboard visualizations. The impact pressure strongly depends on the energy coefficient, *i.e.* the angle of impact. The pressure pulse appears because the air-water mixture acts as a compressible fluid. A waterhammer effect arises thus in the jet, generating the pressure pulse, the pressure waves being in turn released across the free-surface of the jet as a radial outward flow animated by a very high velocity. An iterative process is set-up to estimate the real pressure pulse amplitude because the measured signal is under-sampled. It appears that pressures up to 2 times the stagnation pressure can be reached.

The cut portion of the jet adheres to the bucket backside. At the beginning of the duty cycle, the relative angle of attack of the bucket corresponds that of an hydrofoil at a high angle of attack. The backside acts as the suction side of that pseudo-hydrofoil. A Coanda interaction takes place. The associated depression in turn generates a lift force, that contributes positively on the bucket torque. The separation of the jet occurs for about the same angle of attack whatever the operating conditions for a given test head. The separation angle of attack is equivalent to that obtained in flat flap Coanda experiments. The test head appear to considerably influence the backside flow: the separation is delayed for the lower test heads, while cavitation onset is promoted by the higher test heads. Cavitation reduces the positive torque contribution, and promotes erosion damages. The CFD results show a lack of accuracy in the backside region: the depression amplitude and the the separation line are not satisfactorily predicted. This can be explained by the not enough detailed physical models. The pressure amplitude issue is probably related to the absence of cavitation model, while the separation line location is related to the modelling of the triple-line problem, *i.e.* water-solid-air. Indeed, the free-surface flow separation is dependent on (i) the liquid-wall adhesion and (ii) the surface tension. The most critical issue would to develop a wall adhesion model based on the actual Young's angle [34].

The bucket bulk flow, that transits on the inner surface of the buckets, seems not to be influenced by test head changes within the range investigated. The water film spread rate in the bucket appears to be independent on the discharge, except for the lower discharge coefficients. The mixing losses can be associated with (i) the kinematic conditions, (ii)

the unexpected crossing of streamlines, and (iii) flow interferences due to the deformation of the jet on the backside. The end of the evacuation process of the water reveals a stratification of the flow, with layers moving with directions diverging by up to $\sim 30°$.
The bucket side pressure measurements identify the outflow heeling to be characterized by a stagnation pressure in the lowest regions followed by a depression in the upper region. The consequences on the runner in terms of performances are notwithstanding difficult to assess.
An analysis of the bucket power budget highlights the important contribution of the central area: it accounts for $\sim 70\%$ of the power transferred from the fluid to the bucket. The power signal of the whole runner determined from the measurements show important fluctuations that are strongly dependent on the operating conditions. For the lower energy coefficients, the pressure pulse modulates the whole power signal of the runner. A spectral analysis obtained by FFT evidences that the harmonic contain of the power signal is inversely proportional to the efficiency.
The energy balance of the bucket indicates, that under normal operating conditions, *i.e* close to the best efficiency conditions, the energy distribution is well balanced on the bucket surface, while for the lower discharge conditions, most of the energy transfer occurs in the zones where the feeding process starts.
The Momentum conservation equation integrated over a small volume of control located on top of any pressure sensor permits to monitor the respective influence of the different forces acting on the flow with respect with the bucket angular position. Even if globally the inertia forces dominate, *i.e* the deviation, Coriolis and centrifugal forces, the viscous and surface tension forces outweigh the formers at the end of the evacuation process.

20.2 Contribution of the present work

The present work emphasizes the wide range of time constant scales present in the Pelton turbine bucket flow. Each physical phenomenon involved has its own time and length constants: the compressible effects only last a small fraction of the bucket duty cycle, *i.e.* a few μs, while cavitation and surface tension last 2 orders of magnitude more time.
The scaling effects are difficult to assess, because most of the phenomena involved have an influence on the other ones. For instance, the jet spread and surface quality are influenced by the inertia and surface tension, *i.e.* the Reynolds and Weber numbers. Indeed, the higher the Weber number, the smaller the size of the structures convected by the jet. In turn, the jet topology influences the conditions of the initial impact between the bucket lips and the jet, *i.e.* the Mach number. The bucket bulk flow is most influenced by the inertia forces and the rotation forces, *i.e* the Reynolds and Rossby numbers. The backside flow is influenced by inertia, surface tension and cavitation,*i.e.* Reynolds, Weber and σ_i. The flow stratification is influenced by the Reynolds and Rossby numbers.
It appears, however, that a good understanding and control of the jet is paramount to achieve high efficiencies. The jet must be clean, free from dispersion, and protected from water projections or else the most perfect bucket in the world will not reach the expected performances. Jet spread and perturbations promote the risks of shock-induced erosion of the bucket lips.
The high-pressure pulse is strongly affected by the initial jet/bucket interaction. Its in-

fluence on the bucket torque and power signal should be kept in mind at the stage of performing mechanical dimensioning of the bucket.

The results obtained for the backside flow indicate that the backside cutout area plays an non-negligible role in the energy transfer. It acts as a hydrofoil undergoing the Coanda effect, thus generating lift, and from that positively contributes to the bucket torque. Nevertheless, the Coanda effect induces deformations of the jet, *i.e.* a bending and an enlargement, that have to be taken into account during the design phase. Also, a compromise has to be found to avoid the onset of cavitation, and promote a neat separation early enough to avoid prohibitive mixing losses.

The outflow heeling appears to act positively on the runner performance by scavenging some of the kinetic energy of the water sheets otherwise lost. This indicates that some heeling could be desirable to improve the performances of Pelton turbines. The concerns lie within the risk of cavitation onset and thus erosion damages.

The Momentum exchange analysis shows that since the flow is dominated by inertia forces, Euler models are adequate to obtain first order approximations of the bucket flow. This explains why the classic design methods permit to obtain machines of fair efficiency. But, it also emphasizes that obtaining real improvements requires to adequately take in to account the second order forces, *i.e.* surface tension and viscosity.

20.3 Perspectives

The complexity inherent to the free-surface rotating flow in the Pelton turbine buckets calls for further investigations, both experimentally and numerically.

20.3.1 Experiments

As far as experiments are concerned, the different phenomena highlighted by this study should be investigated separately into more details and in a more fundamental fashion.

- **Jet**. The jet should be examined to verify the influence of the pressure waves generated by the impingement on the bucket, and determine if they can trigger the apparition of perturbations up to the injector nozzle. The diffusion layer build-up should be investigated in order to determine the radial speed of sound, and the pressure waves propagation.

- **Impact problem**. The pressure distribution on the bucket lips during the initial jet/bucket interaction should be measured by means of pressure sensitive materials, like PVDF [79], [68], and with a higher sample rate.

- **Jet separation**. The jet separation process should be investigated more thoroughly. Series of visualizations with more precise angles of view for different test heads are to be performed. A study should conducted to test different bucket backside geometries, thus finding out the best compromise in terms of positive torque contribution, small deformation and neat separation.

20.3.2 Numerical simulation

Classic CFD

In the short term, the 2-Fluid Model computation should be run with a larger number of iterations to reach a complete convergence and determine more precisely the origin of the faked compressibility. Actually the 3 main issues to be addressed are (i) the dispersion of the jet, (ii) the triple line model, and (iii) the cavitation. The triple-line problem can be solved by using a realistic wall adhesion model based on Young's angle definition. Encompassing more physics in the modelling is paramount to more accurately determine the pressure distribution on the backside.

The main drawback associated with the classic CFD approaches for the simulation of Pelton turbines is the need for refined meshes in the whole domain, while the regions of interest for any given time step only represent a fraction of the latter. This dramatically increases the computational cost required to reach satisfactory predictions. Accurate numerical simulations of full-scale facility appears therefore highly difficult.

Particle Models

Meshless Lagrangian particle-based methods appear to be promising approaches to address the problem of mesh resolution associated with the classic CFD. In fact, the results obtained by the SPH [73], [72] and the MPS [78], [77] methods are encouraging. Once correctly validated, these methods will permit less expensive simulations, even for full-scale problems.

They could be useful to obtain the correct streaklines of the various particles. The analysis of the Momentum conservation along these streaklines will provide a complete energy transfer survey in the bucket.

20.3.3 Optimum design

The knowledge of the various particle streaklines will in turn permit the use of optimum design methods based on genetic algorithms [27] to shape the bucket surface in order to reach the highest momentum transfer between the flow and the bucket and thus improving the efficiency, while reducing the mixing losses between the adjacent water filaments.

APPENDICES

Appendix A

Signal processing

A.1 Average and standard-deviation

Let numerical signal $u_n, n = 1, 2, ..., N$ be. The N values are obtained by sampling at time intervals of δt seconds. The values associated with time are:

$$t_n = t_0 + n\Delta t \qquad n = 1, 2, ..., N, \tag{A.1}$$

where t_0 is an arbitrary time reference. Thus, value u_n is expressed as:

$$u_n = u(t_0 + n\Delta t) = u(n\Delta t) \qquad n = 1, 2, ..., N. \tag{A.2}$$

The total length recorded corresponds to $T = N\Delta t$.
The average of the sampled values u_n is given by:

$$\overline{u} = \frac{1}{N}\sum_{n=1}^{N} u_n. \tag{A.3}$$

Equation A.3 is used to obtain the average of static signals, and the variance is defined by:

$$s^2 = \frac{1}{N}\sum_{n=1}^{N}(u_n - \overline{u})^2. \tag{A.4}$$

Moreover, to treat steady random numerical signals, it is better to transform value u_n into a new series of values x_n referred to zero, by calculating:

$$x_n = x(t_0 + n\Delta t) = u_n - \overline{u} \qquad n = 1, 2, ..., N, \tag{A.5}$$

where $\overline{x} = 0$. The associated standard-deviation is therefore expressed as:

$$\sigma = \sqrt{\frac{1}{N}\sum_{n=1}^{N} x_n^2} \tag{A.6}$$

A.2 Phase average

Phase averaging is a powerful tool to study periodic signals. The technique consists in dividing a recorded signal $x(t)$ in n_d independent segments of a length equal to the period T of the phenomenon under consideration. Each segment of signal $x_i(t)$, $i = 0, 1, ..., n_d - 1$ consists of m samples. The phase average is then the average of each sample $j, j = 0, 1, ..., m-1$ that corresponds to each segment i, such that:

$$\overline{x}_j(t) = \frac{1}{n_d} \sum_{i=0}^{n_d-1} x_i(t_j), \qquad j = 0, 1, ..., m-1 \tag{A.7}$$

The result of the phase average of signal $x(t)$ on period T, or $\overline{x_T}(t)$, has 3 components: (i) a mean component $\overline{x}$, (ii) a periodic fluctuating component $\widetilde{x}(t)$, and (iii) the noise component $n(t)$, that includes all the periodic fluctuations that are independent of the signal period T.

$$\overline{x}_T(t) = \overline{x} + \widetilde{x}(t) + n(t) \tag{A.8}$$

The number of segments n_d must be large enough to reduce the noise $n(t)$ to only evidence the information stemming from the signal periodicity.

A.3 Fourier transform

The goal is to express a complex function as a simple linear combination. Let $x(t)$ be a function such that:

$$x(t) = \sum_{i=0}^{\infty} \alpha_i \Psi_i, \tag{A.9}$$

where functions Ψ_i are a set of elementary functions. If the functions are orthogonal, the coefficients α_i are independent. This is referred as a development in orthogonal functions; the best known is the Fourier series. When the Fourier series is generalized to represent a finite interval, the Integral Fourier Transform is obtained, a complex periodic function expressed as:

$$X(f) = \int_{-\infty}^{+\infty} x(t) e^{-j2\pi f t} dt. \tag{A.10}$$

The Fourier Transform can be represented in a finite interval, such that:

$$X(f, T) = \int_{0}^{T} x(t) e^{-j2\pi f t} dt. \tag{A.11}$$

The discrete form of the Fourier Transform is:

$$X(f) = \sum_{t=-\infty}^{+\infty} x(t) e^{-j2\pi f t}. \tag{A.12}$$

From Eq.A.1, such that $t_n = n\Delta t$, $n = 0, ..., N-1$, the following discrete relation is obtained:

$$X(f, T) = \Delta t \sum_{n=0}^{N-1} x_n e^{-j2\pi f t} \tag{A.13}$$

A.4 Spectral analysis of random signals

The term $X(f)$ in Eq.A.10 is a complex function that can be expressed as a function of its real and imaginary parts:

$$X(f) = Re[X(f)] + jIm[X(f)]. \tag{A.14}$$

For a real signal $x(t)$, the real and imaginary parts are respectively expressed as:

$$Re[X(f)] = \sum_{t=-\infty}^{+\infty} x(t)\cos 2\pi ft \tag{A.15}$$

and

$$Im[X(f)] = -\sum_{t=-\infty}^{+\infty} x(t)\sin 2\pi ft \tag{A.16}$$

It is also possible to express the term $X(f)$ as a function of its module and argument:

$$X(f) = |X(f)|e^{j\arg[X(f)]}, \tag{A.17}$$

where $|X(f)|$ is referred as amplitude spectrum, and represent the repartition in the frequency domain of the amplitude of signal $x(t)$. The phase spectrum, $\arg[X(f)]$, expresses the repartition in the frequency domain of the phase of signal $x(t)$. $|X(f)|^2$ is called energy spectrum. The energy spectrum expresses the repartition of the energy in the frequency domain of signal $x(t)$.

A.4.1 Hanning's Window

To suppress discontinuities at the beginning and at the end of a recorded signal, a time window is introduced to record the time-history of the variables. The most known is the Hanning's window:

$$u_h(t) = \begin{cases} \frac{1}{2}(1 - \cos\frac{2\pi t}{T}) = 1 - \cos^2(\frac{\pi t}{T}) & 0 \leq T \\ 0 \text{ otherwise} \end{cases} \tag{A.18}$$

To avoid discontinuities, the spectral density is determined from the Fourier transform using Eq.A.18. It has been shown that to compensate the losses due to the windowing, $X_i(f_k)$ must be multiplied by scale factor $\sqrt{\frac{8}{3}}$. The result is then:

$$X_i(f_k) = \Delta t\sqrt{\frac{8}{3}}\sum_{n=0}^{N-1} x_{in}\exp\left(\frac{-j2\pi kn}{N}\right) \tag{A.19}$$

More details about signal processing can be found in [8] and [63].

Appendix B

Measurement error assessment

A measurement system is constituted by a chain of components, each with its own inaccuracy. The goal is to determine the overall inaccuracy of the whole system. Let consider a parameter N, function of N independent variables u_1, u_2, u_3, ... u_n:

$$N = f(u_1, u_2, ...u_n) \tag{B.1}$$

The individual errors $\pm\Delta u_1$, $\pm\Delta u_2$, will induce the error $\pm\Delta N$. They can be either absolute values or statistical limits like a standard-deviation. Considering the $\pm\Delta u_i$ as absolute limits of the individual errors, the absolute limits of the error N can be calculated by:

$$N \pm \Delta N = f(u_1 \pm \Delta u_1, u_2 \pm \Delta u_2, ..., u_n \pm \Delta u_n) N \pm \Delta N - N = \pm\Delta N \tag{B.2}$$

An approximate solution can be obtained using the Taylor series [107]:

$$\begin{aligned} &f(u_1 \pm \Delta u_1, u_2 \pm \Delta u_2, ..., u_n \pm \Delta u_n) \\ &= f(u_1, u_2, ..., u_n) + \Delta u_1 \frac{\partial f}{\partial u_1} + \Delta u_2 \frac{\partial f}{\partial u_2} + ... + \Delta u_n \frac{\partial f}{\partial u_n} + \\ &\qquad \frac{1}{2}[(\Delta u_1)^2 (\frac{\partial f}{\partial u_1})^2 + \Delta u_2)^2 (\frac{\partial f}{\partial u_2})^2 + ... + \Delta u_n)^2 (\frac{\partial f}{\partial u_n})^2] \end{aligned} \tag{B.3}$$

where all the derivatives are calculated for the known values of the u_i. Assuming the Δu_i to be small, the $(\Delta u_i)^2$ terms are negligible. The absolute error is then given by

$$\Delta N = |\Delta u_1 \frac{\partial f}{\partial u_1}| + |\Delta u_2 \frac{\partial f}{\partial u_2}| + ... + |\Delta u_n \frac{\partial f}{\partial u_n}| \tag{B.4}$$

Equation B.4 features the variables having the most significant influence on the total error [83].

Appendix C

Free water jet

C.1 Jet boundary stratification

Whenever high-speed water jets are discharging into the atmosphere, air bubble entrainment occurs along the air-water interface [41]. Free-surface aeration along the jet interfaces reduces the jet Momentum, Fig.C.1. Three basic flow regions are defined [17]: (i) approach flow region, *i.e.* the flow upstream of the injector; (ii) transition region, *i.e.* flow in the nozzle itself; (iii) aeration flow region. At the edge of the deflector or jet nozzle, a pressure change from the inlet pressure dictated by the total hydraulic energy to a zero pressure gradient. At the beginning of the jet, there is a clear water core, surrounded by an enlarging aerated layer. If the jet is long enough a fully-aerated flow region starts developing downstream of the point where the central portion of the jet becomes aerated.

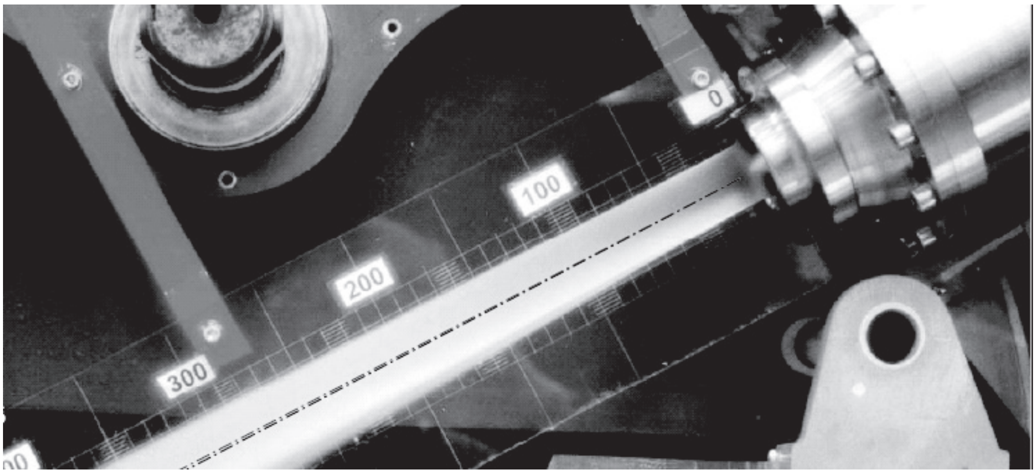

Figure C.1: Jet out of a Pelton turbine injector (Courtesy of VATech Hydro SA).

C.2 Fundamental equations

The air-bubble entrainment along the jet interfaces can be described by means of the continuity equation for air:

$$\overrightarrow{\nabla}(\alpha \overrightarrow{c}) = \overrightarrow{\nabla}(D_T \cdot \overrightarrow{\nabla} \overrightarrow{c}), \tag{C.1}$$

where α is the air content, *i.e.* the void fraction, $\overrightarrow{c}$ the jet velocity and D_T the turbulent diffusivity. For a circular water jet, the continuity equation for air becomes:

$$\frac{C_x}{D_{T_r}} \frac{\partial \alpha}{\partial x} + \frac{\alpha}{D_{T_r}} \frac{\partial c_c}{\partial x} = \frac{1}{r} \frac{\partial}{\partial r} r \frac{\partial \alpha}{\partial r}. \tag{C.2}$$

Equation C.2 assumes a constant diffusivity in the radial direction and is applied to a small control volume along a stream tube. The solution of Eq.C.2 is a series of Bessel functions[17]:

$$\alpha = 0.9 - \frac{1.8}{r_{90}} \cdot \sum_{n=1}^{+\infty} \frac{J_0(rA_n}{A_n J_1(r_{90} A_n)} \exp\left(- \frac{D_T}{C_0} \cdot A_n^2 \cdot x \right), \tag{C.3}$$

where C_0 is the flow velocity at the nozzle, r_{90} is the radial distance from the jet axis where $\alpha = 0.9$, J_0 is the Bessel function of the first kind of order zero, A_n is the positive root of $J_0(r_{90} \cdot A_n) = 0$, and J_1 is the Bessel function of the first kind of order one. Equation C.3 is valid in either the partially-aerated and fully-aerated flow regions. For the $2D$ water jets, the analytical solution of Eq.C.1 in the partially aerated flow region yields:

$$\alpha = \frac{1}{2} \left\{ 1 - erf\left(\frac{r - y}{2\sqrt{\frac{D_T}{C_0} x}} \right) \right\}, \tag{C.4}$$

where the function erf is defined as:

$$erf(u) = \frac{2}{\sqrt{\pi}} \int_0^u \exp(-t^2) dt. \tag{C.5}$$

Equation C.4 was derived and applied by Chanson [17] assuming $\frac{\partial \alpha}{\partial x} \ll \frac{\partial \alpha}{\partial y}$.

C.3 Turbulent diffusivity

D_T averages the effect of the turbulence and of the longitudinal velocity gradient. It is related to the cross-correlation between fluid displacement and the velocity. For circular jets, D_T is deduced from the experimental data, while for $2D$ jets, the turbulent diffusivity at the free-shear layer air-water interface D_T is estimated as:

$$D_T = 0.5 \frac{C_0 \cdot x}{1.2817} (\tan^2 \psi). \tag{C.6}$$

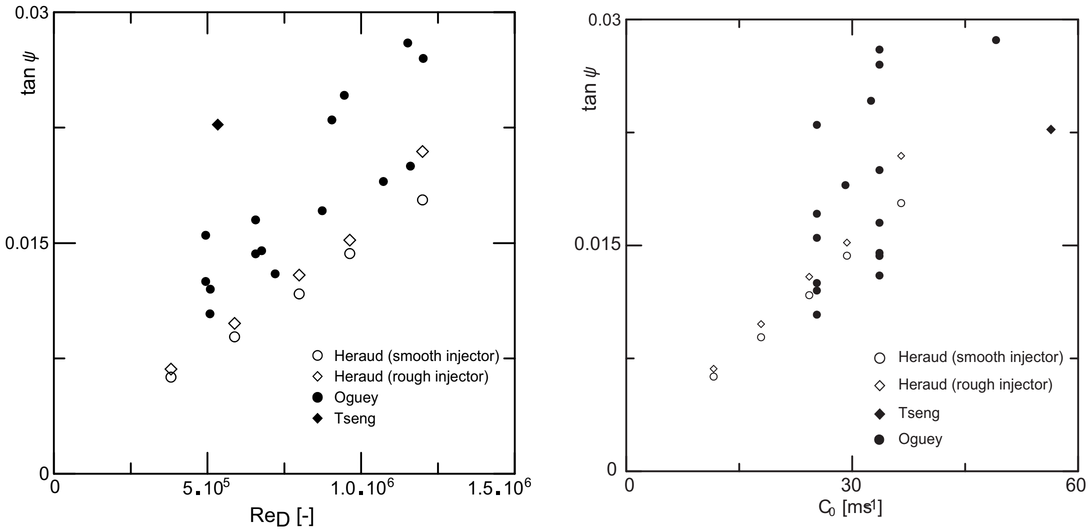

(a) Reynolds number. (b) Jet velocity.

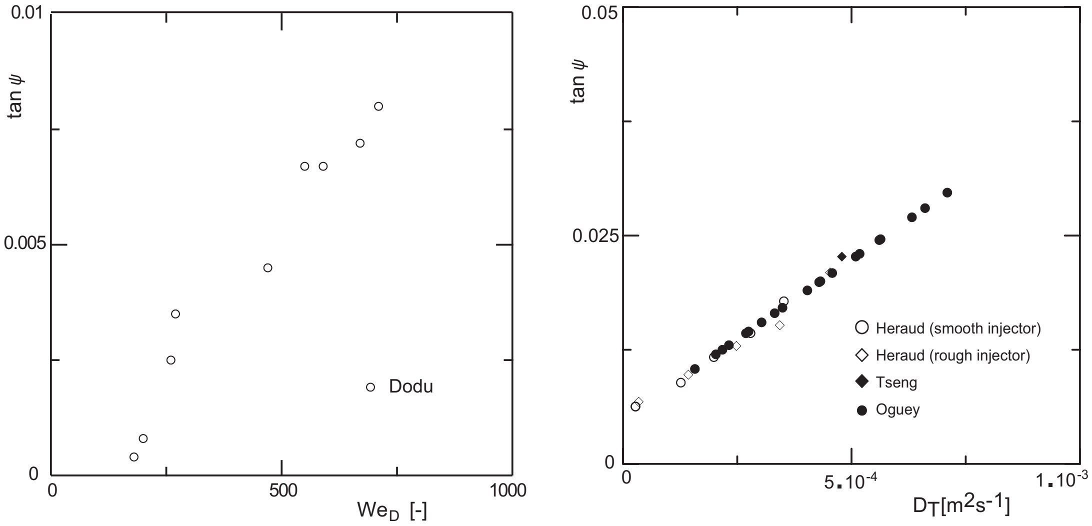

(c) Weber number. (d) Turbulent diffusivity.

Figure C.2: Jet spread angle dependence.

C.4 Spread angle

The spread angle ψ of the air-bubble diffusion layer provides some information on the rate of diffusion of air bubbles. Figure C.2 shows the respective dependence of: (a) the Reynolds number; (b) the jet velocity; (c) the Weber number, and (d) the turbulent diffusivity for 5 sets of different experimental data performed on circular jets. The spread angle ψ appears to be linearly related to the turbulent diffusivity, and can be estimated as:

$$\tan\psi = 34.95 D_T + 0.05. \tag{C.7}$$

The results show little scatter for inlet velocities below $40 m/s$. The regression curve equation is:

$$\tan\psi = 5 \cdot 10^{-4} c_0. \tag{C.8}$$

The correlation with the Weber number is much better than with the Reynolds number [23], but for the later the variety of the results compiled implies great differences in the nozzle sizes and shapes.
Ruff *et al.* [95] and Tseng *et al.* [108] investigated the effects of inflow conditions on the atomization process. They showed that the air-diffusion process is considerably enhanced with fully-developed inflow conditions. The length of the clear water core is shorter and as air-bubbles diffuse rapidly inside the jet. Applications of these results imply that Pelton turbine jets and water cutting jet must be designed with uniform inflow conditions [23]. This is obtained by designing a smooth nozzle shape with a large contraction ratio [45], installing a calming section upstream of the nozzle, *i.e.* with flow straighteners, and reducing the flow turbulence in the water supply system.

C.5 Application to the case studied

The results obtained can be used to estimate the most probable flow characteristics of the water jet feeding the studied runner. The diffusion layer thickness and void fraction radial evolution can be computed from Eq.C.3. The spread angle is assumed to be equivalent to the that measured by Oguey [81] for a similar setup. The jet void fraction profile evolution along the axis is represented by Fig.C.3.

C.6 Speed of sound and void fraction

It is known in the literature that the presence of small amounts of gas in a liquid reduces significantly the velocity at which pressure or sound waves can travel through the mixture [20]. Brennen [14] developed an analytical model describing the evolution of the mixture speed of sound with the volume fraction of air in the mixture, assuming a homogenous mixture of small air bubbles and water.

$$a = \left\{ (\rho_l(1-\alpha_g) + \rho_g\alpha_g \left(\frac{\alpha_g}{np} + \frac{1-\alpha_g}{\rho_l \alpha_l^2} \right) \right\}^{-1/2}, \tag{C.9}$$

where the subscripts l and g refer respectively to the liquid and the gas, n is the polytropic index and p the absolute pressure. Equation C.9 clearly exhibits one of the most remarkable feature of the sonic velocity of a gas/liquid mixture: the speed of sound of the mixture can be much smaller than that of either of its constituents. Figure C.4 represents the speed of sound of a air-water mixture plotted against the mixture void fraction, *i.e.* the volume fraction of air. Sonic velocities as low as $20 m/s$ can occur.

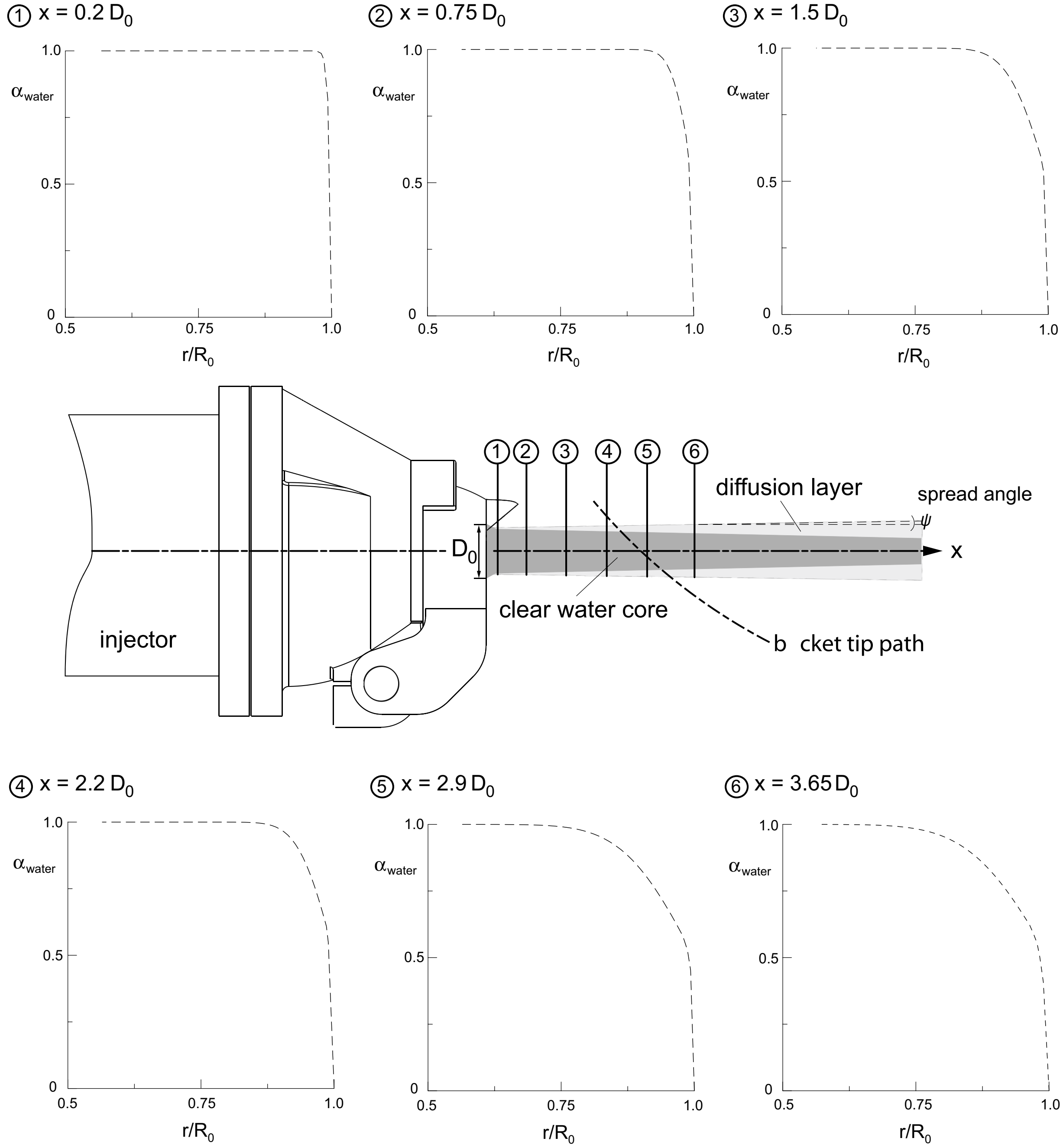

Figure C.3: Jet spread and radial void fraction estimation.

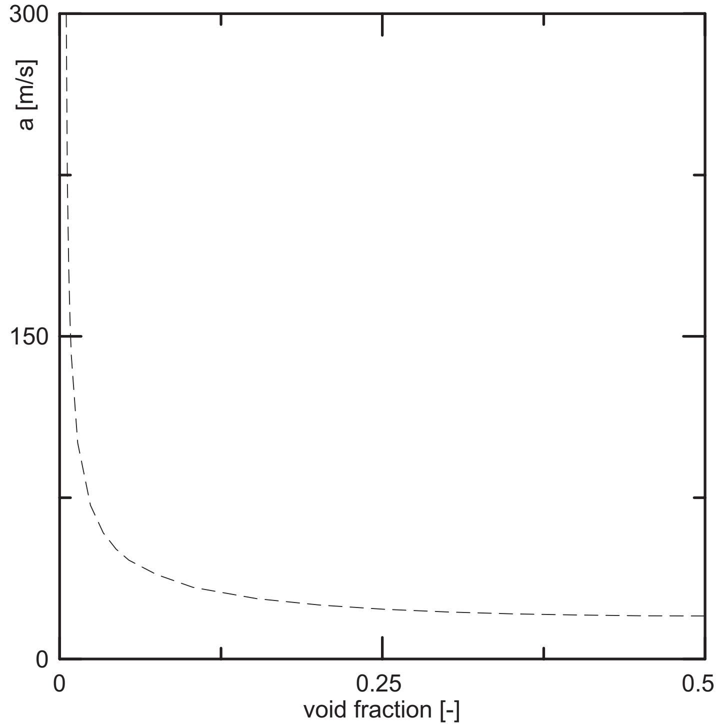

Figure C.4: Speed of sound for air-water mixtures.

Appendix D

Coanda effect

D.1 Definition

The Coanda effect may be described as the phenomenon by which the proximity of a surface to a jet stream will cause the jet to attach itself to and follow the surface contour [120]. When such a surface is placed at an angle to the original jet or nozzle exit, the jet stream will be deflected. Figure D.1 illustrates the Coanda effect between a cylinder and a vertical jet. Two main contributory effects have been identified. (i) The curvature forced upon the jet by the convex body, which is associated with a pressure field involving increased suction forces on the side of the body facing the jet. This effect is satisfactorily explained by the classical potential theory. (ii) Entrainment of fluid into the jet due to turbulent mixing. This induced flow, directed towards the jet, leads to a force on the body

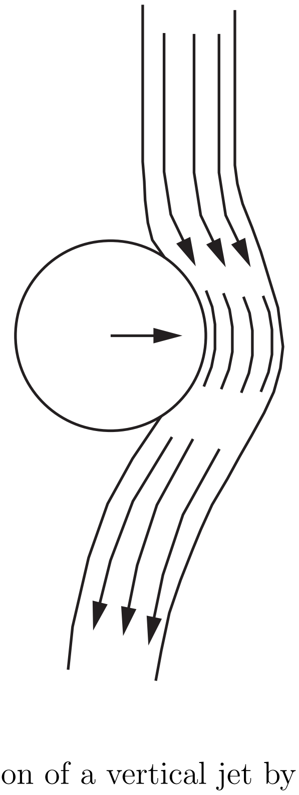

Figure D.1: Deflexion of a vertical jet by a cylindrical body.

in the same direction. This effect thus requires the consideration of viscous phenomena for its explanation.

D.2 Potential flow problem

The potential-flow part of the problem is concerned with with a jet which has a free boundary on one side and a solid wall on the other. In the absence of an external stream, the pressure must be constant along the free boundary, it must be lower than this value along the wall. Separation implies that the pressure at the separation line and also downstream of it along the inner free surface of the jet must be equal to the undisturbed pressure again. Therefore, the pressure distribution along the wall must have an adverse pressure gradient towards the separation line.

D.3 Viscous flow problem: boundary layer along a curved wall

The viscous-flow part of the problem is therefore concerned not only with entrainment effects but also with the development of the boundary layer along the wall, since the latter must be expected to determine the position of the separation line. The boundary layers may differ essentially in some respects from the classical boundary layer along a plane wall, as can be seen on Fig.D.2. Cases (a) and (c) represent the probable shapes of the boundary layer that may develop with a thick jet in relation to the radius of curvature of the wall, with a conventional boundary layer underneath and a free shear layer above. The pressure field along the wall is essentially that obtained from the potential-flow theory. Cases (b) and (d) show the profiles due to thinner jets. The flows there are essentially rotational, and as a consequence, the pressure field even in an inviscid rotational curved flow will differ from that in a corresponding irrotational curved flow. Matters may be further complicated by the presence of a step or a gap between the jet and the wall, as the velocity profile my become fully developed in the jet. Furthermore, the wall curvature may most probably invalidate the assumption, usually made in boundary layer theory, that the pressure remains constant across the boundary layer.

D.4 Inviscid wall-jet

The potential flow solutions developed by Lighthill and Woods [120] showed that for each given value of the deflexion angle of the jet a particular shape of the curved wall is obtained together with the positions of the attachment and separation lines. They explained that the adverse pressure gradient upstream of separation is unlikely to cause an early separation because the pressure at and near this hypothetical point would be less than the pressure of the air outside, and this would suck the jet back again on to the surface.

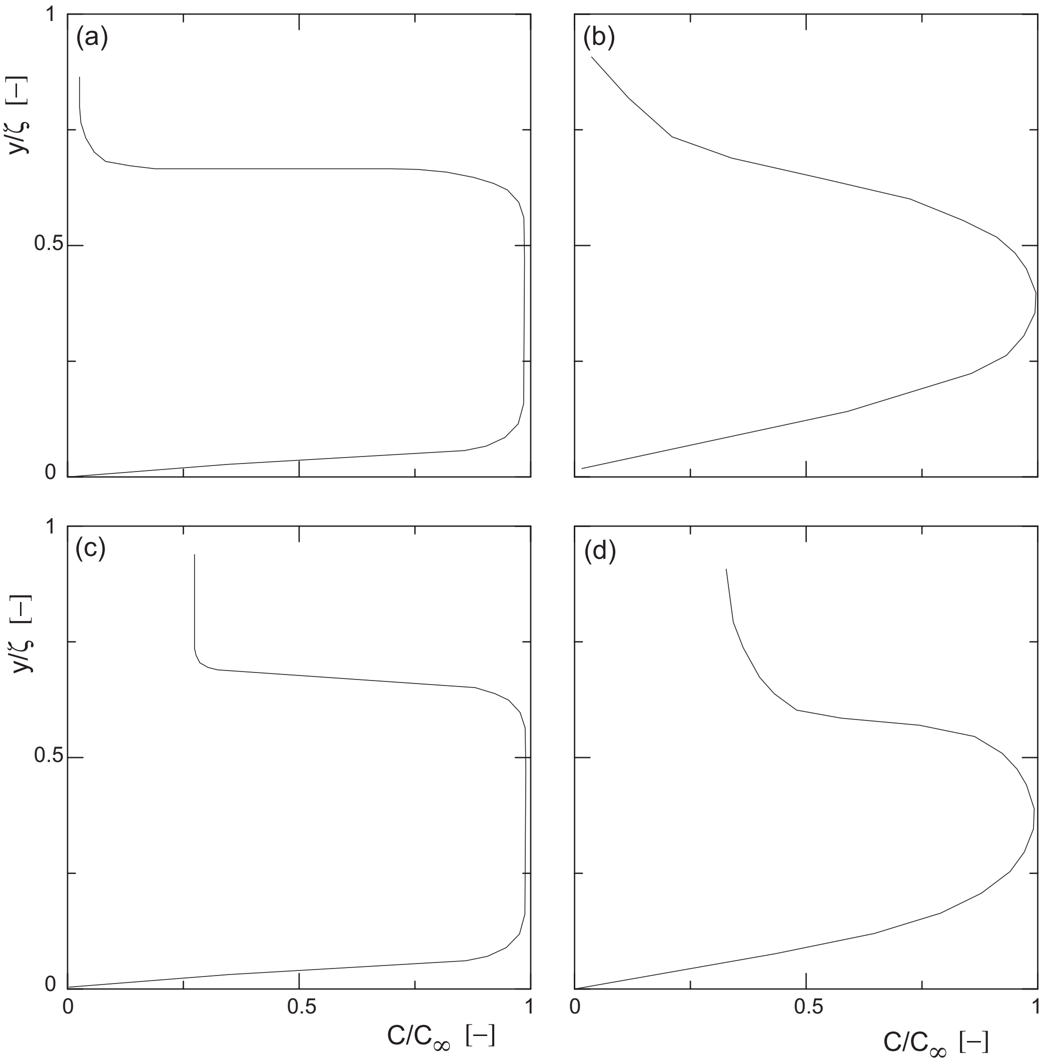

Figure D.2: Possible types of velocity profiles in the Coanda effect.

D.5 Influence of the Reynolds number

Experimental results for a $2D$ flow with the cylinder not only tangential to the jet but also penetrating into it are discussed by Fernholz [120], see Fig.D.3. The penetration ratio, t/h, jet thickness ratio, R/h, and the Reynolds number of the jet were varied. The pressure distribution around the cylinder is found to strongly depend on t/h and on R/h for the lower range of values of this parameter. A value of $t/h \simeq 0.4$ induces the largest deflexion angles. Conditions of separation occurs when R/h becomes too small or t/h too large [114].

D.6 Free-surface flows

The flow is subject to capillary and surface tension, friction and air forces to a small extent. The separation of the liquid from the wall is the result of an instability of the air-liquid interface. Waves appear, with their fronts in the direction of the flow. Their

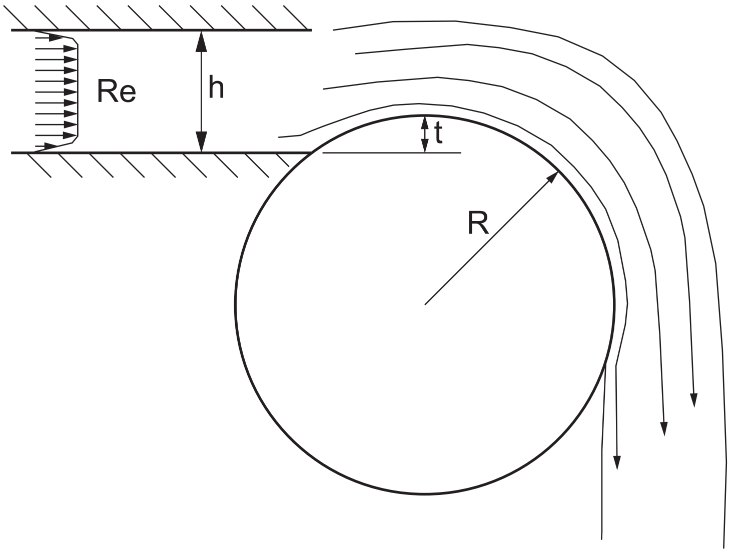

Figure D.3: 2*D* Coanda experiment.

amplitude may grow quickly and the film breaks up into separate jets and finally into droplets.

Bibliography

Bibliography

[1] Angehrn, R. Safety engineering for the 423 mw-pelton-runners at bieudron. In Hydraulic Machinery and Cavitation [47]. Proceedings of the 20^{th} IAHR Symposium.

[2] Angehrn, R., and Dubas, M. Experimental stress analysis on a 260 mw pelton runner. In *Hydraulic Machinery and Cavitation* (Amsterdam, NL, 13-17 September 1982), vol. 2 of *48*, pp. 1–10. Proceedings of the 11^{th} IAHR Symposium.

[3] Angehrn, R., and Dubas, M. Inspection periods of pelton runner. In *Hydraulic Machinery and Cavitation* (Sterling, UK, 1984), pp. 422–444. Proceedings of the 12^{th} IAHR Symposium.

[4] Angehrn, R., Grein, H., Keiser, W., and Kloter, H. The maintenance of pelton turbine runners. *Hydropower & Dams 1*, Issue Two (1994), 35–40.

[5] Angehrn, R., Rettich, J., and Schärer, C. Pelton runner design based on measured unsteady pressure distributions in the bucket. *Hydropower & Dams 6*, Issue Six (1999), 53–57.

[6] Avellan, F., Dupont, P., Kvicinsky, S., Chapuis, L., Parkinson, E., and Vullioud, G. Flow calculations in Pelton turbines - part 2: Free surface flows. In Brekke et al. [13], pp. 294–305. Proceedings of the 19th IAHR Symposium.

[7] Bachman, P., Schärer, C., Staubli, T., and Vullioud, G. Experimental flow studies on a 1-jet model pelton turbine. In Hydraulic Machinery and Cavitation [46], pp. 1–13. Proceedings of the 15^{th} IAHR Symposium.

[8] Bendat, J. S., and Piersol, A. G. *Random data : analysis and measurements procedures*, 2^{nd} ed. John Wiley, 1986. ISBN: 0-471-04000-2.

[9] Bovet, T. *La turbine Pelton: Extrait du cours de machines hydrauliques de T.B. (4ème semestre).* Lausanne: AEEPL, Switzerland, 1952.

[10] Brackbill, J. U., Kothe, D. B., , and Zemach, C. A continuum method for modelling surface tension. *Journal of Computational Physics 100* (1992), 335–354.

[11] Brekke, H. A general study of the design of vertical pelton turbines. In *turboinstitut* (B. Velensek and M. Bajd, 13-15 September 1984), B. Velensek and M. Bajd, Eds., vol. 1, pp. 383–397. Proceedings of the conference on hydraulic machinery and flow measurements.

[12] Brekke, H. State of the art in pelton turbine design. *Hydropower & Dams 1*, Issue Two (1994), 21–28.

[13] Brekke, H., et al., Eds. *Hydraulic Machinery and Cavitation* (Singapore, 9-11 September 1998), vol. 1, World Scientific. Proceedings of the 19th IAHR Symposium.

[14] Brennen, C. E. *Cavitation and bubble dynamic.* Oxford University Press, New York and Oxford, 1995. ISBN 0-19-509409-3.

[15] Brivio, R., and Zappi, O. La cavitazione nelle turbine pelton (parte i). *L'energia elettrica 72*, 2 (1995), 45–49.

[16] Brivio, R., and Zappi, O. La cavitazione nelle turbine pelton (parte ii). *L'energia elettrica 73*, 4 (1996), 266–270.

[17] Chanson, H. Air bubble entrainment in turbulent water jets discharging into the atmosphere. *Transactions of the Australian Civil/Structural Engineering CE39*, 1 (1996), 39–48.

[18] Chapuis, L. *Pelton turbines.* IMHEF - INPG Inter-university intensive and specialized course on Hydraulic Machines Engineering. Lausanne: AEEPL, Switzerland, 2000.

[19] Cook, S. C. Erosion by water-hammer. *Proceedings of the Royal Society A119* (1928), 481–488.

[20] Costigan, G., and Whalley, P. B. Measurements of the speed of sound in air-water flows. *Journal of chemical engineering 66* (1997), 131–135.

[21] Coutier-Delgosha, O., Fortes-Patella, R., and Reboud, J.-L. Evaluation of the turbulence model influence on the numerical simulations of unsteady cavitation. *Journal of Fluids Engineering 125* (2003), 38–45.

[22] Doble, W. A. The tangential water-wheel. *Transactions of the American Institute of Mining Engineers, California Meetting 29* (1899), 852–894.

[23] Dodu, J. Similitude des jets liquides à grande vitesse. In *Comité Machines Hydraulique et Equipement* (Nice, 16-20 September 1960), Société hydrotechnique de France. Proceedings of the 1^{st} IAHR Symposium.

[24] Dormy, E. *Modélisation numérique de la dynamo terrestre.* PhD thesis, Institut de physique du globe de Paris, 1997.

[25] Edgerton, H. E. *Electronic Flash, Strobe*, 2^{nd} ed. The MIT Press, Cambridge, Massachussetts, USA, 1970.

[26] Farhat, M., Natal, S., Avellan, F., Paquet, F., and Couston, M. Onboard pressure measurements and strain fluctuations in a model of a low head francis turbine. In Hydraulic Machinery and Systems [48], pp. 865–871. Proceedings of the 21^{th} IAHR Symposium.

[27] Ferrando, L. *Optimum design procedure for hydraulic turbines*. PhD thesis, École Polytechnique Fédérale de Lausanne, 2006.

[28] Field, J. E. Liquid impact: theory, experiment, applications. *ELSI Conference: invited lecture Wear 233-235* (1996).

[29] Grein, H. Cavitation pitting and rain erosion on pelton runners. In Hydraulic Machinery and Cavitation [46], pp. 1–9. Proceedings of the 15^{th} IAHR Symposium.

[30] Grein, H., Meier, J., and Klicov, D. Efficiency scale effects in pelton turbines. In Hydraulic Machinery, Equipment and Cavitation [50]. Proceedings of the 13^{th} IAHR Symposium.

[31] Grein, H. L. Efficiency prediction for pelton machines. In Velensek and Bajd [110], pp. 109–117. Proceedings of the conference on hydraulic machinery and flow measurements.

[32] Grein, H. L., and Angehrn, R. Service life of pelton runners under corrosion fatigue. In *ASME Winter Annual Meeting, International Symposium on Fluid Machinery Troubleshooting* (Anaheim, California, USA, December 1986), pp. 21–28.

[33] Grozev, G., Obretenov, V., and Trifonov, T. Investigation of the distribution of pressure over the buckets of a pelton turbine. In Velensek and Bajd [110], pp. 119–125. Proceedings of the conference on hydraulic machinery and flow measurements.

[34] Guennoun, F. *Etude physique de la cavitation du bord d'attaque*. PhD thesis, École Polytechnique Fédérale de Lausanne, 2006.

[35] Guibauld, M., Houdeline, J. B., and Philibert, R. Study of the flow in the various sections of a pelton turbine. In *Hydraulic Machinery and Cavitation* (Sao Paulo, Brazil, 14-18 September 1992), pp. 819–831. Proceedings of the 16^{th} IAHR Symposium.

[36] Hana, M. Improvement of a graphical method for calculation of flow on a pelton bucket. In *Hydraulic Machinery and Cavitation* (Dordrecht, NL, 1996), E. Cabrera, V. Espert, and F. Martinez, Eds., vol. 1, Kluwer Academic Publishers, pp. 111–119. Proceedings of the $XVIII$ IAHR Symposium.

[37] Hana, M. A discussion on numerical simulation in pelton turbines. In Brekke et al. [13]. Proceedings of the 19th IAHR Symposium.

[38] Hana, M. *Numerical analysis of non-stationary free surface flow in a Pelton bucket"*. PhD thesis, Norwegian University of Science and Technology, 1999. ISBN: 82-471-0387-7.

[39] He, L., and Sato, K. Numerical solution of incompressible unsteady flows in turbomachinery. *Journal of Fluids Engineering 123* (2001), 680–685.

[40] Henry, P. *Turbomachines hydrauliques*, 1^{st} ed. PPUR, Ecublens, Switzerland, 1992. ISBN 2-88074-209-9.

[41] Héraud, D. *Dispersion des jets liquides: influence des rugosités de paroi.* PhD thesis, Université de Grenoble, 1966.

[42] Heritage, J. R., and Enever, K. J. Surge pressures caused by impact of a high speed water jet on a solid surface. In *Pressure Surges* (Cranfield, Bedford, UK, 21-23 September 1983), BHRA fluid engineering, pp. 213–229. Proceedings of the 4^{th} International Conference on Pressure Surges.

[43] Hirt, C. W., and Nichols, B. D. A computational method for free surface hydrodynamics. *Transaction of the ASME: Journal of Pressure Vessel Technology 103*, 2 (1981), 136–141.

[44] Hirt, C. W., and Nichols, B. D. Volume of fluid(vof) method for the dynamics of free boundaries. *Journal of Computational Physics 39*, 1 (1981), 201–225.

[45] Hussain, A. K. M. F., and Ramjee, V. Effects of the axisymmetric contraction ratio on free-stream turbulence. *Journal of fluids engineering 98* (1976), 506–515.

[46] *Hydraulic Machinery and Cavitation* (Belgrade, Yugoslavia, 11-14 September 1990). Proceedings of the 15^{th} IAHR Symposium.

[47] *Hydraulic Machinery and Cavitation* (Charlotte, 7-9 August 2000), World Scientific. Proceedings of the 20^{th} IAHR Symposium.

[48] *Hydraulic Machinery and Systems* (Lausanne, Switzerland, 9-12 September 2002), EPFL-LMH. Proceedings of the 21^{th} IAHR Symposium.

[49] *Hydraulic Machinery and Systems* (Stockholm, Sweden, 29 June-2 July 2004), Vattenfall. Proceedings of the 22^{nd} IAHR Symposium.

[50] *Hydraulic Machinery, Equipment and Cavitation* (Montreal, Août 1986). Proceedings of the 13^{th} IAHR Symposium.

[51] Ishii, M. *Thermo-Fluid Dynamic Theory of Two-Phase Flow.* Collection de la Direction des Études et Recherches d'Électricité de France. Eyrolles, Paris, France, 1975.

[52] Janetzky, B. *Ein Verfahren zur Berechnung instationärer Strömungen mit freier Oberfläche.* PhD thesis, Universität Stuttgart, 2001.

[53] Janetzky, B., Göde, E., Ruprecht, A., Keck, H., and Schärer, C. Numerical simulation of the flow in a pelton bucket. In Brekke et al. [13]. Proceedings of the 19th IAHR Symposium.

[54] Johnson, B. K. *Optics and optical instruments*, 1^{st} ed. Dover Publications, Inc, New York, 1960.

[55] Johnson, W., and Wickers, G. W. Transient stress distribution caused by water-jet impact. *Journal of Mechanical Engineering Science 15*, 4 (1973), 302–310.

[56] KECK, H., SCHÄRER, C., CUÉNOD, R., AND CATENI, A. Pelton technology for new plants and modernization schemes. *Hydropower & Dams 4*, Issue Two (1997), 104–108.

[57] KOROBKIN, A. Global characteristics of jet impact. *Journal of fluid mechanics 307* (1996), 63–84.

[58] KOSHIZUKA, S., TAMAKA, H., AND OKAY, Y. A particle method for incompressible viscous flow with fluid fragmentation. *Journal of Computational Fluid Dynamics 4* (1995), 29–46.

[59] KOVALEV, N. N. *Hydroturbines - design and construction.* Mashiostroite l'noi literatury, Moscow-Leningrad, 1961.

[60] KUBOTA, T., NAKANISHI, Y., HAN, F., LIU, J., AND MASUDA, J. Deviation angle of a free jet in pelton turbines. In Hydraulic Machinery and Cavitation [47]. Proceedings of the 20^{th} IAHR Symposium.

[61] KUBOTA, T., XIA, J., TAKEUCHI, H., SAITO, T., AND J. MASUDA, Y. N. Numerical analysis of free water sheet flow on pelton buckets. In Brekke et al. [13]. Proceedings of the 19th IAHR Symposium.

[62] KUHLMANN, H. C., AND RATH, H. J. *Free surface flows.* Springer publishing, Wien, Austria, 1998. ISBN 3-211-83140-1.

[63] KUNT, M. *Traitement des signaux numériques*, deuxième ed., vol. XX. Presses polytechniques romandes, Lausanne, Switzerland, 1984. ISBN: 2-88074-060-6.

[64] KVICINSKY, S. *Méthode d'analyse des écoulements 3D à surface libre: application aux turbines Pelton.* PhD thesis, École Polytechnique Fédérale de Lausanne, 2002.

[65] KVICINSKY, S., KUENY, J. L., AND AVELLAN, F. Numerical and experimental analysis of the free surface flows in a 3d non-rotating pelton bucket. In *The 9^{th} international Symposium on transport phenonmena and dynamic rotating machinery* (Honolulu, Hawaii, USA, 10-14 February 2002).

[66] KVICINSKY, S., KUENY, J. L., AVELLAN, F., AND PARKINSON, E. Experimental and numerical analysis of free surface flows in a rotating bucket. In Hydraulic Machinery and Systems [48], pp. 359–364. Proceedings of the 21^{th} IAHR Symposium.

[67] KVICINSKY, S., LONGATTE, F., AVELLAN, F., AND KUENY, J. L. Free surface flow : experimental validation of volume of fluid (vof) method in the plane wall case. In *Proceedings of the 3^{rd} ASME/JSME Joint Fluids Engineering Conference* (San Francisco, California, USA, 18-23 July 1999).

[68] LEE, I., AND SUNG, J. J. Piezoelectric film for sensing unsteady wall pressure fluctuations. *1997 ASME Fluids Engineering Division Summer Meeting FEDSM '97-3208* (June 22-26 1997), 1–3.

[69] LOWY, R. Efficieny analysis of pelton wheels. *Transactions of the ASME 66* (1944), 527–538.

[70] Lucy, L. A numerical approach to the testing of the fission hypothesis. *Journal of Astronomy 82*, 12 (1977), 1013–1024.

[71] Mack, R., and Moser, W. Numerical investigations of the flow in a pelton turbine. In Hydraulic Machinery and Systems [48], pp. 373–378. Proceedings of the 21^{th} IAHR Symposium.

[72] Marongiu, J., Leboeuf, F., and Parkinson, E. Numerical simuation of the flow in a pelton turbine using the meshless method sph: a new simple solid boundary treatment. In 7^{th} *European Turbomachinery Conference (submitted to and accepted for publication)* (Athens, Greece, 2007).

[73] Marongiu, J. C., Leboeuf, F., Favre, J. M., and Parkinson, E. Numerical simulation of the flow in a pelton turbine using the meshless method sph. In *Hydro 2006 Conference* (Porto Caras, Greece, 25-28 September 2006). Hydro 2006: Development, Management, Performances.

[74] Menter, F. Two-equation eddy-viscosity turbulence models for engineering applications. *AIAA-Journal 32*, 8 (1994).

[75] Milanese, F. Un cas particulier de caviation dans les turbines pelton. In Hydraulic Machinery, Equipment and Cavitation [50]. Proceedings of the 13^{th} IAHR Symposium.

[76] Monaghan, J. J. Smoothed particle hydrodynmics. *Annual Review of Astronomics and Astrophysics 30* (1992), 543–574.

[77] Nakanishi, Y., Fuji, T., Morinaka, M., and Wachi, K. Numerical simulation of flows on pelton turbine buckets by particle method, part ii. In *Hydraulic Machinery and Systems* (Yokohama, Japan, 17-21 September 2006), Yokohama National University. Proceedings of the 23^{nd} IAHR Symposium.

[78] Nakanishi, Y., Kubota, T., and Shin, T. Numerical simulation of flows on pelton turbine buckets by particle method. In Hydraulic Machinery and Systems [48], pp. 379–384. Proceedings of the 21^{th} IAHR Symposium.

[79] Nitsche, W., Mirow, P., and Szodruch, J. Piezo-electric foils as a mean of sensing unsteady surface forces. *Experiments in Fluids 7*, 8 (September 1989), 111–118.

[80] Nonoshita, T., Matsumoto, Y., Kubota, T., and Ohashi, H. Calculation of the jet accompanied with water droplets in a pelton turbine. In *Cavitation and gas-liquid flow in fluid machinery and devices* (Hilton Head, South Carolina, USA, 13-18 August 1995), S. Ceccio, Ed., vol. 226. The American Society of Mechanical Engineers.

[81] Oguey, P. *Etude théorique et expérimentale de la dispersion du jet dans la turbine Pelton.* Société du bulletn technique de la Suisse Romande, Lausanne, Switzerland, 1944.

[82] Oguey, P. *Le calcul du rendement dans la roue de turbine Pelton*, f. rouge ed. 4. Librairie de l'Université, Lausanne, Switzerland, 1948.

[83] Paratte, P. A., and Robert, P. *Systèmes de mesure*, 1^{st} ed., vol. XVII of *Traité d'électricité*. PPUR, Ecublens, 1986.

[84] Parkinson, E., Vuilloud, G., Geppert, L., and Keck, H. Analysis of pelton turbine flow patterns for improved runner-component interaction. *Hydropower & Dams*, Issue Five (2002), 100–103.

[85] Pereira, F. *Prédiction de l'érosion de cavitation: approche énergétique.* PhD thesis, École Polytechnique Fédérale de Lausanne, 1997.

[86] Pereira, F., Farhat, M., and Avellan, F. Dynamic calibration of transient sensors by spark generated cavity. *Proceedings of IUTAM Symposium on Bubble Dynamics and Interface Phenomena* (September 1993).

[87] Perrig, A., Avellan, F., Kueny, J. L., Farhat, M., and E.Parkinson. Flow in a pelton turbine bucket: Numerical and experimental investigations. *Transactions of the ASME: Journal of Fluids Engineering 128*, 4 (2006), 350–358.

[88] Perrig, A., Farhat, M., Avellan, F., Parkinson, E., Garcin, H., Bissel, C., Valle, M., and Favre, J. Numerical flow analysis in a pelton turbine bucket. In Hydraulic Machinery and Systems [49]. Proceedings of the 22^{nd} IAHR Symposium.

[89] Pope, S. B. *Turbulent Flows.* Cambridge University Press, 2000. ISBN 0-521 59886-9.

[90] Raabe, J. The negative efficiency scale effect in pelton turbines and its causes. In *Hydraulic Machinery and Systems* (Tokyo, Japan, August 1980), pp. 689–702. Proceedings of the 10^{nd} IAHR Symposium.

[91] Raabe, J. *Hydropower.* VDI-Verlag GmbH, Düsseldorf, 1985.

[92] Reboud, J.-L., Stutz, B., and Coutier-Delgosha, O. Two-phase flow structure of cavitation : Experiment and modeling of unsteady effects. In *Proc. Third Int. symposium on cavitation* (Grenoble, France, April 1998), vol. 1, pp. 39–44.

[93] Risberg, S., and Haugen, J. O. Upgrading of pelton turbines - observations of how turbine design influence on model to prototype efficiency scaling. In Hydraulic Machinery and Systems [49]. Proceedings of the 22^{nd} IAHR Symposium.

[94] Rodi, W. *Turbulence models and their application in hydraulics -A state of the art review*, second ed., vol. AIRH. 1984. ISBN 90-212-7002-1.

[95] Ruff, G. A., Sagar, A. D., and Faeth, G. M. Structure and mixing properties of pressure-atomized sprays. *AIAA 27*, 7 (1989), 901–908.

[96] Ryhming, I. L. *Dynamique des fluides*, 2^{eme} ed. PPUR, Ecublens, Switzerland, 1991. ISBN 2-88074-224-2.

[97] Sadlo, F., Peikert, R., and Parkinson, E. Vorticity based flow analysis and visualization for pelton turbine design optimization. *Proceedings of IEEE Visualization '04* (October 10-15 2004), 179–186.

[98] Senocak, I. *Computational Methodology for the Simulation Turbulent Cavitating Flows.* PhD thesis, University of Florida, 2002.

[99] Shivamoggi, B. K. *Theoretical Fluid Dynamics*, 2^{nd} ed. John Wiley and sons, New York, New York, USA, 1997.

[100] Sick, M., Keck, H., Parkinson, E., and Vuilloud, G. New challenges in pelton research. In *Hydro 2000 Conference* (Bern, Switzerland, 2000). Hydro 2000 Conference.

[101] Skalak, R., and Feit, D. Impact on the surface of a compressible fluid. *Journal of Engineering for industry, Transactions of the ASME* (1966), 325–331.

[102] Stewart, H. B., and Wendroff, B. Two-phase flow: Models and methods. *Journal of Computational Physics 56* (1984), 363–409.

[103] Tenot, A. *Turbines hydrauliques et régulateurs automatiques de vitesse*, eyrolles ed., vol. Livre II. Paris, France, 1932.

[104] Tenot, A. *Turbines hydrauliques et régulateurs automatiques de vitesse*, eyrolles ed., vol. Livre I. Paris, France, 1932.

[105] Teodorescu-Tintea, C. On a new functional principle in the theory of gas turbines based on the coanda effect. the turbine fitted with depressive blades. *Rev. Roum. Sc. Tech. Mec. Appl. 12*, 1 (1967), 85–101.

[106] Traversaz, M., Leroy, P., Zoppé, B., and Maître, T. Numerical study of pelton bucket flow comparison of fluent and cfx results. In Hydraulic Machinery and Systems [48], pp. 365–372. Proceedings of the 21^{th} IAHR Symposium.

[107] Truong, T. V. *Techniques de mesure*, 4^{th} ed. Polycopié EPFL. DGM, Ecublens, 1999.

[108] Tseng, L. K., Ruff, G. A., and Faeth, G. M. Effects of gas density on the structure of liquid jets in still gases. *AIAA 30*, 6 (1992), 1537–1544.

[109] Vaidyanathan, R., Senocak, I., Wu, J., and Shyy, W. Sensitivity evaluation of a transport-based turbulent cavitation model. *Journal of Fluids Engineering 125* (2003), 447–458.

[110] Velensek, B., and Bajd, M., Eds. *turboinstitut* (Ljubljana, Yugoslavia, 13-15 September 1988). Proceedings of the conference on hydraulic machinery and flow measurements.

[111] Vercellini, R. Contribution à l'analyse des résultats d'essais de turbines pelton. Tech. Rep. 8, Informations techniques Charmilles, 1961.

[112] Versteegand, H.-K., and Malalasekera, W. *An introduction to Computational Fluid Dynamics: The finite volume method.* Pearson Prentice Hall, New York, 1995. ISBN 0-582 21884-5.

[113] Vivier, L. *Turbines hydrauliques et leur régulation.* Albin Michel, Paris, 1966.

[114] von Glahn, U. H. Use of the coanda effect for obtaining jet deflection and lift with a single flat-plate deflection surface. *National Advisory Committee for Aeronautics, tech. note n*°4272 (1958), 1–49.

[115] Vullioud, G. *Les turbines Pelton.* IMHEF - INPG programme inter-universitaire de formation à Lausanne et Grenoble. Lausanne: AEEPL, Switzerland.

[116] Wagenbach, W. *Neuere Turbinenanlagen : Auf Veranlassung von Professor E. Reichel und unter Benutzung seines Berichtes "Der Turbinenbau auf der Weltausstellung in Paris 1900" bearbeitet.* Julius Springer, Berlin, Germany, 1905.

[117] Walker, D. T. On the origin of the 'surface current' in turbulent free-surface flows. *J. Fluid Mech. 339* (1997), 275–285.

[118] Webster, J. Analysis of jet-type impulse turbines. *Water Power* (1971), 287–292.

[119] Wilcox, D. C. *Turbulence Modeling for CFD*, 2^{nd} ed. DCW Industries Inc., Washington DC, 1998. ISBN 0-963 6051-5-1.

[120] Wille, R., and Fernholz, H. Reports on the first european mechanics colloquium on the coanda effect. *Journal of Fluid Mechanics 23* (1965), 801–819.

[121] Zoppé, B. *Simulation numérique et analyse de l'écoulement dans les augets des turbines Pelton.* PhD thesis, INPG, 2004.

List of Figures

1.1 Pelton turbine original patent document. 4
1.2 6-injector vertical-axis Pelton runner [40]. 5
1.3 2-injector horizontal-axis Pelton turbine [40]. 5

2.1 External stroboscopic flow visualization (Courtesy of VATech Hydro SA). 8
2.2 Pressure pulse signal [66]. 10
2.3 Test runner. 13
2.4 Test runner during assembly. 13
2.5 Hillchart and operating points investigated. 14

3.1 Velocity of a water particle in a runner channel (a) in meridian and (b) horizontal planes. 19

4.1 Schematized view of a Pelton turbine. 23
4.2 Idealized velocity triangle in a $2D$ bucket. 24
4.3 Power and torque output as a function of peripheral velocity coefficient. 25
4.4 Relative paths of the water particles. 27
4.5 Bucket rearward flow deviation. 27

5.1 surface tension. 31

7.1 Bucket angular datum definition. 45

8.1 The Pelton test rig of VA Tech Hydro SA. 49
8.2 Test rig casing and plexiglas window. 50

9.1 Wheatstone bridge of a piezo-resistive sensor. 51
9.2 Instrumented shaft main organs. 52
9.3 Synchronization diagram of the instrumented shaft. 53
9.4 Location of the 43 pressure sensors. 53
9.5 Instrumented runner construction. 55
9.6 Calibration curves and relative errors obtained for 4 sensors. 57

10.1 Karl Storz 3.8 mm diameter borescope. 61
10.2 Onboard endoscope location and field of observation. 62
10.3 Experimental setup for the onboard visualizations. 63
10.4 Trigger chain for the onboard visualizations. 64
10.5 Distal lens wiping system. 65
10.6 External visualization configuration, frontal view. 66
10.7 External visualization configuration, top view. 67

11.1 Apparent grid displacement. Continuous line: actual grid. Dashed line: apparent grid. 69
11.2 Simplified optical model. 70
11.3 Apparent grid interpolation. 71
11.4 Thickness measurement validation test setup. 71
11.5 Thickness measured by refraction vs. reference thickness. 72
11.6 Film thickness error evolution. 73

12.1 Unstructured meshes used for the numerical simulations. 77
12.2 Computational domain and boundary conditions applied. 78
12.3 Mesh dependency. 79
12.4 Bucket zones. 80
12.5 Comparison of the pressure coefficients, part I. 81
12.6 Comparison of the pressure coefficients, part II. 82
12.7 Comparison of the water film thickness. 83
12.8 Comparison of the relative flow patterns, part I. 85
12.9 Comparison of the relative flow patterns, part II. 86

13.1 Duty cycle sequence 89
13.2 Bucket onboard film sequence, OP1, $\psi_1/\psi_1^{\wedge} = 0.89$, $\varphi_{B_2}/\varphi_{B_2}^{\wedge} = 1.07$. 91
13.3 Bucket onboard film sequence, OP3, $\psi_1/\psi_1^{\wedge} = 1.07$, $\varphi_{B_2}/\varphi_{B_2}^{\wedge} = 1.20$. 92
13.4 Bucket onboard film sequence, OP5, $\psi_1/\psi_1^{\wedge} = 1.00$, $\varphi_{B_2}/\varphi_{B_2}^{\wedge} = 0.95$. 93
13.5 Bucket onboard film sequence, OP14, $\psi_1/\psi_1^{\wedge} = 1.000$, $\varphi_{B_2}/\varphi_{B_2}^{\wedge} = 0.54$. 94
13.6 Jet surface perturbation by droplets impact, OP1, $\psi_1/\psi_1^{\wedge} = 0.89$, $\varphi_{B_2}/\varphi_{B_2}^{\wedge} = 1.07$. 95
13.7 Bucket external observation, OP1, $\psi_1/\psi_1^{\wedge} = 0.89$, $\varphi_{B_2}/\varphi_{B_2}^{\wedge} = 1.07$. 95

14.1 Initial jet/bucket contact. 97
14.2 Erosion damages in the cutout area of a prototype turbine. 98
14.3 $2D$ velocity triangle at the instant of impact. 99
14.4 $2D$ wedge impact on a water surface. 99
14.5 Kinematic path of the tip. 100
14.6 Bucket angle of setting definition. 101
14.7 Variation of the angle of attack γ with respect to ψ_1 and D_2. 102
14.8 Configuration of wedge at the instant of impact. 103
14.9 Wetted surface of wedge in $(x - t)$-plane. 103
14.10 Impact problem solution. 104
14.11 Jet surface protuberances and craters convected. 104
14.12 Spillway effect during the jet cut. 106
14.13 Erosion damages in reduced scale models [15]. 107
14.14 Zone with high pressure peaks, $\varphi_{B_2}/\varphi_{B_2}^{\wedge} = 1.12$, $\psi_1/\psi_1^{\wedge} = 0.89$, $H = 20m$. 108
14.15 Pressure peak evolution with respect to φ_{B_2}, ψ_1, and H'. 109
14.16 Sensor 14 during initial jet impact. 110
14.17 Path of the lateral flow. 111
14.18 Impact peak determination procedure. 112

15.1 Backside pressure signals, $H = 20m$, $s/s^{\wedge} = 1.34$. 114
15.2 Backside pressure signals, $H = 35m$, $s/s^{\wedge} = 1.34$. 115

15.3 Backside pressure signals, $H = 60m$, $s/s^\wedge = 1.34$. 116
15.4 Backside pressure signals, $H = 80m$, $s/s^\wedge = 1.34$. 117
15.5 Evolution with respect to ψ_1 of bucket j relative angle of attack α along bucket j duty cycle. 118
15.6 Definition of the Bucket Hydrodynamic Chord, BHC. 119
15.7 BHC pressure distribution, OP1($\psi_1/\psi_1^\wedge = 0.89$ and $\varphi_{B_2}/\varphi_{B_2}^\wedge = 1.07$). . . 120
15.8 BHC pressure distribution, OP3($\psi_1/\psi_1^\wedge = 1.12$ and $\varphi_{B_2}/\varphi_{B_2}^\wedge = 1.20$). . . 121
15.9 BHC pressure distribution, OP14($\psi_1/\psi_1^\wedge = 1.00$ and $\varphi_{B_2}/\varphi_{B_2}^\wedge = 0.54$) . 122
15.10 Successive stagnation points at jet front. 123
15.11 Rotation-induced pressure variation on the bucket backside. 124
15.12 Coanda effect on the bucket backside. (a) Longitudinal effect; (b) transversal effect. 124
15.13 Coanda effect observed, $OP1(\psi_1/\psi_1^\wedge = 0.89$ and $\varphi_{B_2}/\varphi_{B_2}^\wedge = 1.07)$. . . . 125
15.14 Erosion pits observed on the resin buckets. 127
15.15 Bucket ribs angle δ_{ribs}. 128
15.16 Experimental backside torque. 129
15.17 Fragmented jet impingement on the bottom surface of the bucket. . . . 129

16.1 Definition of the 5 bucket zones. 131
16.2 Pressure signals, OP1($\psi_1/\psi_1^\wedge = 0.89$, $\varphi_{B_2}/\varphi_{B_2}^\wedge = 1.07$). 132
16.3 Pressure signals, OP3($\psi_1/\psi_1^\wedge = 1.07$, $\varphi_{B_2}/\varphi_{B_2}^\wedge = 1.20$). 133
16.4 Pressure signals, OP5($\psi_1/\psi_1^\wedge = 1.00$, $\varphi_{B_2}/\varphi_{B_2}^\wedge = 0.95$). 134
16.5 Pressure signals, OP14($\psi_1/\psi_1^\wedge = 1.000$, $\varphi_{B_2}/\varphi_{B_2}^\wedge = 0.54$). 135
16.6 Water film thickness signal, $\psi_1/\psi_1^\wedge = 0.89$. 136
16.7 Water film thickness signal, $\psi_1/\psi_1^\wedge = 1.12$. 137
16.8 Water film thickness signal, $\psi_1/\psi_1^\wedge = 1.00$. 138
16.9 Relative velocity change with respect to the radial position. 141
16.10 Crossing of streamlines. 142
16.11 Formation of the T-shaped tumescence. 143
16.12 Interference mixing. 144
16.13 Flow stratification. 145
16.14 Velocity profile evolution. 146

17.1 Lateral face pressure signals, $H = 20m$. 148
17.2 Lateral face pressure signals, $H = 35m$. 149
17.3 Lateral face pressure signals, $H = 60m$. 150
17.4 Lateral face pressure signals, $H = 80m$. 151
17.5 Lateral zones of the bucket. 152
17.6 Outlet heeling, frontal area. 152

18.1 Delaunay triangulation and definition of the bucket zones. 156
18.2 Bucket power distribution. 157
18.3 Runner power fluctuations. 158
18.4 Runner power amplitude spectra. 160

19.1 Bucket j energy distribution. 162
19.2 Sensor l volume of control. 163
19.3 Euler Momentum transfer vs. force measurement, sensor 15. 164

19.4 Force comparison, sensor 15. 165

C.1 Jet out of a Pelton turbine injector (Courtesy of VATech Hydro SA). . 183
C.2 Jet spread angle dependence. 185
C.3 Jet spread and radial void fraction estimation. 187
C.4 Speed of sound for air-water mixtures. 188

D.1 Deflexion of a vertical jet by a cylindrical body. 189
D.2 Possible types of velocity profiles in the Coanda effect. 191
D.3 $2D$ Coanda experiment. 192

List of Tables

2.1 Characteristic scales of the flow in a Pelton turbine model. 7
2.2 Test runner data. 12
2.3 Operating points investigated. 15

8.1 VA Tech horizontal axis Pelton turbine test rig characteristics. 49

9.1 Sensors characteristics. 52
9.2 Sensors distribution. 53
9.3 Huber characteristics. 55

10.1 High-speed camera specifications. 61
10.2 Flashlamps specifications. 61
10.3 Frame rates and exposure time. 65

11.1 Uncertainties on the primary variables. 73

12.1 Mesh dimensions, model comparison. 75
12.2 Mesh dimensions, detailed simulation. 76
12.3 Specifications of the Mixture Model. 76

15.1 Minimum pressure coefficient recorded vs. theoretical cavitation inception condition, sensor 31. 126

Index

Angle
    outflow, 24
ArcNet, 52

BCPS, 63
    definition, 60
Bessel
    function, 184
BHC, 118, 126
Blur
    distance, 59
Borescope, 60, 61, 64, 71, 72, 80, 90, 125, 169
Boundary
    conditions, 76
Boussinesq, 40
Bucket
    angle of attack, 98, 107, 113, 118, 123, 125, 126, 139, 140, 159, 170
    angle of impact, 98, 99, 101
    angle of setting, 26, 101, 155
    backside, 8, 12, 27, 113, 123, 126, 147, 161, 172
    center of pressure, 126
    cutout, 8, 9, 27, 84, 90
    design, 12
    duty cycle, 12, 14, 45, 73, 84, 89, 90, 97, 113, 127, 155, 163, 171
    hydrodynamic chord, 118
    inner surface, 8, 10, 12, 62, 77, 169, 170
    lips, 8, 89, 97, 105, 171, 172
    number, 26
    outer edge, 75, 90, 109, 141
    outflow angle, 12
    power, 155, 171
    ribs, 90, 113, 124, 140
    root, 62, 90, 140
    sides, 12
    splitter, 26, 62, 90, 97, 141, 169
    tip, 8, 89, 97, 98
    zone, 156

Calibration
    dynamic, 56
    static, 54, 55, 169
Cavitation, 97, 153, 170, 172
    bubble, 125
    impact, 126
    inception, 125
Centrifugal
    force, 32
Channel, 52
Coanda
    effect, 123, 126, 140, 147, 170, 172, 189
Conservation equation
    2-Fluid, 36
    mixture, 37, 38
Coriolis
    acceleration, 142
    force, 31, 32, 142, 171

Delaunay
    triangulation, 155, 157
Delay line, 63
Density, 37
    spectral, 179
Diffusion
    numerical, 80
Discharge
    coefficient, 25
Discretization
    spatial, 75
Doble, 3
Domain
    computational, 75, 76
Drift velocity, 37

Ekman
    layer, 143
Energy
    coefficient, 12, 26, 89, 101
    exchange, 141
    kinetic, 23, 111, 155, 161
    transfer, 155, 161
Enthalpy, 37
Erosion
    damage, 8, 105, 126, 170
Euler
    equation, 21, 23, 24

Falaise
    effect, 141
FFT, 159, 171
Flash
    duration, 60, 61, 63
    jitter, 63
    Xenon, 61
Flow
    interference, 141
    stratification, 142
Fourier
    transform, 159, 178, 179
Frame
    rate, 63
Free-surface, 103, 170
    flow, 3, 7, 11, 13, 169, 172, 191
Friction, 24
Froude
    number, 7, 33
    similitude, 33

Guide
    factor, 60

Hanning
    window, 179
Heat transfer, 37
Heeling
    inlet, 27
    outflow, 12, 26, 54, 75, 147, 171
Hillchart, 12
Hydraulic
    efficiency, 7, 25, 26
Hydrofoil, 113, 123, 125, 172
Hysteresis
    error, 54, 55

Interaction
    jet/bucket, 8, 9, 12, 170–172
Interface, 3
    air-water, 10, 183
    jet, 184

Jet
    attachment, 113, 123, 126
    axis, 26, 105, 184, 186
    boundary, 170, 183
    core, 108
    deformation, 171
    deviation, 127
    diameter, 12, 26, 89, 90, 107, 161
    disintegration, 124, 125, 142
    energy, 127
    front, 90, 105, 108, 111, 123, 139, 157, 170
    generator, 26, 97, 98, 100, 123
    impact, 105, 107, 110, 139, 140
    interface, 183
    momentum, 183
    outburst, 90, 105, 170
    periphery, 103, 108
    separation, 90, 113, 123, 125, 159, 170
    spread, 104, 171, 185, 187
    surface, 89, 95, 97, 104, 105, 126

Kinetic
    momentum theorem, 19
Knight
    wheel, 3, 62

Laser, 10
Loss
    factor, 24
    mixing, 140, 141

Mach
    number, 98, 101, 104, 108, 171
    number(edge), 102–104
Model
    2-Fluid, 35, 36, 75, 76, 78, 80, 84, 109, 169, 173
    2-Phase Homogeneous, 11, 37, 38, 75, 78–80, 84, 169

  drift, 38
  hydroacoustic, 98, 104, 170
  mixture, 11, 37
Momentum
  of angular Momentum, 19
  of Momentum, 20
  angular, 126
  conservation, 75, 161, 171, 173
  transfer, 155, 161

Navier-Stokes
  equation, 11, 31, 32
Needle
  stroke, 107
Newton
  law of motion, 29
  second law, 161

Pelton, 3
  turbine, xi, 3, 7, 11, 169, 172
Piezo-resistive, 51
Pitch, 26
Power
  budget, 155
  distribution, 155
  fluctuation, 158
Prandtl, 40
Pressure
  coefficient, 46, 107, 123
  sensor, 52, 98

Refraction, 69
Reynolds
  equation, 39
  number, 7, 33, 125, 171, 185, 186, 191
  stress averaging, 39
  stress tensor, 39, 41
  theorem, 29, 30
Rossby
  number, 33, 171
Runner
  efficiency, 159
  torque, 126

Scale effects, 171
Sensitivity
  sensor, 55
Similitude
  criteria, 7
  kinematic, 123
Sine
  theorem, 69
Snell
  law, 70, 72
Spectrum
  amplitude, 179
  energy, 179
  Phase, 179
Speed
  coefficient, 28
  peripheral coefficient, 24, 25
  specific, 153
  specific coefficient, 26
Speed of sound, 101
Spillway
  effect, 105, 111, 170
Spread
  rate, 170
Stall, 124
Standard deviation, 177
Step-up, 8, 33
Surface tension, xii, 14, 37, 171, 172, 191
  coefficient, 30, 36, 39
  force, 31, 39, 125, 171

Taylor
  series, 181
Test rig, 49, 169
Thickness, 46
Trigger
  chain, 63, 65
  signal, 63
Tumescence, 141
Turbine
  design, 26
  impulse, 23
Turbulence
  stress-ω, 44
Turbulent
  blending function, 42
  diffusivity, 184, 185
  dissipation rate, 40
  intensity, 76
  kinetic energy, 40–42
  length scale, 76

  - mixing length, 40
  - Specific dissipation rate, 44
  - specific dissipation rate, 41, 42
  - Viscosity, 43
  - viscosity, 40–42
  - viscosity coefficient, 40
  - viscous dissipation, 40

Velocity
  - triangle, 99, 113, 123

Visualizations, 8, 59, 60, 169, 170
  - external, 9, 12, 64, 169
  - onboard, 12, 14, 61, 63, 65, 72, 169, 170

Void fraction, 184, 186

Volume fraction, 36, 37

Waterhammer
  - effect, 105, 170
  - equation, 108

Weber
  - number, 7, 33, 125, 171, 186

Wheatstone
  - bridge, 51

List of publications

2006	Perrig, A., Valle, M., Farhat, M., Parkinson, E., Favre, J., Avellan, F. *Onboard flow visualizations in a Pelton turbine bucket.* Proceedings of the 23^{nd} IAHR Symposium, Yokohama, 17-21 September
2006	Perrig, A., Avellan, F., Kueny, J.-L., Farhat, M., Parkinson, E. *Flow in a Pelton Turbine Bucket: Numerical and Experimental Investigations.* Transactions of the ASME: Journal of Fluids Engineering, vol.128(4), March 2006, 350-358
2005	Valle, M., Favre, J., Parkinson, E., Perrig, A., Farhat, M. *Scientific Data Management for Visualization Implementation Experience.* Proceedings of the SimVis 2005 conference, Magdeburg, 2-3 March
2004	Perrig, A., Farhat, M., Avellan, F., Parkinson, E., Garcin, H., Bissel, C., Valle, M., Favre, J. *Numerical flow analysis in a Pelton turbine bucket.* Proceedings of the 22^{nd} IAHR Symposium, Stockholm, 29 June-2 July

Vitae

Alexandre PERRIG
Ch. de Bérée 44
1010 Lausanne (VD)

Tél.:	+41 21 652 94 19	Suisse
Portable:	+41 78 710 28 46	Né le 26 décembre 1975
E-mail:	alexandre.perrig@epfl.ch	Marié

FORMATION ET TITRES

2006	Venture Challenge, UNIL-EPFL, Lausanne Cours Entrepreneurship et business plan.
1995-2001	École Polytechnique Fédérale de Lausanne (EPFL), Suisse **Diplôme d'Ingénieur Mécanicien**. Orientation Ingénerie des Fluides et de l'Énergie. Travail de diplôme à Virginia Tech, Blacksburg, USA. Etude de la combustion de méthane dans un écoulement supersonique.
1991-1994	Gymnase de Bellerive, **Maturité Fédérale**, type A(Latin-Grec), baccalauréat ès lettres, avec mention.

EXPÉRIENCES PROFESSIONNELLES

2002- 2006	Laboratoire de Machines Hydrauliques (LMH), EPFL **Assistant doctorant**. Activités de recherche et de développement. Etude des écoulements $3D$ instationnaires à surface libre dans les. turbines Pelton. Doctorat en collaboration avec VATech Hydro SA. - Mise au point de techniques de visualisations rapides de l'écoulement dans les. parties tournantes de machines hydrauliques. - Mesure de pression embarquées. - Calculs numériques. Encadrement de diplômants, préparation de séances d'exercice et d'examens.
2001	Laboratoire de Machines Hydrauliques (LMH), EPFL **Ingénieur** *R&D*. Conception d'un stand d'essai pour jet d'eau.
1995-2001	Armée Suisse, Forces terrestres, **Premier-lieutenant**, of lm chars. Management, instruction, gestion de crise, organisation personnelle.
1999	Laboratoire de Transfert de Chaleur et de Masse (LTCM), EPFL **Assistant-étudiant**.
1998	Algroup Alusuisse, Sierre, Suisse **Stage** d'usinage. Conception et fabrication d'une machine à vapeur miniature.

LANGUES

Français	Langue maternelle.
Anglais	Avancé.
Allemand	Avancé.
Portugais (Brésil)	Moyen.

COMPÉTENCES INFORMATIQUES

Systèmes d'exploitation	Windows, MS-DOS, Unix (IBM-AIX).
Programmation	Fortran, LabView, Visual Basic.
CFD	CFX10.
CAO	Catia.
Bureautique	MS-Office, Latex.
Multimédia	Suite Adobe.

SPORTS & LOISIRS

Sports	Fitness, trekking en montagne.
Loisirs	Vol (voltige, vol aux instruments), voyages, photographie, cuisine.